

**Springer Series in  
GEOMECHANICS & GEOENGINEERING**

Jacek Tejchman  
Jan Kozicki

**Experimental and Theoretical  
Investigations of Steel-Fibrous  
Concrete**

 Springer

# Springer Series in Geomechanics and Geoengineering

---

Editors: Wei Wu · Ronaldo I. Borja

Jacek Tejchman and Jan Kozicki

---

Experimental and  
Theoretical Investigations  
of Steel-Fibrous Concrete

**Professor Wei Wu**, Institut für Geotechnik, Universität für Bodenkultur, Feistmantelstraße 4, 1180 Vienna, Austria, E-mail: wei.wu@boku.ac.at

**Professor Ronaldo I. Borja**, Department of Civil and Environmental Engineering, Stanford University, Stanford, CA 94305-4020, USA, E-mail: borja@stanford.edu

## **Authors**

Prof. Jacek Tejchman  
Faculty of Civil and Environmental Engineering,  
Gdansk University of Technology  
Narutowicza 11/12, 80-952 Gdansk-Wrzeszcz  
E-mail: tejchmk@pg.gda.pl

Dr. Jan Kozicki  
Faculty of Civil and Environmental Engineering,  
Gdansk University of Technology  
Narutowicza 11/12,  
80-952 Gdansk-Wrzeszcz  
E-mail: jkozicki@pg.gda.pl

ISBN 978-3-642-14602-2

e-ISBN 978-3-642-14603-9

DOI 10.1007/978-3-642-14603-9

Springer Series in Geomechanics and Geoenvironmental Engineering ISSN 1866-8755

Library of Congress Control Number: 2010933356

© 2010 Springer-Verlag Berlin Heidelberg

This work is subject to copyright. All rights are reserved, whether the whole or part of the material is concerned, specifically the rights of translation, reprinting, reuse of illustrations, recitation, broadcasting, reproduction on microfilm or in any other way, and storage in data banks. Duplication of this publication or parts thereof is permitted only under the provisions of the German Copyright Law of September 9, 1965, in its current version, and permission for use must always be obtained from Springer. Violations are liable for prosecution under the German Copyright Law.

The use of general descriptive names, registered names, trademarks, etc. in this publication does not imply, even in the absence of a specific statement, that such names are exempt from the relevant protective laws and regulations and therefore free for general use.

*Type Design and Cover Design:* Scientific Publishing Services Pvt. Ltd., Chennai, India.

Printed on acid-free paper

5 4 3 2 1 0

springer.com



# Contents

<b>1 Introduction.....</b>	<b>1</b>
<b>2 General.....</b>	<b>3</b>
<b>3 Literature Overview.....</b>	<b>27</b>
3.1 Properties of Concrete with Steel Fibres.....	27
3.1.1 Quasi-Static Experiments.....	27
3.1.2 Dynamic Experiments.....	79
3.2 Properties of Reinforced Concrete with Steel Fibres.....	113
3.3 Conclusions.....	169
<b>4 Theoretical Models.....</b>	<b>171</b>
<b>5 Discrete Lattice Model.....</b>	<b>181</b>
5.1 Simulations of Fracture Process in Plain Concrete.....	193
5.2 Simulations of Fracture Process in Fibrous Concrete.....	216
5.2.1 Two-Dimensional Simulations of Uniaxial Extension.....	218
5.2.2 Three-Dimensional Simulations of Uniaxial Extension.....	247
5.2.3 Two-Dimensional Simulations of Three-Point Bending .....	266
5.3 Conclusions.....	267
<b>6 Epilogue .....</b>	<b>269</b>
References.....	271
<b>List of Symbols.....</b>	<b>287</b>
<b>Summary.....</b>	<b>289</b>

# 1 Introduction

**Abstract.** In this chapter, main disadvantages of concrete as a construction material are first described. Next, positive aspects from an application of short discrete fibres in concrete are stressed. In addition, parameters influencing the properties of concrete with fibres are briefly discussed. The outline of the book is also given.

Concrete is still the most widely used construction material since it has the lowest ratio between cost and strength as compared to other available materials. However, it has two undesirable properties, namely: low tensile strength and large brittleness (low energy absorption capacity) that cause the collapse to occur shortly after the formation of the first crack. Therefore, the application of concrete subjected to impact, earth-quaking and fatigue loading is strongly limited. To improve these two negative properties and to achieve a partial substitute of conventional reinforcement, an addition of short discontinuous randomly oriented fibres (steel, glass, synthetic and natural) can be practiced among others. Steel fibres are the most used in concrete applications due to economy, manufacture facilities, reinforcing effects and resistance to the environment aggressiveness. By addition of steel fibres, the following properties of plain concrete: tensile splitting strength, flexural strength, first cracking strength, toughness (area under the stress-strain curve), stiffness, durability, impact resistance, fatigue and wear strength increase, and deflection, crack width, shrinkage and creep are reduced (Shah and Rangan 1971, Bentur and Mindess 1990, Balaguru and Shah 1992, Zollo 1997). In turn, compressive strength can slightly increase (Shah and Rangan 1971, Mohammadi et al. 2008) or slightly decrease (Altun et al. 2007). Addition of steel fibres aids in converting the brittle characteristics to a ductile one. Fibres limit the formation and growth of cracks by providing pinching forces at crack tips. They bear some stress that occurs in the cement matrix and transfer the other portion of stress at stable cement matrix portions. Real effects of fibre addition can be observed as a result of the bridging stress offered by the fibres after the peak load. The fibre reinforced concrete specimens develop first a pattern of fine distributed cracks instead of directly failing in one localized crack. This is an important feature as it allows one for the design of structures that can provide a high margin of safety. The degree of concrete improvement depends upon many different factors such as: size, shape, aspect ratio (ratio between length and diameter), volume fraction, orientation and surface characteristics of fibres, ratio between fibre length and maximum aggregate size, volume ratio between long and short fibres and concrete class. The fibre orientation depends on the specimen size and flow

direction of the fresh concrete against the casting direction (Granju and Ringot 1989, Redon and Chermant 1999).

Fibre-reinforced concrete has found many applications in tunnel linings, wall cladding, bridge decks, pavements, slabs on grounds, factory (industrial) floors and slabs, dams, pipes, fire protection coatings, spray concretes (Balaguru and Shah 1992, Krstulovic-Opара et al. 1995, Falkner and Henke 2000, Schnütgen and Teutsch 2001, Walraven and Grünewald 2002). It can be also used as an efficient method for repair, rehabilitation, strengthening and retrofitting of existing concrete structures (Li et al. 2000).

In spite of positive properties, fibrous concrete did not find such acknowledgment and application as usual concrete. There do not still exist consistent dimensioning rules due to the lack sufficient large-scale static and dynamic experiments taking mainly into account the effect of the fibre orientation.

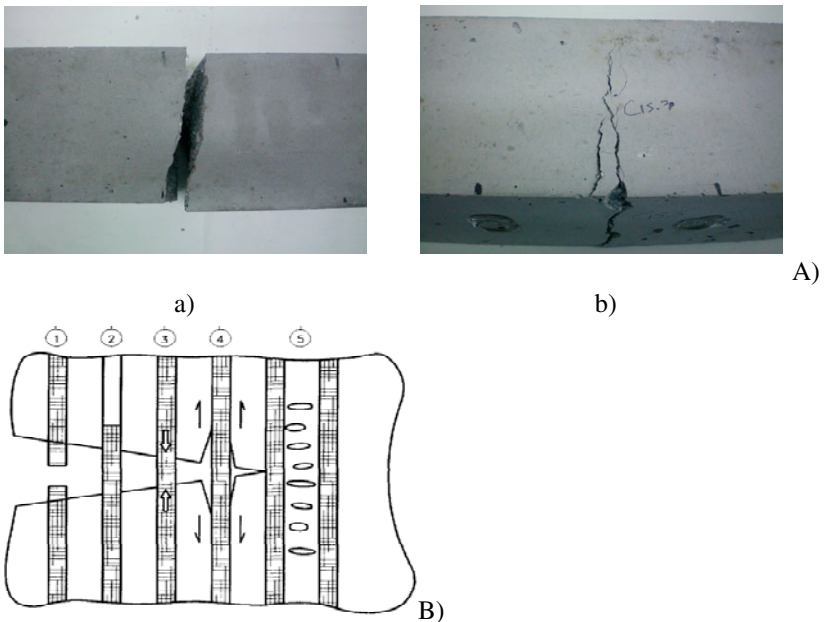
The intention of the book is twofold: first to summarize the most important mechanical and physical properties of steel-fibre-added concrete and reinforced concrete on the basis of numerous experiments described in the scientific literature, and second to describe a fracture process at meso-scale both in plain concrete and fibrous concrete using a novel discrete lattice model in different quasi-static boundary value problems (Kozicki and Tejchman 2007a, 2007b, 2008).

The book includes 6 Sections and is organized as follows. After a short introduction in Section 1, Sections 2 summarizes the most important properties of fibrous concrete. Section 3 includes detailed descriptions of experimental results on concrete and reinforced concrete elements with steel fibres from the scientific literature. Next, theoretical models from the scientific literature applied to fibrous concrete are shortly described (Section 4). In Section 5, our novel discrete lattice model is first outlined. Later, numerical results on the basis of a discrete lattice model are demonstrated for different quasi-static boundary value problems involving a fracture process in plain concrete (Section 5.1) and fibrous concrete with straight steel fibres (Section 5.2). Numerical results are qualitatively compared with corresponding laboratory tests. Finally, general conclusions from the research and future research directions are enclosed (Section 6).

## 2 General

**Abstract.** This chapter describes the most important physical and mechanical properties of concrete strengthened with steel fibres. First, steel fibres applied to concrete are shortly described. Later, some experimental results are enclosed indicating mostly a positive effect of fibres on properties of plain concrete.

Fibres are added to inhibit a propagation of cracks in concrete which occur due to its low tensile strength. Plain concrete specimens usually fail catastrophically by a single crack and separation into two pieces (Fig.2.1A). On the contrary, fibre-reinforced concrete specimens, even those with a small fibre volume fraction, retain post-cracking ability to carry loads (usually few short and narrow cracks are created, Gröbl et al. 2001, Soulioti et al. 2010) (Fig.2.1A). Fig.2.1B demonstrates ways in which fibres act to absorb energy and control the crack growth.



**Fig. 2.1** Fibrous concrete: A) cracks in concrete element subjected to bending without fibres (a) and with waved fibres (b) (Soulioti et al. 2010), B) energy-absorbing fibre/matrix mechanisms: 1) fibre failure, 2) fibre pull-out, 3) fibre bridging, 4) fibre/matrix debonding, 5) matrix cracking (Zollo 1997)

Fibres can be short (as separate elements) or long (as mats). They are made from a steel wire or steel sheets with the yield stress of 500-2500 MPa. Individual fibres are produced in an almost limitless variety of geometric forms including: prismatic (rounded or polygon cross-section with smooth surface or deformed throughout or only at ends), irregular cross-section (cross-section varies along the length) or collated (multifilament or monofilament networks). The fibres can be straight, crimped, hooked or corrugated (Fig.2.2, Tab.2.1). The degree of concrete improvement depends upon many different factors such as: size, shape, aspect ratio, volume fraction, concentration, orientation and surface characteristics of fibres, ratio between fibre length and maximum aggregate size, volume ratio between long and short fibres and concrete class (Zollo 1997). The fibre orientation depends on the specimen size and flow direction of the fresh concrete; fibres align mainly with the flow of the fresh concrete (Stähli et al. 2008). The minimum content of fibres should be 0.5% of the concrete volume. The most suitable volume fraction values for concrete mixes are between 1.0% and 2.5%. Since the inclusion of steel fibre reduces concrete workability, the maximum fibre content is about 3% for mixing by vibration and 1.2-1.4% for mixing by whirling.

The optimum volume depends on the aspect ratio of fibres (Fig.2.3). Good workability of fibrous concrete is expected if

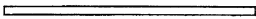


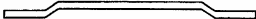



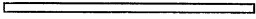


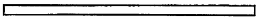
$$p \frac{l_f}{d_f} < 100-150 \quad (\text{for the maximum grain size of 10 mm}) \quad (2.1)$$

and

$$p \frac{l_f}{d_f} < 160-200 \quad (\text{for the maximum grain size of 2 mm}), \quad (2.2)$$

where  $p$  – fibre content in vol.%,  $l_f$  – fibre length and  $d_f$  – fibre diameter. For usual concrete, fibres with a length of 25-60 mm and diameter of 0.25-1.00 mm are applied (aspect ratio  $l_f/d_f=25-100$ ). In the case of shotcrete, the thickness of fibres is about 0.3-0.5 mm and the aspect ratio  $l_f/d_f$  lies between 30-150.

Increasing the content of fibres may have a positive effect on the mechanical properties, but because fibres are not all necessarily aligned in the direction of stress, the effectivity is debatable. It would be the best to align fibres in the direction of stress, which might lead to improved performance of FRC in a structure, probably against lower cost.

		Firm			
	○	A	Trefil	WIREX,	
	○	A	ARBED	EUROSTEEL	
	□	B	Australian Wire	FIBRESTEEL	
	○	A	Bekaert	DRAMIX	
	○	A	National-standard	DUOFORM	
	◐	D	National-standard	MELT-EXTRACTED	
	◐	C	HAREX	HAREX	
	○	A	Stahlfasertechnik		
	◑	A	Stax		
	○	A	Thibo		
	□	B	US-Steel		

**Fig. 2.2** Different forms of steel fibres (Grübl et al. 2001)

The required anchorage length of fibres  $l_H$  can be calculated for  $d_f=0.4$  mm as

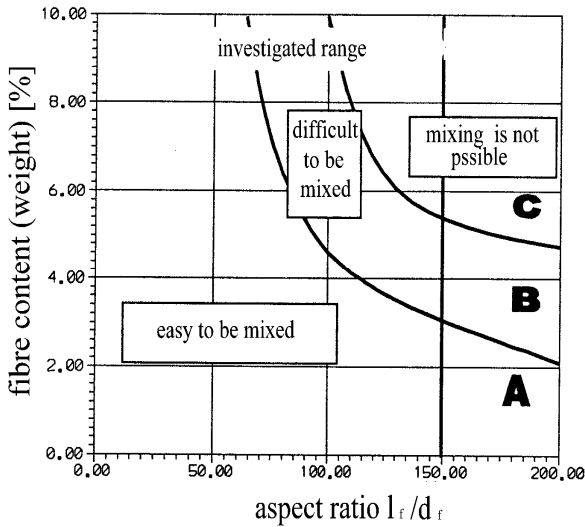
$$l_H = \frac{d_f f_y}{4\tau_m} = \frac{0.4 \times 1400}{4 \times 5} = 28 \text{ mm}, \quad (2.3)$$

where  $f_y$  - yield stress and  $\tau_m$  - mean bond shear stress. If a single fibre is long as twice as the bond length, the tensile strength is reached in the half of fibres (Fig.2.4). For one crack beyond the half of the fibre length, a short end of fibres will be pulled out. If the total fibre length is significantly longer as the double bond-length, all cracks can reach the tensile strength. Within a static range, the fibre length should be 4 times longer than the required bond length.

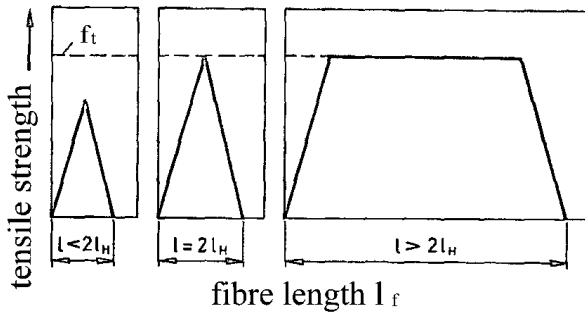


**Table 2.1** Production of fibres, typical cross-sections, strengths and contractors (Lohrmann 1999)

Execution	Length [mm]	Cross-section	Form Surface characteristics	Strength [MPa]	Firm
Drawing	12-100	circle $d_f=0.25-1.2$ mm	straight (smooth, rough)	1000-1500	Trefil Wirex
Drawing Cold forming	30-60	circle $d_f=0.4-1.0$ mm	bent at ends (smooth)		Bekert Dramix
	40-60	circle $d_f=0.6-1.0$ mm	bent along length (smooth)		ARBED Eurosteel
	40-60	circle $d_f=0.6-1.0$ mm	compressed along length (smooth)		National Standard Duoform
	40-60	circle $d_f=0.5-0.8$ mm	compressed at ends (smooth)		Thibo
Milling Prestressing	15-60	sickle $A_f=0.2-0.8$ mm <sup>2</sup>	straight (smooth)	700-1000	Harex
	15-60	sickle $A_f=0.2-0.8$ mm <sup>2</sup>	formed at ends (smooth, rough)		
Forming	20-60	sickle $A_f=0.2-0.8$ mm <sup>2</sup>	straight or corrugated (smooth, rough)	500-1000	
Cutting	40-60	segment $A_f=0.2-0.8$ mm <sup>2</sup>	straight or formed at ends (smooth)		US-Steel Australien Wire
Remelting	19-76	circular segment	straight (smooth)		Ribbon technology



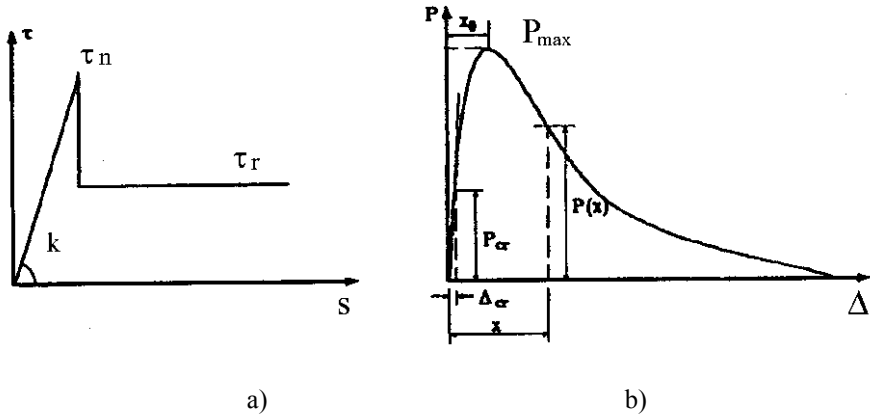
**Fig. 2.3** Workability of concrete with steel fibres against fibre content and fibre aspect ratio divided into 3 regions A, B and C (Szumigala et al. 2001)



**Fig. 2.4** Tensile response of fibres dependent upon their length ( $l_H$  - required bond-length) (Grübl et al. 2001)

The pull-out behaviour depends upon roughness, geometry, diameter, orientation and end anchorage of fibres and type of the cement matrix. Fig.2.5 shows a simplified theoretical relationship between bond strength and slip and an experimental curve between force and horizontal displacement. For the fibres Wirex 40/0.6, the following values can be assumed: peak shear bond stress  $\tau_{ii}=3.9$  MPa, residual shear bond stress  $\tau_{ri}=0.75$  MPa and initial stiffness  $k=3444$  MPa. In turn,

for the fibres Dramix 40/0.6, the following values can be chosen:  $\tau_i=12.8$  MPa,  $\tau_r=0.75$  MPa and  $k=8290$  MPa. The results of other pull-out experiments are shown in Figs.2.6 and 2.7.

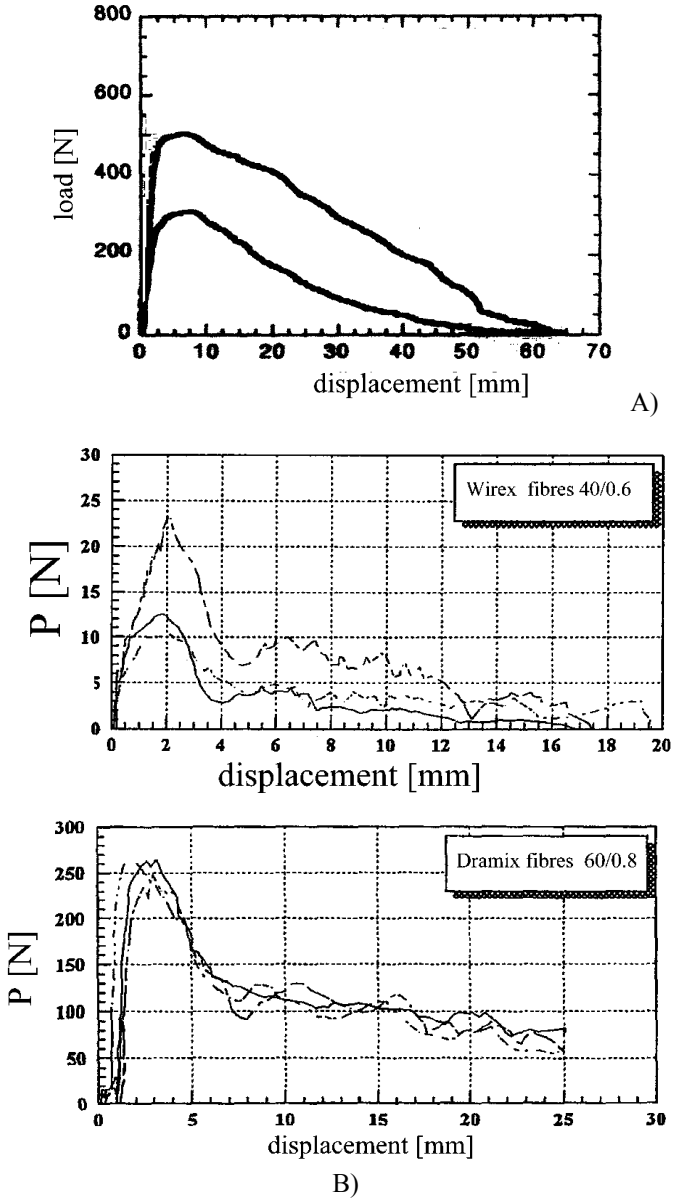


**Fig. 2.5** Pull-out behavior: a) theoretical simplified bond strength against slip  $\tau=f(s)$  (Banthia 1990), b) experimental force against displacement (Lin 1999)

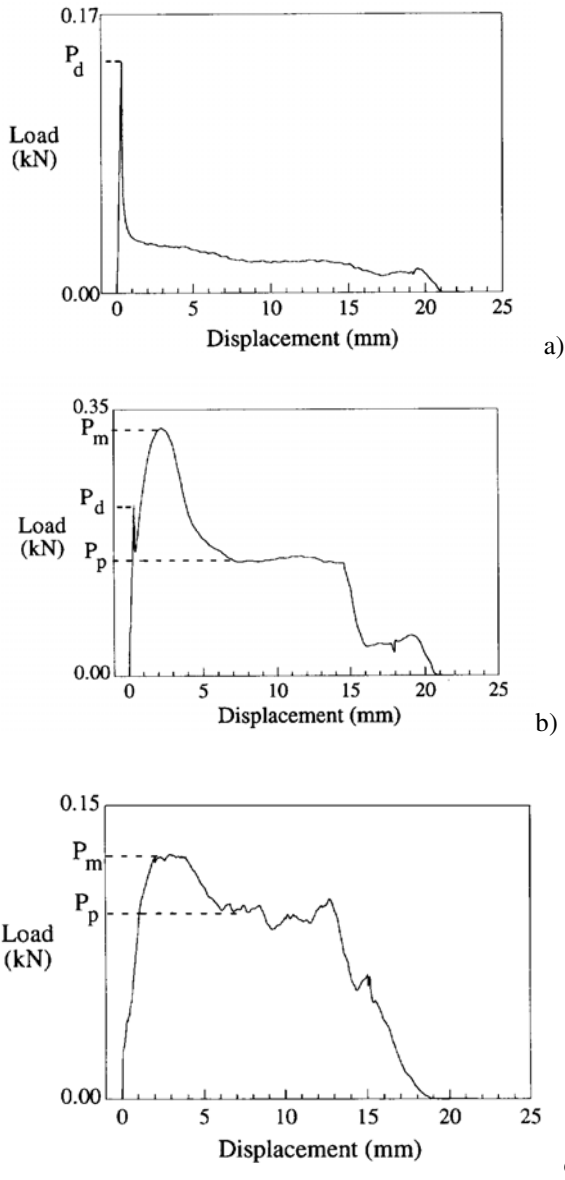
Steel fibres can be distributed uniformly in concrete with respect to the direction and grade of compaction (3D system). If most of fibres are put parallelly to a specific plane, a 2D system is created. If fibres are parallel in one direction, a system 1D takes place. The effectivity of fibres is 100% (system 1D), 30-37% (system 2D, casual orientation), 10-40% (system 2D, ortogonal orientation) and 0-20% (system 3D). There exist different methods to measure the structure of fibrous concretes with respect to the distribution and orientation of fibres:

- a) x-rays (Stroeven and Shah 1978, Szumigala et al. 2001, Robins et al. 2003),
- b) opto-analytic method (Schönlin 1983, Tye et al. 2007),
- c) using electro-magnetic field (Wichmann et al. 1999),
- d) using magnetic field (Linsel 2005),
- e) CT-scan (Stähli et al. 2008),
- f) by manual counting of fibres in failure cross-sections (Hilsdorf et al. 1985).

For fibrous concrete, cements are applied with a class not lower than 42.5. The ratio  $w/c$  should be 0.42-0.50. The cement content is higher than for usual concrete and should be (without fly ash): 550-600 kg/m<sup>3</sup> (particles up to 2 mm), 500-550 kg/m<sup>3</sup> (particles up to 4 mm), 450-500 kg/m<sup>3</sup> (particles up to 8 mm), 350-400 kg/m<sup>3</sup> (particles up to 16 mm). The aggregate with a diameter of 8-12 mm is usually used. The maximum aggregate size should be limited to one-third of  $l_f$ .



**Fig. 2.6** Experimental pull-out behavior of steel fibres (force against displacement): A) by Banthia 1990) and B) by Bui (1991)



**Fig. 2.7** Experimental pull-out load versus displacement for 1.0 mm diameter hooked steel fibre: a) straight fibre, b) fibre with bend angle of  $23^\circ$ , c) fibre with bend angle of  $33^\circ$  (Pompo et al. 1996)

If the aggregate is smaller than 2 mm, a high cement content has to be used that increases however shrinkage and brittleness. Addition of fibres increases a sand point (ratio between the content of aggregate 0-2 mm and the remaining aggregate), since fibres loosen the aggregate mix. Therefore, the aggregate should have the grain content of 2 mm higher by 5% resulting from the optimum sand point (50-60% for the particle size up to 8 mm, 35-45% for the particle size up to 16 mm). It is recommended to use fly ash as filling (20-40% of the cement mass) to improve workability and to reduce hydration heat. It is important to use plasticizers to maintain the workability of fresh concrete (the dosage of plasticizer is about 1% of the binder content of concrete).

The mixing time of fibres with concrete is about 5 min. A procedure for mixing fibre-reinforced concretes involves the following. First, the gravel and sand are placed in a concrete mixer and mixed for 1 min. Second, the cement and fibres are spread and dry mixed for 1 min. Third, the water (90%) is added and mixed for approximately 2 min. Fourth, the remaining water (10%) and plasticizer are added and mixed 3 min. Finally, the freshly mixed fibre-reinforced concrete is cast into specimens mold and vibrated simultaneously to remove any air remained entrapped.

Fibrous concret can be mixed by vibration, whirling, press moulding, dehydration, press moulding with dehydration and densification in a magnetic field. The first, second and fifth methods are the most effective ones.

Steel fibres improve in plain concrete:

- a) flexural tensile strength,
- b) splitting tensile strength,
- c) compressive strain at peak load,
- d) ductility and toughness,
- e) first cracking strength,
- f) stiffness,
- g) durability,
- h) impact resistance,
- i) fatigue,
- j) shock vibration resistance,
- k) wear strength,
- l) freeze-thaw resistance,
- m) shrinkage,
- n) creep.

The use of fibre reinforcement in concrete/shotcrete can greatly enhance the compressive ductility and toughness also at early ages (Ding and Kusterle 2000). In turn, the concrete workability decreases and concrete sorptivity and volumetric weight increase at the same time with a growth of the fibre volume (Atis and Karahan 2009).



Fig.2.8 shows the experimental stress-strain curves for different fibre contents during uniaxial compression and tension in tests by Schnütgen (1981). The compressive and tensile strength, strain corresponding to the failure load and material ductility increased with increasing fibre volume. The fibre orientation influences compressive strength (Fig.2.9) that was smaller when the fibres were parallel to the loading direction (Bonzel and Schmidt 1984). The bearing capacity and ductility of fibre concrete increased with increasing aspect ratio  $l_f/d_f$  (David and Naaman 1985) (Fig.2.10). However, some experiments indicated (Atis and Karahan 2009) that the compressive strength could be even smaller. This may be due to the physical difficulties in providing a homogeneous distribution of steel fibres within concrete (causing drop in compressive strength as compared to plain concrete).

Bending experiments were carried out by Ward and Li (1990) with 3 different beam heights: 63.5 mm, 114 mm and 228 mm (ratio between span and height was 3). The fibres were 25 mm or 50 mm long with a diameter of 0.88 mm. The flexural strength increased with increasing fibre content (Figs.2.11 and 2.12), and decreasing beam height (Fig.2.13) and fibre length (Fig.2.14). The deflection index (ratio between deflection for maximum load and deflection corresponding to first crack) increased with increasing fibre number as well (Fig.2.15). The specimen size influenced the fibre orientation (Soroushian and Lee 1990).

The higher the strain velocity, the larger was the compressive strength (Fig.2.16) (Eib et al. 1991).

The effect of the fibre content on the flexural tensile strength was shown by Gopalaratnam and Shah (1985) for different strain velocities (Fig.2.17). The strength increased with increasing strain velocity and aspect ratio of fibres.

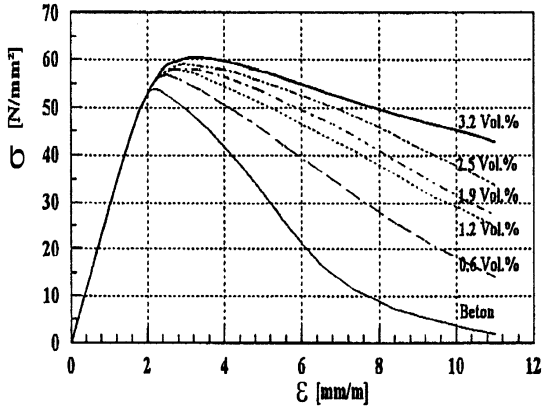
Addition of hooked fibres (0.9%,  $l_f=50$  mm) increased the shear strength by 30-40% (Grübl et al. 2001). In the case of torsion, the building elements carried larger rotation angles (5-22°/m against 0.1°/m) (Grübl et al. 2001). Therein, the energy absorption was higher in fibrous concrete (Fig.2.18).

The impact resistance increased in fibrous concrete as well (Figs.2.19 and 2.20) (Grübl et al. 2001, Schulz 2002). The reduction of the fatigue modulus (defined as the ratio between the stress range and the corresponding deformation range within a load cycle) was only 30% for fibrous concretes (Cachim et al. 2002).

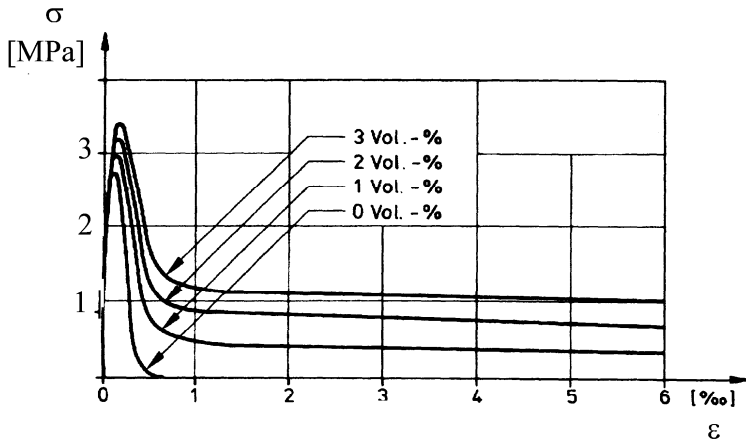
Fig.2.21 summarizes the effect of fibres on the behavior of concrete under different loadings (Walton and Majumdar 1975). The largest strength increment occurred under shear, impact loading and splitting tension.

The presence of fibres can decrease wear abrasion (Figs.2.22 and 2.23) (Schulz 2002, Horszczaruk 2008).

The fibre inclusion causes that a crack width is significantly reduced (expressed by a smaller flow rate of water in cracked concrete) (Fig.2.24) (Schulz 2002).

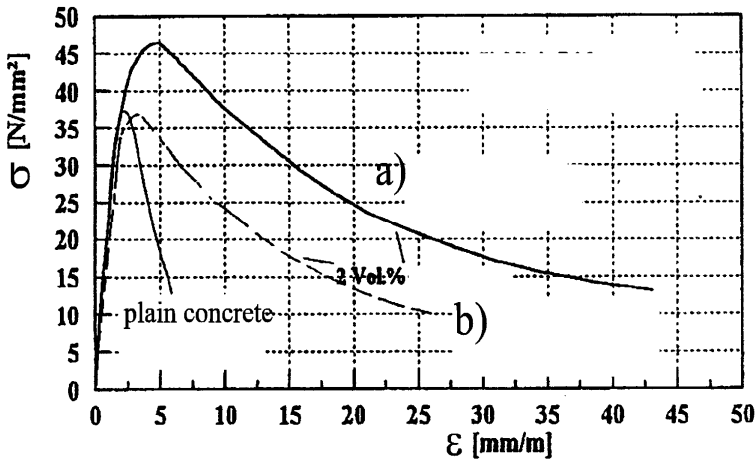


a)

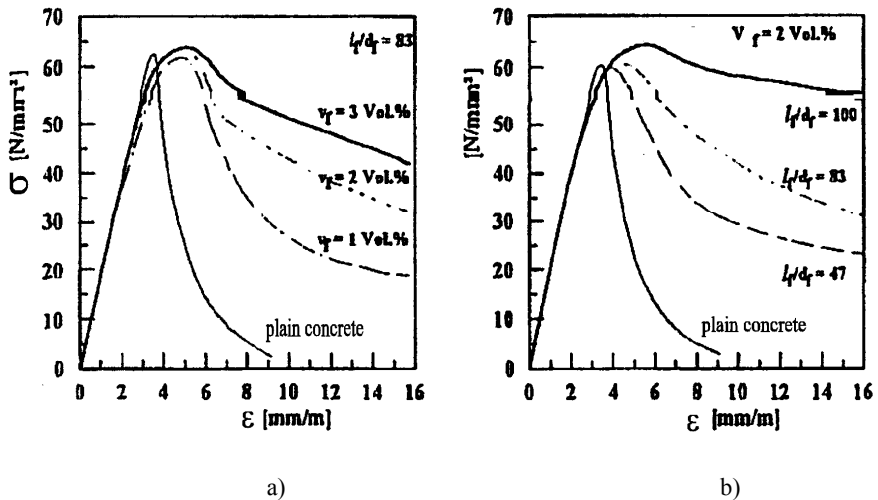


b)

**Fig.2.8** Uniaxial compressive stress-strain (a) and uniaxial tensile stress-strain curve (b) for different fibre contents (Schnütgen 1981)



**Fig. 2.9** Stress-strain curves for plain concrete and for concrete with 2% vol. of straight smooth steel fibres 25/0.4 mm measured during uniaxial compression on cylindrical cores  $\phi 10/20$  cm: a) fibre concrete compressed in direction of mixing, b) fibre concrete compressed in direction perpendicular to mixing (Bonzel and Schmidt 1984)



**Fig. 2.10** Stress-strain curves during uniaxial compression: a) influence of fibre content, b) effect of aspect ratio  $l/d_f$  (David and Naaman 1985)

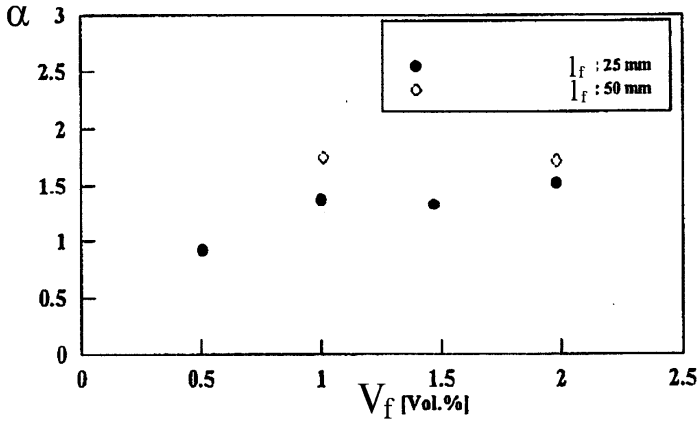


Fig. 2.11 Influence of fibre content on the ratio of flexural strength to splitting tensile strength (beam height 114 mm) (Ward and Li 1990)

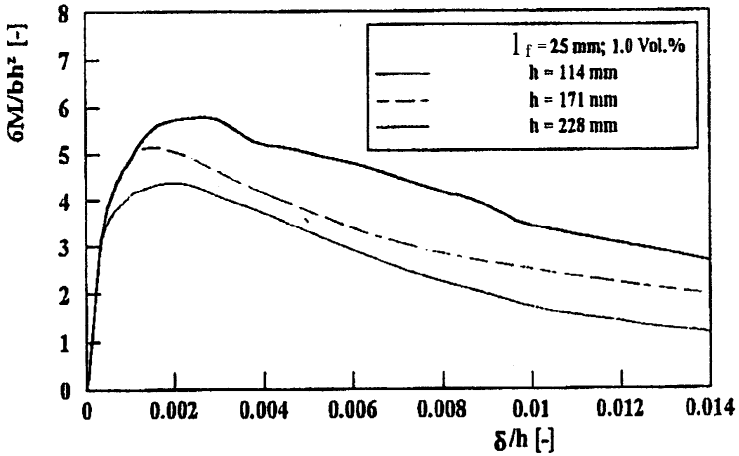
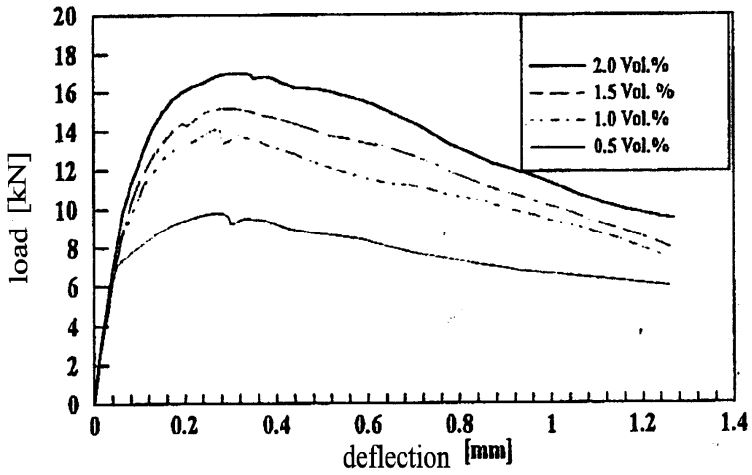
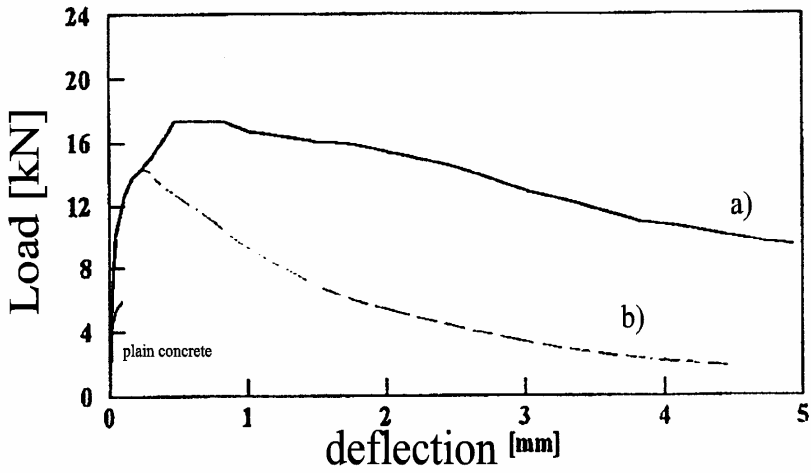


Fig. 2.12 Normalized load-deflection curves for steel fibre concrete with fibre length of 25 mm for different beam heights (Ward and Li 1990)



**Fig. 2.13** Load-deflection curves for steel fibre concrete beams with fibre length  $l_f=25$  mm (beam height  $h=114$  mm) (Ward and Li 1990)



**Fig. 2.14** Load-deflection curves for steel fibre concrete beams with different fibre lengths  $l_f$ : a)  $l_f=50$  mm, b)  $l_f=25$  mm (beam height  $h=114$  mm) (Ward and Li 1990)

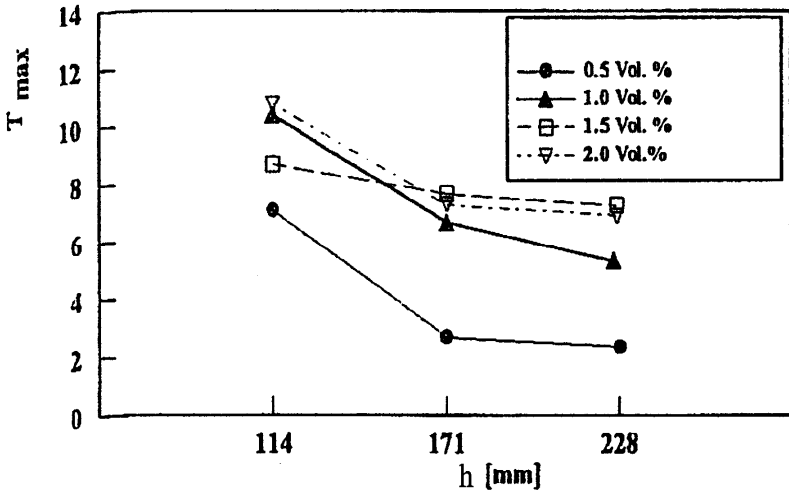


Fig. 2.15 Effect of beam depth and fibre content on deflection index ( $l_f=25$  mm) (Ward and Li 1990)

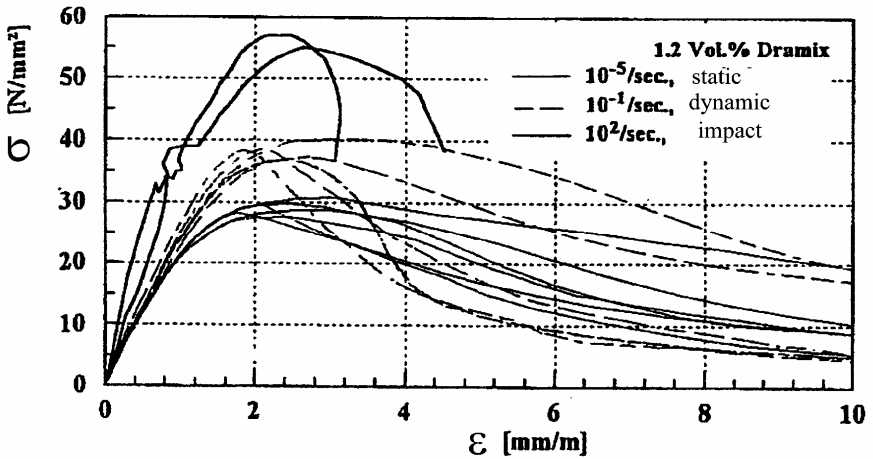
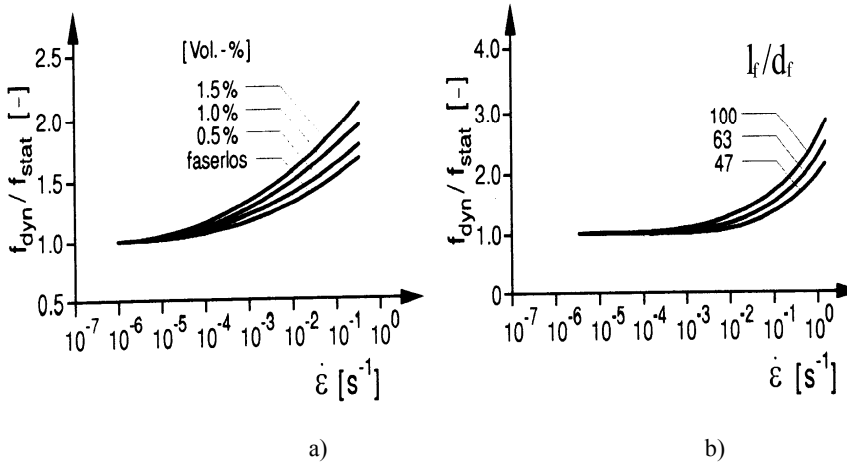
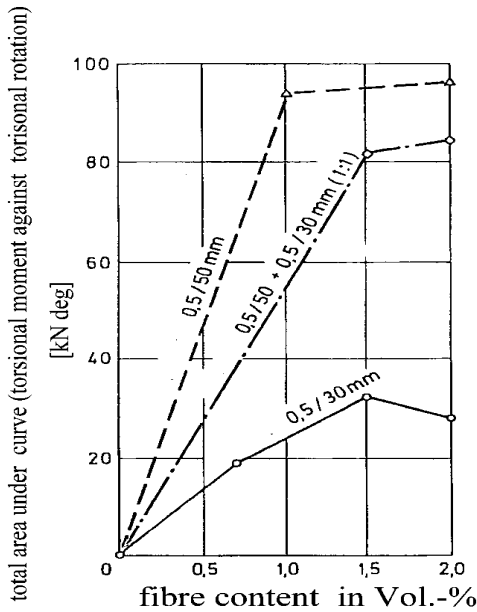


Fig. 2.16 Effect of strain rate on stress-strain curve during uniaxial compression (Eibl et al. 1991)

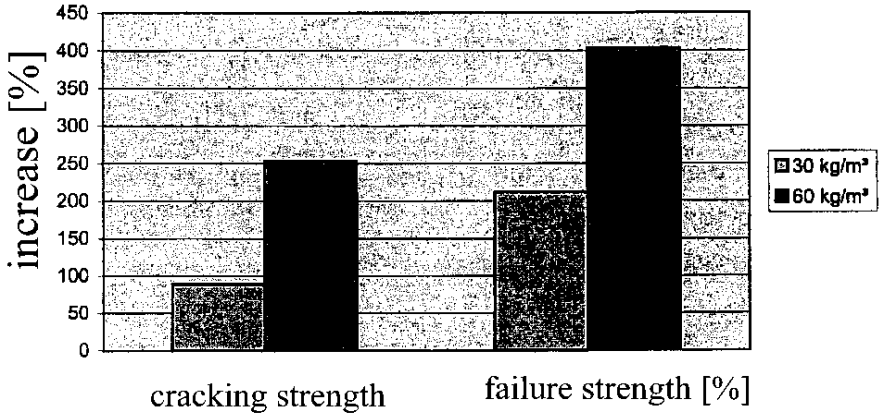




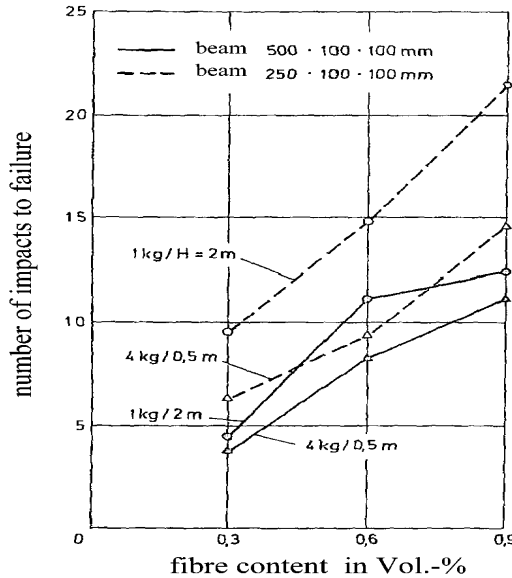
**Fig. 2.17** Relative flexural tensile strength versus strain velocity (a) and aspect-ratio (b) (Gopalaratnam and Shah 1985)



**Fig. 2.18** Effect of steel fibres on energy absorption during torsion (beams with cross-section of  $305 \times 152 \text{ mm}^2$ , fibres  $d_f=0.5 \text{ mm}$ ,  $l_f=30$  and  $l_f=50 \text{ mm}$ ) (Grübl et al. 2001)



**Fig. 2.19** Increase of impact strength in % for concrete with steel fibres of 30 kg/m<sup>3</sup> and 60 kg/m<sup>3</sup> (Schulz 2002)



**Fig. 2.20** Effect of fibre content on impact resistance (straight fibres  $d_f=0.3$  mm,  $l_f=30$  mm, fall weight 1 kg from height of 2 m or 4 kg from height of 0.5 m) (Grübl et al. 2001)

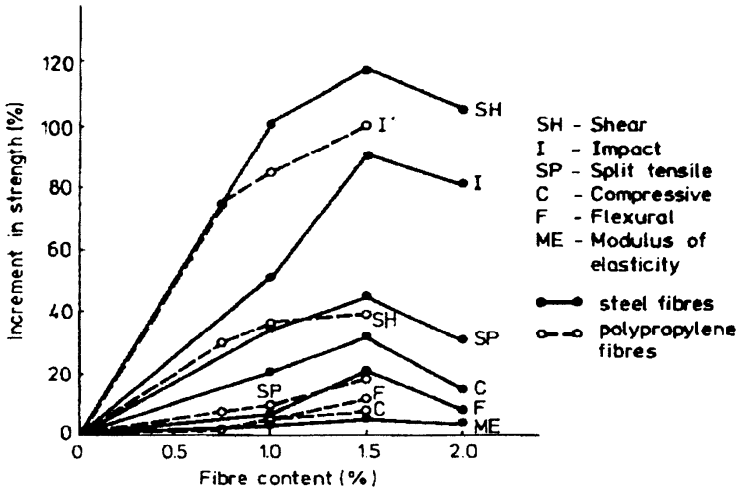


Fig. 2.21 Properties of steel and polypropylene reinforced concrete under different loading (Walton and Majumdar 1975)

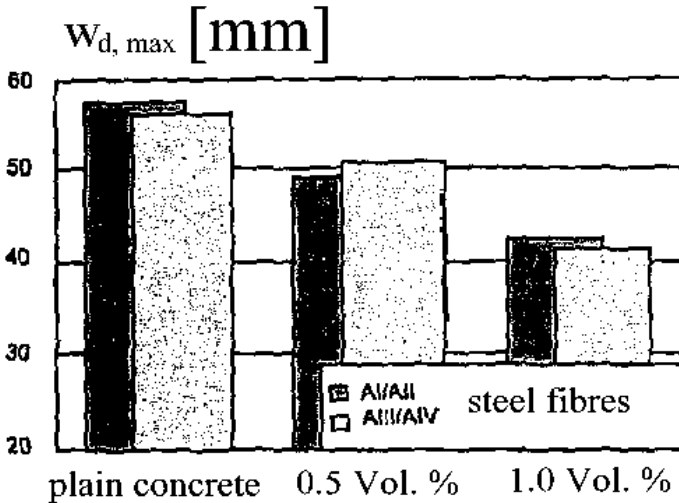
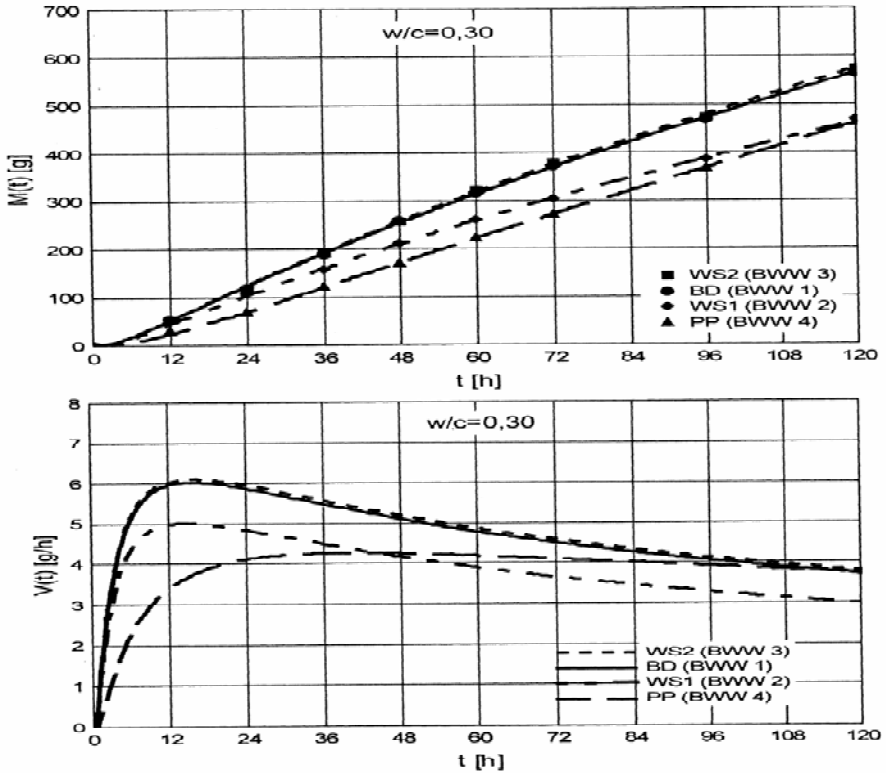


Fig. 2.22 Effect of fibres on abrasion (Schulz 2002)



**Fig. 2.23** Effect of fibre content on wear abrasion for cement-water ratio of  $w/c=0.30$ : BD – plain concrete, WS1 – fibrous concrete 30/50, WS2 – fibrous concrete 50/100, PP – concrete with polypropylene 19 mm ( $M$  – mass reduction,  $V$  – velocity of mass reduction) (Horszczaruk 2008)

Steel fibres help restrain shrinkage due to drying of the cement matrix (Swamy and Stavrides 1979, Mangat and Azari 1988, Atis and Karahan 2009). Fig.2.25 shows the drying shrinkage in experiments by Atis and Karahan (2009). On the basis of 210 days drying shrinkage, concrete mixtures that contained 0.25%, 0.50%, 1.0% and 1.5% steel fibre resulted with 10%, 21%, 25% and 26% reductions in drying shrinkage, when compared to the reference Portland cement mixture. A higher reduction can be obtained by addition of fly ash (Atis and Karahan 2009). According to Sivakumar and Santhanam (2007a), plastic shrinkage cracks can be reduced significantly (by 50–99%) due to fibres compared to plain concrete.

Unfortunately, addition of steel fibres into concrete mixture significantly increases the sorptivity coefficient. This may be due to increased porosity (capillary pores) in the cement paste in contact zones close to fibres (Atis and Karahan 2009).

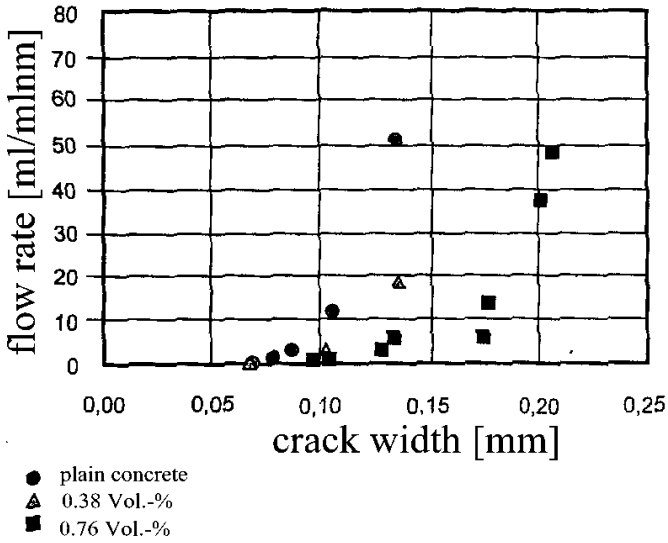


Fig. 2.24 Flow rate of water in cracked plain and fibrous concrete (Schulz 2002)

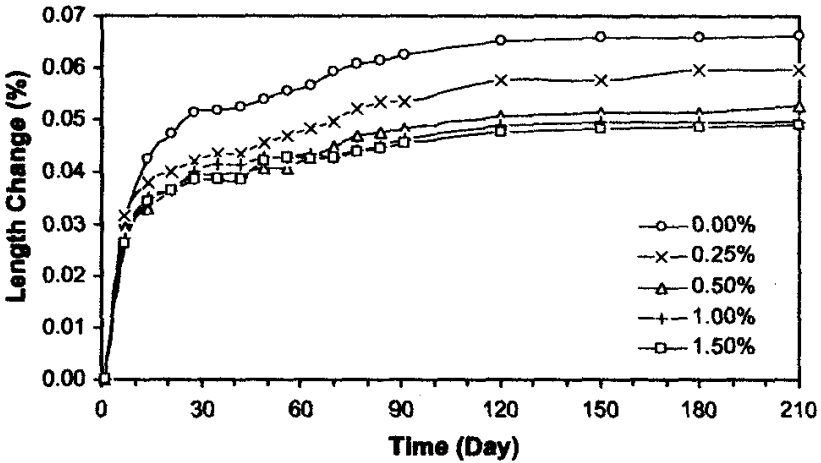
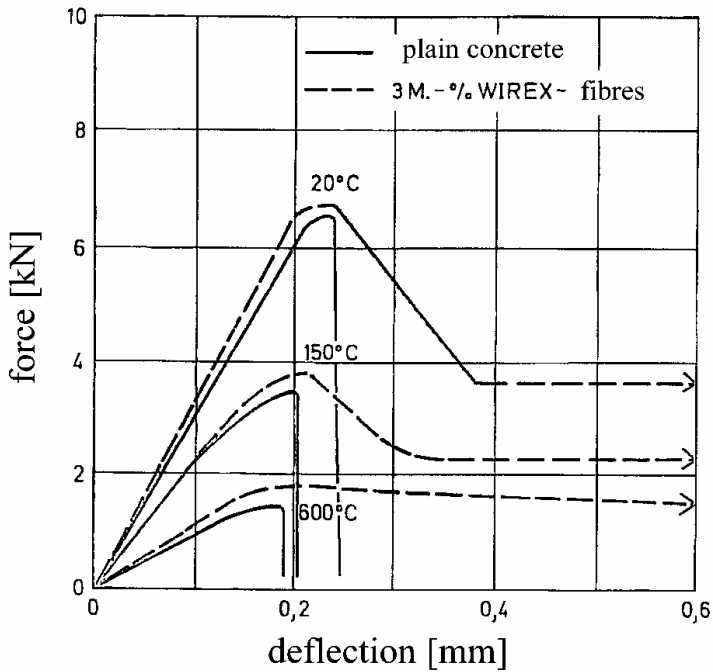


Fig. 2.25 Shrinkage of fibre reinforced Portland concrete versus time with different fibre content (Atis and Karahan 2009)



**Fig. 2.26** Load-deflection curves for concrete beam at different temperatures (Grübl et al. 2001)

The freeze-thaw resistance of steel fibre concrete was found to slightly increase when compared to concrete without fibres. It is known that when water freezes, its volume increases by about 9%. Due to volume changes of water, concrete begins to expand and cause tensile stress, which disintegrates concrete when the tensile strength is exceeded. However, randomly distributed fibres in a concrete mixture restrain this expansion and reduce the freeze-thaw damage to concrete.

Adding fibres in concrete reduces creep damage by 20-35% (Mangat and Azari 1985, Zhang 2003). The higher the fibre content, the lower is the composite creep (Zhang 2003). With the same fibre content and fibre geometry, the higher is the moduli ratio between fibre and matrix, and the smaller is the composite creep strain. High elastic modulus fibres are more effective than those with low elastic modulus as far as composite creep deformation reduction is concerned. Fibre aspect ratio strongly influences the composite creep behavior. For the same fibre content, composite creep decreases nonlinearly and gradually trends to a constant with an increase of the fibre aspect ratio.

In addition, the fibres delay failure at high temperatures (through a significant increase of material ductility) (Fig.2.26).

The steel fibres can be used to reactive powder concrete (RPC), i.e. ultra high strength, superplasticized, silica fume concrete which uses fine sand with particle sizes in the range of 100-400  $\mu\text{m}$  (Shaheen and Shrive 2007). The compressive strength of such concrete is up to 800 MPa and flexural strength is up to 140 MPa. Such material is an excellent candidate for structures subjected to high and low cycle fatigue. The steel fibres can be also used to self-compacting concrete with a current generation of superplasticizers (Walraven and Grünwald 2002, Grünwald 2004, Markovic 2006).

The flexural toughness is very important parameter in assessing the influence of fibres on the post-peak response of concrete composites; is a measure of the energy absorption capacity of fibres and is characterized by the area under the load-deflection curve up to a specific deflection. The standard flexural toughness can be determined using ASTM C-1018 (USA) 1997, JCI method (Japan) 2003 and DBV-Merblatt (Germany) 2001. In the procedure described by ASTM C-1018 method (Fig.2.27), the toughness is expressed as a ratio of the amount of energy required to deflect the beam to a specified deflection, expressed as multiples of the first crack deflection during three-point bending (specimen 150 mm  $\times$  150 mm  $\times$  700 mm).

The toughness index  $I_5$  is defined as

$$I_5 = A_3 / A_1, \quad (2.4)$$

where  $A_3$  and  $A_1$  are the areas of the load deflection curve up to  $3\delta$  and  $\delta$ , respectively ( $\delta$  is the deflection at first crack). The indices  $I_{10}$ ,  $I_{20}$  and  $I_{30}$  are calculated as the ratios of the area under the load deflection curve up to 5.5, 10.5 and 15.5 times the first crack deflection divided by the area up to the first crack deflection, respectively.

On the other hand, in the JCI method (2003), the toughness  $T_{JCI}$ , is defined as the area under the load deflection curve up to a deflection of 1/150 of span ( $\delta_{150}$ , Fig.2.28). By accounting for the beam size and span,  $T_{JCI}$  is presented using the toughness factor,  $\sigma_b$  as follows

$$\sigma_b = \frac{T_{JCI} L}{\delta_{150} b h^2}, \quad (2.5)$$

where  $T_{JCI}$  is the energy absorbed (flexural toughness),  $\delta_{150}$  is the deflection of  $L/150$  of span and  $L$ ,  $b$  and  $h$  are the span, width and depth of the specimen section, respectively.

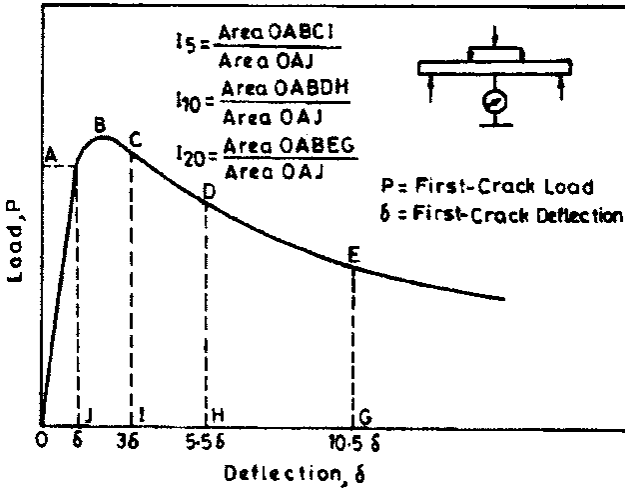


Fig. 2.27 Definition of flexural toughness indices according to ASTM C-1018 (Mohammadi et al. 2008)

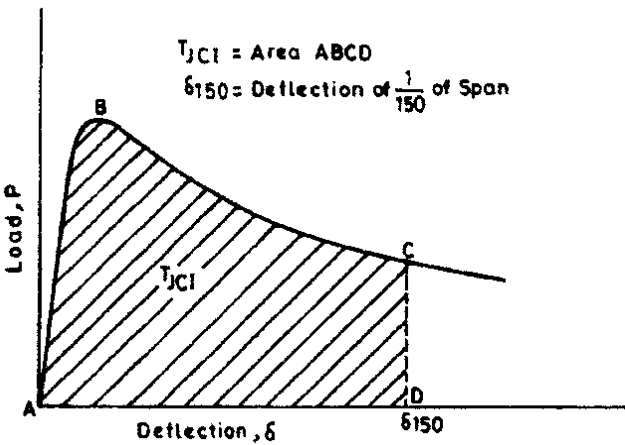


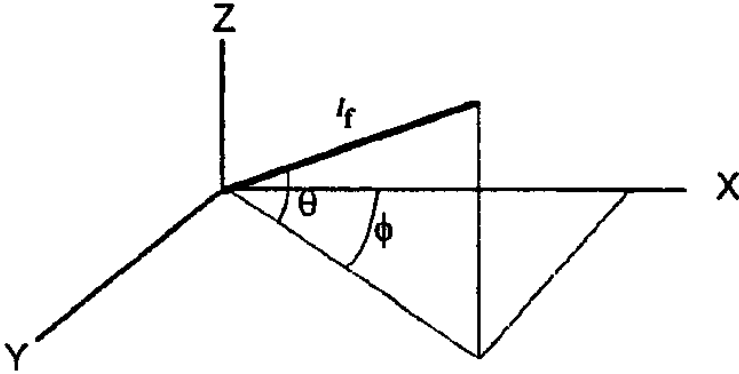
Fig. 2.28 Definition of flexural toughness by JCI method (Mohammadi et al. 2008)

The properties of fibrous concrete strongly depend on the fibre orientation, when vibration needles are inserted in the fresh concrete. The three-dimensional orientation coefficient of fibres is defined as (Lin 1999)



$$\eta_\theta = \frac{N \int_0^{\pi/2} \int_0^{\pi/2} l_f \cos\theta \cos\phi d\theta d\phi}{N l_f (\pi/2)^2}, \quad (2.6)$$

where  $N$  – number of fibres in the observed volume, and  $\theta$  and  $\Phi$  - project angles (Fig.2.29).



**Fig. 2.29** Random orientation of a fibre (Lin 1999)

## 3 Literature Overview

**Abstract.** In this chapter, the results of quasi-static and dynamic experiments with concrete and reinforced concrete specimens including steel fibres are described in detail. The experiments have been carried out mainly in 10 last years in different foreign research centers. Attention is paid to advantageous properties of fibrous concrete and fibrous reinforced concrete as compared to plain or reinforced concrete.

### 3.1 Properties of Concrete Including Steel Fibres

#### 3.1.1 Quasi-Static Experiments (Strain Rate $\dot{\varepsilon} \leq 1 \times 10^{-4}$ 1/s)

##### Experiments by Lin (1999)

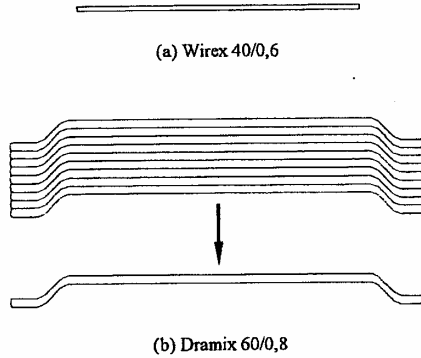
The experiments were carried out on uniaxial compression and tension, eccentric compression and tension and bending using straight round fibres Wirex 40/0.6 and crooked round fibres Dramix 60/0.8 (Fig.3.1). The fibre content varied between 0 kg/m<sup>3</sup>, 47 kg/m<sup>3</sup> (content by volume of concrete was 0.6%) and 94 kg/m<sup>3</sup> (volumetric content was 1.2%), respectively. The maximum aggregate diameter was 16 mm. The orientation coefficients were different in both directions. The fibres were more oriented horizontally, i.e. the direction perpendicular to the direction of concrete compaction was dominant. The orientation coefficient calculated along the cross-section as

$$\eta_{\theta} = \frac{1}{M} \sum_{i=1}^M \cos \theta_i, \quad (3.1)$$

was about 0.71-0.75 (horizontally) and 0.42-0.43 (vertically), where  $M$  – total amount of fibres in the cross-section and  $\theta$  - inclination angle with respect to the axis.

Fig.3.2 shows the compressive stress-strain curves for cylindrical samples (diameter  $d=100$  mm, height  $h=250$  mm) of plain concrete C30/37, Wirex concrete (1.2%) and Dramix concrete (1.2%) for different strain velocities. Both compressive strength and material ductility increased with increasing fibre content. In the case of plain concrete, compressive strength and brittleness grew

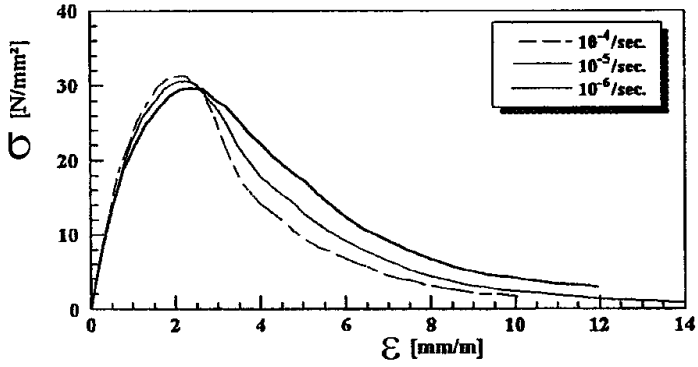
with increasing strain velocity. However, in the case of fibrous concrete, a consistent relationship between strength and strain velocity was not found due to a different random distribution of fibres. The compressive strength was larger for samples taken vertically from the mix (Fig.3.3) due to the fact that in this case fibres were oriented more horizontally (i.e. perpendicularly to vertical cracks created during compression).



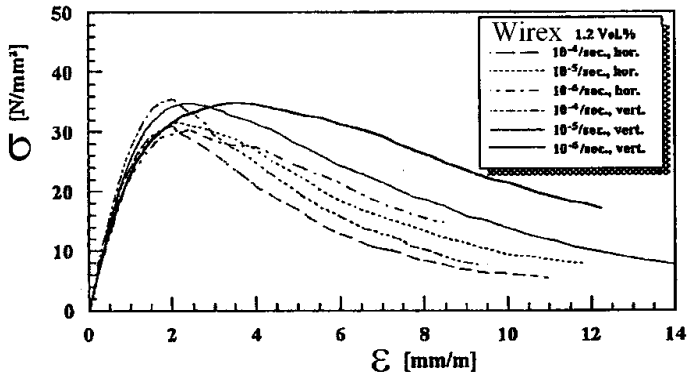
**Fig. 3.1** Steel fibres: Wirex (a) and Dramix (b) used in experiments by Lin (1999)

The experimental results on eccentric compression are demonstrated in Figs.3.4 and 3.5 with prismatic specimens  $100 \times 100 \times 250 \text{ mm}^3$ . The larger the eccentricity, the lower was the strength for plain and fibre concrete. When the eccentricity was equal to  $e/d=1.6$ , the entire cross-section was compressed. The vertically taken fibre concrete samples were stronger (than those taken horizontally) since more fibres were perpendicularly oriented to the vertical load (i.e. more fibres were perpendicular to cracks). For a larger eccentricity of  $e/d=1/3$ , the horizontally taken samples with fibres showed the highest strength. The strength decreased obviously with increasing eccentricity  $e$ . The effect of loading velocity was insignificant.

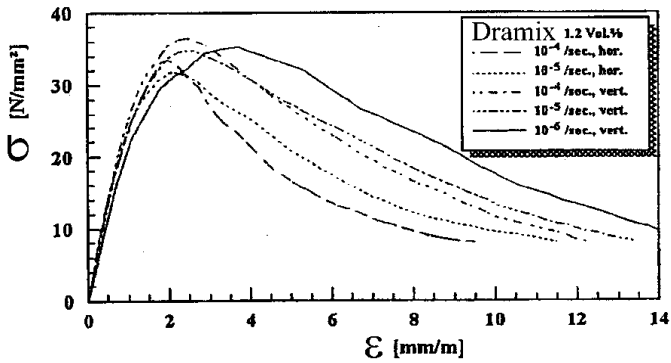
The experimental results on uniaxial tension are shown in Figs.3.6-3.8. The tensile strength and fracture energy increased with increasing fibre content and orientation coefficient. They were higher for samples taken horizontally (more fibres were located in this case perpendicularly to tensile cracks). This increase was more evident for a high fibre content (1.2%) and a high orientation coefficient ( $\eta_0 > 0.5$ ). This increase was also more pronounced for crooked Dramix fibres than for straight Wirex fibres.



a)



b)



c)

Fig. 3.2 Experimental uniaxial compressive stress-strain curves for different strain rate: a) plain concrete, b) Wirex concrete, c) Dramix concrete (Lin 1999)

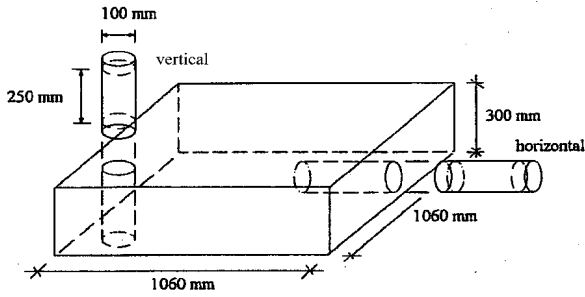
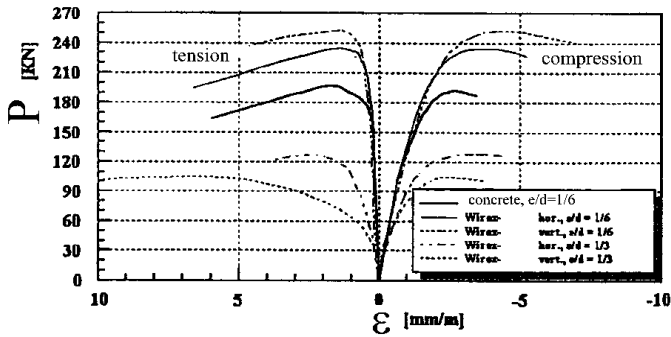
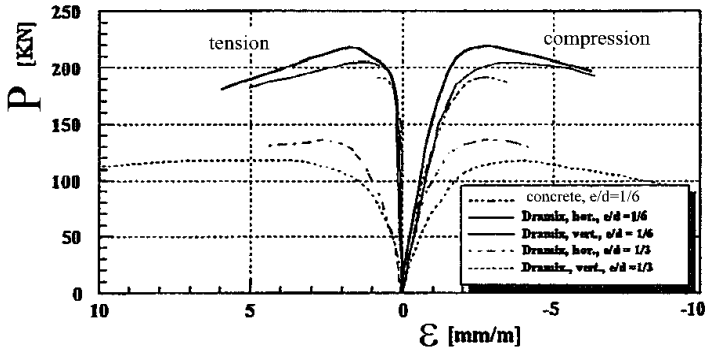


Fig. 3.3 Drilling of test samples from a concrete block (Lin 1999)

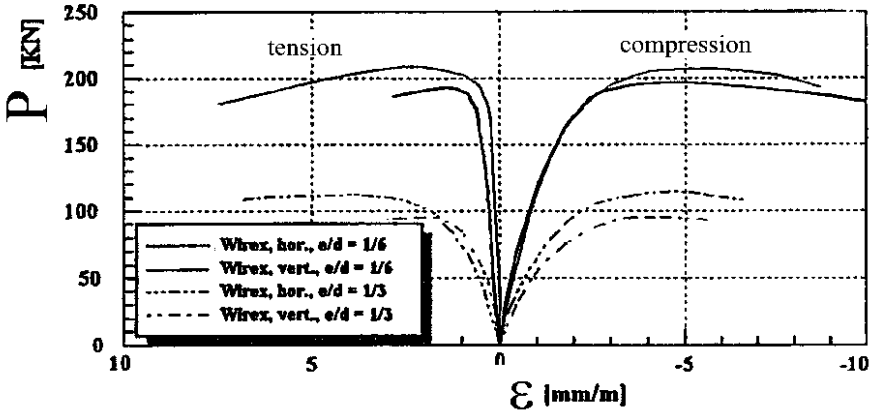


a)

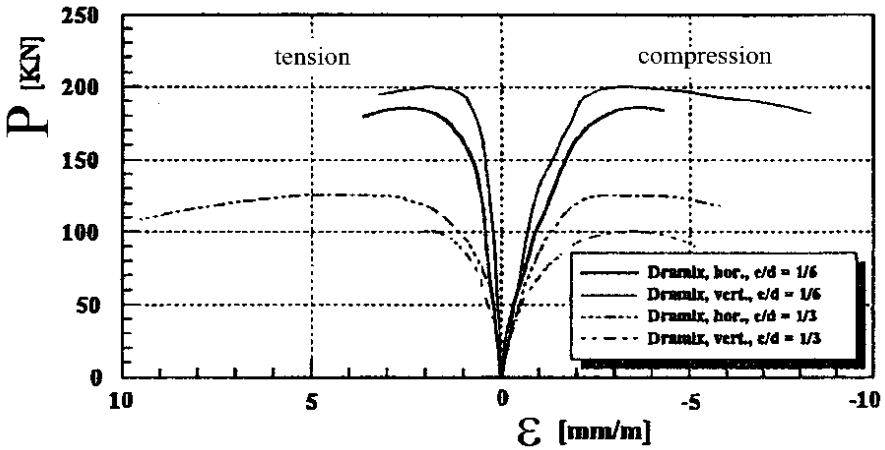


b)

Fig. 3.4 Experimental results of eccentric compression ( $\mathcal{E}=10^{-4}$  1/s): plain concrete and fibre concrete (1.2%): a) Wirex concrete, b) Dramix concrete (Lin 1999)



a)



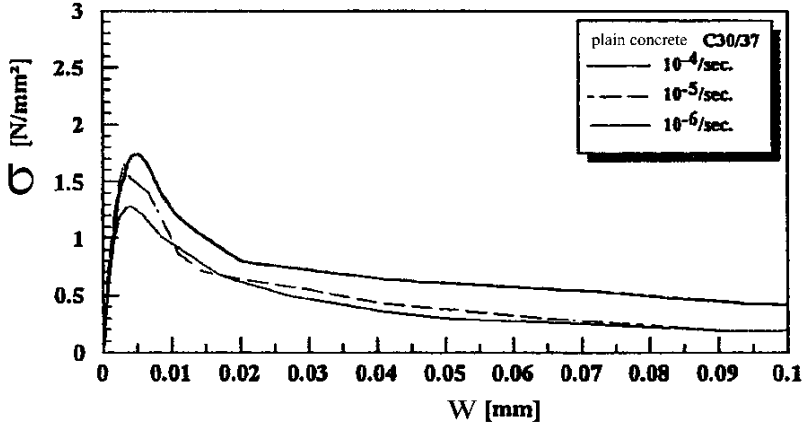
b)

Fig. 3.5 Experimental results of eccentric compression ( $\mathcal{E}=10^{-6}$  1/s): plain concrete and fibre concrete (1.2%): a) Wirex concrete, b) Dramix concrete) (Lin 1999)

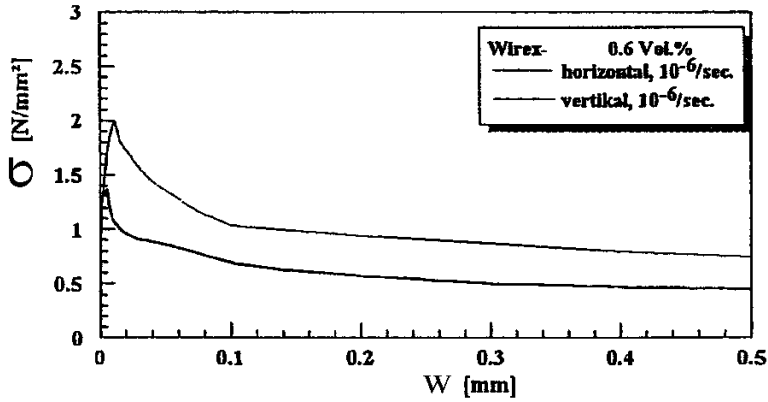
Tab.3.1 and Figs.3.9-3.13 show the results from flexural tests during three-point bending with beam heights of 100 mm, 200 mm, 480 mm and 780 mm and the ratio between the span and height of 5. The notched and unnotched beams were used.

The flexural tensile strength increased with increasing fibre content, orientation coefficient and decreasing beam height. The samples taken horizontally were

stronger. The orientation coefficient decreased asymptotically with increasing beam height (the contribution of fibres which were parallel to a free boundary was larger for smaller beam heights). The fracture energy was more dependent upon the fibre orientation than upon the beam height.

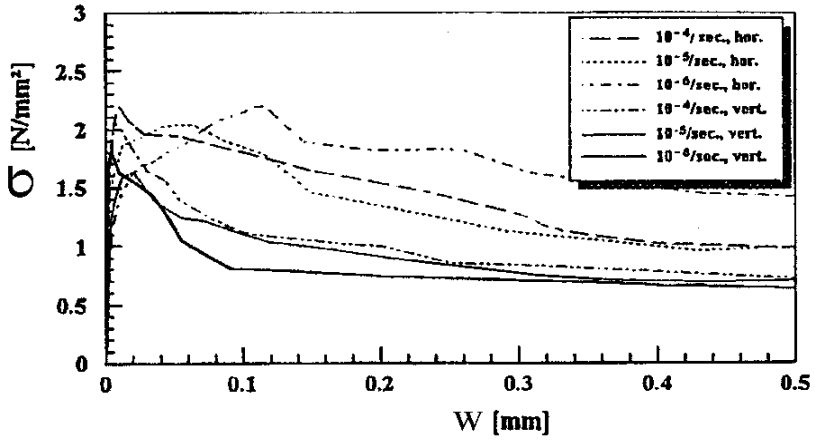


a)

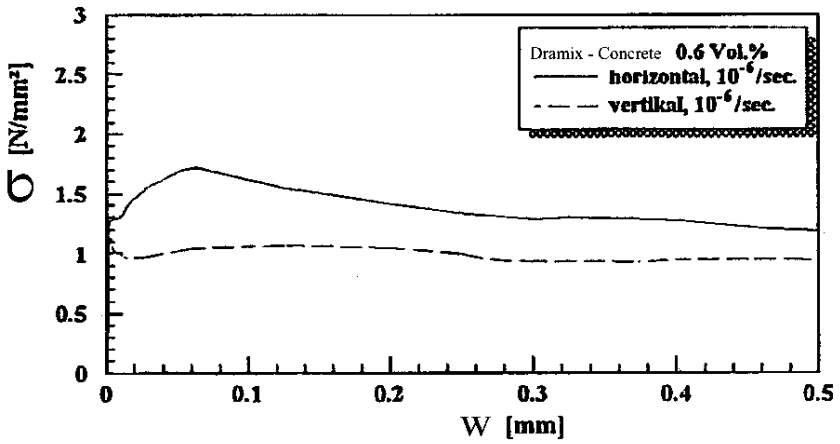


b)

**Fig. 3.6** Experimental tensile strength  $\sigma$  versus crack opening  $w$  during uniaxial tension: a) plain concrete C30/37, b) Wirex concrete (0.6%), c) Wirex concrete (1.2%), d) Dramix concrete (0.6%), e) Dramix concrete (1.2%) (Lin 1999)



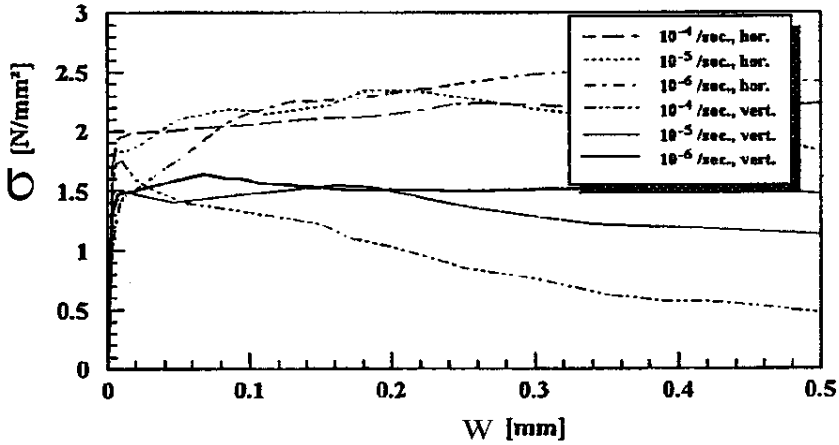
c)



d)

Fig. 3.6 (continued)





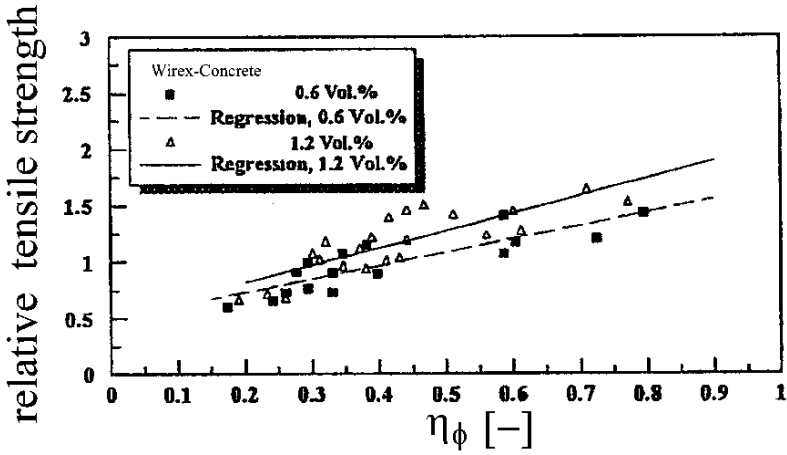
(e)

Fig. 3.6 (continued)

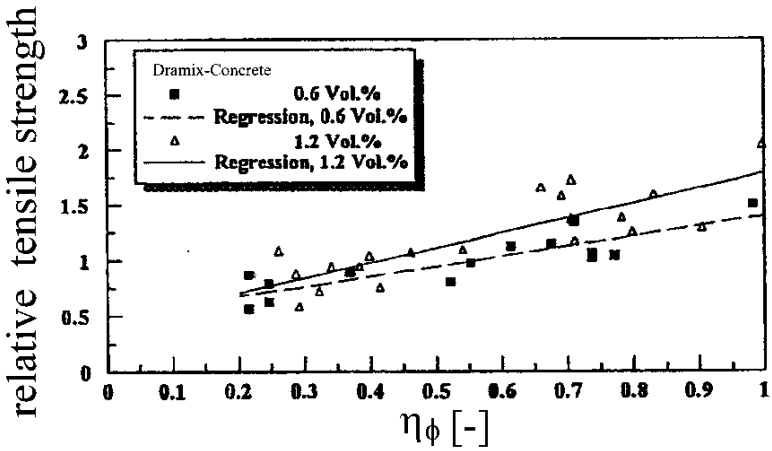
### Experiments by Yazici et al. (2007)

Hooked-end bundled steel fibres with three different ratios  $l/d_f$  ( $l/d_f = 45, 65$  and  $80$ ) were used. The diameter and length of three types of steel fibres were  $0.62, 0.90,$  and  $0.75$  mm and  $30, 60,$  and  $60$  mm, respectively. The tensile strength of steel fibres was  $1250, 1000$  and  $1200$  MPa, respectively. Three different fibre volumes  $V_f$  were added to concrete mixes at  $0.5\%, 1.0\%$  and  $1.5\%$  by volume of concrete. The average compressive strength was  $40$  MPa. The compressive and split tensile strength was determined on  $150$  mm cubes. In addition, flexural strength tests were performed on  $100 \times 100 \times 600$  mm<sup>3</sup> prismatic specimens. The workability of reinforced concrete mixture was dramatically decreased for fibres with  $l/d_f$  ratio of  $80$  and  $V_f$  of  $1.0\%$  and  $1.5\%$ . The unit weight of concrete increased with fibres used (this increase varied with the aspect ratio and volume of fibres).

The results of compressive, tensile and flexural strengths are given in Tab.3.2. The compressive strengths of SFRCs were higher by about  $4\text{--}19\%$  than the control plain concrete mixture. The compressive strengths of specimens of  $45$  aspect ratio were higher with increasing  $V_f$ . But, for  $65$  and  $80$  aspect ratios, the compressive strengths only increased up to  $1\%$  fibre volume. The specimens with the fibre volume of  $1.5\%, 1.0\%$ , and  $0.5\%$  had the highest compressive strength for the aspect ratios of  $45, 65,$  and  $80$ , respectively.

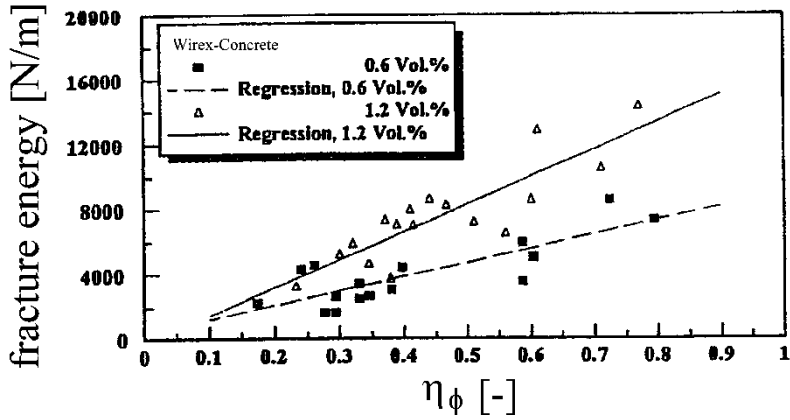


a)



b)

Fig. 3.7 Dependence of tensile strength of Wirex (a) and Dramix (b) concrete on fibre orientation (Lin 1999)



a)

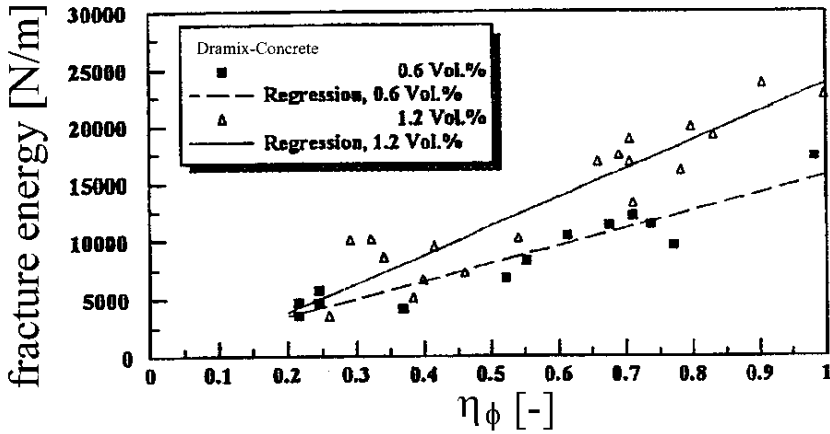


Fig. 3.8 Dependence of fracture energy of Wirex (a) and Dramix (b) concrete on fibre orientation from tensile tests (Lin 1999)

The split tensile strengths of SFRCs were higher by about 11-54% than the control mixture. For all volume fractions, the split tensile strength of SFRCs was higher with increasing fibre content and  $l_f/d_f$  ratio. Especially, utilization of 1.5% fibre volume was more efficient on the split tensile strength.

The flexural strengths of SFRC were higher by about 3-81% than plain concrete. Steel fibres significantly improved the flexural strength of concrete

compared to the compressive and split tensile strength. Besides, the flexural strength of SFRC was significantly improved with increasing  $l_f/d_f$  ratio and  $V_f$ .

**Table 3.1** Overview of results from flexural tests ( $f_f$  – flexural tensile strength,  $G_f$  – fracture energy,  $\eta_\phi$  - orientation coefficient) (Lin 1999)

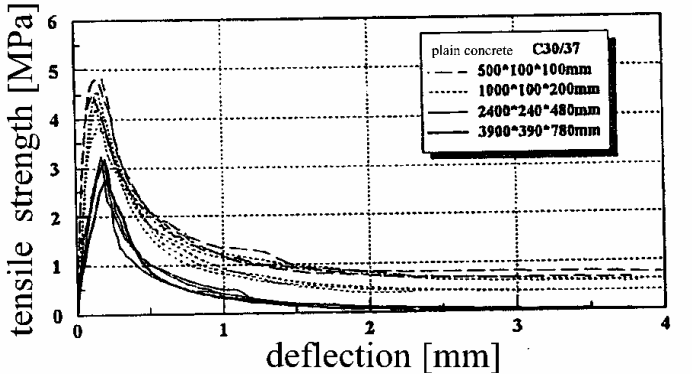
Beam	500×100×100 mm <sup>3</sup>			1000×100×200 mm <sup>3</sup>			2400×240×480 mm <sup>3</sup>			3900×390×780 mm <sup>3</sup>		
Concrete type	$f_f$	$G_f$	$\eta_\phi$	$f_f$	$G_f$	$\eta_\phi$	$f_f$	$G_f$	$\eta_\phi$	$f_f$	$G_f$	$\eta_\phi$
	[MPa]	[N/m]	[-]	[MPa]	[N/m]	[-]	[MPa]	[N/m]	[-]	[MPa]	[N/m]	[-]
Plain concrete	4.72	140	-	4.21	133	-	3.72	103	-	2.6	85	-
Wirex concrete (1.2%)	9.90	9446	0.50	7.20	7282	0.70	5.52	7350	0.37	-	-	-
Dramix concrete (1.2%)	11.10	12198	0.55	6.47	15307	0.69	11.10	12198	0.42	5.0	11250	0.38

### Experiments by Falkner and Henke (2000)

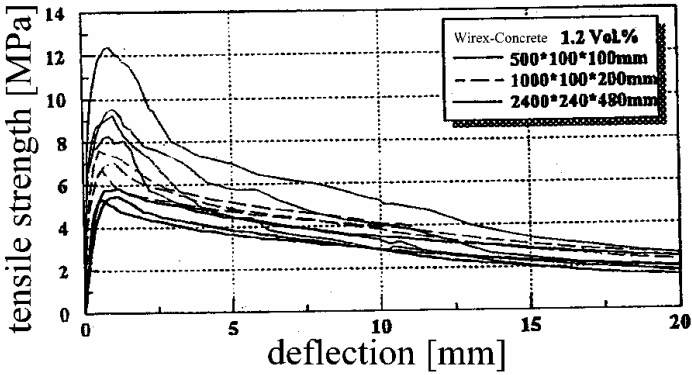
Laboratory experiments were carried out with back-anchored underwater concrete slabs and jointless non-ballasted tracks for rail. In the first case, the size of the slab was 0.28×3×3 m<sup>3</sup>. The slab was prestressed with 9 anchors to model hydrostatic water pressure (Fig.3.14). Three tests were carried out: with a plain concrete slab (called UB1), a fibre-reinforced slab with 60 kg of Dramix steel fibre 60/0.8 (called UB2) and a fibre-reinforced slab with 40 kg of Dramix fibre 50/0.6 (called UB3), respectively.

The failure load and deformation corresponding to this load were significantly higher in the case of concrete slabs including steel fibres (Fig.3.15). The slab of plain concrete broke into pieces. However, the fibre-reinforced concrete could be lifted up in one piece after the experiment's end (plastic failure was observed).

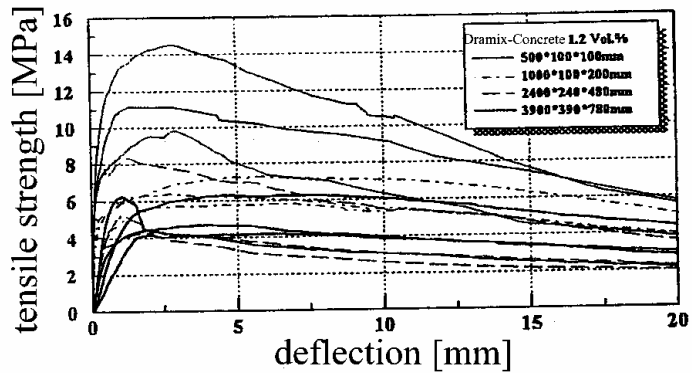
The jointless railway slabs (Fig.3.16) (including usual steel reinforcement) without fibres and with addition of 40 kg/m<sup>3</sup> fibres Dramix 50/0.6 were investigated under cyclic dynamic loading. The results are shown in Figs.3.17 and 3.18.



a)

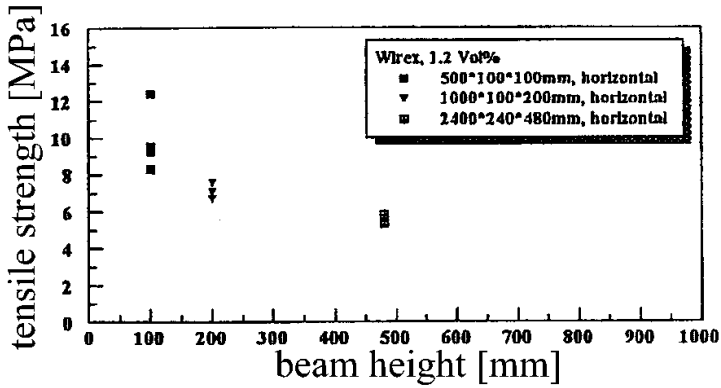


b)

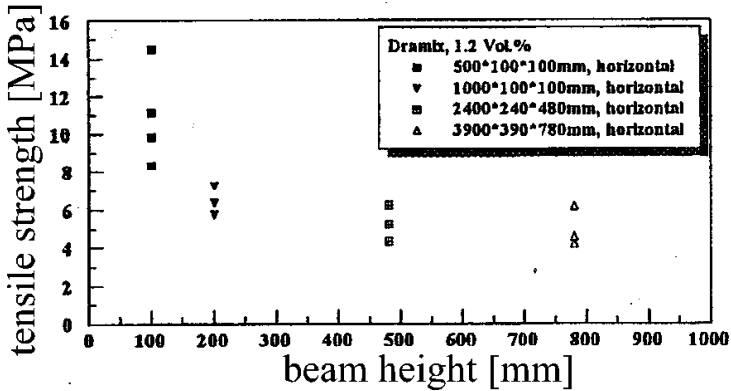


c)

**Fig. 3.9** Experimental flexural stress-deflection curves of notched concrete beams with different beam depths: a) plain concrete, b) Wirex concrete (1.2%), c) Dramix concrete (1.2%) (Lin 1999)



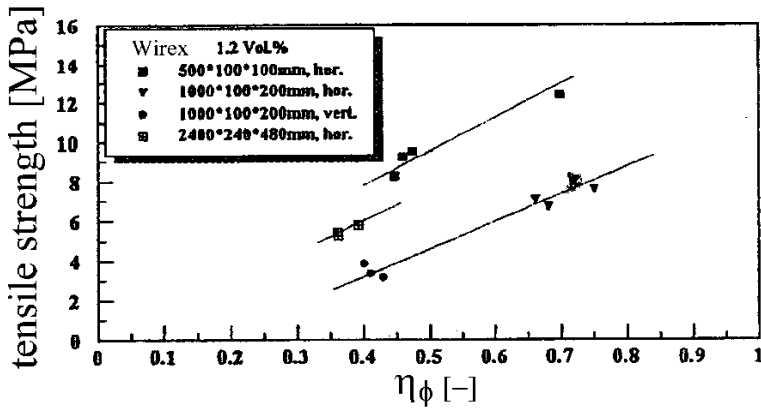
a)



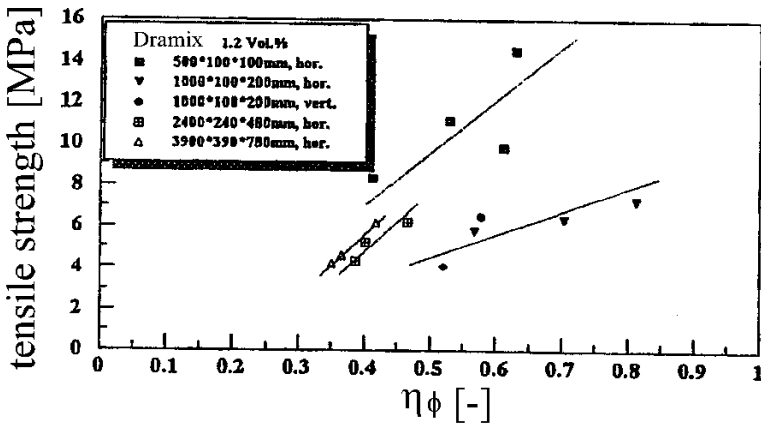
b)

**Fig. 3.10** Experimental flexural stress-deflection curves of notched concrete beams with different beams: a) Wirex concrete (1.2%), b) Dramix concrete (1.2%) (Lin 1999)

The maximum crack width of the reinforced concrete slab was 0.9 mm after 3 mln. strain cycles. In turn, the maximum crack width of the reinforced concrete slab with fibres was only 0.2 mm after 3 mln. cycles. The failure load was higher as well (it increased from 320 kN up to 490 kN). This result was confirmed during measurements on the real object. After 2.5 years, the maximum crack width of the real track slab including steel fibres was only 0.05 mm, in contrast to the track slab without fibres, where the maximum crack width was equal to 0.2 mm.



a)



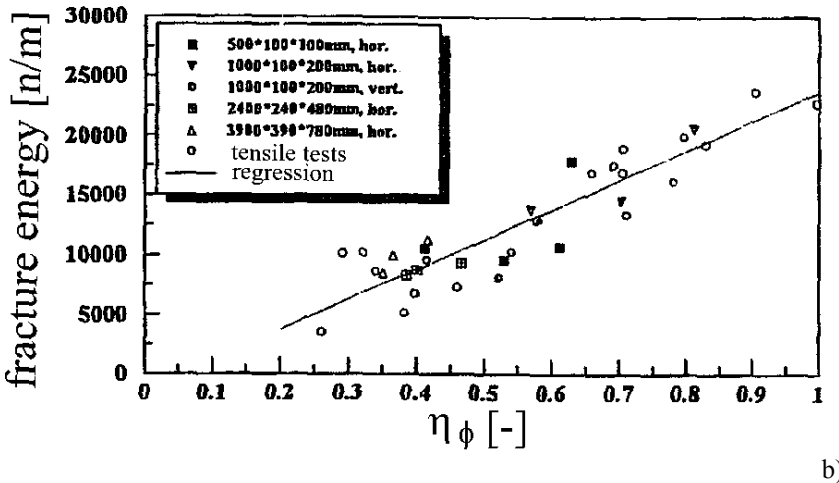
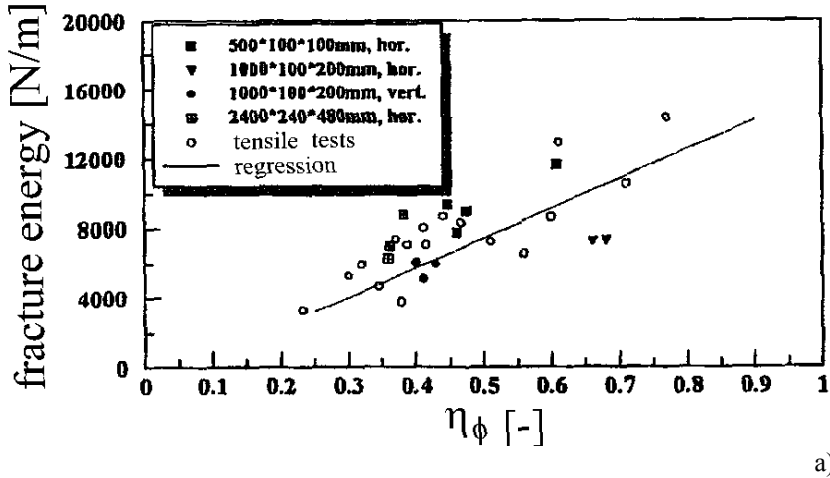
b)

**Fig. 3.11** Experimental flexural tensile strength against fibre orientation of notched concrete beams with different beam depths: a) Wirex concrete (1.2%), b) Dramix concrete (1.2%) (Lin 1999)

### Experiments by Altoubat et al. (2008) and Roesler et al. (2004)

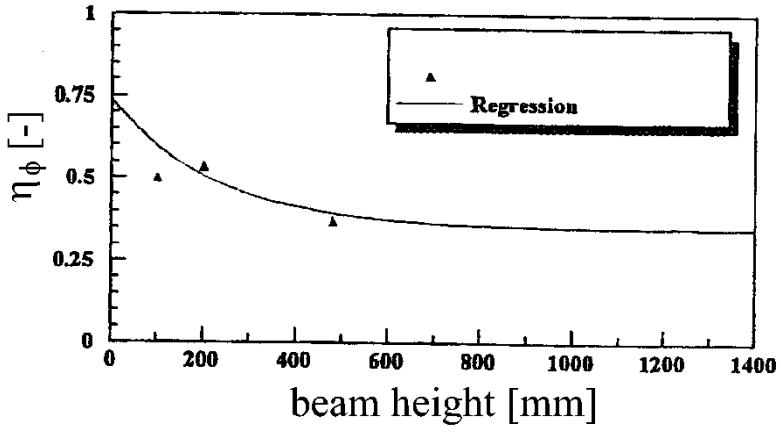
A small- and large-scale testing program was conducted to compare the structural behavior of fibre-reinforced concrete slabs under interior and edge loading conditions and under a standard flexural beam loading configuration. Two steel fibre types and one synthetic fibre type were evaluated in the testing program. The slab dimensions selected for large-scale tests were 2.2 m by 2.2 m with a nominal thickness of 0.127 m. Seven slabs were cast with two slabs containing discrete

steel fibres (crimped 50/1.3 mm and hooked-end 60/0.92 mm), three slabs with synthetic fibres at two volume percentages, and two plain concrete slabs (plain). The hooked-end fibres were introduced into the concrete mix at 0.35% by volume or 27.3 kg/m<sup>3</sup> and the crimped fibres were added at a rate of 0.50% by volume or 39 kg/m<sup>3</sup>.

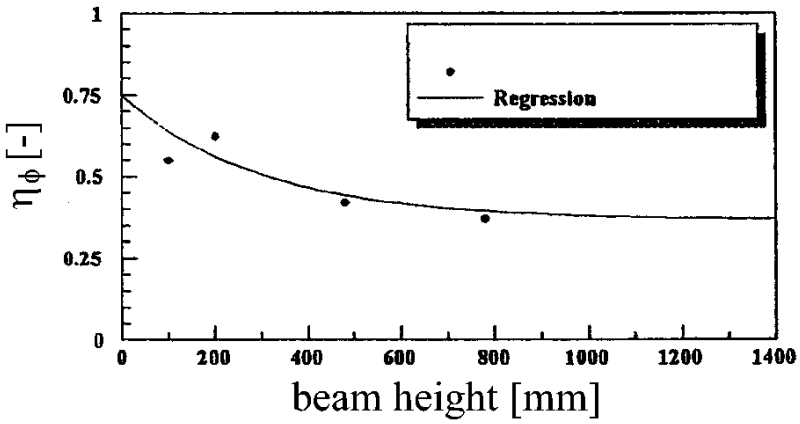


**Fig. 3.12** Experimental fracture energy against fibre orientation of notched concrete beams with different beam depths: a) Wirex concrete (1.2%), b) Dramix concrete (1.2%) (Lin 1999)





a)



b)

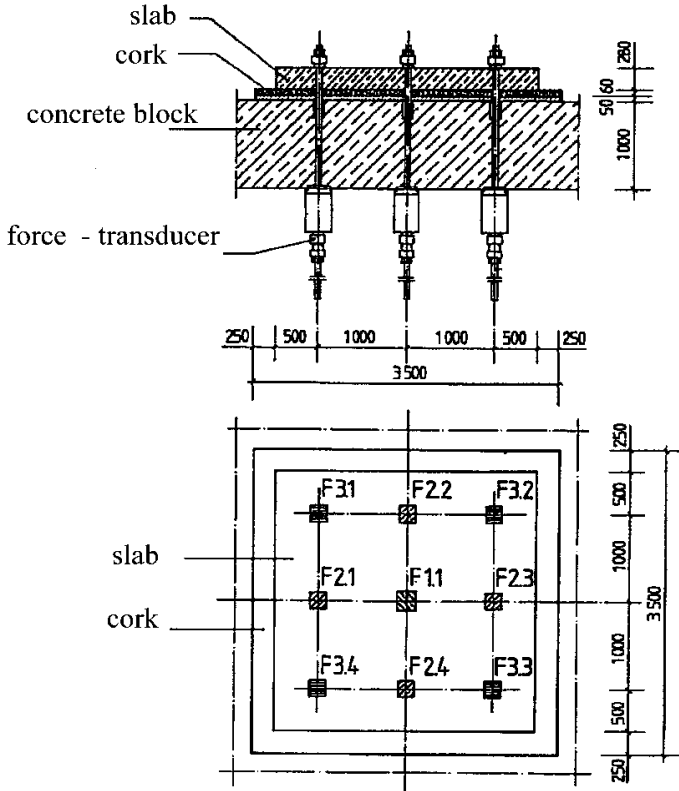
**Fig. 3.13** Experimental correlation between orientation coefficient and beam height: a) Wirex concrete (1.2%), b) Dramix concrete (1.2%) (Lin 1999)

**Table 3.2** Mechanical properties of concrete mixtures ( $f_c$  – uniaxial compressive strength,  $f_{st}$  – splitting tensile strength,  $f_f$  – flexural tensile strength) (Yazici et al. 2007)

Nr.	$l/d_f$	$V_f$ [%]	$f_c$ [MPa]	$f_{st}$ [MPa]	$f_f$ [MPa]
1	-	-	49.1	4.1	5.9
2	45	0.5	50.8	4.5	6.1
3	45	1.0	53.7	4.7	6.3
4	45	1.5	57.7	4.7	7.8
5	65	0.5	53.5	4.5	6.2
6	65	1.0	58.3	4.8	8.1
7	65	1.5	56.4	6.3	9.3
8	80	0.5	56.0	4.6	6.4
9	80	1.0	58.3	5.2	9.7
10	80	1.5	52.1	5.9	10.8

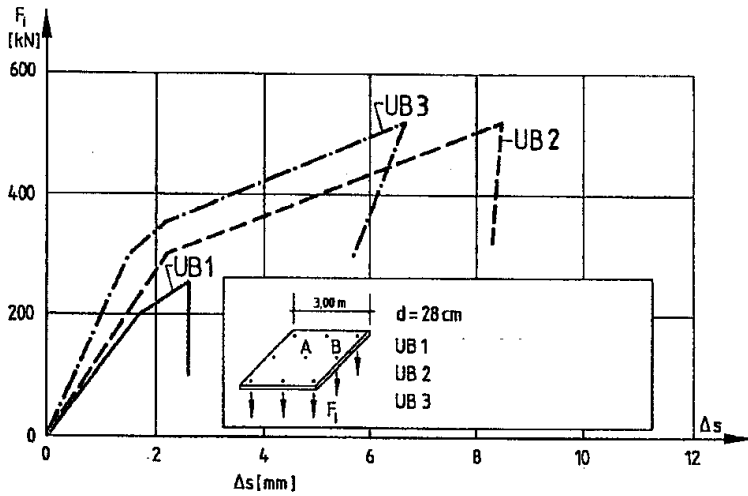
Compressive and flexural strength specimens were sampled at the same time the slabs were cast (Tab.3.3). The equivalent flexural strength of the synthetic and steel fibre reinforced concretes was determined on beam specimens (500 mm×150 mm×150 mm) loaded in three-point bending according to ASTM C1609-05.

Seven slabs were tested during large-scale tests (Tab.3.3). Five slabs were center-loaded and two slabs were edge-loaded. The load versus deflection plot for the center-loaded slabs can be seen in Fig.3.19 for plain concrete and steel fibres. In addition, the results with synthetic fibres are depicted. The load-deflection responses of the slabs were similar up to the point where the first flexural crack occurred at approximately 2–3 mm of deflection. The flexural crack, or hinge, was defined when there was a sudden reduction in load carrying capacity of the slab. At this point, the bending resistance of the slab decreased dramatically orthogonal to a flexural crack. Other load reductions were associated with additional flexural cracks at the bottom of the slab approximately orthogonal to the first flexural crack.

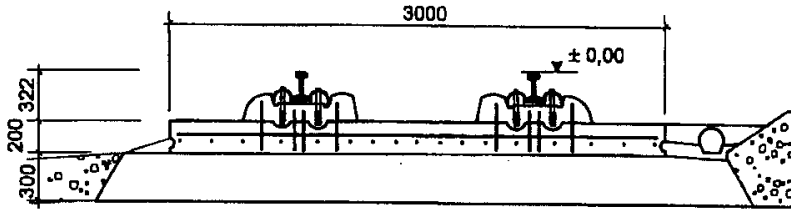


**Fig. 3.14** Experimental set-up for slabs (Falkner and Henke 2000)

The initial flexural cracks always initiated at the slab bottom near the interior and propagated vertically upward and towards the slab edges. The collapse or ultimate load of the slab could be seen as the level in which no further increase in load was reached with increasing magnitudes of slab deformation. The ultimate load was associated with either flexural cracking occurring on the top of the slab or punching shear failure. In Fig.3.19, the shape of the load–deflection curves of the FRC slabs relative to the plain concrete slab demonstrated an improved global structural response. The addition of fibres increased the ultimate capacity of the plain concrete slab.



**Fig. 3.15** Results of test loading for slabs with plain concrete (UB1) and steel fibrous concrete:  $60 \text{ kg/m}^3$  (UB2) and  $40 \text{ kg/m}^3$  (UB3) ( $\Delta s$  - displacement difference between points A and B) (Falkner and Henke 2000)

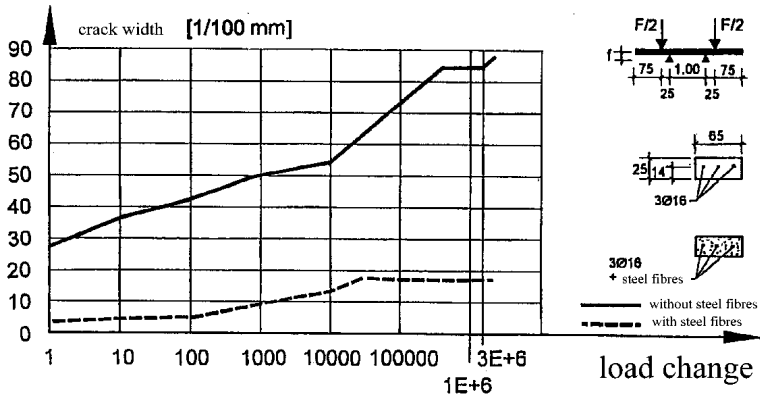


**Fig. 3.16** Jointless railway system (Falkner and Henke 2000)

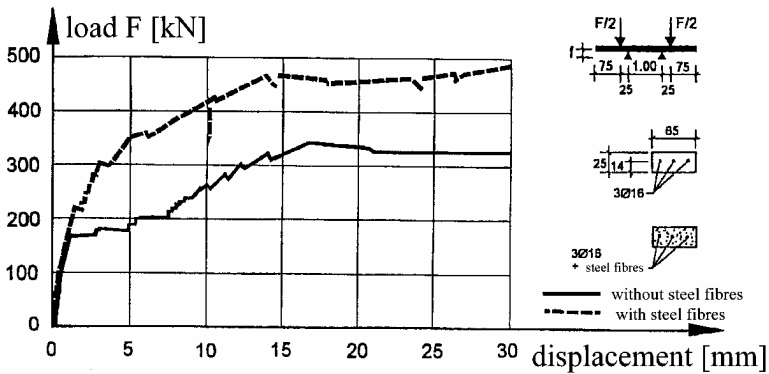
### Experiments by Glinicki (2004)

The three-point bending tests were performed with the beam specimens  $150 \times 150 \times 500 \text{ mm}^3$  and  $100 \times 100 \times 600 \text{ mm}^3$  using different hooked fibres. The results showed a linear increase of the equivalent flexural strength with increasing fibre volume (Fig.3.20 and 3.21) according to the formula

$$f_{eq} = 0.73 + 8.06V_f \frac{l_f}{d_f} \quad (3.2)$$



**Fig. 3.17** Maximum crack width depending on number of loading cycles (Falkner and Henke 2000)



**Fig. 3.18** Load-deflection diagram of test slabs (Falkner and Henke 2000)

Tables 3.4 and 3.5 present the effect of hooked fibres on the equivalent flexural strength of different concretes on the basis of three-point bending tests (Glinicki 2004). The equivalent flexural strength increased with an increase of fibre volume, fibre aspect ratio and concrete class. The higher the concrete class, the fibre effect was diminished.

**Table 3.3** Experimental design and summary of large and small-scale testing results (Altoubat et al. 2008)

Concrete type	FRC crimped steel fibre	FRC hooked steel fibre	FRC synthetic fibre	FRC synthetic fibre	FRC synthetic fibre	Plain concrete	Plain concrete
Fibre dosage [%]	0.5	0.35	0.32	0.48	0.48	0	0
Loading location	center	center	center	center	edge	center	edge
Slab thickness [mm]	131.8	131.8	131.8	131.8	131.6	139.7	131.6
Flexural crack load [kN]	167	141	143	143	125	108	99
Ultimate load [kN]	220	228	195	195	131	135	-
Increase in flexural cracking [%]	54	31	32	32	28	-	-
Increase in ultimate cracking [%]	62	68	44	44	32	-	-
Compressive strength [MPa]	37.2	34.2	31.8	31.8	31.8	41.1	41.1
Flexural strength [MPa]	5.28	4.68	4.82	4.82	4.82	4.73	4.73
Equivalent flexural strength ratio at 3 mm displacement	35	43	39	39	39	3	3

Glinicki (2004) reported on the experiments carried out at the Greenwich University with concrete and fibre-concrete slabs  $3.0 \times 3.0 \text{ m}^2$  on soil. The thickness was 130 mm and 150 mm. The slabs were centrally loaded on the area of  $100 \times 100 \text{ mm}^2$ . Fig.3.22 shows the results of a cracking and failure force for concrete slab (0) and slabs reinforced with polypropylene fibres (PP) (volume content –  $0.9 \text{ kg/m}^3$ ), steel nets (200 mm $\times$ 200 mm $\times$ 6 mm) (S) and steel hooked fibres 60/1.0 mm and 60/0.8 mm(HS). Similar results are shown in Fig.3.23, where additionally the effect of polypropylene fibres of  $l_f=19 \text{ mm}$  is enclosed (PS).

In experiments, a significant positive effect of steel fibres on the flexural strength independently of the slab thickness was observed. The effect of hooked fibres turned out to be always stronger.

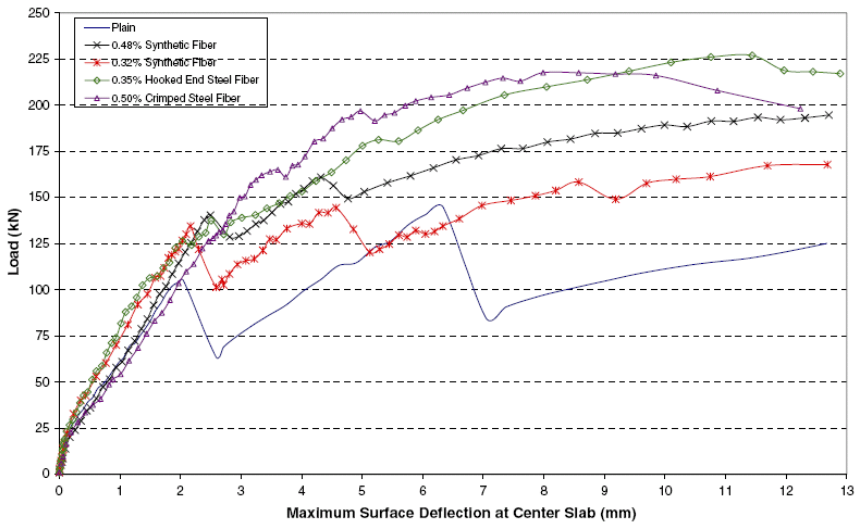
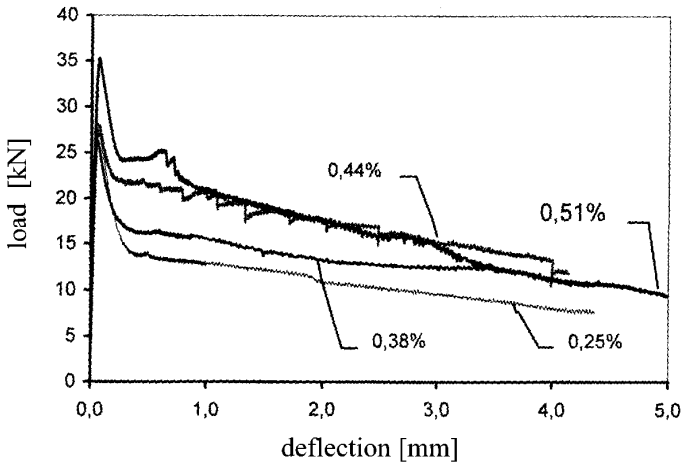


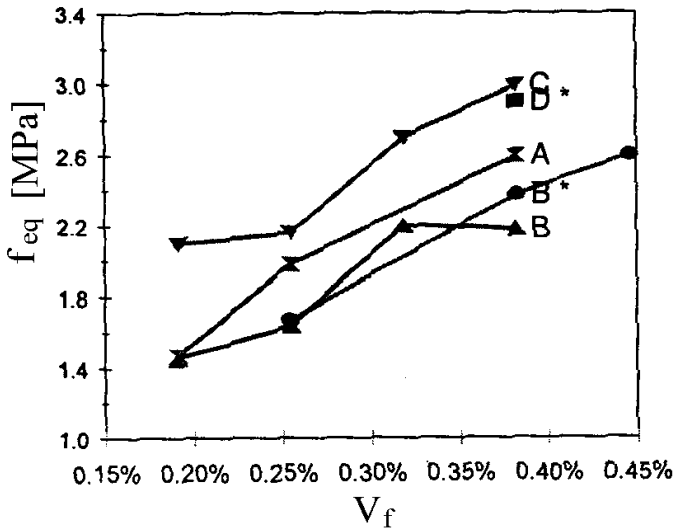
Fig. 3.19 Load versus deflection for center-loaded concrete slabs (Altoubat et al. 2008)

### Experiments by Szumigala et al. (2001)

Three-point bending tests were carried out at the Technical University of Poznań (Szumigala et al. 2001). The beam dimensions were  $150 \times 150 \times 600 \text{ mm}^3$ . The steel fibres were straight with  $l_f/d_f=50/1$ . An almost linear correlation between the equivalent flexural strength and fibre dosage was obtained (Tab.3.6). The number of active fibres in the single failure cross-section was: 11-22 (for fibre content of  $25 \text{ kg/m}^3$ ), 19-40 (for  $35 \text{ kg/m}^3$ ) and 21-46 (for  $45 \text{ kg/m}^3$ ). Thus, the equivalent flexural strength was proportional to the content of active fibres.



**Fig. 3.20** Typical experimental load-deflection curves during three-point bending with different volume dosage of fibres ( $l_f=50$  mm,  $d_f=1.0$  mm) (Glinicki 2004)



**Fig. 3.21** Experimental effect of fibre content  $V_f$  on the equivalent flexural strength  $f_{eq}$ : A)  $l_f=60$  mm,  $d_f=1.0$  mm, B)  $l_f=50$  mm,  $d_f=1.0$  mm, C)  $l_f=60$  mm,  $d_f=0.8$  mm, D)  $l_f=60$  mm,  $d_f=0.8$  mm (\* - beams  $150 \times 150$  mm<sup>2</sup>, remaining - beams  $100 \times 100$  mm<sup>2</sup>) (Glinicki 2004)



**Table 3.4** Effect of fibre dosage on the equivalent flexural strength for different concrete class (hooked steel fibres Dramix RC-80/60-BN,  $l_f=60$  mm,  $d_f=0.75$  mm) (Glinicki 2004)

Fibre content [kg/m <sup>3</sup> ]	C20/25 [MPa]	C25/30 [MPa]	C30/37 [MPa]	C35/40 [MPa]	C40/50 [MPa]
20	1.9	2.3	2.6	2.8	3.0
25	2.3	2.7	3.0	3.2	3.3
30	2.7	3.1	3.3	3.5	3.6
35	3.0	3.3	3.6	3.8	3.9
40	3.3	3.5	3.9	4.1	4.2
45	3.4	3.6	4.0	4.2	4.3
50	3.5	3.7	4.1	4.3	4.4

**Table 3.5** Effect of fibre dosage on the equivalent flexural strength for different concrete class (hooked steel fibres Dramix RC-65/60-BN,  $l_f=60$  mm,  $d_f=0.90$  m) (Glinicki 2004)

Fibre content [kg/m <sup>3</sup> ]	C20/25 [MPa]	C25/30 [MPa]	C30/37 [MPa]	C35/40 [MPa]	C40/50 [MPa]
20	1.7	2.0	2.3	2.5	2.7
25	2.1	2.4	2.7	2.9	3.1
30	2.4	2.8	3.1	3.3	3.4
35	2.8	3.1	3.4	3.6	3.7
40	3.1	3.3	3.6	3.8	3.9
45	3.2	3.4	3.7	3.9	4.0
50	3.3	3.5	3.8	4.0	4.1

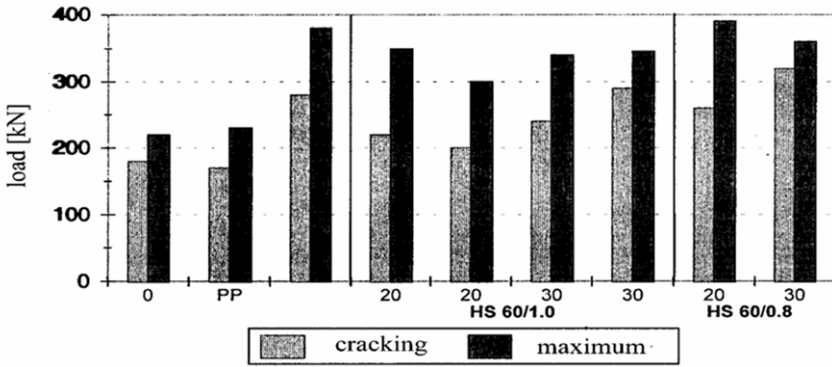


Fig. 3.22 Effect of fibre content on cracking force and failure force from experiments (slab thickness 150 mm) (Glinicki 2004)

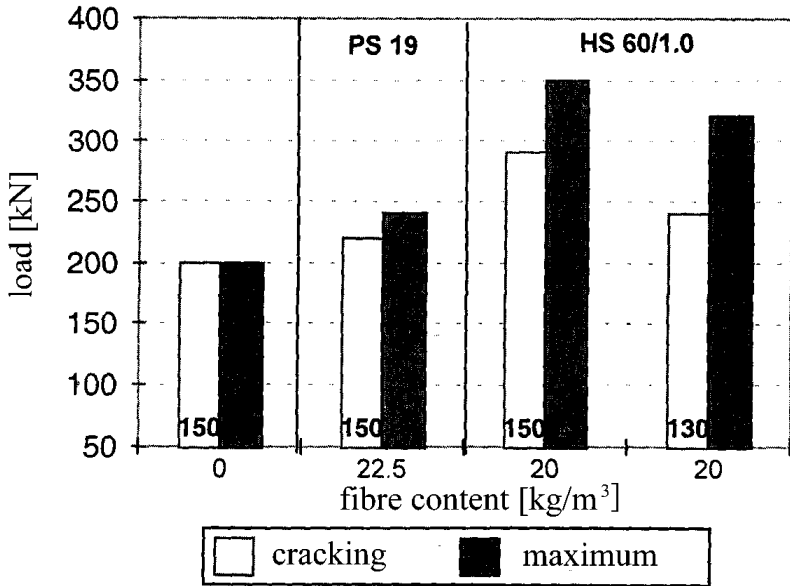


Fig. 3.23 Effect of fibre content on cracking force and failure force from experiments (slab thickness 130 mm and 150 mm) (Glinicki 2004)

**Table 3.6** Effect of fibre content in equivalent flexural strength from bending tests (Szumigala 2001)

Fibre content	25 kg/m <sup>3</sup>	30 kg/m <sup>3</sup>	35 kg/m <sup>3</sup>	40 kg/m <sup>3</sup>	45 kg/m <sup>3</sup>
Equivalent flexural strength	2.1±0.3 MPa	2.55 MPa	3.0±0.6 MPa	3.2 MPa	3.4±0.7 MPa

### Experiments by Chenkui and Guofan (1995)

The experiments were conducted with crushed limestone with maximum size 20 mm or 40 mm. Three kinds of fibres were used: 25 mm in length with aspect ratio 43 (I), 35 mm in length with aspect ratio 60 (II) and 45 mm in length with aspect ratio 77 (III). The volume percentage of fibres was varied from 0% up to 2%. The crushed stone was divided into two ranges: medium stone with sizes from 20 mm to 40 mm and fine stone with sizes from 5 mm to 20 mm.

In the case of uniaxial compression, the effect of aggregate maximum size was negligible. During splitting tension (Fig.3.24), the strengthening effect of steel fibre was different depending on the content of steel fibre and ratio of fine stone to medium stone. At the same fraction of steel fibre by volume, the tensile strength decreased with an increase in the ratio of medium stone of size 20-40 mm. The tensile strength was also affected by the aspect ratio of steel fibres: the longer were the steel fibres, the higher was the tensile strength (Fig.3.25). Thus, steel fibres could be also used to reinforced concrete elements which contain larger aggregates.

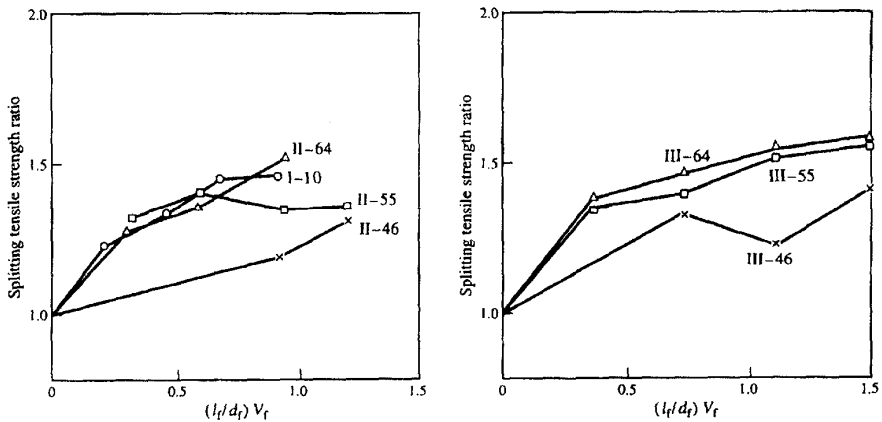
In the case of bending, the flexural strength increased with increasing fibre content (this increase was greater with the maximum aggregate size of 20 mm) (Fig.3.26). Fig.3.27 presents the load-deflection curves. The addition of fibres improved significantly the flexural toughness (Figs.3.27 and 3.28). The effect of the fibre length and aggregate size on the toughness was slight.

### Experiments by Topcu and Canbaz (2007)

The experimental investigations to study the effects of replacement of cement (by weight) with three percentages of fly ash and effects of addition of steel and polypropylene fibres were performed. Utilization of fly ash (FA) in concrete technology becomes more common. FA causes environmental pollution and the cost of storage of FA is very high. When some types of FA replaces with cement in concrete mixture, fresh concrete workability increases, early strength and shrinkage of hardened concrete can decrease (Atis 2003), and permeability

decreases due to filling the micro-pores of concrete (Atis 2004). In addition, FA positively affects durability of concrete and mortar like freeze-thaw resistance, sulphate resistance, alkali-silica reaction and abrasion resistance (Atis 2002).

Steel fibres (denoted by SF) used in the study were wires 35/0.35 mm with their two ends having been twisted (obtained by the cold drawn process). Plastic propylene fibres (denoted by PP1 and PP2) were mostly used for reinforcing mortar and concrete composites. These fibres were used as fibrillated film, varying from 50 to 100  $\mu\text{m}$  in diameter (length 12-23 mm). Fly ash was used as replacement of cement, at the levels of 0, 10, 15 and 20% by weight.



**Fig. 3.24** Test results of splitting tensile strength ( $l_f$  – length of fibres,  $d_f$  – diameter of fibres,  $V_f$  - volume fraction of fibres) (Chenkui and Guofan 1995)

First, slump tests were carried out to determine the consistency of fresh concrete (Tab.3.7). Ultrasonic pulse velocity, rebound hammer, resonance frequency, compressive strength, splitting-tensile strength and bending strength tests were applied on hardened concrete specimens (Figs.3.29-3.33, Tab.3.8). The slump values of fresh concretes decreased related to fibre addition of concrete (Tab.3.7). Fibres caused a 2–8% decrease in the workability of concrete (fibres hindered the flowability of fresh concrete and this caused a decrease in workability). Conversely, the workability was kept in constant when adding FA. The maximum amount of FA in concrete was limited up to 25%. In turn, the value of 15% was advisable (up to 7% savings can be gained).

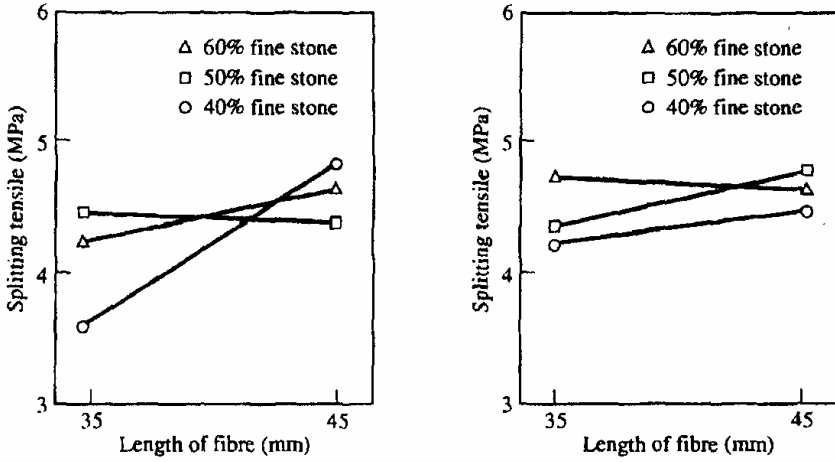


Fig. 3.25 Relationship between splitting tensile strength and length of steel fibres from experiments with different aspect ratio of fibres (Chenkui and Guofan 1995)

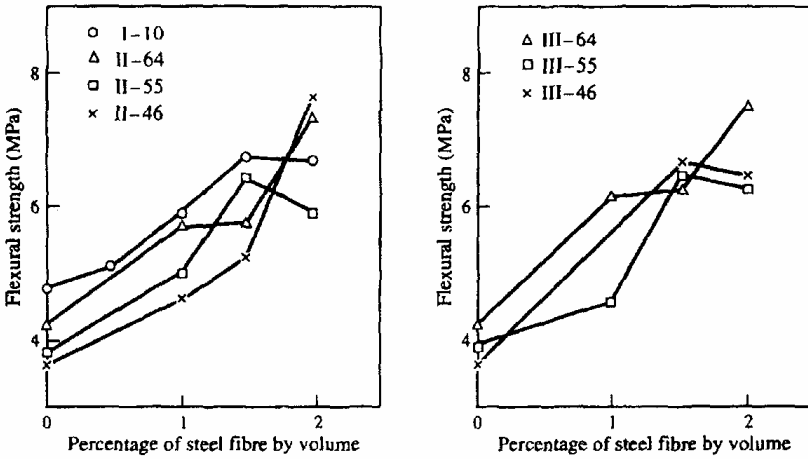


Fig. 3.26 Flexural test results (Chenkui and Guofan 1995)

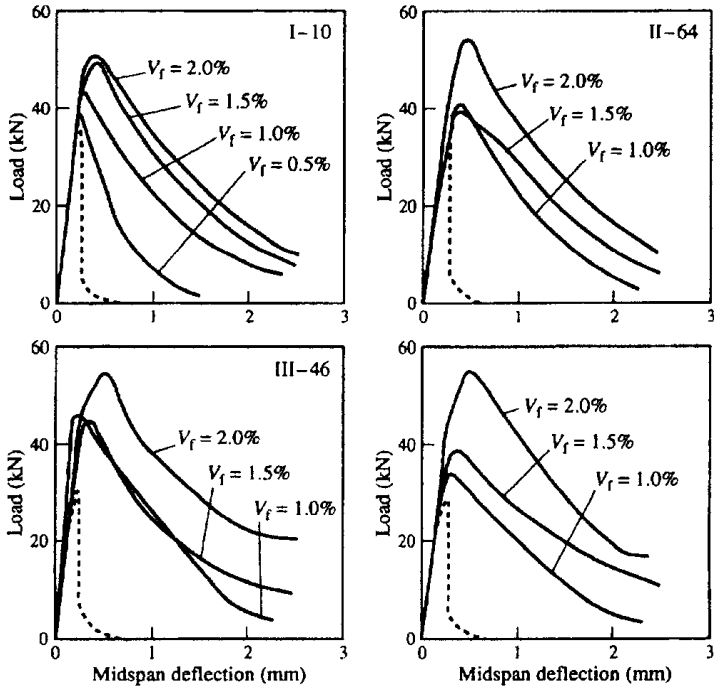


Fig. 3.27 Typical experimental load-deflection curves from bending tests (Chenkui and Guofan 1995)

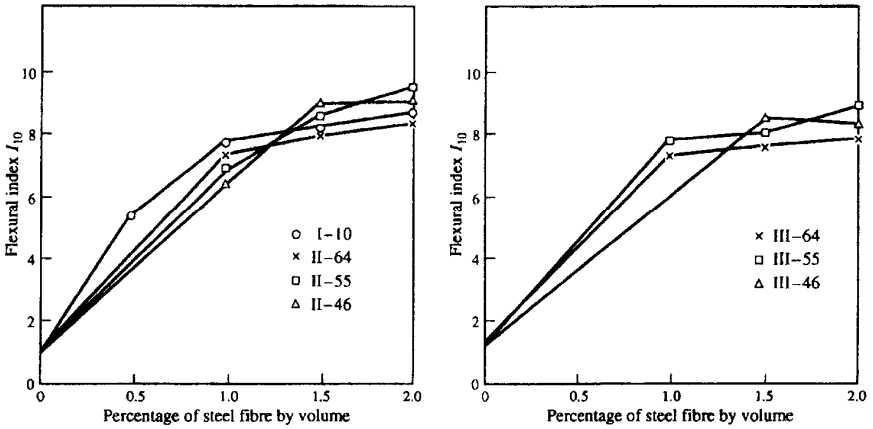


Fig. 3.28 Curves of toughness index  $I_{10}$  by ASTM C 1018 against volume fraction of fibres (Chenkui and Guofan 1995)

**Table 3.7** Results of slump tests (Topcu and Canbaz 2007)

Specimen	Fly ash content [%]	Fibre type	Fibre content [%]	Slump [mm]
A1	10	-	-	70
A2	10	PP1	0.08	67
A3	10	PP2	0.05	65
A4	10	SF	0.65	68
B1	15	-	-	69
B2	15	PP1	0.08	66
B3	15	PP2	0.05	64
B4	15	SF	0.65	66
C1	20	-	-	68.5
C2	20	PP1	0.08	65
C3	20	PP2	0.05	66
C4	20	SF	0.65	67

The compressive strength of concrete produced with fibres increased as compared to concrete without fibres. In turn, a decrease in the compressive strength was observed due to the FA replacement. The increment in the compressive strength of concrete was observed up to 90%, 18% and 95% for PPI, PPII and steel fibres, respectively. In the bending strength, the decrement was seen for the FA replacement ratio at about the level of 12%. However, the increases in the compressive strength were observed up to 114%, 1% and 130% for PPI, PPII and steel fibres, respectively. In the splitting-tensile strength, the decrements were also seen for FA concrete, but fibre addition provided increments. Especially, increments in steel fibre reinforced concretes were noticeable as 54%. A decrease was determined in ultrasonic pulse velocity and resonance frequency values for addition of fibres.

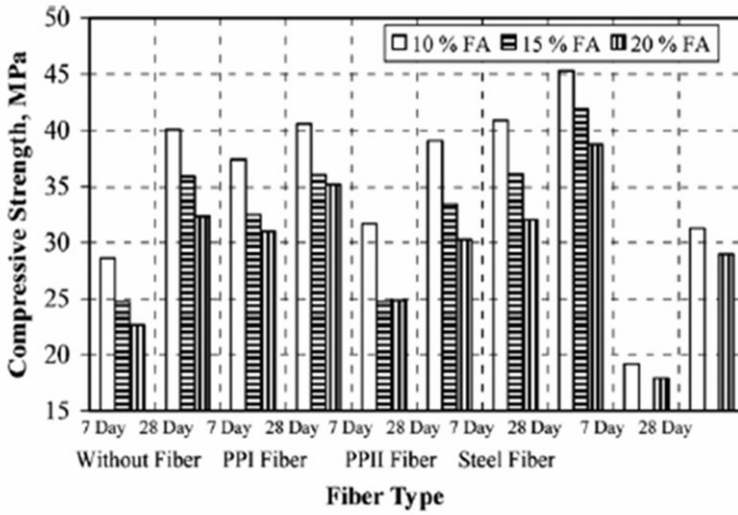


Fig. 3.29 Cylindrical compressive strength versus fibre type (Topcu and Canbaz 2007)

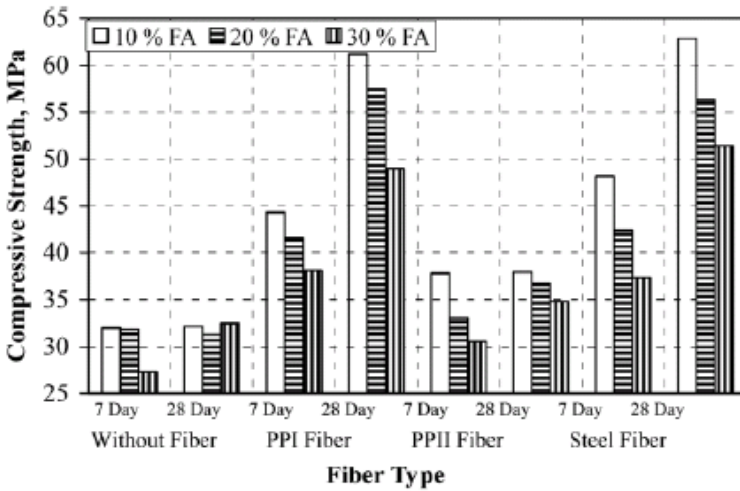
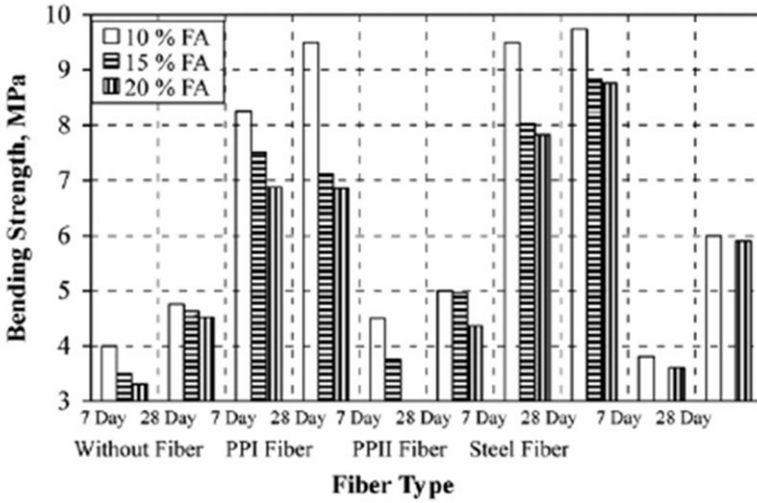
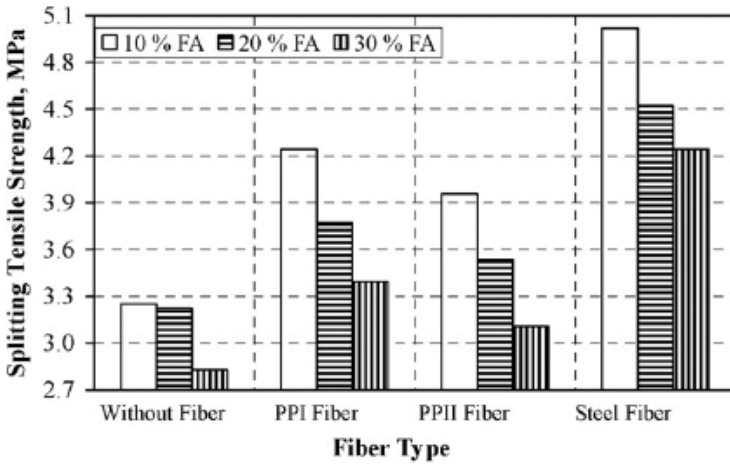


Fig. 3.30 Cubic compressive strength versus fibre type (Topcu and Canbaz 2007)





**Fig. 3.31** The change of bending strength versus fibre type for different content of fly ash (Topcu and Canbaz 2007)



**Fig. 3.32** The change of splitting-tensile strength versus fibre type for different content of fly ash (Topcu and Canbaz 2007)

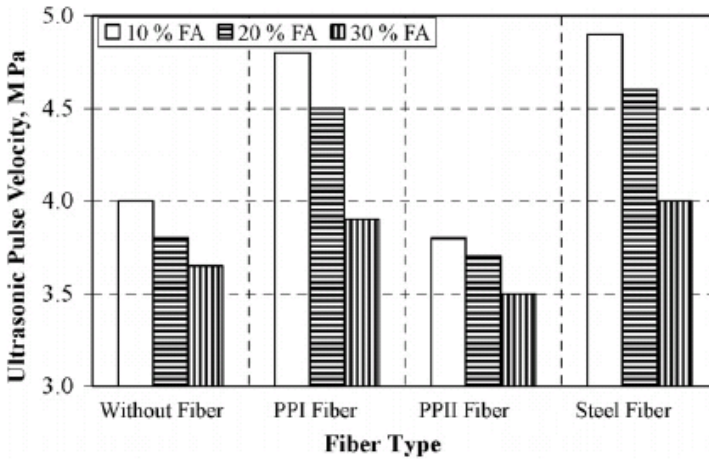


Fig. 3.33 Ultrasonic pulse velocity versus fibre type (Topcu and Canbaz 2007)

### Tests by Balendran et al. (2002)

The effect of the concrete type (normal and lightweight) was investigated by Balaguru and Shah (1992), Wafa and Ashour (1992), Balaguru and Foden (1996) and Balendran et al. (2002). In the tests by Balendran et al. (2002), compression, splitting and bending tests were performed (Figs.3.34 and 3.35). Four mixes were used: plain limestone concrete (LSP), fibre-reinforced limestone concrete (LSF), plain lightweight concrete (LTGP) and fibre-reinforced lightweight concrete (LTGF). The maximum size of crushed limestone was 10 mm and 6 mm, respectively. The amount of steel fibre was 1% by volume of concrete (3% by weight). The fibres were round and straight and were 0.25 mm in diameter and 15 mm in length. The basic properties of four concrete mixes are given in Tab.3.9. The density and compressive strength of fibre-reinforced concretes were about the same as those of the plain counterparts. The cylinder splitting tensile strength and modulus of rupture increased for both normal and lightweight concrete by the introduction of fibres. Cylinder splitting tensile strength of fibre-reinforced concrete was about twice as high as that of plain concrete for both normal and lightweight concretes. In the case of the modulus of rupture, there was a 2.5-times increase for lightweight concrete and only a smaller increase for normal weight concrete.

For plain concrete mixes, there was no obvious size effect on prism splitting tensile strength. For fibre-reinforced concrete, there was a size effect in the prism splitting strength with smaller sizes up to 150 mm. The prism splitting tensile of

lightweight aggregate concrete was improved more than normal weight concrete. The flexural strength decreased as the specimen size became larger. The size effect was more prominent in lightweight concrete. Addition of fibres on normal weight concrete resulted in a much less increase in the flexural strength than in lightweight concrete. The toughness indices (by ASTM C 1018) for different mixes in three-point and four-point bending are given in Tabs.3.11 and 3.12 and Fig.3.36. The toughness indices were higher for lightweight concrete than for normal weight concrete. They were not sensitive to the specimen size.

### **Experiments by Mohammadi et al. (2008)**

Ordinary Portland cement, crushed stone coarse aggregates having a maximum size 12.5 mm and river sand were used. The specimens incorporated two different aspect ratios of corrugated steel fibres, namely 40 (fibre size  $0.6 \times 2.0 \times 50 \text{ mm}^3$ ) and 20 (fibre size  $0.6 \times 2.0 \times 25 \text{ mm}^3$ ) by weight of the longer and shorter fibres in mix proportions of 100–0%, 65–35%, 50–50%, 35–65% and 0–100% at each of the fibre volume fractions of 1.0%, 1.5% and 2.0%. The tensile strength of 25 mm and 50 mm long fibres was 826 MPa and 801 MPa, respectively. The specimens used for compressive strength tests were  $150 \times 150 \times 150 \text{ mm}^3$  cubes, for split tensile strength tests  $150 \times 300 \text{ mm}$  cylinders and for static flexural strength tests  $100 \text{ mm} \times 100 \text{ mm} \times 500 \text{ mm}$  beams.

Tab.3.10 and Figs.3.34 and 3.35 present the results of splitting tests on different prismatic specimens and of three-point bending tests on different notched beams.

The workability of concrete decreased uniformly with increasing fibre content. The fibre aspect ratio had significant influence on the workability of the fresh mix. A lower aspect ratio of fibres resulted in higher compaction factors or lower inverted slump cone time. The tendency of fibres to clump together was markedly reduced in the case of concrete with fibres of a lower aspect ratio compared to concrete with fibres of a higher aspect ratio. Further, more uniform dispersion of smaller fibres was obtained in concrete as compared to larger fibres. Excessive fibre balling, even at higher volume fractions, was reduced resulting in better workability of concrete containing shorter fibres.

The results of the compressive and split tensile strength of plain concrete and SFRC are given in Tab.3.13 and Figs.3.37 and 3.38.

There was an increase in the compressive strength varying from 3% to 26% on addition of fibres. There was an increase in the compressive strength varying from 3% to 21%, 11% to 25% and 7% to 26% for concrete mixes having 1.0%, 1.5% and 2.0% volume fractions of fibres, respectively. However, for a particular mix, there was an optimum volume fraction of fibres that gave the maximum strength and this was 2.0% with 100% short fibres and the maximum increase in the compressive strength was 26%. The maximum increase in the compressive

strength for other mixes was observed at a fibre volume fraction of 1.5%. It may be concluded that on increasing the percentage of short fibres in concrete mix and with an increase in the gross fibre content in the mix, the compressive strength increased.

**Table 3.8** Test results (Topcu and Canbaz 2007)

Specimen	Relative compressive strength after 7 days [%]	Relative compressive strength after 28 days [%]	Relative bending strength after 7 days [%]	Relative bending strength after 28 days [%]	Relative splitting strength after 18 days [%]
A1	100	100	100	100	100
A2	131	101	206	200	130
A3	111	97	113	105	122
A4	143	113	238	205	154
B1	86	89	88	97	99
B2	114	90	188	150	116
B3	87	83	94	105	109
B4	126	105	201	186	139
C1	79	81	83	95	87
C2	108	88	172	144	104
C3	87	76	72	92	96
C4	112	97	196	185	130

**Table 3.9** Basic properties of 4 mixes (Balendran et al. 2002)

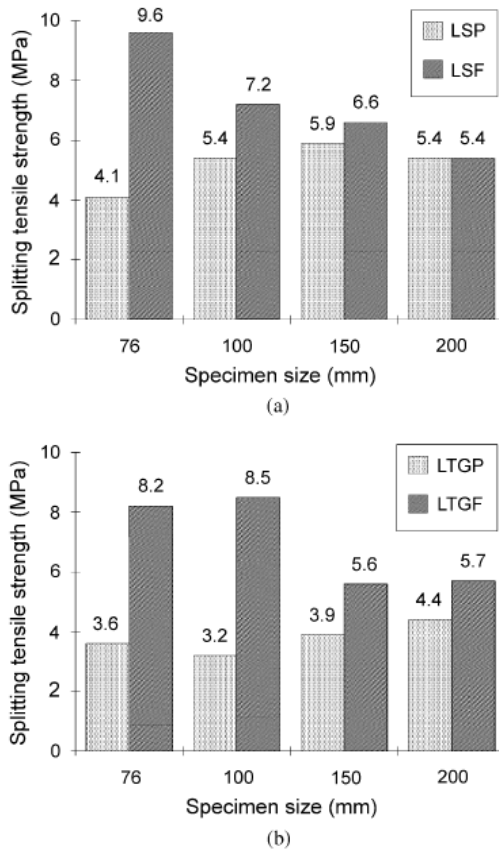
Concrete	Density [kg/m <sup>3</sup> ]	Uniaxial compressive strength [MPa]	Modulus of rupture [MPa]	Cylinder splitting tensile strength [MPa]
LSP	2430	113	4.6	4.5
LSF	2470	115	6.3	10.5
LTGP	2015	90	1.7	3.3
LTGF	2030	91	6.0	6.2

**Table 3.10** Flexural strength and prism splitting tensile strength (Balendran et al. 2002)

Concrete	Flexural strength [MPa] specimen size a)	Flexural strength [MPa] specimen size b)	Flexural strength [MPa] specimen size c)	Prism splitting tensile strength [MPa] specimen size d)	Prism splitting tensile strength [MPa] specimen size e)	Prism splitting tensile strength [MPa] specimen size f)	Prism splitting tensile strength [MPa] specimen size g)
LSP	7.9	5.6	4.9	4.1	5.4	5.9	5.4
LSF	11.3	6.1	5.6	9.6	7.2	6.6	5.4
LTGP	5.9	3.3	2.7	3.6	3.2	3.9	4.4
LTGF	11.3	9.3	7.9	8.2	8.5	5.6	5.7

Specimen size:

a) 50×100×200×300 mm<sup>4</sup>, b) 100×100×400×500 mm<sup>4</sup>, c) 2000×100×800×840 mm<sup>4</sup>, d) 76×76×100 mm<sup>3</sup>, e) 100×100×100 mm<sup>3</sup>, f) 150×150×150 mm<sup>3</sup>, g) 200×200×200 mm<sup>3</sup>.



**Fig. 3.34** Effects of fibre and specimen size on prism splitting tensile strength: a) normal weight concrete, b) lightweight concrete (Balendran et al. 2002)

There was an increase in the tensile strength up to 20–27%, 26–51% and 30–59% with fibrous concrete mixes including 1.0%, 1.5% and 2.0% volume fractions of fibres, respectively. For a particular mixed aspect ratio of fibres, there was an increase in strength with an increase of the fibre content in concrete. The maximum increase in the split tensile strength of 59% with respect to plain concrete was observed for a mix ratio of 65% long fibres and 35% short fibres at a fibre volume fraction of 2.0%.

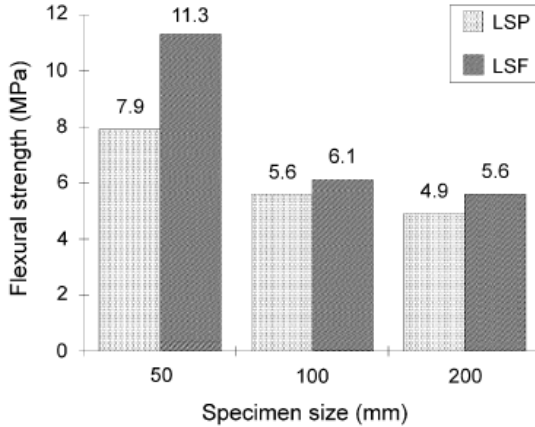
**Table 3.11** Toughness indices in three-point bending tests on notched beams (Balendran et al. 2002)

Concrete	Toughness indices I5			Toughness indices I10			Toughness indices I30		
	specimen size			specimen size			specimen size		
	a)	b)	c)	a)	b)	c)	a)	b)	c)
LSF	5.0	4.7	4.3	10.0	9.1	7.0	31	26	17
LTGF	6.6	6.5	6.6	16.0	16.1	16.3	60	63	60

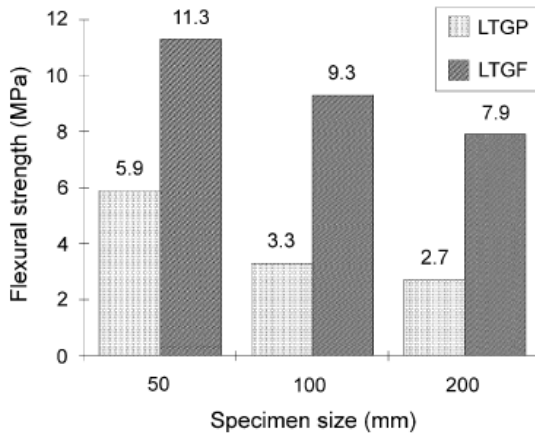
Specimen size: a) 50×100×200×300 mm<sup>4</sup>, b) 100×100×400×500 mm<sup>4</sup>, c) 2000×100×800×840 mm<sup>4</sup>.

The static flexural strength test results for various mixes with a mixed aspect ratio of fibres corresponding to different volume fractions are presented in Tab.3.15 and Figs.3.39 and 3.40. The maximum increase in the static flexural strength, taken as average of three batches, varied from 34% to 42%, 44% to 76% and 52% to 100% for concrete mixes having 1.0%, 1.5% and 2.0% volume fractions of fibres, respectively. The maximum increase in the static flexural strength of 100% was observed for concrete with 100% long fibres at a fibre volume fraction of 2.0%. The peak loads, first crack loads and the corresponding centre-point deflections, taken as average for the three batches, with different mixed aspect ratios and different volume fractions of fibres are listed in Tab.3.16. An increase in the centre point deflection corresponding to the ultimate load, taken as average of three batches, was observed to vary between 28–61%, 45–95% and 43–167% for concrete mixes having 1.0%, 1.5% and 2.0% fibre volume fractions, respectively. Further, the maximum increase in the ultimate load deflection of 61%, 95% and 167% with respect to plain concrete was for fibrous concrete specimens having 100% long fibres for .0%, 1.5% and 2.0% volume fractions of fibres, respectively. There was an increase in the first crack load of the order of 16–26%, 26–33% and 34–49% for concrete mixes having 1.0%, 1.5% and 2.0% fibre volume fractions, respectively (Tab.3.16). The maximum increase in the first crack load of 26%, 33% and 49% with respect to plain concrete was observed with 100% short fibres, at all three fibre volume fractions. The maximum increase in the first crack deflection of 14–21% with respect to plain concrete specimens was obtained for fibrous concrete specimens with a fibre volume fraction of 1.0–2.0%, respectively. The load deflection curves for steel fibrous concrete specimens for a given fibre mix ratio are presented in Figs.3.40–3.44. The longer fibres had a greater influence on the peak load and deflection at the peak load. A comparison of the first crack and ultimate loads in Tab.3.16 shows that fibre reinforcement exercised greater influence on the ultimate load of the composite than on the first crack load. Up to a fibre content of 2.0%, the first crack load and ultimate load were found to increase with an increase of the volume fraction of fibres in

concrete. The fibre volume fraction and the use of a mixed aspect ratio of fibres were more effective in influencing the ultimate load and deflection than the first crack load and the corresponding deflection. The first crack deflection was only slightly influenced by the fibre volume fraction and the use of mixed aspect ratio of fibres had an insignificant effect on the first crack deflection.



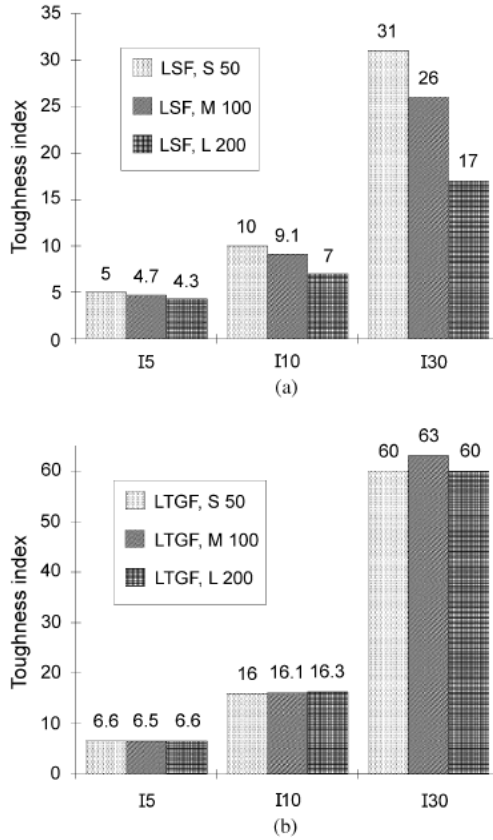
(a)



(b)

**Fig. 3.35** Effects of fibre and specimen size on flexural strength: a) normal weight concrete, b) lightweight concrete (Balendran et al. 2002)





**Fig. 3.36** Toughness indices of fibre-reinforced concretes in bending: a) normal weight concrete, b) lightweight concrete (Balendran et al. 2002)

**Table 3.12** Toughness indices in four-point bending tests on notched beams (Balendran et al. 2002)

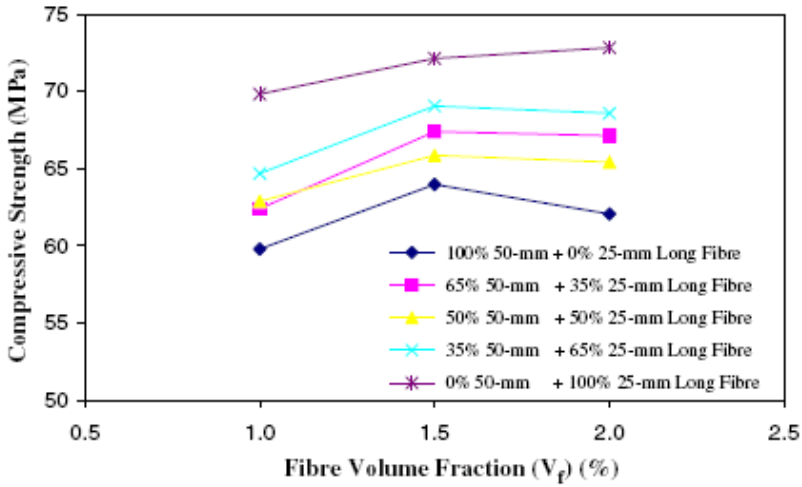
Concrete	Toughness index I5	Toughness index I10	Toughness index I30
LSF	5.0	10	28
LTGF	6.2	15	55

**Table 3.13** Compressive and split tensile strength results of plain concrete and SFRC (Mohammadi et al. 2008)

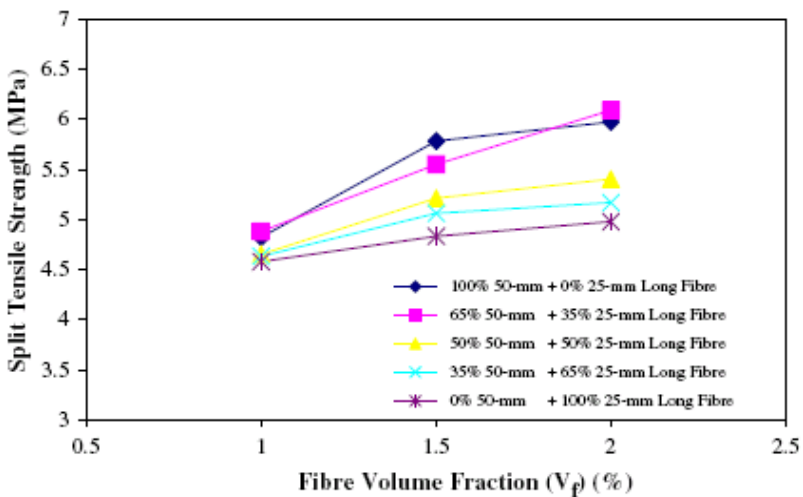
Fibre mix 50 mm long fibres [%]	Fibre mix 25 mm long fibres [%]	Fibre volume fraction [%]	Cube compression strength [MPa]	Split tensile strength [MPa]
0	0	0	57.8	3.8
100	0	1.0	59.8	4.8
65	35	1.0	62.4	4.9
50	50	1.0	62.9	4.7
35	65	1.0	64.7	4.6
0	100	1.0	69.8	4.6
100	0	1.0	64.0	5.8
65	35	1.5	67.4	5.6
50	50	1.5	65.9	5.2
35	65	1.5	69.1	5.1
0	100	1.5	72.1	4.8
100	0	2.0	52.1	6.0
65	35	2.0	67.1	6.1
50	50	2.0	65.4	5.4
35	65	2.0	68.6	5.2
0	100	2.0	72.8	5.0

The toughness index for plain concrete was taken equal to 1.0 in the ASTM method, because plain concrete flexural test specimens failed immediately after the formation of the first crack. The TJCI indices I5, I10 and I20 increased with increasing fibre content and increasing percentage of long fibres. The residual strength factors R5,10 and R10,20 increased with increasing fibre volume fraction and percentage of long fibres. The indices I5 and I10 were relatively less sensitive to the use of mixed aspect ratio of fibres. The absolute toughness values computed using the JCI method, viz., I20, R5,10 and R10,20 appeared to be more sensitive to variations of the fibre content and mixed aspect ratio. Further, a comparison of toughness indices showed that the mixes with long fibres had higher indices than those with short fibres. The first crack toughness (TFC) increased with increasing fibre volume fraction and increasing content of shorter fibres in the mix. The maximum values of TFC were obtained for a mix with 100% short fibres, for all three volume fractions. The toughness indices were found to be sensitive to the volume fraction and percentage of the longer fibres in the concrete mix. Higher values of the toughness indices were obtained at higher fibre volume fractions and at higher percentage of the longer fibres in the concrete mix in contrast to the first crack toughness values. Short fibres were more effective in arresting micro-cracks whereas longer fibres were more effective in arresting macro-cracks. The ultimate load increased with an increase of the aspect ratio. Hence the longer fibres were offering more resistance to the pull out of fibres out of the concrete matrix because of their better bond characteristics being longer in length. The material achieved the best performance at a fibre volume fraction of 2.0% in all the tests.

The fibre combination of 65% 50 mm + 35% 25 mm long fibres at a fibre volume fraction of 2.0% gave the best performance in split tensile strength tests. The best fibre combination for the flexural strength was 100% 50 mm long fibres at a fibre content of 2.0%, however, the difference in the performance in terms of flexural strength of SFRC containing 100% 50 mm fibres and 65% 50 mm + 35% 25 mm long fibres was only 1.47%, 4.31% and 6.60% at a fibre content of 1.0%, 1.5% and 2.0%, respectively. Similarly, the difference in the performance in terms of the compressive strength of SFRC containing 100% 25 mm fibres and 65% 50 mm + 35% 25 mm long fibres was 11.00%, 6.90% and 8.19% at a fibre content of 1.0%, 1.5% and 2.0%, respectively. Higher values of the toughness indices were obtained at higher fibre volume fractions and at higher percentage of longer fibres in concrete in contrast to the first crack toughness values. For the compressive strength, split tensile strength and flexural strength of SFRC, a fibre combination of 65% 50 mm + 35% 25 mm long fibres was the best.



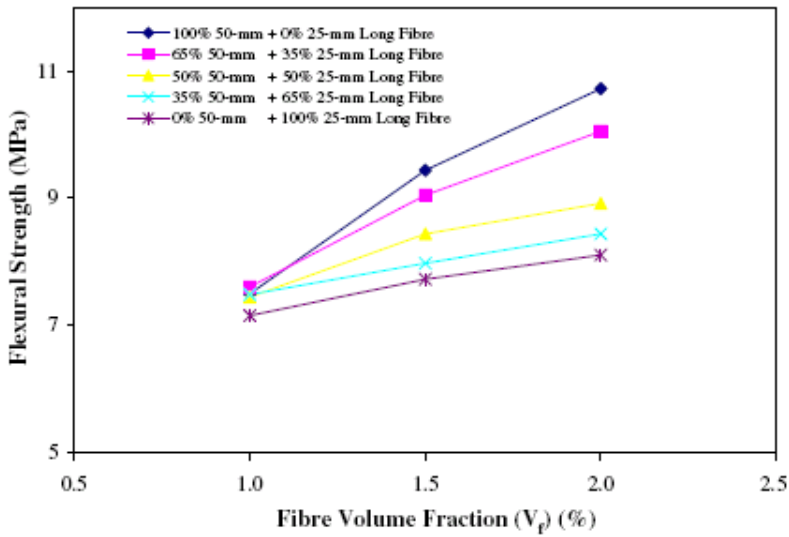
**Fig. 3.37** Cube compressive strength of fibrous concrete with mixed aspect ratio of fibres at different fibre volume fractions (Mohammadi et al. 2008)



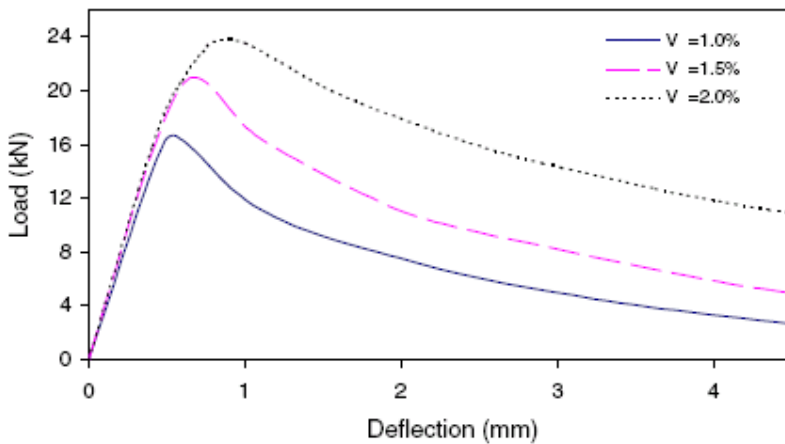
**Fig. 3.38** Split tensile strength of fibrous concrete with mixed aspect ratio of fibres at different fibre volume fractions (Mohammadi et al. 2008)

**Table 3.14** Static flexural test results of plain concrete and SFRC (Mohammadi et al. 2008)

Fibre mix 50 mm long fibres [%]	Fibre mix 25 mm long fibres [%]	Fibre volume fraction [%]	Flexural strength (average of 3 batches) [MPa]
0	0	0	5.4
100	0	1.0	7.5
65	35	1.0	7.6
50	50	1.0	7.5
35	65	1.0	7.5
0	100	1.0	7.2
100	0	1.0	9.4
65	35	1.5	9.1
50	50	1.5	8,4
35	65	1.5	8.0
0	100	1.5	7.7
100	0	2.0	10.7
65	35	2.0	10.1
50	50	2.0	8.9
35	65	2.0	8.4
0	100	2.0	8.1



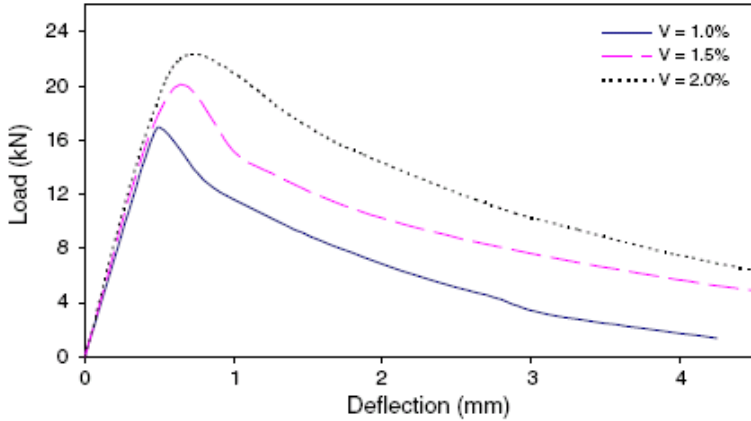
**Fig. 3.39** Static flexural strength of fibrous concrete with mixed aspect ratio of fibres at different fibre volume fractions (Mohammadi et al. 2008)



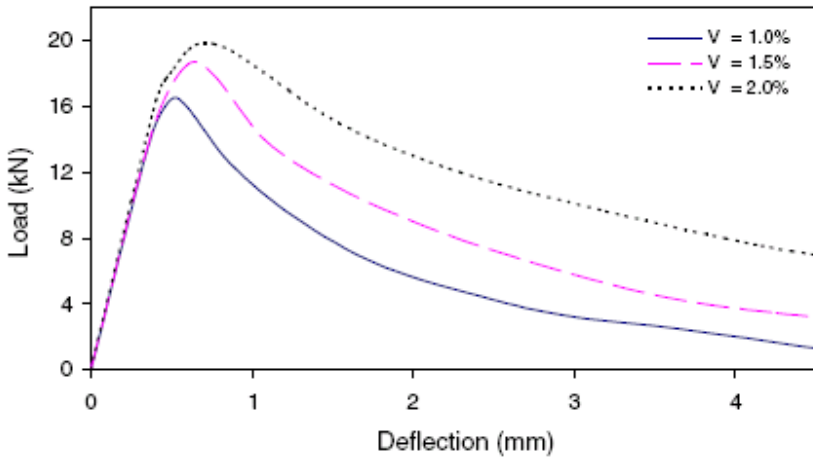
**Fig. 3.40** Load-deflection curves for fibrous concrete with mixed aspect ratio of fibres (100% 50 mm + 0% 25 mm long fibre) at different fibre volume fractions during bending (Mohammadi et al. 2008)

**Table 3.15** Maximum flexural loads, first crack loads and corresponding deflections (Mohammadi et al. 2008)

Fibre mix 50 mm long fibres [%]	Fibre mix 25 mm long fibres [%]	Fibre volume fraction [%]	Maximum flexural load [kN]	Deflection corresponding to maximum flexural load [mm]	First crack load [kN]	Deflection corresponding to first crack load [mm]
0	0	0	11.9	0.34	11.9	0.34
100	0	1.0	16.7	0.55	13.8	0.40
65	35	1.0	16.9	0.50	14.5	0.40
50	50	1.0	16.6	0.53	14.4	0.39
35	65	1.0	16.0	0.51	14.4	0.39
0	100	1.0	15.9	0.43	14.9	0.40
100	0	1.0	21.0	0.66	15.2	0.40
65	35	1.5	20.1	0.65	15.4	0.40
50	50	1.5	18.8	0.65	15.0	0.40
35	65	1.5	17.7	0.59	15.6	0.39
0	100	1.5	17.2	0.50	15.9	0.40
100	0	2.0	23.8	0.90	15.9	0.41
65	35	2.0	22.3	0.72	16.3	0.41
50	50	2.0	19.8	0.77	16.4	0.40
35	65	2.0	18.8	0.61	16.8	0.41
0	100	2.0	18.0	0.48	17.7	0.40



**Fig. 3.41** Load-deflection curves for fibrous concrete with mixed aspect ratio of fibres (65% 50 mm + 35% 25 mm long fibre) at different fibre volume fractions (Mohammadi et al. 2008)



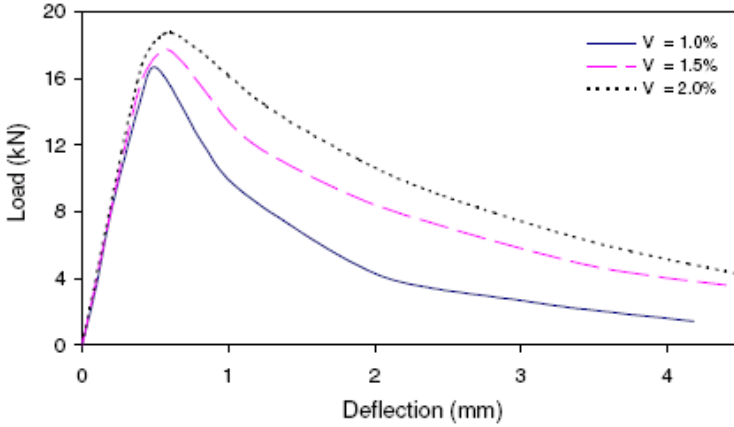
**Fig. 3.42** Load-deflection curves for fibrous concrete with mixed aspect ratio of fibres (50% 50 mm + 50% 25 mm long fibre) at different fibre volume fractions (Mohammadi et al. 2008)

### Experiments by Sivakumar and Santhanam (2007b)

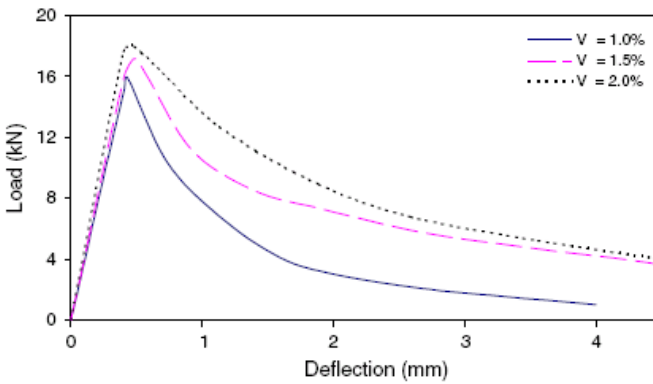
The effect of a hybrid combination of metallic and non-metallic fibres was investigated by Bentur and Mindess (1990), Komlos et al. (1995), Yao et al. (2003) and Sivakumar and Santhanam (2007b). The fibres used by Sivakumar and



Santhanam (2007b) were hooked steel, polypropylene, polyster and glass (Tab.3.16), respectively. The concrete strength was 60 MPa and its workability was 75-125 mm.



**Fig. 3.43** Load-deflection curves for fibrous concrete with mixed aspect ratio of fibres (35% 50 mm + 65% 25 mm long fibre) at different fibre volume fractions (Mohammadi et al. 2008)



**Fig. 3.44** Load-deflection curves for fibrous concrete with mixed aspect ratio of fibres (0% 50 mm + 100% 25 mm long fibre) at different fibre volume fractions (Mohammadi et al. 2008)

The volume fractions of various fibres used in mixtures are given in Tab.3.17. The following specimens were prepared: 100 mm cubes (compression tests), 100 mm×200 mm cylinders (split tensile strength tests) and 100×100×500 mm<sup>3</sup> beam

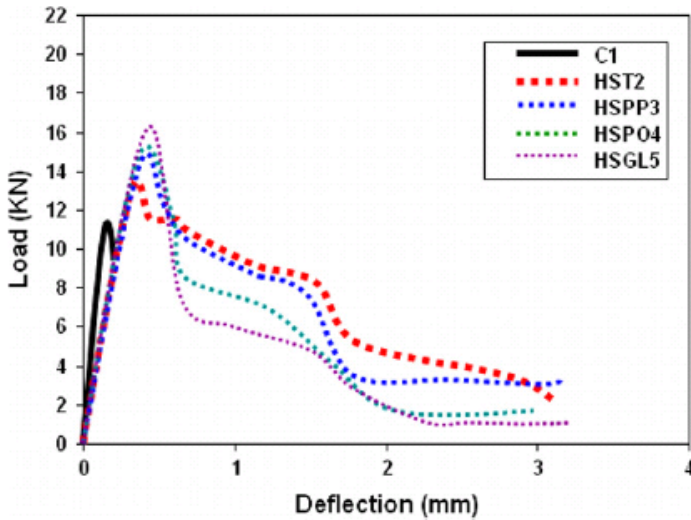
specimens (flexural tests). A load-deflection plot during three-point bending is shown in Fig.3.45. The results for the compressive and split tensile strength and modulus of elasticity for all mixtures are presented in Tab.3.18. An enhancement in the compressive strength compared to control concrete occurred for the steel fibre concrete and all hybrid fibre concretes. The maximum increase in the compressive strength was only of the order of 15%. The concretes with individual non-metallic fibres did not register any increase in the compressive strength. For all fibre concrete mixtures, there was a corresponding increase in the modulus of elasticity as compared to the control concrete. The split tensile strengths of hybrid fibre concretes were found to be higher as compared to reference and mono-steel fibre concrete. The hybrid fibre concretes containing steel and polypropylene (HSPP3 and HSPP6) showed the highest split tensile strength among all concretes. The glass fibres, possibly owing to their short lengths did not perform as well as the other two non-metallic fibres.

**Table 3.16** Physical and mechanical properties of various fibres used (Sivakumar and Santhanam 2007b)

Property	Hooked steel	Polypropylene	Glass	Polyster
Length [mm]	30	20	6	12
Diameter [mm]	0.5	0.10	0.01	0.05
Aspect ratio	60	200	600	240
Specific gravity	7.8	0.9	2.72	1.35
Tensile strength [MPa]	1700	450	2280	970
Elastic modulus [GPa]	200	5	80	15
Failure strain [%]	3.5	18	3.6	35

The flexural testing results are presented in Tab.3.19 and in Fig.3.46. Compared to concrete without fibres, all fibre-reinforced concretes showed an appreciable increase in the flexural strength. Among all fibre concretes, a hybrid combination of steel and polyster showed the maximum flexural strength. The

reason could be due to a smaller length and high aspect ratio of polyester fibres, which gave a high reinforcement index. A steel–polypropylene and steel glass combination showed a reasonable increase in the flexural strength compared to plain and mono-steel fibre concrete. Also listed in Tab.3.19 are the residual loads for concretes in flexure, which indicated the load carrying capacity of the material even after failure. These were determined experimentally by loading the specimen up to the peak load, unloading, and then reloading to failure. A steel polypropylene hybrid combination showed the maximum residual load among all hybrid fibre concretes, while the concretes with glass fibres behaved the worst. The retention of the load carrying capacity after failure decreased with an increase of the non-metallic fibre content in hybrid combinations, indicating that the main contributor to the residual load was the steel fibres.



**Fig. 3.45** Typical load-deflection plot for various hybrid fibre concretes (Sivakumar and Santhanam 2007b)

The toughness for various fibre concretes is given in Tab.3.19 and in Fig.3.47. All fibrous concretes yielded a higher flexural toughness compared to plain concrete. Compared to mono-steel fibre concrete, a steel–polypropylene combination only, for a low dosage of polypropylene fibres (0.12%) was tougher. However, all other fibre combinations performed worse than individual steel fibre concrete, and the toughness was found to decrease with an increase in the dosage of non-metallic fibres. The post-peak behaviour, which contributes mainly to a difference in toughness between concrete without fibres and concrete with fibres, was mainly dominated by steel fibres.

**Table 3.17** Dosage of different fibre combinations used (Sivakumar and Santhanam 2007b)

Mixture	Volume fraction of hooked steel [%]	Volume fraction of non-metallic fibre [%]	Fibre dosage [kg/m <sup>3</sup> ]				Total fibre dosage [kg/m <sup>3</sup> ]
			S	PP	PO	G	
C1	0	-	-	-	-	-	-
HST2	0.5	-	39.98	-	-	-	38.98
HSPP3	0.38	0.12	27.22	1.34	-	-	28.56
HSP04	0.38	0.12	27.22	-	1.82	-	29.04
HSGL5	0.38	0.12	27.22	-	-	3.84	31.06
HSPP6	0.25	0.25	19.44	2.26	-	-	21.70
HSPO7	0.25	0.25	19.44	-	3.36	-	22.80
HSGL8	0.25	0.25	19.44	-	-	6.77	26.21
HSPP9	0.12	0.38	9.36	3.41	-	-	12.77
HSP010	0.12	0.38	9.36	-	5.14	-	14.50
HSGL11	0.12	0.38	9.36	-	-	10.32	19.68
PP12	-	0.5	-	4.5	-	-	4.5
PO13	-	0.5	-	-	6.72	-	6.72
GL14	-	0.5	-	-	-	13.63	13.63

Note: S –steel fibre, PP – polypropylene fibre, PO – polyster fibre, G – glass fibre.

**Table 3.18** Compressive loading tests of various fibre contents (Sivakumar and Santhanam 2007b)

Mixture of Tab. 3.17	Mean compressive strength [MPa]	Mean split tensile strength [MPa]	Mean modulus of elasticity [GPa]
C1	56.1	4.1	31.1
HST2	59.2	5.2	33.2
HSPP3	61.1	5.3	34.8
HSP04	62.4	5.2	35.2
HSGL5	59.2	5.3	34.1
HSPP6	64.7	5.5	35.1
HSP07	58.6	5.4	35.6
HSGL8	60.3	4.9	34.
HSPP9	63.4	4.9	35.5
HSP010	64.2	5	35.6
HSGL11	62.0	4.8	34.8
PP12	56.1	4.4	33.1
PO13	55.1	4.7	34.8
GL14	57.8	4.3	33.7

In the case of steel–polypropylene fibre concrete (with polypropylene fibres at 0.12%), there was an enhancement over steel fibrous concrete possibly as a result of a contribution by polypropylene fibres at small crack widths. As compared to polyester and glass fibres that were single strand fibres, polypropylene fibres were fibrillated, which could have resulted in an improved post-peak performance. However, with increasing dosages of polypropylene fibres, there was a decrease in toughness of steel–polypropylene concrete, since there were not enough steel

fibres in the system for bridging the wider cracks. The worst performance was seen with a steel-glass fibre combination, possibly due to a short length of glass fibres (fibres got pulled out easily). The ductility of fibre reinforced concrete depended primarily on the fibre ability to bridge the cracks at high levels of strain. Thus, stiffer fibres provided better crack bridging; this explained a good performance of steel fibres compared to polyester or polypropylene. Although, the glass fibres have the reasonably high stiffness and tensile strength, they got pulled out easily at high crack widths because of their smaller lengths, and thus did not contribute significantly to the post-peak performance compared to steel fibres. The experiments showed that steel fibres could be replaced to a small extent with non-metallic fibres (mainly polypropylene) to provide a similar toughness to steel fibre concrete. In addition, the early age crack resistance was offered by polymeric fibres.

In addition, Fig.3.48 shows the results of the equivalent flexural strength of various hybrid fibre concretes. The equivalent flexural strength followed the same trend as the toughness.

### 3.1.2 Dynamic Experiments (Strain Rate $\dot{\epsilon} > 1 \times 10^{-4}$ 1/s)

There are laboratory tests available for determining the dynamic properties and impact resistance of steel-fibre-reinforced concrete. These may be broadly categorized into drop weight impact tests and projectile impact tests (Suaris and Shah 1984, ACI 1999). A number of experimental studies on the impact behaviour of SFRC have been carried out and all of these studies, regardless of the test method employed, demonstrated that the impact resistance of SFRC is, in general, substantially higher than that of plain concrete. Song et al. (2004) applied the drop weight impact test method to evaluate the impact resistance of concrete and found that, by adding 1.5% by volume of steel fibres to plain concrete, the average number of blows required to produce the first crack could be increased by 418% and the average number of blows required to cause failure could be increased by 518%. On the other hand, Ong et al. (1999) applied the projectile impact test method using a projectile with a hemispherical nose and found that the amounts of impact energy required to cause failure of concrete slabs, each containing 1% or 2% by volume of steel fibres, were respectively 100% and 136% higher than that of plain concrete.

Below, the dynamic experiments performed by Lohrmann (1999), Komlos et al. (1995), Chenkui and Guofan (1995), Wang et al. (1996), Lee and Barr (2004), and Kwan and Ng (2007) are comprehensively described.

**Table 3.19** Flexural loading test results for various fibre concretes (Sivakumar and Santhanam 2007b)

Mixture	Hooked steel fibre [%]	Non-metallic fibre [%]	Ultimate load [kN]	Ultimate flexural strength [MPa]	Residual load [kN]	Flexural toughness (up to 3 mm deflection) [Nm]
C1	-	-	11.6	5.2	0	1.7
HST2	0.5	0	13.4	6.0	9.1	21.4
HSPP3	0.38	0.12	14.9	6.7	9.3	22.7
HSP04	0.38	0.12	15.8	7.1	9.1	19.5
HSGL5	0.38	0.12	14.1	6.3	2.5	15.2
HSPP6	0.25	0.25	15.9	7.3	5.4	18.1
HSPO7	0.25	0.25	14.6	6.6	4.8	17.0
HSGL8	0.25	0.25	15.8	7.1	1.3	13.6
HSPP9	0.12	0.38	15.2	6.8	4.1	15.2
HSP010	0.12	0.38	15.8	7.1	0	10.2
HSGL11	0.12	0.38	13.7	6.2	0	10.5
PP12	-	0.5	12.5	5.6	2.2	7.9
PO13	-	0.5	14.1	6.3	0.0	6.0
GL14	-	0.5	13.2	6.0	0.0	6.3

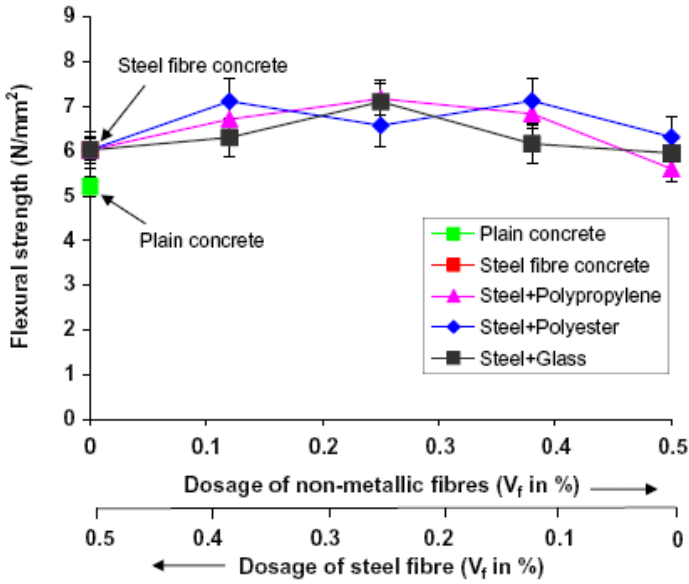


Fig. 3.46 Flexural strength of various hybrid fibre contents (Sivakumar and Santhanam 2007b)

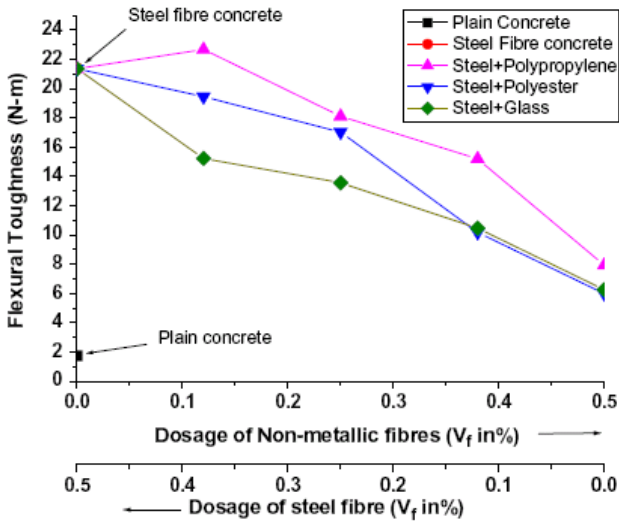
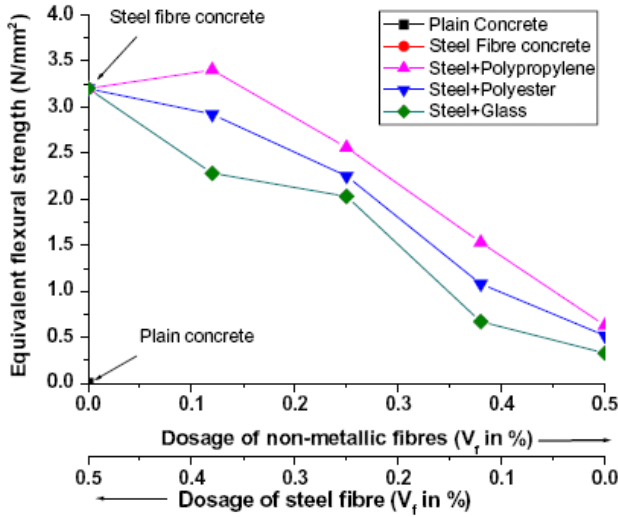


Fig. 3.47 Flexural strength of various hybrid fibre contents (Sivakumar and Santhanam 2007b)





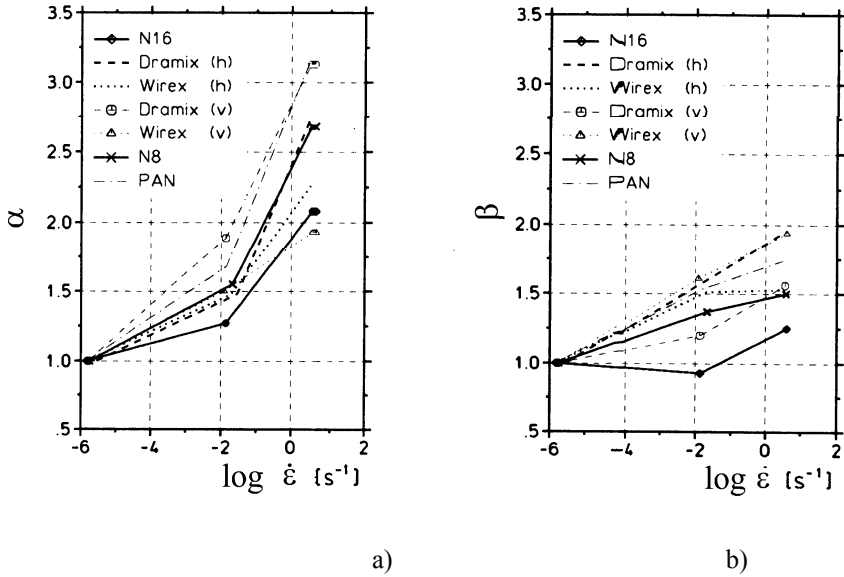
**Fig. 3.48** Flexural strength of various hybrid fibre contents (Sivakumar and Santhanam 2007b)

### Experiments by Lohrmann (1999)

The experiments were carried out with plain concrete and fibrous concrete specimens. In the first case, concretes C30/37 with 2 different maximum aggregates were used: 16 mm (N16) and 8 mm (N8). In the second case, concretes with the maximum aggregate diameter of 16 mm included steel hooked fibres Dramix 60/0.8 mm (1.2%) or steel straight fibres Wirex 40/0.6 mm (1.2%), and concrete with the maximum aggregate diameter of 8 mm included polyacrylic straight fibres PAN 6/0.1 mm (1.2%). Static, dynamic and impact tests were carried out. The impact tests were performed by means of the Split-Hopkinson-Bar method. The samples were taken horizontally and vertically from a concrete block.

The results of splitting tensile tests with notched cylindrical specimens for different loading velocities ( $h=100$  mm,  $\phi=75$  mm) are shown in Figs.3.49-3.54 and Tabs.3.20-3.24.

The results showed that the elastic modulus, tensile strength, fracture energy and strain corresponding to the peak increased with increasing strain velocity, in particular, for specimens including fibres. In some static tests, the tensile strength of fibre reinforced specimens was found, however, to be smaller than those without fibres (Tab.3.20). The tensile strength was larger when fibres were oriented in the loading direction, i.e. perpendicularly to cracks (for samples taken horizontally).



**Fig. 3.49** Effect of strain velocity on ratio between dynamic and static tensile strength (a) and between dynamic and static strain corresponding to tensile strength (b) with respect to static values ('h' - samples taken horizontally, 'v' - samples taken vertically) (Lohrmann 1999)

The results of uniaxial compression tests with cylindrical specimens ( $h=250$  mm,  $\phi=100$  mm) are shown in Figs.3.55-3.56 and Tabs.3.25-3.27.

The results show that the uniaxial compressive strength and fracture energy increased with increasing loading velocity, in particular for impact loading. The material ductility increased with increasing fibre content. However, the compressive strength did not increase with increasing fibre amount due to an increase of voids. The compressive strength was larger when fibres were oriented perpendicularly in the loading direction (for samples taken vertically).

### Experiments by Komlos et al. (1995)

Steel and polypropylene were used as hybrid reinforcement: smooth straight steel fibres with length of 40 mm and a diameter of 0.4 mm and chopped polypropylene fibres in multifilament fibrillated form with a length of 36 mm. The maximum hybrid fibre volume fraction (polypropylene fibres+steel fibres) was 1%.

The loading characteristics were as follows: static, low strain rate monotonic loading 0.08 mm/s and dynamic high stress rate monotonic loading (single blow impact energy of 10 Nm at 0.33 Hz). The number of loading cycles was  $10^5$ . The results of experiments are summarized in Tabs.3.28-3.30 and Fig.3.58.

**Table 3.20** Results of tension tests for different strain velocities (Lohrmann 1999)

	$\dot{\mathcal{E}} = 1.9 \times 10^{-6}$ Static [1/s]		$\dot{\mathcal{E}} = 1.9 \times 10^{-2}$ Dynamic [1/s]		$\dot{\mathcal{E}} = 3.9$ Impact [1/s]	
Mix	$f_t$ [MPa]	$\varepsilon_t$ [ $10^{-4}$ ]	$f_t$ [MPa]	$\varepsilon_t$ [ $10^{-4}$ ]	$f_t$ [MPa]	$\varepsilon_t$ [ $10^{-4}$ ]
N16(h)	2.58	1.83	3.27	1.71	5.36	2.28
Dramix (h)	2.25	1.37	3.32	2.21	6.14	2.66
Dramix (v)	1.87	1.58	3.54	1.89	5.85	2.46
Wirex (h)	2.87	1.68	4.28	2.54	6.52	2.57
Wirex (v)	2.60	1.32	3.89	2.13	5.01	2.57
N8 (h)	1.73	1.23	2.68	1.68	4.63	1.85
PAN (h)	1.85	1.53	3.11	2.34	5.80	2.66

The experiments showed that the optimum fibre content relationship was mostly affected by a mix composition. The quasi-static properties were worse with increasing amount of PP fibres (Tab.3.28). However, the fracture and impact energy, toughness and ductility were substantially improved by the increased volume fraction of PP fibres during dynamic tests.

### Experiments by Wang et al. (1996)

The behaviour of steel fibrous concrete (SFRC) beams under impact loading was studied. Three types of fibres were used: 38 mm long fibrillated polypropylene fibre, 30 mm long hooked-end steel fibres and 50 mm long crimped steel fibres. The specimen types are described in Tab.3.31. An instrument drop-weight machine with an impact hammer weighing 60.3 kg was used. For these tests, the

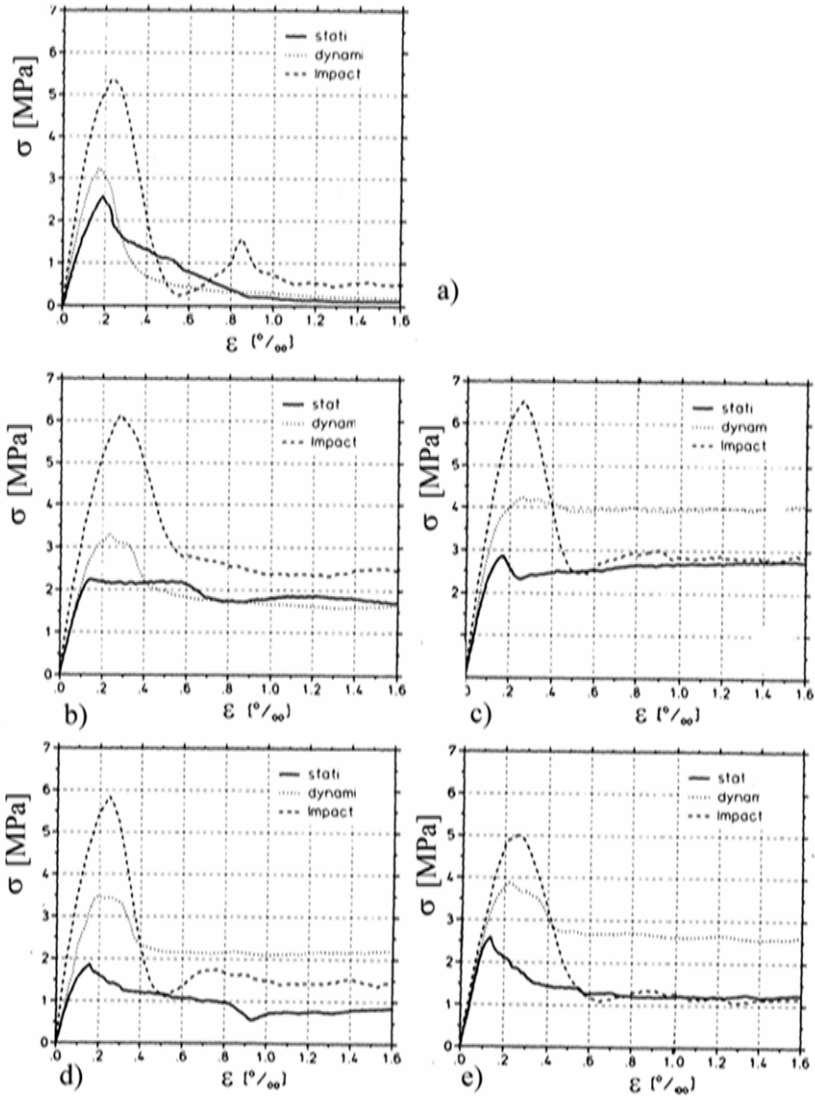
drop height was held at 150 mm throughout (Fig.3.59). The FRC specimens were cast in  $102.4 \times 102.4 \times 355.6$  mm<sup>3</sup> molds. The basic matrix mix design was 1.0:0.4:2.4:2.2 (cement:water:fine aggregate:coarse aggregate) with a maximum aggregate size of 10 mm.

**Table 3.21** Fracture energies for elongation of 500  $\mu$ m for different tests (Lohrmann 1999)

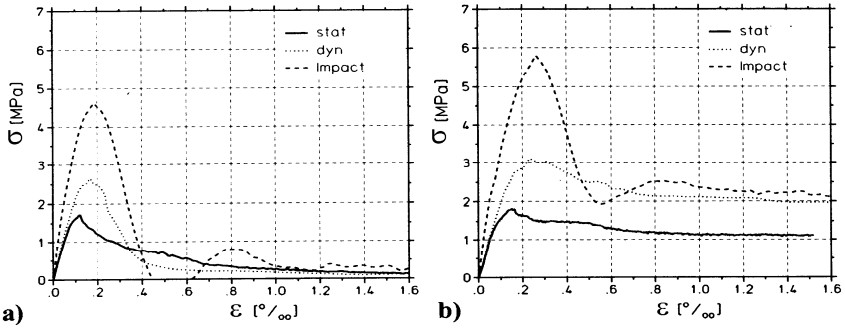
	Static tests	Dynamic tests	Impact tests
Mix	$G_f$ [N/m]	$G_f$ [N/m]	$G_f$ [N/m]
N16 (h)	145	129	51
Dramix (h)	795	799	70
Dramix (v)	384	1020	61
Wirex (h)	943	1570	71
Wirex (v)	543	1010	56
N8 (h)	86	97	37
PAN (h)	372	631	64

*v*- vertical, *h* – horizontal

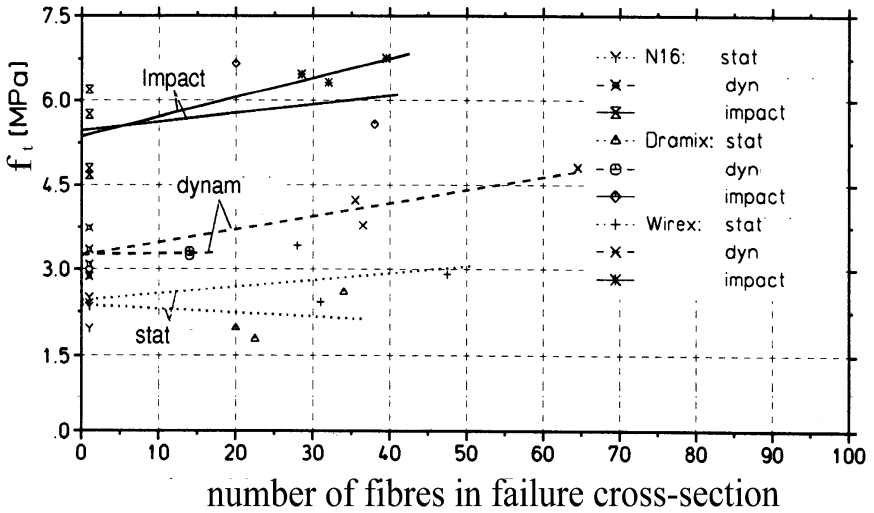
The detailed test results for all of the specimens tested are given in Tab.3.32. The “total work done” is represented by the entire area under the tup load-deflection curve; “fracture energy” is represented by the area under the bending load vs. deflection curve. When the beam was not broken by a particular impact, almost all the work done by the falling hammer was transferred into fracture energy. When the beam was broken into two or more pieces by an impact, part of the work done by the beam was transferred into kinetic energy of the broken pieces. In this case, the energy consumed in the fracture process itself was less than the work done by the falling hammer. The plain concrete specimens, the polypropylene fibre specimens, and the steel fibre specimens for fibre contents up to 0.5% by volume all broke completely under the fast blow. However, specimens reinforced with 0.75% or more of hooked steel fibres required two blows to cause the beams to break completely; and one specimen with 0.75% crimped steel fibres required three blows (specimen ID’s with an “s” or “9” as the last symbol in Tab.3.32). The given deflections were all obtained from integration of the acceleration records



**Fig. 3.50** Stress-strain curves for static, dynamic and impact tests: a) plain concrete (N16), b) Dramix (h), c) Wirex (h), d) Dramix (h), e) Wirex (v) (Lohrmann 1999)



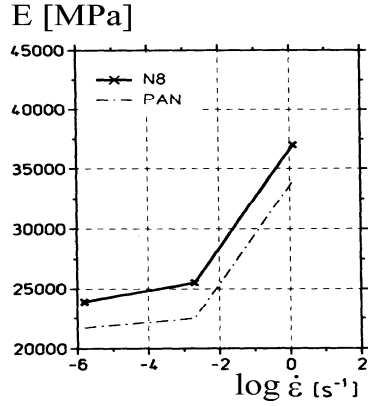
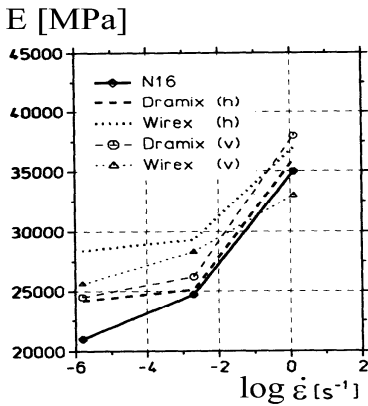
**Fig. 3.51** Stress-strain curves for static, dynamic and impact tests: a) plain concrete (N8), b) PAN (Lohrmann 1999)



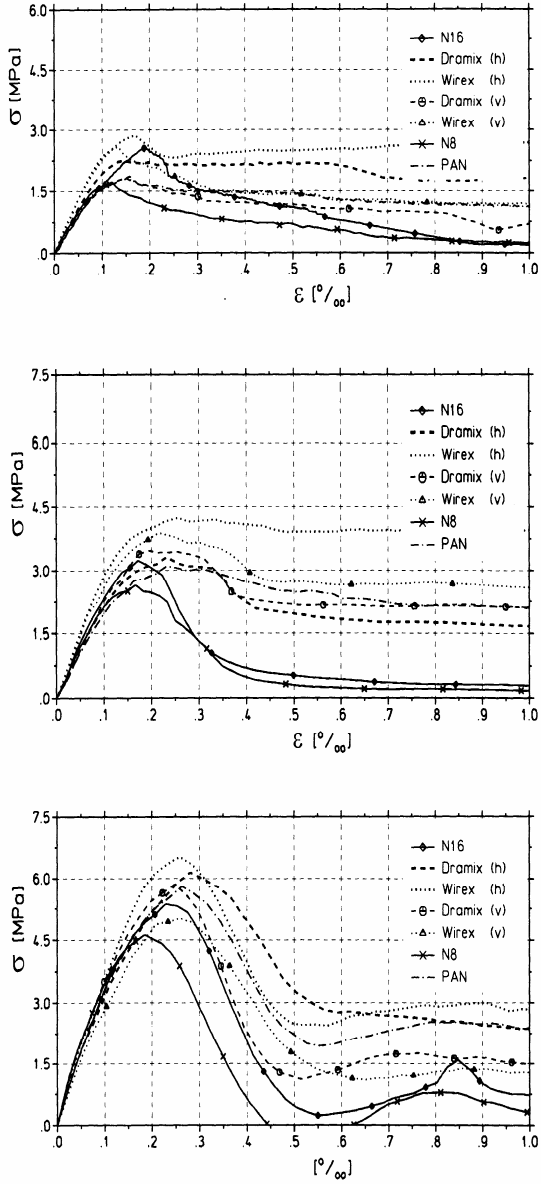
**Fig. 3.52** Effect of strain velocity on uniaxial tensile strength for different fibre content against the number of fibres (Lohrmann 1999)

**Table 3.22** Number of fibres in the failure cross-section (Lohrmann 1999)

Fibre type	Strain velocity	Number of fibre	Tensile strength [MPa]
Dramix concrete	static	25.5	2.25
	dynamic	14.0	3.32
	impact	29.0	6.14
Wirex concrete	static	35.5	2.89
	dynamic	45.5	4.28
	impact	33.3	6.52



**Fig. 3.53** Effect of strain velocity on initial modulus of elasticity for different fibre content (Lohrmann 1999)



**Fig. 3.54** Stress-strain curves for different strain velocities and concrete specimens: static (top), dynamic (middle), impact (bottom) (Lohrmann 1999)



**Table 3.23** Ratio between dynamic and static fracture energy (for elongation of 2000  $\mu\text{m}$ ) (Lohrmann 1999)

	$G_f(\text{dyn})/G_f(\text{stat})$ for elongation of 500 $\mu\text{m}$	$G_f(\text{dyn})/G_f(\text{stat})$ for elongation of 500 $\mu\text{m}$	$G_f(\text{dyn})/G_f(\text{stat})$ for elongation of 500 $\mu\text{m}$	$G_f(\text{dyn})/G_f(\text{stat})$ for elongation of 2000 $\mu\text{m}$
Mix	Static tests	Dynamic tests	Impact tests	Impact tests
Dramix (h)	1.0	1.01	1.45	0.84
Dramix (v)	1.0	2.66	1.62	2.77
Wirex (h)	1.0	1.66	1.15	1.94
Wirex (v)	1.0	1.86	0.84	1.66
PAN (h)	1.0	1.70	1.73	1.59

**Table 3.24** Ratios between material parameters for samples taken horizontally and vertically (Lohrmann 1999)

Material property sample (horiz.)/ sample (vertic.)	Mix	Static loading	Dynamic loading	Impact loading
Tensile strength	Dramix	1.20	0.94	1.05
	Wirex	1.11	1.10	1.30
Strain corresponding to peak	Dramix	0.87	1.17	1.08
	Wirex	1.27	1.19	1.00
Fracture energy	Dramix	1.72	0.84	1.77]
	Wirex	1.56	1.41	1.81

**Table 3.25** Results of compression test for different strain velocities (Lohrmann 1999)

Mix	Static tests • $\dot{\mathcal{E}} = 2.4 \times 10^{-5}$ 1/s • $\dot{\mathcal{E}} = 2.2 \times 10^{-5}$ 1/s		Dynamic tests • $\dot{\mathcal{E}} = 5.9 \times 10^{-2}$ 1/s • $\dot{\mathcal{E}} = 8.9 \times 10^{-3}$ 1/s		Impact tests • $\dot{\mathcal{E}} = 12.2$ 1/s • $\dot{\mathcal{E}} = 7.9 \times 10^{-2}$ 1/s	
	$f_c$ [MPa]	$\epsilon_f$ [10 <sup>-4</sup> ]	$f_c$ [MPa]	$\epsilon_f$ [10 <sup>-4</sup> ]	$f_c$ [MPa]	$\epsilon_f$ [10 <sup>-4</sup> ]
N16	32.3	19.1	41.6	21.3	54.0	24.9
	29.4	20.08	33.8	22.2	38.0	22.2
Dramix	29.1	21.9	38.0	23.8	53.9	23.9
	31.6	30.05	35.7	23.4	39.2	27.3
Wirex	28.5	23.5	49.0	23.4	64.4	26.0
	27.6	24.1	33.6	21.7	35.6	21.7
N8	36.1	26.9	43.0	28.1	59.6	29.9
	31.1	21.6	38.2	23.2	40.9	21.6
PAN	32.6	27.4	40.1	28.6	52.7	30.3
	26.0	24.8	30.8	22.4	32.9	22.4

**Table 3.26** Ratio between fracture energy for vertically and horizontally taken samples using different loading velocities (for elongation of 2000  $\mu\text{m}$ ) (Lohrmann 1999)

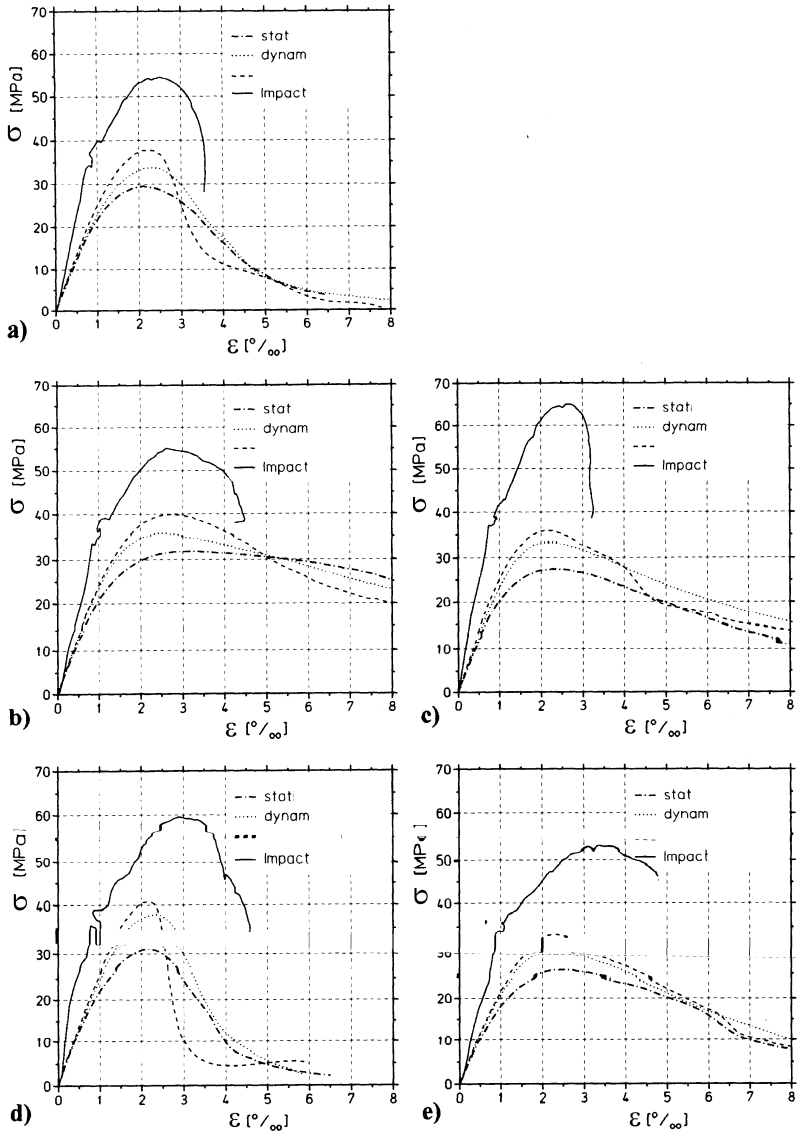
Mix	$G_f(\text{vertical})/G_f(\text{horizontal})$	$G_f(\text{vertical})/G_f(\text{horizontal})$
	Static tests	
	Dynamic tests	
N16	0.95	0.97
Dramix	1.25	1.09
Wirex	1.32	0.93
N8	0.82	0.76
PAN	1.31	1.07

**Table 3.27** Effect of fibres on fracture energy for different loading velocities with respect to plain concrete (Lohrmann 1999)

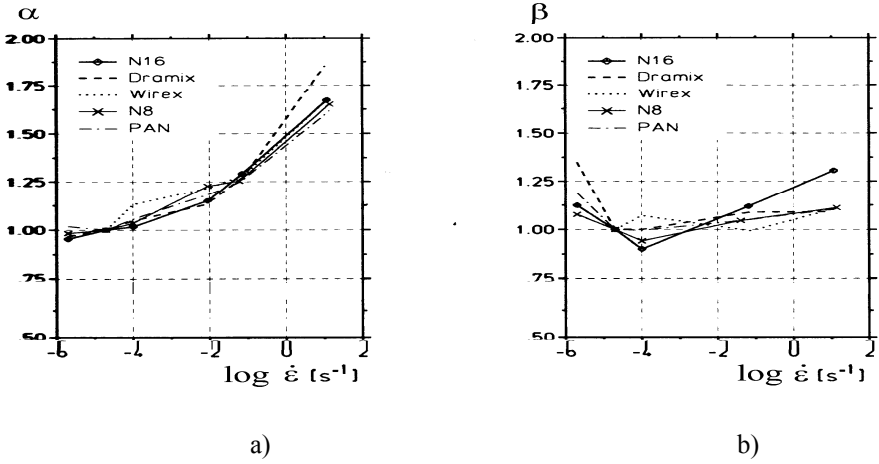
Mix	Static tests	Dynamic tests
Dramix	2.03, 2.16	2.01, 2.01, 2.22
Wirex	1.87, 1.65	1.44, 1.71, 1.91
PAN	1.52, 1.90	1.45, 1.91, 2.39

Fig.3.61 shows typical load-deflection curves for beams with 0.5%, 0.75% and 1.5% by volume of hooked steel fibres. The fracture energy of the beams increased with increasing fibre content (Fig.3.62). However, the fracture energies at 0.25% and 0.5% fibre volumes were not much greater than those for plain concrete; their load-deflection curves were very similar. A large jump in fracture energy occurred between 0.5% and 0.75% fibres. Beyond 0.75% fibres, an increase in fracture energy with increasing fibre content was again modest. The steel fibres increased the peak bending load only slightly; the major contribution of steel fibres to fracture energy lied in the significantly increased maximum beam deflections, which grew from about 0.4 mm for plain concrete to as high as 3 mm for the 1.5% fibre content. The beams with 0.75% fibres or more required two blows to bring about failure. They deflected further, and absorbed additional energy when subjected to the second blow (which did cause failure in all cases). For a fibre content of 0.75% or more, the fibres had a much greater tendency to pull out rather than to break. Occasionally, a second flexural crack appeared beside the main flexural crack. One possible explanation for the large jump in fracture energies between 0.50% and 0.75% fibres may be differences in a fracture process. For lower fibre contents, the total failure event lasted about 1 ms and the average deflection was about 0.8 mm. The fibres had a greater tendency to break. For higher fibre contents, the total failure event lasted for more than 5 ms and the average deflection was 4-5 mm, consistent with a fibre pull-out rather than a fibre breaking mode of failure. At these higher fibre contents, the fibres were able to support sufficient load to necessitate a second blow to cause failure.

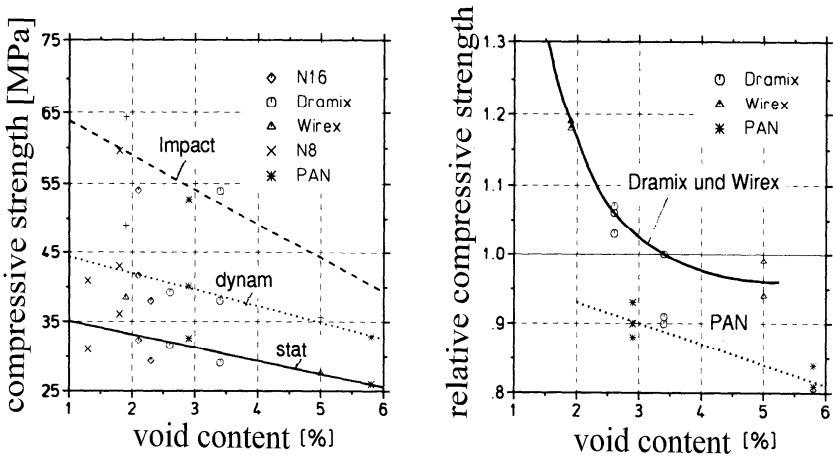
Fig.3.60 shows the fracture energies for the different concretes tested. The values represent the average of the two or three specimens tested of each type. Adding polypropylene fibres to the beams did not bring about much improvement in fracture energies as compared to the unreinforced matrix. Even at 0.50% polypropylene fibres by volume, an increase was only by about 2 1%. The beams made with 0.75% by volume crimped steel fibres had similar load-deflection curves (Fig.3.66) and about the same fracture energies as those made with 0.75% hooked steel fibres, and they too failed primarily in a fibre pull-out mode. Thus, the effectiveness of these two types of fibres was similar.



**Fig. 3.55** Effect of strain velocity on compressive strength for different mixes (Lohrmann 1999)



**Fig. 3.56** Effect of strain velocity on ratio between dynamic and static compressive strength (a) and between dynamic and static strain corresponding to tensile strength (b) (Lohrmann 1999)



**Fig. 3.57** Effect of void content for different mixes on: a) compressive strength, b) relative compressive strength (Lohrmann 1999)

**Table 3.28** Average values of static mechanical characteristics (Komlos et al. 1995)

Mix	Fibre volume fraction [%]	Flexural strength [MPa]	Compressive strength [MPa]	Splitting strength [MPa]	Modulus of elasticity [GPa]
A	0	3.5	40.4	3.1	38.7
B	0.2 (PP)+0.8 (S)	5.1	40.6	4.0	37.4
C	0.3 (PP)+0.7 (S)	4.8	38.3	3.8	37.1
D	0.5 (PP)+0.5 (S)	4.3	30.7	3.7	36.7

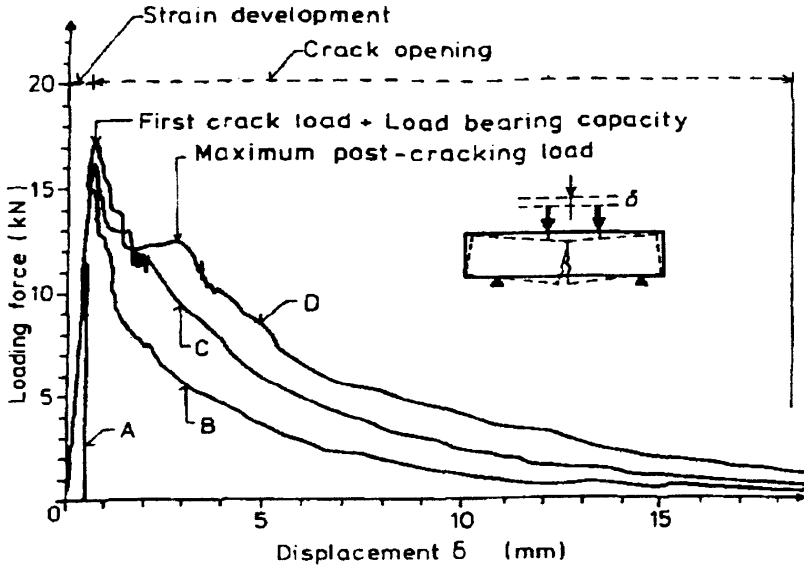
PP - polypropylene fibres, S – steel fibres.

**Table 3.29** Impact strength on cylinders 150 mm long and 60 mm in diameter (Komlos et al. 1995)

Mix	Fibre volume fraction [%]	Impact strength without previous loading history [Nm]		Impact strength after repeated loading cycles $10^5$ in compression [Nm]	
		At first crack	At failure	At first crack	At failure
A	0	90	130	40	120
B	0.2 (PP)+0.8 (S)	170	990	130	890
C	0.3 (PP)+0.7 (S)	210	1200	190	1200
D	0.5 (PP)+0.5 (S)	250	1280	220	1270

**Table 3.30** Properties of specimens after repeated loading cycles (Komlos et al. 1995)

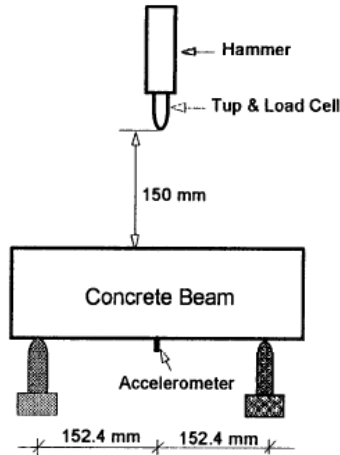
Mix	Compressive strength [MPa]			Load-bearing capacity [kN]			Maximum flexural load in post-cracking stage [kN]			Number of loading cycles up to deflection of 15 mm		
A	37.1	26.4	32.5	10.3	11.7	-	0	0	0	0	0	0
B	41.2	40.6	40.0	17.3	18.2	16.7	-	-	-	15270	7930	4852
C	35.2	36.0	37.5	15.5	16.0	16.3	9.1	13.8	10.5	2248	768	23181
D	30.5	31.1	32.5	13.5	14.4	15.0	9.4	12.6	8.7	6300	1827	8455



**Fig. 3.58** Typical working diagrams of FRC specimens A, B, C, D of Tab.3.28 (Komlos et al. 1995)

**Table 3.31** Specimen types (Wang et al. 1996)

Specimen type	Fibres used
N	no fibres
P1	0.25% polypropylene fibres, 38 mm long
P2	0.50% polypropylene fibres, 38 mm long
S1	0.25% hooked steel fibres, $\phi 0.5 \times 30$ mm
S2	0.50% hooked steel fibres, $\phi 0.5 \times 30$ mm
S3	0.75% hooked steel fibres, $\phi 0.5 \times 30$ mm
S4	1.00% hooked steel fibres, $\phi 0.5 \times 30$ mm
S5	1.50% hooked steel fibres, $\phi 0.5 \times 30$ mm
W	0.75% crimped steel fibres, $\phi 1.0 \times 50$ mm

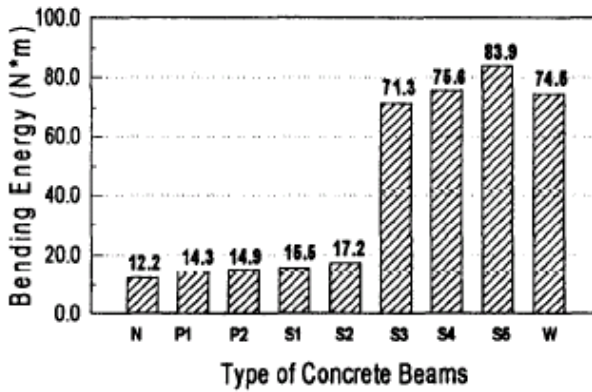


**Fig. 3.59** Impact test setup (Wang et al. 1996)

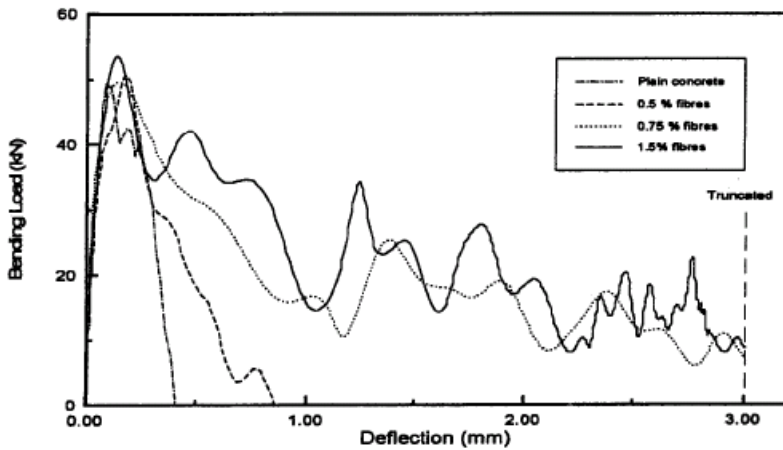


**Table 3.32** Summary of impact tests of beams (average values) (Wang et al. 1996)

Specimen of Tab. 3.31	Maximum tup load [kN]	Maximum bending load [kN]	Total deflection [mm]	Total work done [Nm]	Fracture energy [Nm]
N	74.8	51.2	0.46	19.1	12.2
P1	71.8	52.4	0.52	21.3	14.3
P2	58.0	45.1	0.65	19.6	14.9
S1	52.9	39.5	0.79	19.6	15.5
S2	68.2	51.3	0.72	22.8	17.2
S3	61.6	49/0	5.29	74.8	71.3
S4	70.1	53.0	4.10	82.8	75.6
S5	69.7	59.3	3.93	91.7	83.9
W	68.7	51.0	5.97	601.1	74.5



**Fig. 3.60** Fracture energy of concrete beams with different types of fibres of Tab. 3.31 (Wang et al. 1996)



**Fig. 3.61** Bending load vs. deflection curve for concrete beams with hooked steel fibres (Wang et al. 1996)

### Tests by Lee and Barr (2004)

Fatigue may be defined as a process of progressive and permanent internal structural changes in a material subjected to repeated loading. In concrete, these changes are mainly associated with a progressive growth of internal micro-cracks, which results in a significant increase of irrecoverable strain. At the macro-level, this manifest itself as changes in the material mechanical properties. Tab.3.33

summarizes the different classes of fatigue loading. The mechanism of fatigue failure in concrete or mortar can be divided into three distinct stages (Gao and Hsu 1998) The first stage involves weak regions within concrete or mortar and is termed flaw initiation. The second stage is characterized by slow and progressive growth of inherent flaws to a critical size and is generally known as micro-cracking. In the final stage, when a sufficient number of unstable cracks have formed, a continuous or macro-crack develops, eventually leading to failure. A fatigue crack growth can be divided into two distinct stages (Hori et al. 1992, Kolluru et al. 2000): the first stage is a deceleration stage, where the rate of crack growth decreases as the crack grows and the second stage is an acceleration stage, where there is a steady increase in the crack growth rate right up to failure. A widely accepted approach for engineering practice is based on empirically derived S–N diagrams, also known as Wöhler curves. There are numerous fatigue experiments in literature (Saito 1987, Cornelissen, 1984, Zhang et al. 2000, Su and Hsu1988, Yin and Hsu1995, Ramakrishnan and Lokvik 1992, Morris and Garrett 1981, Kwak et al. 1991, Spadea and Bencardino 1997, Rafeeq et al. 2000, Johnston and Zemp 1991, Grzybowski and Meyer 1993, Zhang and Stang 1998, Naaman and Hammoud 1998).

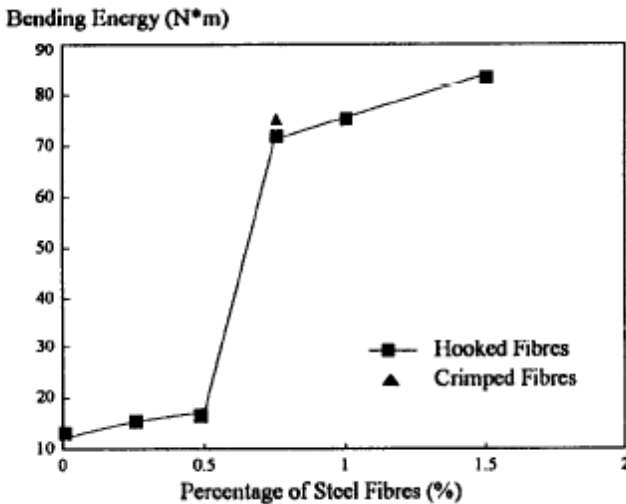
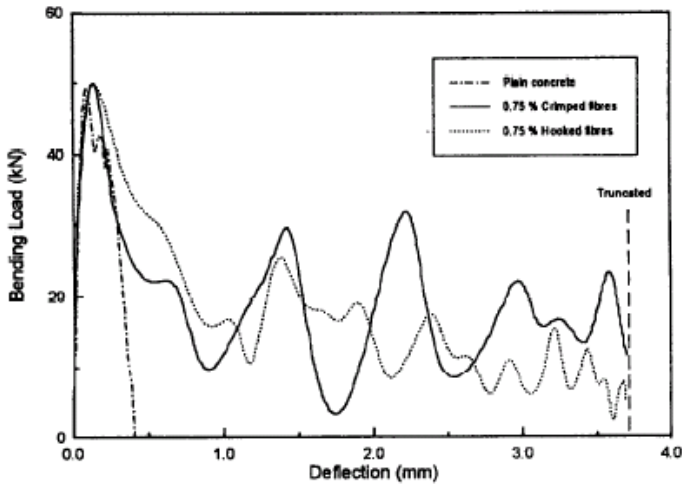


Fig. 3.62 Fracture energy of concrete beams with steel fibres (Wang et al. 1996)



**Fig. 3.63** Bending load vs. deflection curve for concrete beams with 0.75% crimped steel fibres (Wang et al. 1996)

Generally, the addition of steel fibres can significantly improve the bending fatigue performance of concrete members (Johnston and Zemp 1991, Grzybowski and Meyer 1993, Zhang and Stang 1998). The addition of fibre reinforcement has a dual effect on the cyclic behaviour of concrete. Fibres are able to bridge micro-cracks and retard their growth, thereby enhancing the composite performance under cyclic loading. On the other hand, the presence of fibres increases the pore and initial micro-crack density, resulting in strength decrease. The overall outcome of these two competing effects depends significantly on the fibre volume (Grzybowski and Meyer 1993). The presence of fibres does not seem to enhance the fatigue life of concrete under compressive fatigue loading. On the other hand, fibre addition benefits the fatigue performance under flexural fatigue loading.

Fig.3.64a shows the S–N curve obtained from an analysis on the test results extracted from the literature (Grzybowski and Meyer 1993, Paskova and Meyer 1997, Cachim 1999, Do et al. 1993) for plain concrete in compression. On the other hand, Figs.3.64b and 3.64c present the S–N curves for SFRC containing 0.5% and 1.0% of fibres under compression fatigue loading, respectively. Fatigue tests show significant spread in results. For a more meaningful comparison, Fig.3.64d shows linear regression lines for results shown previously. There appears to be a slight degradation in the fatigue life of SFRC relative to plain concrete under compression loading. This was attributed to the introduction of additional flaws within the concrete matrix by fibres.

Figure 3.65a presents the S–N curve for plain concrete under flexural loading. Similarly, Figs.3.65b and 3.72c give the S–N curves for SFRC containing 0.5%

and 1.0% of fibres under flexural loading, respectively. Similarly the R2 values are significantly less than unity for these test results but are slightly better than those observed for the compression test results. Finally, Fig.3.65d compares the linear regression lines for all three test results in flexure. Contrary to the observations for compressive fatigue loading, there appears to be a significant benefit derived from the fibre addition. The improvement is slightly greater when the fibre content is increased from 0% to 0.5% as compared to the improvement achieved between 0.5% and 1.0%. A comparison between the contradictory trends between SFRC under compressive and flexural fatigue loading suggests that SFRC is more effective under the latter condition.

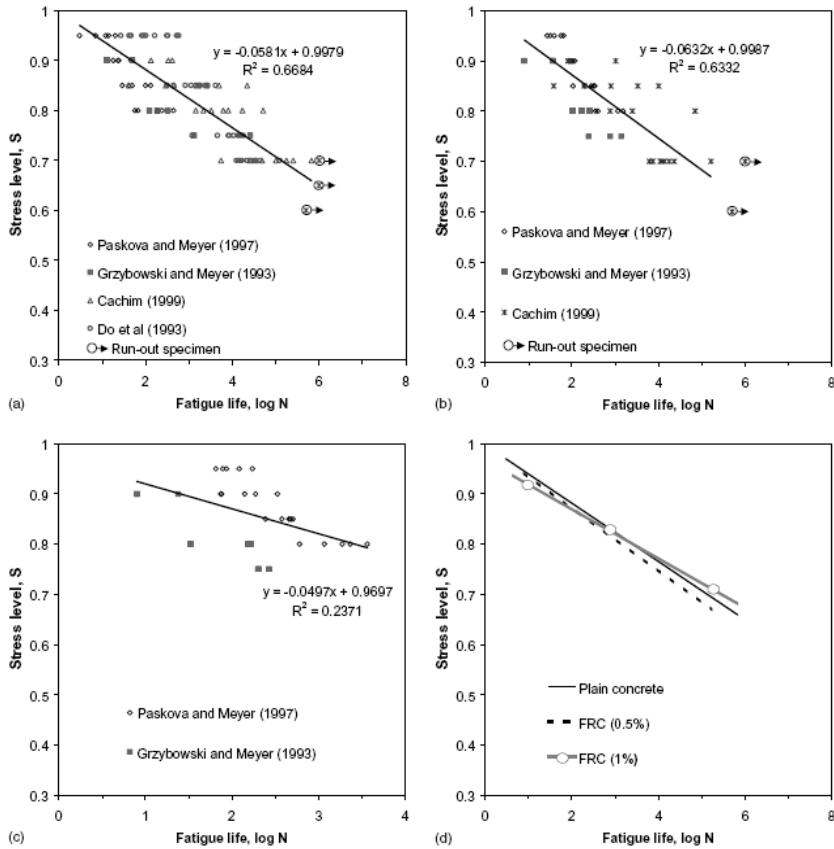
**Table 3.33** Classes of fatigue load (Hsu 1981)

Low-cycle fatigue			High-cycle fatigue				Super-high-cycle fatigue		
1	$10^1$	$10^2$	$10^3$	$10^4$	$10^5$	$10^6$	$10^7$	$10^8$	$10^9$
structures subjected to earthquakes			airport pavements	highway and railway bridges, highway pavements			mass rapid transit structure	sea structures	

### Experiments by Chenkui and Guofan (1995)

Fatigue experiments were carried out with crushed limestone with a maximum size 20 mm or 40 mm. Three kinds of fibres were used: a) 25 mm in length with aspect ratio 43, b) 35 mm in length with aspect ratio 60, c) 45 mm in length with aspect ratio 77. The volume percentage of fibres  $V_f$  was varied from 0% up to 2%. The crushed stone was divided into two ranges: medium stone with sizes from 20 mm to 40 mm and fine stone with sizes from 5 mm to 20 mm.

Fig.3.66 shows that steel fibres substantially improve the flexural fatigue strength of concrete (by about 60 times). In turn, Fig.3.67 presents the results of the mid-span deflection in a fatigue test (it increased with increasing  $V_f$ ). The fatigue flexural strength was also found to be higher in the case of larger aggregates (Sun et al. 1992).

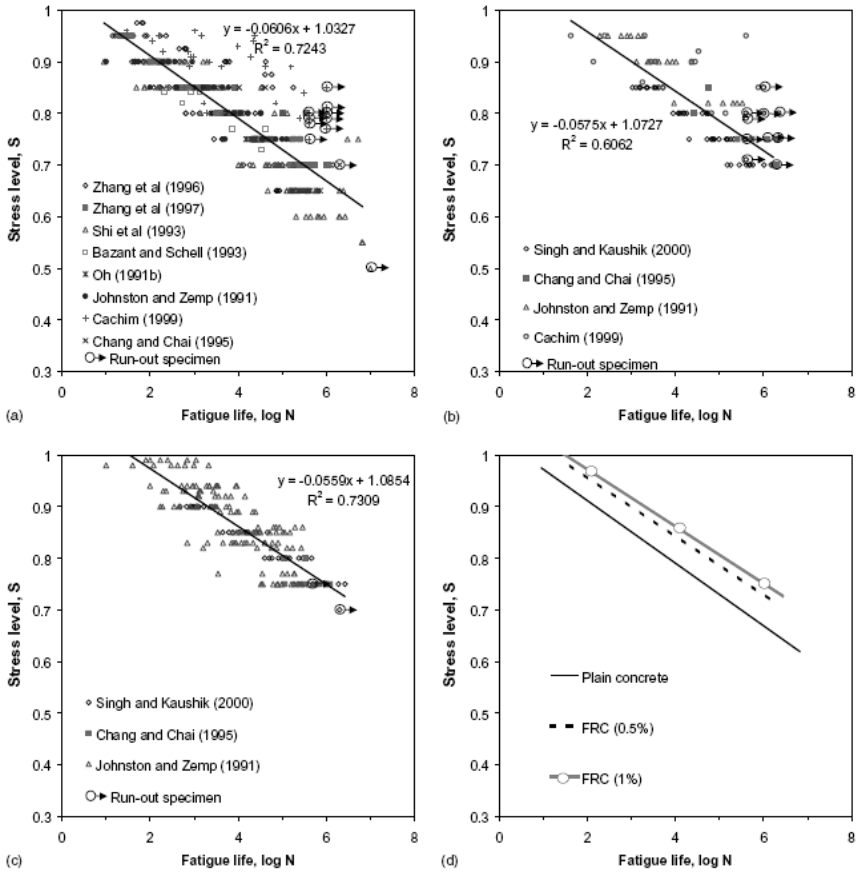


**Fig. 3.64** a) S–N curve for plain concrete under compression, b) S–N curve for SFRC (0.5% fibre content) under compression, c) S–N curve for SFRC (1.0% fibre content) under compression. (N.B. change of scale for  $\log N$ ), d) comparison between S–N curves for plain and SFRC (0.5% and 1.0% fibre content) under compression (Lee and Barr 2004).

### Experiments by Kwan and Ng (2007)

There has been little research on the shock vibration resistance of SFRC. The nature of shock vibration resistance is quite different from that of impact resistance. First, when there is an impact, the concrete structure is at the point of impact subjected to a concentrated bending moment or a punching shear force that may be large enough to cause bending or punching shear failure. On the other hand, when there is shock vibration, a shock wave propagates through the concrete structure producing alternate tensile and compressive stresses that are large enough to cause transverse cracking. Second, most of impact tests were performed when concrete was fully hardened and the steel fibre–concrete matrix bond was

fully developed because the concrete structure was not expected to be impact-resistant while concrete was still green. However, most of shock vibration tests were performed within a few days or even a few hours after casting of concrete because concrete is generally more vulnerable to shock vibration damage when it is still green and it is the shock vibration generated by construction activities near freshly cast concrete that causes the greatest problem.



**Fig. 3.65** a) S–N curve for plain concrete under flexural loading, b) S–N curve for SFRC (0.5% fibre content) under flexural loading, c) S–N curve for SFRC (1.0% fibre content) under flexural loading, d) comparison between S–N curves for plain and SFRC (0.5% and 1.0% fibre content) under flexural loading (Lee and Barr 2004)

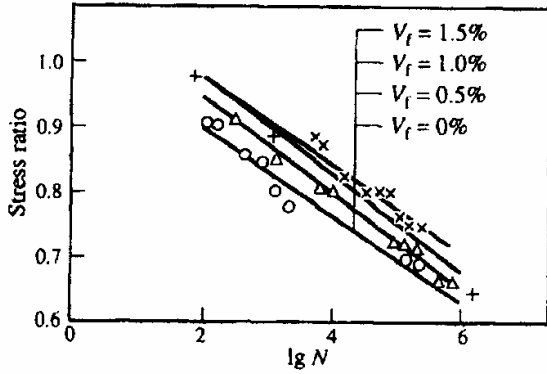


Fig. 3.66 Relationships between stress ratio and fatigue life (Chenkui and Guofan 1995)

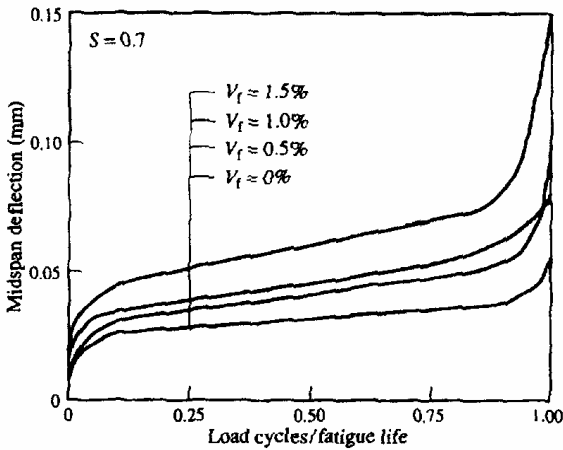


Fig. 3.67 Mid-span deflection in fatigue test process (Chenkui and Guofan 1995)

In total, seven concrete mixtures with the same target mean 28-day cube strength of 50 MPa but different steel fibre contents ranging from 0 to 4% by volume were designed. They were assigned mixture numbers of A, B, C, D, E, F and G, in the order of an increasing steel fibre content. The ordinary Portland cement of class 52.5N was used as the only cementitious material and the water/cement ratio adopted was 0.52. The fine aggregate (5 mm maximum size)



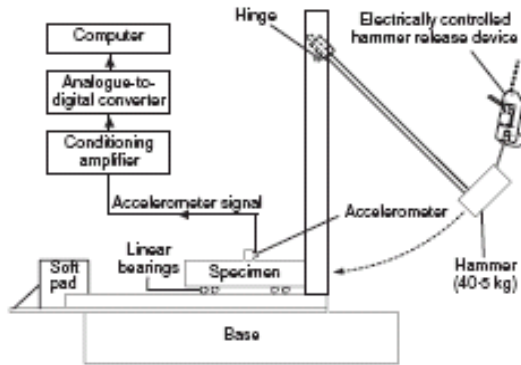
and the coarse aggregate (20 mm maximum size) were both crushed granite rock while the fine-to-total aggregate ratio was set at 0.4. During trial mixing, it was found that as the steel fibre content increased to beyond 1%, the workability dropped significantly. In order to compensate for a gradual reduction in workability arising from an increasing steel fibre content, at a steel fibre content higher than 1%, both the paste volume and super-plasticizer dosage were increased to maintain a reasonable workability.

The type of steel fibres used in this study was Dramix RL-45/50-BN. It had a nominal tensile strength of 1000 MPa. Each steel fibre has a diameter of 1.05 mm and an overall length of 50 mm corresponding to an aspect ratio of approximately 48. Hooks were formed at the ends of the fibres to provide further mechanical anchorage on top of the shear bond so as to increase the pullout strength from the concrete matrix. From each concrete mixture, three batches of concrete were produced, each batch for measuring the shock vibration resistance of the concrete at one of the three designated ages of 12 h, 1 day and 7 days. Out of each batch of concrete, six 150 mm cubes, six 150 × 300 mm cylinders and thirteen 100×100×500 mm prisms were cast.

The shock vibration tests were conducted in accordance with the method illustrated by the test set-up in Fig.3.68. After applying shock vibration, the short-term effects were evaluated by observing the appearance of cracks and measuring the immediate change in ultrasonic pulse velocity, while the long-term effects were evaluated by continuing to cure the specimens and measuring their 28-day direct tensile strength and cube strength.

The quality control test results (i.e. the material properties of the concrete at 28-day age) are listed in Tab.3.34. The mean 28-day cube strength of the seven concrete mixtures varied between 49.9 and 52.6 MPa with a range of only 5%. On the other hand, the other results revealed that the split cylinder tensile strength, direct tensile strength and cube strength increased steadily but at different rates with the steel fibre content.

The material properties of the 21 batches of concrete at the time of performing the shock vibration test are presented in Tab.3.35. The cube strength, split cylinder tensile strength and ultrasonic pulse velocity all increased with the concrete age. Furthermore, unlike the cube strength at 28-day age, which appeared to be independent of the steel fibre content, the cube strength at earlier ages increased significantly with the steel fibre content at a rate that was generally higher at an earlier age (age ≤ 1 day) and lower at a later age (age > 1 day). The split cylinder tensile strength also increased significantly with the steel fibre content. However, the ultrasonic pulse velocity was basically unaffected by the steel fibre content.



**Fig. 3.68** Schematic diagram of test set-up for shock vibration test (Kwan and Ng 2007)

**Table 3.34** Material properties at 28-day age (Kwan and Ng 2007)

Mixture number (fibre content by volume [%])	Mean cube compressive strength [MPa]	Mean split cylinder tensile strength [MPa]	Mean direct tensile strength [MPa]	Mean cube compressive strength [MPa]
A (0)	50.6	3.28	2.64	49.5
B (0.5)	50.6	3.49	2.87	53.2
C(1.0)	51.5	3.88	2.93	57.0
D (1.5)	51.5	4.59	2.99	60.7
E (2.0)	50.8	4.94	3.34	62.4
F (3.0)	52.6	6.11	3.56	66.6
G (4.0)	49.8	6.50	3.70	63.0

**Table 3.35** Material properties at time of shock vibration test (Kwan and Ng 2007)

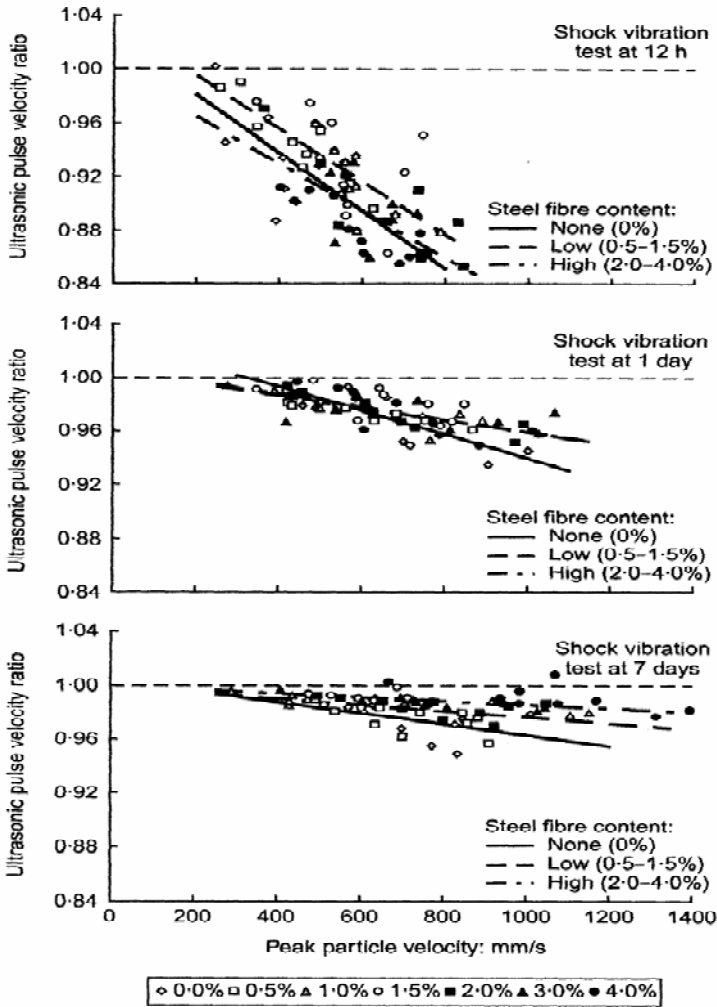
Mixture number of Tab. 3.34 (fibre content by volume [%])	Age	Mean cube compressive strength [MPa]	Mean split cylinder tensile strength [MPa]	Ultrasonic pulse velocity: [m/s]
A (0)	12 h	3.6	0.37	2753
	1 day	11.8	1.16	3383
	7 days	36.2	2.97	4336
B (0.5)	12 h	5.3	0.56	2997
	1 day	12.8	1.27	3317
	7 days	38.3	2.96	4130
C(1.0)	12 h	8.4	0.98	2930
	1 day	13.7	1.50	3328
	7 days	39.7	3.24	4312
D (1.5)	12 h	8.6	1.06	2935
	1 day	13.6	1.50	3203
	7 days	41.1	3.96	4309
E (2.0)	12 h	9.1	1.28	3002
	1 day	19.7	2.45	3435
	7 days	42.6	4.62	4323
F (3.0)	12 h	11.8	1.32	2869
	1 day	22.8	2.97	3524
	7 days	41.4	5.00	4366
G (4.0)	12 h	10.0	1.44	2828
	1 day	22	3.10	3405
	7 days	40.4	5.15	4278

These cracks were all so fine that they were hardly observable. Moreover, they were all found on prisms cast of concrete with steel fibre content less than 2% (i.e. concrete mixtures A, B, C or D). No visible crack was found on prisms cast of concrete with a steel fibre content equal to or higher than 2% (i.e. concrete mixtures E, F or G). All cracked prisms had direct tensile strength ratios lower than 0.8. Hence, regardless of whether or not concrete contained steel fibres, when

a crack was observed. The tensile strength was significantly reduced. On the other hand, among the prisms whose direct tensile strength ratios were lower than 0.8, only 11 out of 42 (26%) showed visible cracks and 31 out of 42 (74%) did not show any visible cracks. This revealed that there might have been micro-cracks formed in concrete that were unobservable by naked eyes. When relying on the observation of cracks to detect vibration damage, there was a missing rate of 74%. The above missing rate was higher than that for plain concrete. This may be attributed to the high effectiveness of steel fibres in controlling cracking, which rendered the cracks formed due to shock vibration to be hardly observable or even unobservable. At a steel fibre content of 2% or higher, steel fibres were quite effective in controlling cracking of concrete afflicted by shock vibration damage.

Among 210 prisms subjected to shock vibration up to intensities that should be large enough to cause significant damage, only 11 prisms were cracked. One of the 11 cracked prisms, which was cast of plain concrete (i.e. cast of concrete mixture A) and was subjected to shock vibration at 7 days up to a ppv of 1186 mm/s was actually broken into two pieces. The other ten cracked prisms were found to have transverse hairline cracks formed within the middle third along the length of the prisms.

The effects of the shock vibration applied on the ultrasonic pulse velocity of the concrete are studied by plotting the ultrasonic pulse velocity ratio against the ppv of the shock vibration, as shown in Fig.3.69. Regardless of the concrete age and steel fibre content, the ultrasonic pulse velocity ratio decreased significantly when the ppv increased. Since a reduction in ultrasonic pulse velocity ratio is in some sense a measure of the extent of damage, this indicated that the short-term damage caused by shock vibration was generally larger at higher ppv. A reduction in an ultrasonic pulse velocity due to shock vibration was substantially larger at earlier concrete age. With steel fibres added, the rate of a reduction in an ultrasonic pulse velocity with the ppv became slower. Hence, at the same ppv, the short-term damage caused to concrete containing steel fibres was generally less severe than that caused to plain concrete. Nevertheless, at an early age of 12 h, there was a little difference between the rate of reduction in an ultrasonic pulse velocity for concrete containing steel fibres and that for plain concrete, indicating that the short-term damage caused to concrete containing steel fibres was the same as that caused to plain concrete. Hence, at an age of 12 h, the addition of steel fibres had rather low effectiveness in alleviating the short-term damage caused by shock vibration.



**Fig. 3.69** Ultrasonic pulse velocity ratio against peak particle velocity (Kwan and Ng 2007)

The direct tensile strength ratio decreased when the ppv increased, showing clearly that the long-term damage caused by shock vibration was generally larger at higher ppv. The results for the shock vibration tests carried out at 12 h showed that the direct tensile strength ratio of plain concrete decreased significantly when the ppv increased while the direct tensile strength ratio of concrete containing steel fibres remained more or less the same even when the ppv increased to fairly large values (as depicted by the almost horizontal trend lines). In fact, after subjected to

shock vibration, all prisms cast of concrete containing steel fibres had their direct tensile strength ratios remaining higher than 0.8 (reduction in direct tensile strength less than 20%) and some even had their direct tensile strength ratios higher than 1.0 (no reduction in the direct tensile strength). Hence, although the addition of steel fibres was not really effective in alleviating the short-term damage caused by shock vibration applied at 12 h, in the longer term provided enough steel fibres were added and concrete was subsequently properly cured, the 28-day direct tensile strength of concrete subjected to shock vibration at 12 h could be kept at not less than 0.8 times that of the same concrete not subjected to any shock vibration. The addition of steel fibres is actually quite effective in improving the shock vibration resistance of concrete at the age of 12 h. The results for the shock vibration tests carried out at 1 day and 7 days also showed that a reduction in the direct tensile strength ratio with the ppv was generally smaller for concrete containing steel fibres than for plain concrete. Hence, the addition of steel fibres was also effective in improving the shock vibration resistance of concrete at such ages. After subjected to shock vibration, some prisms cast of concrete containing steel fibres had their direct tensile strength ratios falling below 0.8, the addition of steel fibres was less effective in improving the shock vibration resistance at such later ages than at 12 h.

The effects of the shock vibration applied on the 28- day cube strength of the concrete are shown in Fig.3.71. The cube strength ratios of nearly all prisms regardless of the steel fibre content, the concrete age at which the shock vibration was applied and the intensity of the shock vibration applied, were within a narrow range between 0.9 and 1.1. Hence, shock vibration had basically no effect on the compressive strength of the concrete regardless of whether concrete contained steel fibres or not.

A correlation between the short- and long-term damage was highly dependent on both the concrete age and steel fibre content (Fig.3.72). The results for tests carried out at 12 h showed that although many prisms had insignificant reduction in an ultrasonic pulse velocity (more than 2% reduction or ultrasonic pulse velocity ratio lower than 0.98), very few of these prisms, which were all cast of plain concrete, had significant a reduction in the direct tensile strength (more than 20% reduction or a direct tensile strength ratio lower than 0.8). There was basically no correlation between the short- and long-term damage. Concrete containing steel fibres was able to recover to the extent that no significant the long-term damage could be detected by the 28-day tests. On the other hand, the results carried out at 1 day and 7 days showed that at such later ages, there was a higher correlation between the short- and long-term damage. At an age of 1 day or later, once short-term damage was incurred after the application of shock vibration, concrete did not fully recover and at least a part of the short-term damage remained as long-term damage. The ability of SFRC to recover after having incurred the short-term damage was higher at earlier concrete age and at a higher steel fibre content applied at later age. Overall, the addition of steel fibres

was more effective in improving the shock vibration resistance of concrete at age within 1 day than at later age.

According to Bonzel and Dahms (1981), the impact resistance of fibrous concrete is significantly higher (Fig.3.73). It grows with increasing fibre dosage.

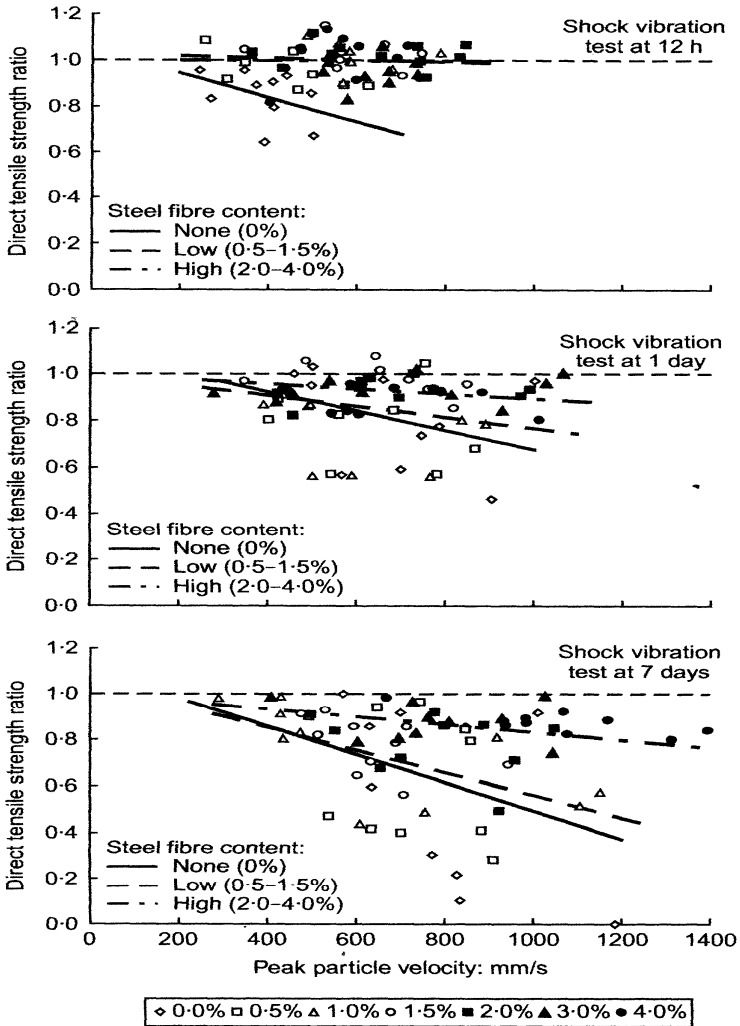


Fig. 3.70 Direct tensile strength ratio against peak particle velocity (Kwan and Ng 2007)

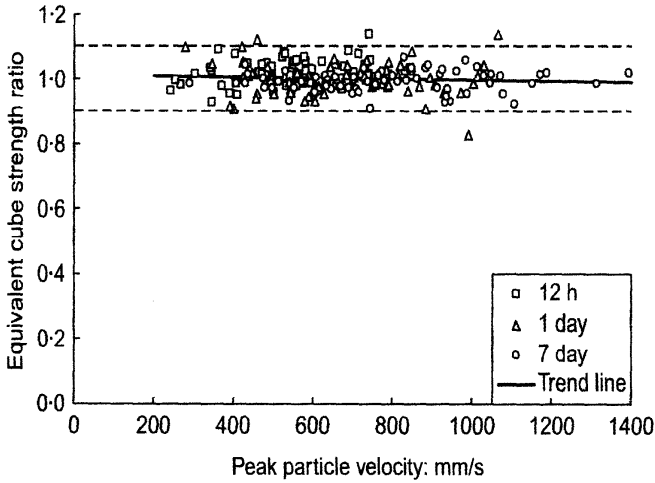


Fig. 3.71 Cube strength ratio against peak particle velocity (Kwan and Ng 2007)

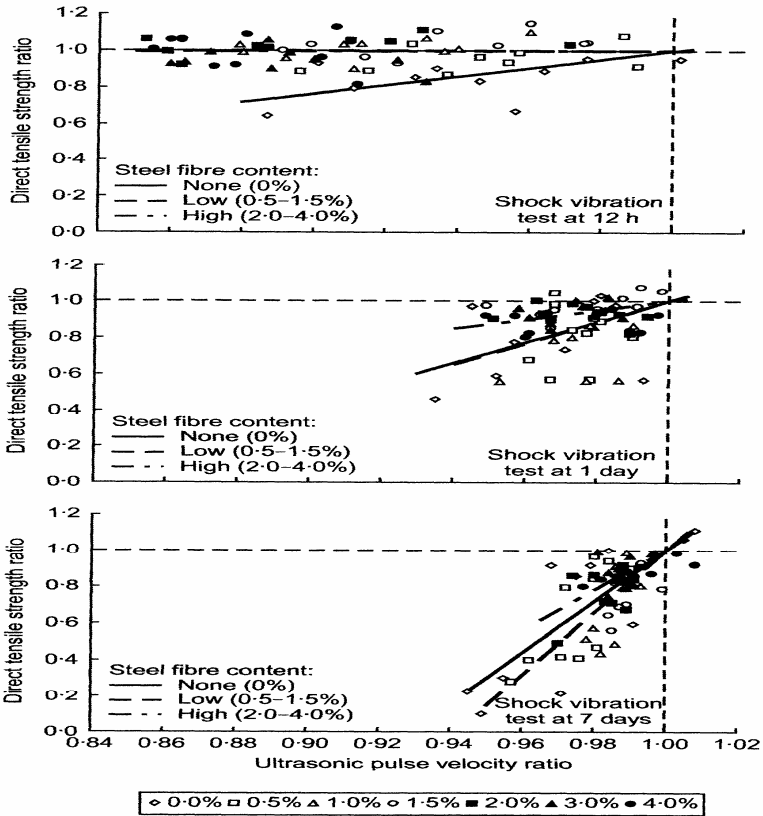
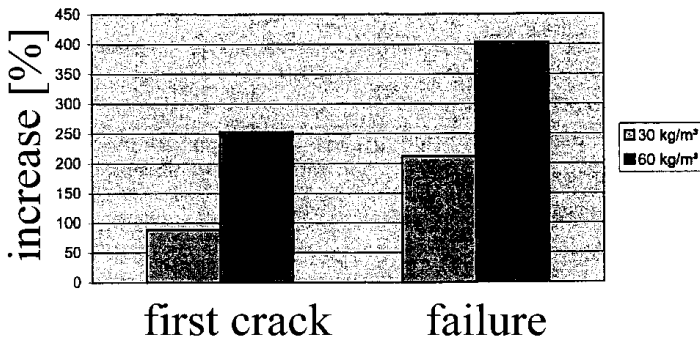


Fig. 3.72 Correlation between short- and long-term damage (Kwan and Ng 2007)





**Fig. 3.73** Increase of impact resistance of concrete with steel fibres (Bonzel and Dahms 1981)

### 3.2 Properties of Reinforced Concrete Including Steel Fibres

The application of steel fibres results in the improved ductility of reinforced concrete structural members such as beams and slabs (Shah 1990, Bentur and Mindess 1990, Shah and Ouyang 1991, Al-Taani and Al-Feel 1990, Ashour et al. 1992, Swamy et al. 1993, Shin et al. 1994, Tan et al. 1995, Frosch, 2000, Khuntia and Stojadinovic 2001, Mirsayah and Banthia 2002, Padmarajaiah and Ramaswamy 2001). Furthermore, steel fibres act as an additional shear reinforcement of concrete improving the stiffness, shear strength, shear toughness and resistance to diagonal cracking. Combination of steel and non-metallic fibres was found to be extremely effective in FRC beams of high-strength concrete (Noghabai 2000). The effect of SFs on cracks in RC beams under tension was carefully investigated by Gopalaratnam et al. (1991), Lim and Oh (1999), Chunxiang and Patnaikuni (1999), Hartman (1999), Lohrmann (1999), Alavizadeh-Fahrang (1999), Furlan and Hanai (1999), Abdul-Ahad and Aziz (1999), Foster and Attard (2001), Dupont and Vandewalle (2002), Paine et al. (2002), Ganesan and Shivananda (2002), Campione et al. (2005a), Altun et al. (2007), Haktanir et al. (2007), Juarez et al. (2007), Smadi and Bani Yasin (2008).

#### Experiments by Altun et al. (2007)

The experiments by Altun et al. (2007) were performed with reinforced concrete beams of  $300 \times 300 \times 2000$  mm<sup>3</sup> under simple bending with the same steel reinforcement having steel fibres at dosage of 0 kg/m<sup>3</sup>, 30 kg/m<sup>3</sup> and 60 kg/m<sup>3</sup> with C20 (12 beams) and C30 (9 beams) class concrete. The SFs used in the study were of Dramix Rc-80/06,0-Bn type, each having a diameter of 0.75 mm and a length of 60 mm. The stirrups were dense to provide strong shear resistance.

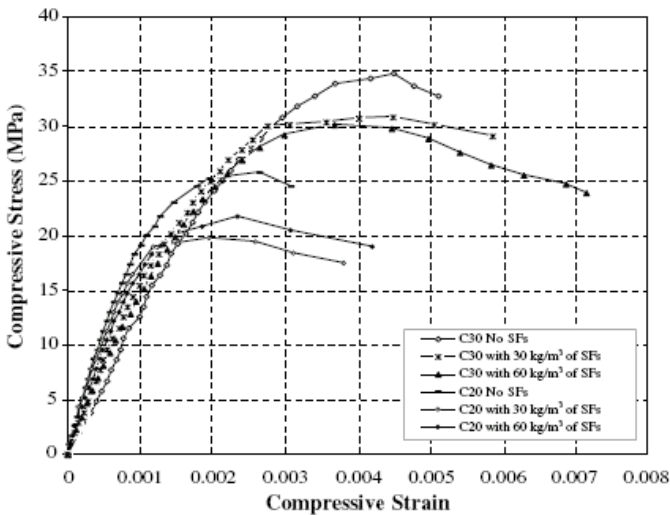
Figure 3.74 shows the average stress-strain relationship during uniaxial compression determined experimentally for plain concrete and SFAC. In turn, Tab.3.36 includes the experimental results of the average compressive strength,

modulus of elasticity, split tensile strength, flexural strength and toughness measured on  $150 \times 300 \text{ mm}^2$  cylindrical samples and  $150 \times 150 \times 750 \text{ mm}^2$  prisms.

The results of experiments during four-point beam loading are presented in Tab.3.37. The theoretical ultimate bending moment was computed by a conventional ultimate strength approach.

The experimentally obtained ultimate loads versus mid-span deflection relationship for the RC and SFARC beams produced with C20 and C30 class of concrete are given in Fig.3.75. In turn, the experimentally determined ultimate load-SFs dosage and toughness-SFs dosage relationships are drawn in Figs.3.76 and 3.77.

As result of experiments on uniaxial compression, the ultimate strength insignificantly decreased and the toughness appreciably increased. In the case of bending experiments, the ultimate loads and the flexural toughness significantly increased. The SFs dosage of  $30 \text{ kg/m}^3$  was better than that of  $60 \text{ kg/m}^3$ . The difference between experimental ultimate loads and theoretical ultimate loads was significant (Tab.3.37).



**Fig. 3.74** The average stress-strain relationships determined experimentally for plain concrete and SFRC: a) C 20, b) C30, c) C20 with  $30 \text{ kg/m}^3$  of SFs, c) C20 with  $60 \text{ kg/m}^3$  of SFs, c) C30 with  $30 \text{ kg/m}^3$  of SFs, c) C30 with  $60 \text{ kg/m}^3$  of SFs (Altun et al. 2007)

### Experiments by Lim and Oh (1999)

Fibre reinforced concrete beams ( $100 \times 180 \times 1700 \text{ mm}^3$ ) in shear during four-point bending were tested. The span length of members was 1300 mm and the shear span length was 400 mm. The volume fraction of steel fibres varied from 0% to 2% and the ratios of stirrups from 0% to 100% of the required shear reinforcement. Round straight steel fibres of 0.7 mm diameter and 42 mm length were used with the ultimate strength

of 1784 MPa. Gravel had a maximum aggregate size of 10 mm. Longitudinal deformed steel bars 16 mm diameter (tensile steel), 10 mm diameter (compressive steel) with yield strength of 420 MPa, and 6 mm diameter deformed steel bars for stirrups were used. The mix had a compressive strength of 35 MPa.

The addition of steel fibres increased the uniaxial compressive strength, flexural strength and tensile splitting strength. An increase was greatest in the tensile splitting strength. The uniaxial compressive strength increased by about 25% when fibres were introduced into the concrete by up to 2% by volume (Fig.3.78). An increase of the flexural strength was about 55% (Fig.3.78). The splitting strength was more than doubled when 2% fibre volume was used (Fig.3.78).

**Table 3.36** Average mechanical properties of different combinations of concrete measured on 150×300 mm<sup>2</sup> cylindrical samples and 150×150×750 mm<sup>2</sup> prisms (Altun et al. 2007)

Type of concrete	Concrete class	Average compressive strength [N/mm <sup>2</sup> ]	Modulus of elasticity [N/mm <sup>2</sup> ]	Split tensile strength [N/mm <sup>2</sup> ]	Flexural strength [N/mm <sup>2</sup> ]	Toughness [kN mm]
No SFs	C20	24.4	29500	1.59	5.4	200
C20-30		22.5	27500	2.30	8.3	446
C20-60		22.6	26000	2.55	9.8	474
No SFs	C30	34.8	32950	1.95	7.8	306
C30-30		30.8	32200	2.71	9.4	415
C30-60		30.2	32050	3.01	11.4	462

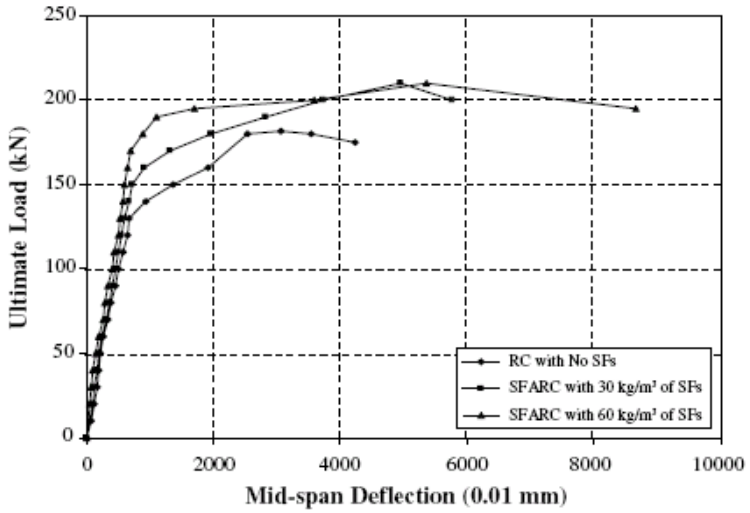
All beams exhibited a similar linear behaviour from initial loading up to the occurrence of the first hair-line crack (Figs.3.79-3.81). After the formation of cracks, all beams exhibited non-linear load-deflection characteristics. Beams without shear reinforcement failed soon after the formation of the diagonal crack. The mode of failure changed from shear to flexural as the fibre content exceeded 1%. Ductility was also enhanced significantly with the fibre addition. The inclusion of steel fibres eliminated the occurrence of concrete spalling. The beams with stirrups exhibited a smaller improvement in the ultimate strength. Thus, the use of fibre reinforcement can reduce the amount of shear stirrups required.

The effect of the fibre contents on cracking shear strength (which significantly increased) is demonstrated in Fig.3.82. An increase of the ultimate shear strength was negligible (Fig.3.83).

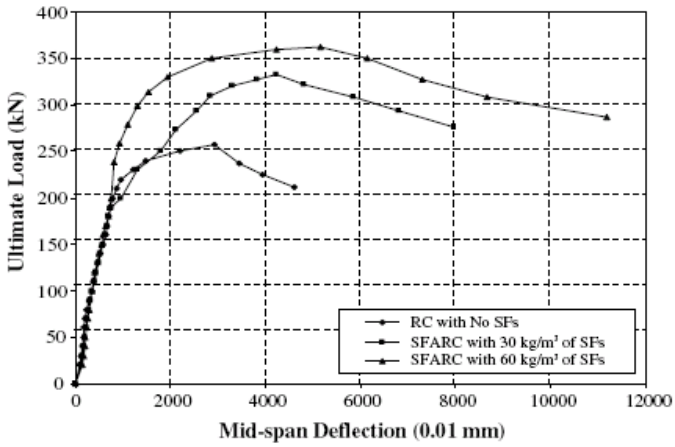
The effect of SFs on cracks in RC beams in shear was also investigated by Swamy and Bahla (1985), Mansur et al. (1986), Narayanan and Darwish (1988), Casanova and Rossi (1997) and Iman et al. (1997).

**Table 3.37** Results of bending experiments on RC and SFRC beams (Altun et al. 2007)

Beam sample	Concrete class	SF dosage [kg/m <sup>3</sup> ]	Tensile steel [mm]	Measured ultimate load [kN]	Toughness [kN mm]	Experimental ultimate load/theoretical ultimate load	
C20-1-0	C20	0	2φ16	184.5	5495	1.46	
C20-2-0				202.0	5970	1.60	
C20-3-0				201.6	5830	1.60	
C20-4-30		30		2φ16	201.9	27835	1.60
C20-5-30					202.3	27550	1.61
C20-6-30					210.0	29501	1.67
C20-7-60		60		2φ16	210.3	29830	1.67
C20-8-60					211.0	30800	1.67
C20-9-60					209.0	29800	1.66
C30-1-0	C30	0	2φ16	262.3	10782	1.77	
C30-2-0				260.2	9925	1.75	
C30-3-0				250.9	10965	1.69	
C30-4-30		30		2φ16	320.3	26382	2.16
C30-5-30					330.0	27989	2.22
C30-6-30					357.2	29856	2.40
C30-7-60		60		2φ16	370.5	29979	2.49
C30-8-60					368.8	30045	2.48
C30-9-60					352.5	29460	2.38

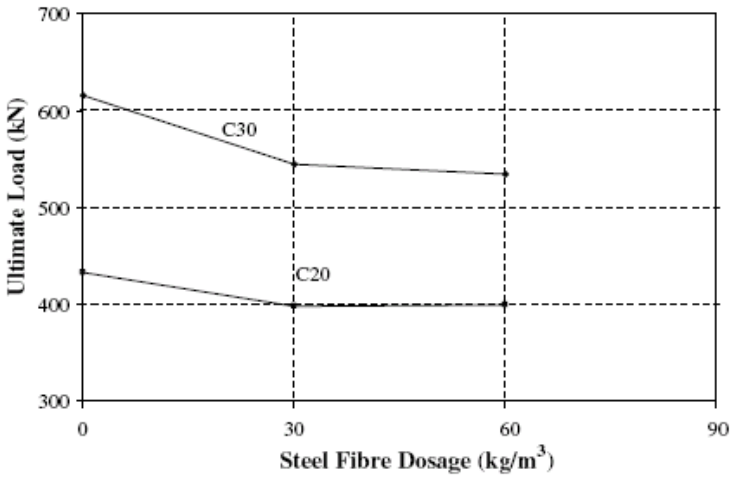


A)

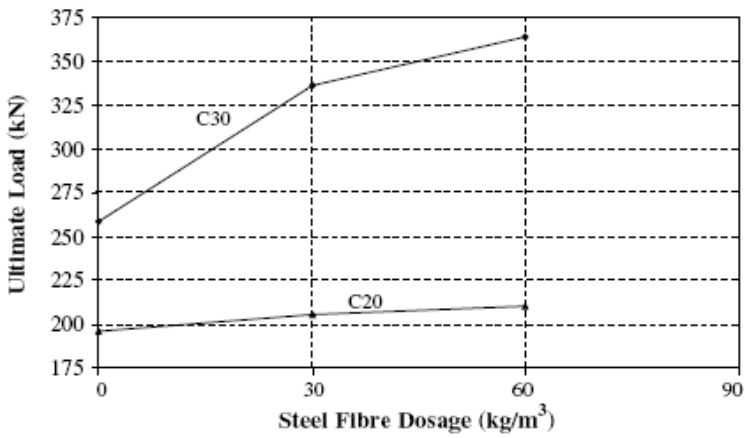


B)

**Fig. 3.75** The average ultimate load versus mid-span deflection relationships determined experimentally for the 3 groups SFRC beams with C20 (A) and C30 (B) class of concrete (Altun et al. 2007)

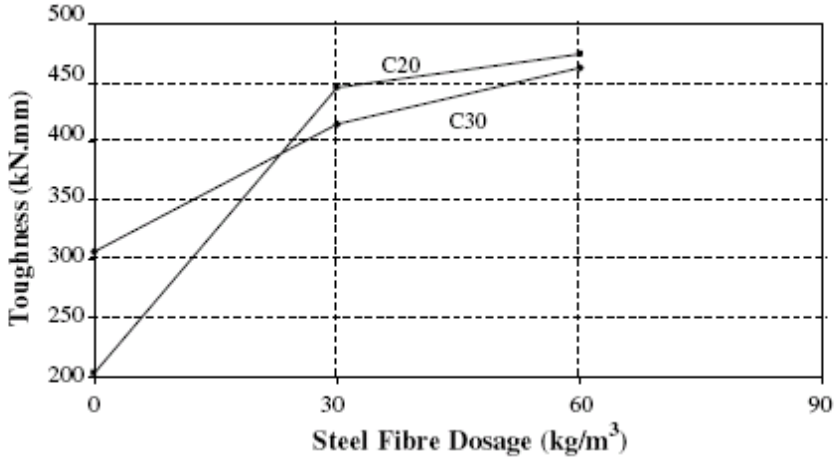


A)

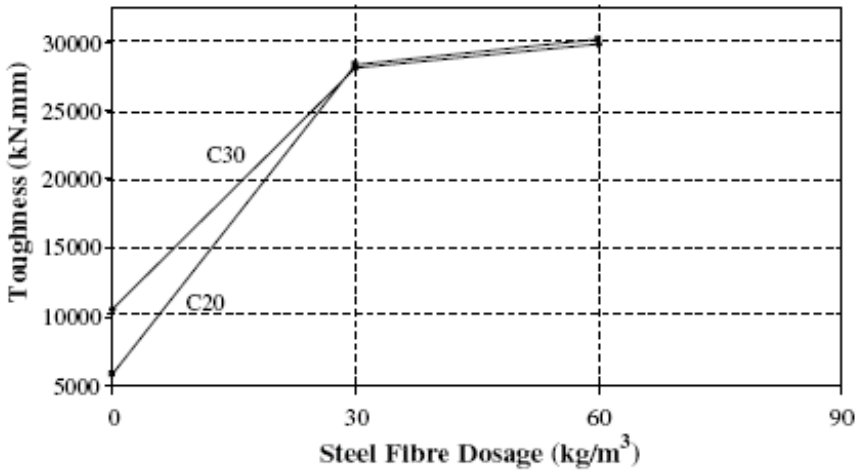


B)

**Fig. 3.76** Steel-fibre dosage versus experimental ultimate load relationships for C20 and C30 classes of concrete: A) uniaxial compression, b) bending (Altun et al. 2007)

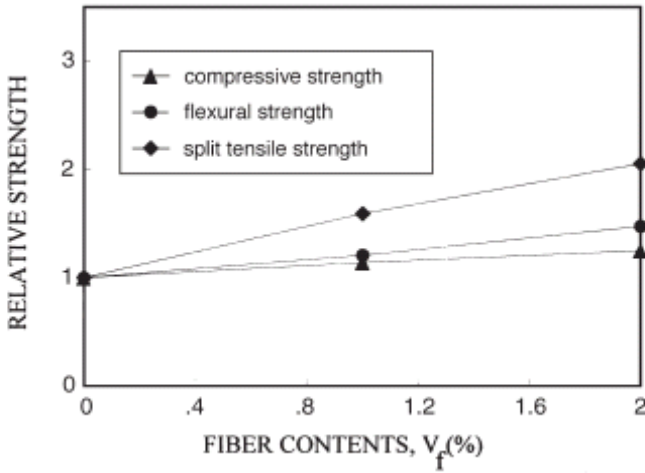


A)

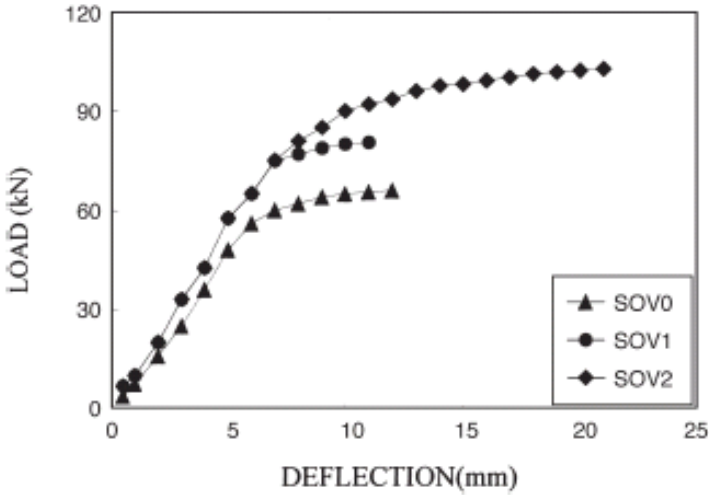


B)

**Fig. 3.77** Steel-fibre dosage versus experimental toughness relationships for C20 and C30 classes of concrete: A) uniaxial compression, b) bending (Altun et al. 2007)

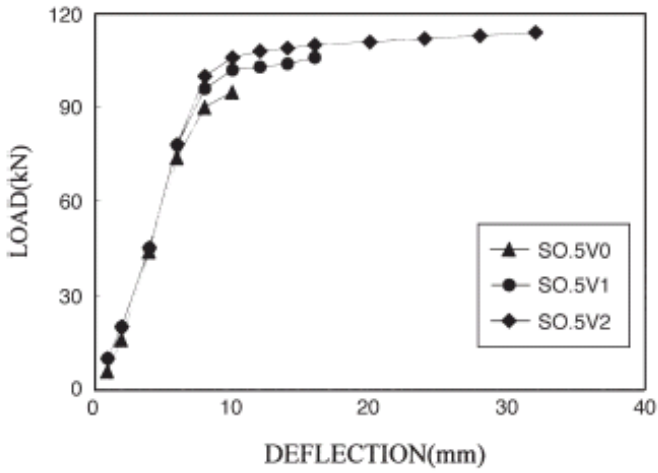


**Fig. 3.78** Comparison of various relative strengths due to the addition of steel fibres (Lim and Oh 1998)

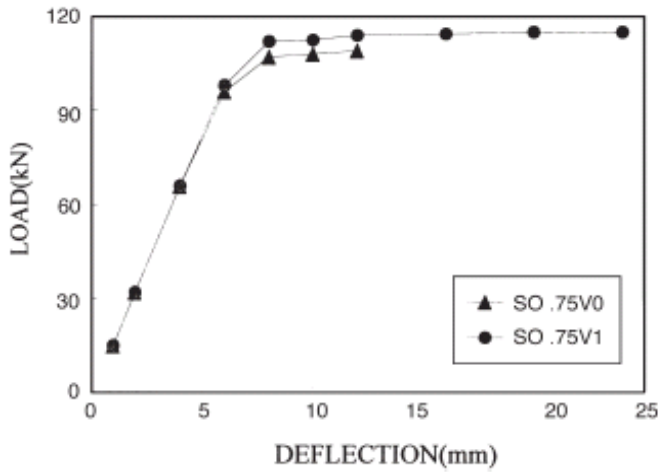


**Fig. 3.79** Load-deflection curves for beams without stirrups with fibre contents: SOV0 - 0%, SOV1-1%, SOV2-2% (Lim and Oh 1998)





**Fig. 3.80** Load-deflection curves for beams with 50% of conventional stirrups with fibre contents: SO.5V0-0%, SO.5V1-1%, SO.5V2-2% (Lim and Oh 1998)



**Fig. 3.81** Load-deflection curves for beams with 75% of conventional stirrups with fibre contents: SO.75V0-0%, SO.75V1-1% (Lim and Oh 1998)

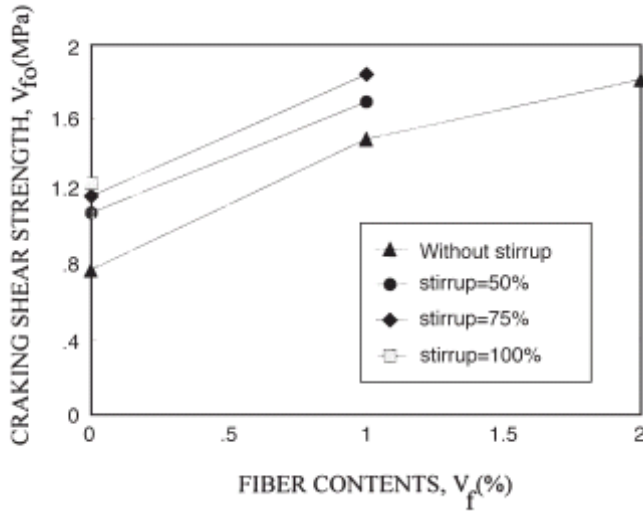


Fig. 3.82 Cracking shear strength versus fibre content (Lim and Oh 1998)

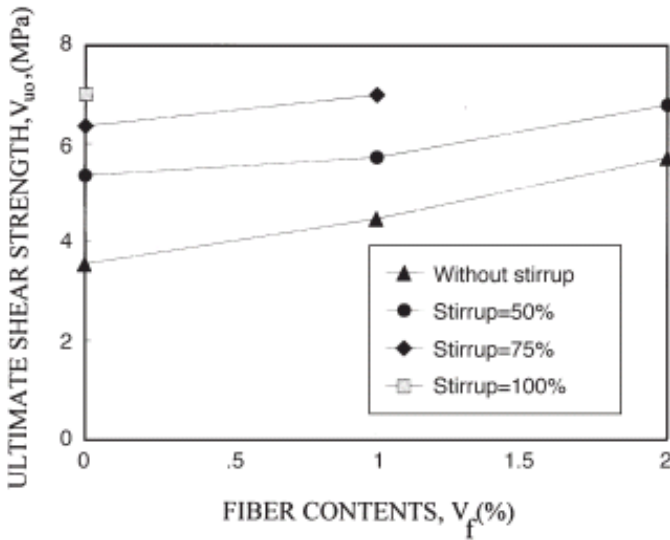


Fig. 3.83 Ultimate shear strength versus fibre content (Lim and Oh 1998)

### Experiments by Haktanir et al. (2007)

The steel fibres Dramix RC80/60-BN of Bekaert and ZP-308 were used (the total length and cross-sectional diameter were 60 mm and 0.75, and 30 mm and 0.75 mm, respectively). Figure 3.84 shows the average stress-strain curves and Tab.3.38 reports the average findings. The compressive strength of fibrous concrete with a steel fibres dosage of 25 kg/m<sup>3</sup> was 10% greater than plain concrete and their secant modulus of elasticity did not deviate from each other.

The results of three-edge-bearing tests on concrete 500 mm pipe size with and without steel fibres are shown in Tabs.3.39 and 3.40. The three-edge-bearing strength of steel-fibre concrete pipes was higher than those of reinforced-concrete pipes.

The effect of the steel-fibre dosage on the ultimate load per meter of the effective length is given in Fig.3.85. A longer RC80/60-BN type of steel fibres was more efficient than a shorter ZP-308 type.

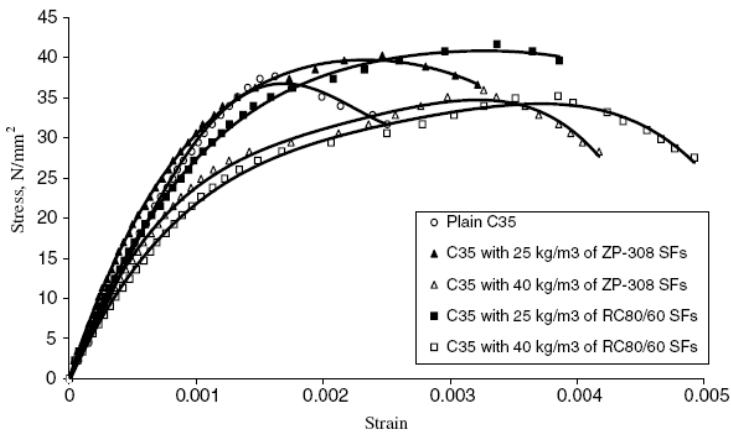


Fig. 3.84 Stress-strain diagrams of different concrete used in pipes (Haktanir et al. 2007)

### Experiments by Chunxiang and Patnaikuni (1999)

Three types of enlarger-end steel fibres with different dimensions to study effect of fibre on the deflection, cracking behaviour and ductility of reinforced concrete beams during three-point bending were used. All beams were provided with shear reinforcement and had a constant cross-section of 120×150 mm<sup>2</sup> and a constant length of 2000 mm. Three types of steel fibres were used with a content of 75 kg/m<sup>3</sup> which corresponded to a content of about 1% by volume. 16 mm deformed

steel bars having about 400 MPa of yield strength were used. The cross-sections of all three types of fibres were rectangular with sizes: 18×0.4×0.3 mm (type I), 18×0.6×0.3 mm (type II) and 25×0.6×0.4 mm (type III). The aspect ratios  $l_f/d_f$  were 46, 38 and 45, respectively. The results of the compressive strength and slump are given in Tab.3.41. Load-displacement curves are in Fig.3.88.

**Table 3.38** Mechanical properties of the C35 class of concretes with and without steel fibres measured on three 150×300 mm<sup>2</sup> cylindrical samples (Haktanir et al. 2007)

Type of concrete	Average ultimate load [kN]	Average compressive strength [N/mm <sup>2</sup> ]	Average secant modulus of elasticity [kN/mm <sup>2</sup> ]
C35, plain	665	37.6	32.0
C35 with 25 kg/m <sup>3</sup> of ZP-308	711	40.2	33.3
C35 with 40 kg/m <sup>3</sup> of ZP-308	630	35.6	29.6
C35 with 25 kg/m <sup>3</sup> of RC80/60-BN	736	41.6	30.8
C35 with 40 kg/m <sup>3</sup> of RC80/60-BN	624	35.3	25.8

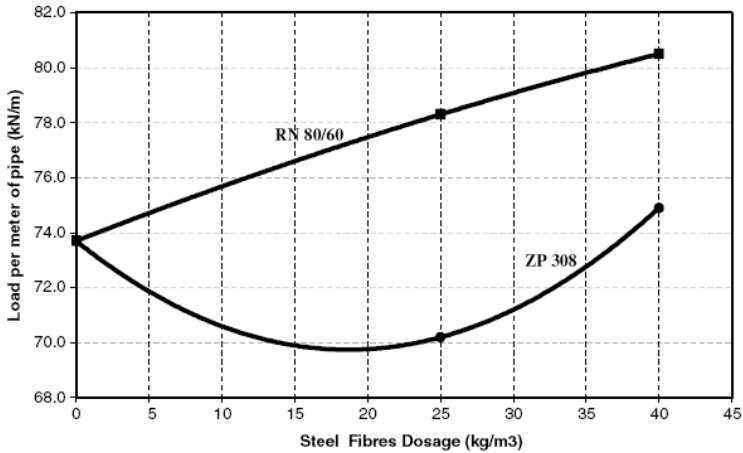
Fig.3.87 and Tab.3.42 compare concrete beams with steel fibres and plain concrete beams. With the addition of steel fibres, beams showed a steeper slope in the ascending part which means that the beams possessed a higher flexural rigidity and showed a milder slope in the descending part which means that the beams possessed ductility. The ultimate load was higher and the displacements before failure were larger. Thus, the ultimate load-central displacement ratio was significantly improved. The types I and II were better than the type III.

**Table 3.39** Summary of the three-edge-bearing tests on concrete pipes with and without steel fibres (Haktanir et al. 2007)

Type of pipe	Average ultimate load [kN]	Average ultimate load per meter length of pipe [kN/m]	Relative difference with respect to RC pipes [%]
CP	64.5	43.0	-
RCP	110.6	73.7	-
SFCP-ZP-25	105.3	70.2	-5
SFCP-ZP-40	112.3	74.9	+2
SFCP-80/60-25	117.4	78.3	+6
SFCP-80/60-40	120.8	80.5	+9

**Table 3.40** Measured crack sizes at 60% of the ultimate load during the three-edge bearing tests on concrete pipes with and without steel fibres (Haktanir et al. 2007)

Type of pipe	Width of crack [mm]	Length of crack [mm]
CP	1.5-1.8	550-650
RCP	0.22-0.28	266-297
SFCP-ZP-25	0.07-0.10	117-169
SFCP-ZP-40	0.03-0.06	87-93
SFCP-80/60-25	0.02	79-85
SFCP-80/60-40	0.02	48-53



**Fig. 3.85** Relationship between three-edge-bearing strengths of steel-fibre-concrete pipes versus steel fibre dosage for ZN 308 and RN 80/60 types of steel fibres as compared to reinforced concrete pipes (Haktanir et al. 2007)

#### Experiments by Juarez et al. (2007)

The experimental program included the test of 16 reinforced concrete beams with dimensions of  $2000 \times 150 \times 250 \text{ mm}^3$  under four-point bending. The beams were designed to fail in diagonal tension. All beams were reinforced with three longitudinal bars located at an effective depth,  $d=216 \text{ mm}$  and plain wire stirrups of diameter 6.35 mm. The steel fibres of 25 mm length were used at different volumes ( $V_f$ ), 0%, 0.5%, 1.0% and 1.5%. Two twin beams were cast for each dosage of fibres and a concrete compressive strength combination ( $f_c=18.9 \text{ MPa}$  (A) and  $f_c=36.7 \text{ MPa}$  (B)).

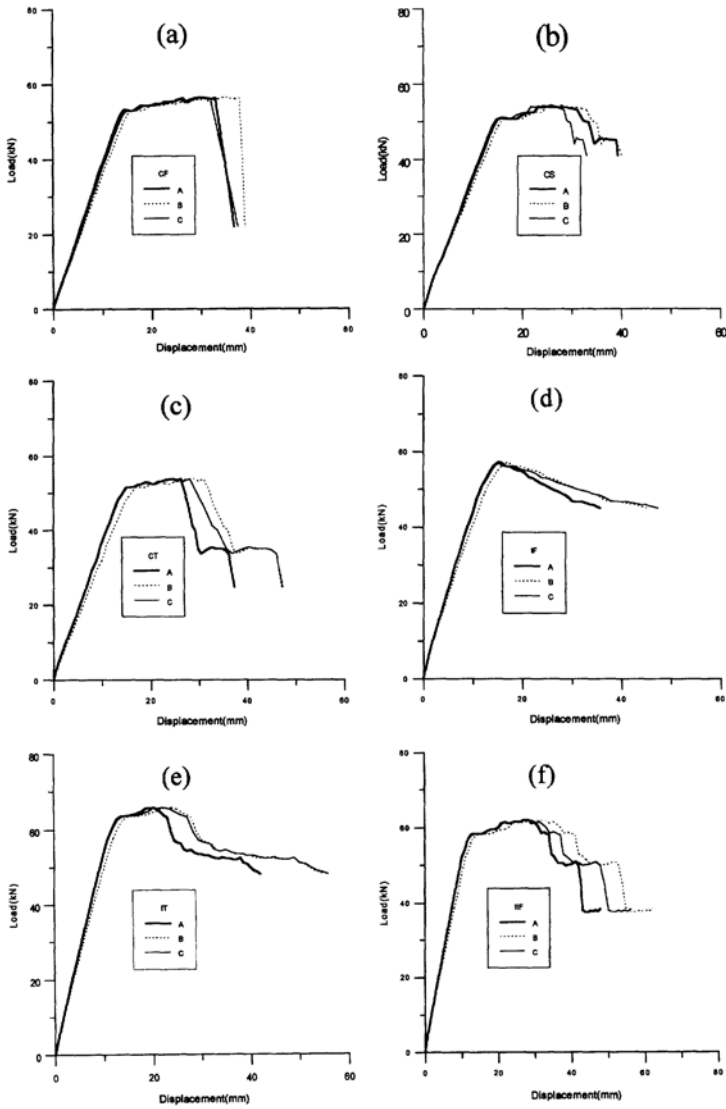
Fig.3.88 shows the load-displacement curves for each beam. The strength of beams with fibres was higher than those without them.

Some information about a cracking process is listed in Tab.3.44.and Fig.3.89 The steel fibres increased a cracking moment and reduced a number of cracks. The width of cracks was also smaller (Casanova et al. 1997, Furlan et al. 1997).

**Table 3.41** Workability and compressive strength (Chunxiang and Patnaikuni 1999)

Beam nr	Fibre type	Slump [mm]	Flow time [s]	Compressive strength after 28 days [MPa]	Compressive strength after 76 days [MPa]
IF	I	55	17	64.1	79.9
IT	I	150	9	66.1	81.1
IIF	II	35	30	79.9	95.7
IIS	II	15	28	82.6	91.9
IIT	II	60	23	77.9	92.2
IIIF	III	110	14	73.5	84.5
IIIS	III	45	35	78.1	81.0
CF	without fibres	150	17	64.8	78.4
CS	without fibres	150	8	68.1	74.3
CT	without fibres	100	11	64.6	72.8

The incorporation of fibres improved the toughness of the composite. Figure 3.88 shows that FRC beams exhibit higher ductility and higher shear strength when compared to the reference beams. The group A of beams demonstrates up to two-fold improvement of the ductility versus the group B. However, the main effect of fibre reinforcement was related to the improvement of the shear strength as the volume fraction of fibres increased. The group B beams with  $V_f=1.5\%$  showed the shear strength increase of 54% versus the reference beams, and for the group A beams with  $V_f=1.5\%$ , the increase was 12%. For these beams, the test shear strength of the FRC beams was higher than that assumed by the ACI-318 Code nominal shear strength, by 17% and 30%, respectively. The addition of fibres reduced the width of diagonal tension cracks, improving the transmission of shear load and redistribution of the stresses between the concrete matrix, fibres and stirrups.



**Fig. 3.86** Load-displacement curves (B – mid-point, A – point at distance 250 mm from mid-point on the left, C - point at distance 250 mm from mid-point on the right) (Chunxiang and Patnaikuni 1999)



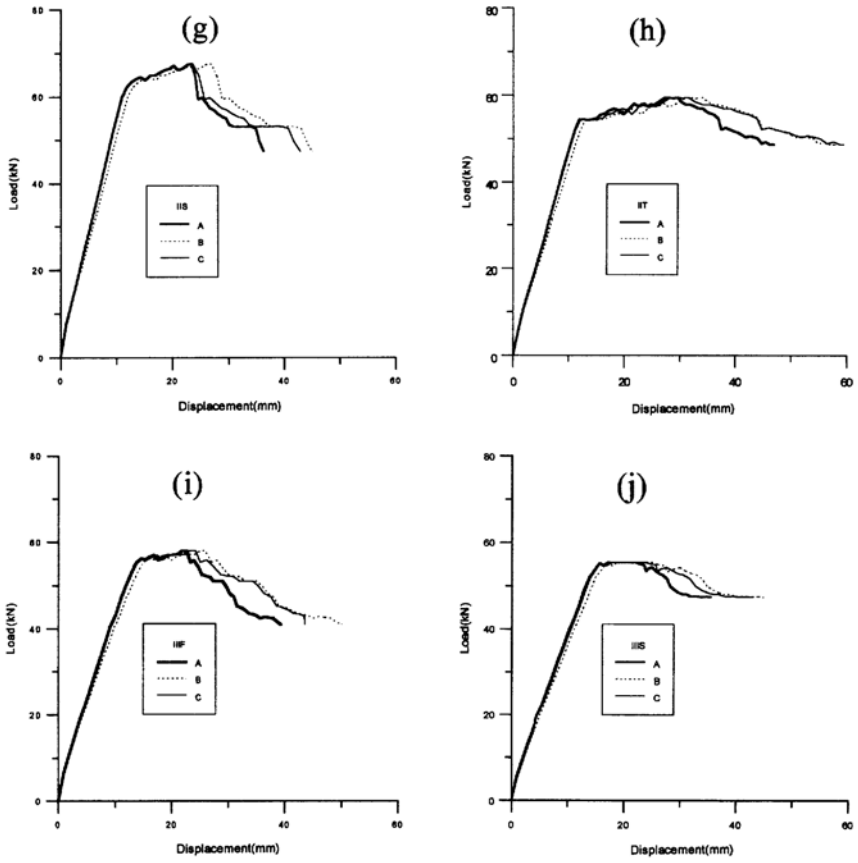


Fig. 3.86 (continued)

**Table 3.42** Characteristics of concrete beams in load-displacement curve (Chunxiang and Patnaikuni 1999)

Beam nr.	Displacement at yield (mid-point) [mm]	Displacement at ultimate (mid-point) [mm]	Yield load [kN]	Ultimate load [kN]
IF	17.0	17.0	57.2	57.2
IT	15.0	22.0	63.4	65.6
IIF	15.0	31.0	58.2	61.8
IIS	16.0	27.0	64.6	67.6
IIT	13.0	31.0	54.4	59.4
IIIF	16.0	25.0	56.2	58.0
IIIS	17.0	19.0	55.2	55.4
CF	16.5	31.0	53.0	56.4
CS	16.0	28.0	50.6	54.2
CT	16.0	29.0	51.6	53.8

An increase in the concrete compressive strength provided only 9% improvement of the nominal shear strength. With a rise of  $V_f$ , the shear load required to attain the yield strain in longitudinal reinforcement also increased. This behavior was mainly observed for the beams with lower concrete strength, when the reference beams failed without yielding of the longitudinal reinforcement. The longitudinal reinforcement yielded in all beams with the higher concrete strength prior to their failure in shear. This could be explained by the improved bonding between the fibres and concrete matrix, resulting in the enhancement of ductility. In both cases, the important effect of the addition of fibres was in the improvement of ductility. For concrete with  $f_c=36.7$  MPa, the longitudinal reinforcement in beams with  $V_f>1.0\%$  reached the ultimate strain of three times

greater than that of the reference beams. The strains in stirrups indicated that prior to cracking of the beams, the stresses were relatively low, and, in most cases, were in compression. After cracking, the stresses in stirrups increased. The effect of the fibres on corresponding strains was small, even though for beams with  $f_c=18.9$  MPa higher shear strength was observed at the increased  $V_f$ . With an increase in the volume of fibres, the number of cracks also increased, resulting in a significantly reduced crack width (Fig.3.89). The load level at the first shear crack increased in all beams with increasing fibre content. The load level at the first shear crack increased in all beams with an increasing fibre content. However, the first cracks in flexure appeared at the same load levels for all beams. Therefore, the compressive strength or fibre content had little effect on this parameter. The addition of fibres was very effective to hinder the shear crack formation; this effect was somehow improved for the composites based on concrete of the higher compressive strength. The failure of beams occurred in a concrete compression zone when diagonal tension cracks propagated to a compression zone bridging the opposite zones of the load (Fig.3.89).

### Experiments by Abdul-Ahad and Aziz (1999)

The ultimate strength of reinforced concrete T-beams reinforced with conventional steel bars and steel fibres were studied. A total of eight conventionally reinforced concrete T-beams were investigated. They were divided into two groups (group one and group two), Fig.3.90. The group one was divided into four over-reinforced concrete T-beams (G10, G11, G12 and G13) with a volume fraction of steel fibres of 0%, 0.5%, 1% and 1.5%, respectively. The group two was also divided into four under-reinforced concrete T-beams (G20, G21, G22 and G23) with a volume fraction of steel fibres of 0%, 0.5%, 1% and 1.5%, respectively. All beams were geometrically similar having the cross-section of  $b_f=250$  mm,  $b_w=100$  mm,  $h_f=60$  mm and  $h=210$  mm, the total length of 2000 mm and the span length of 1800 mm between supports. The load was applied at mid-span by two-point load (500 mm space between them). Six cylinders (150×300) mm<sup>2</sup> were cast for determination of the compressive and indirect tensile strengths and also three beams (100×100×500) mm<sup>3</sup> were cast for the modulus of rupture. The mix proportion of 1:2:2 (cement, sand, crushed aggregate) with a water cement ratio of 0.57 all by weight was used. The well graded sand and crushed aggregate with the maximum size of 9.5 mm was used. The steel fibres were low carbon hooked 50×0.5 mm<sup>2</sup> in dimension with the tensile strength of 1150 MPa.

The results are shown in Tab.3.45 and the load-deflection relationships for each group are shown in Figs.3.91 and 3.92.

**Table 3.43** Crack number at various loading stages (Chunxiang and Patnaikuni 1999)

Beam	Number of cracks at load $P \leq 20$ kN	Number of cracks at load $P \leq 30$ kN	Number of cracks at load $P \leq 40$ kN	Number of cracks at load $P \leq 50$ kN
IF		6		11
IT			5	
IIF			16	
IIS		7	13	
IIT		11	13	
IIIF		7	10	17
IIIS	3	9	9	17
CF			19	
CS	12	17	20	
CT	10		17	

For a given deflection, the beams with steel fibres resisted a higher load than the beams without them. The deflection at the first crack was also less for the fibrous reinforced beams even though the first cracking load was much higher. By using a steel fibre content of 0.5%, 1% and 1.5%, the ultimate load increased by 7.2%, 12.4% and 10.6% for the group one and 5.64%, 7.74% and 10.35% for the group two, respectively. The compression reinforcement decreased the deflection before the ultimate load, but there was a negligible difference in deflection between beams with and without compression reinforcement. The beam G13 had a lower ultimate load when compared with the beam G12, because when the discontinuous short fibres were used there was a limit beyond which fibre addition did not improve the composite strength. This limit depended on the fibre characteristics as well as the method of fabrication used in the preparation of the composite beyond a certain amount of steel fibres was ascribable to an increase in its porosity.

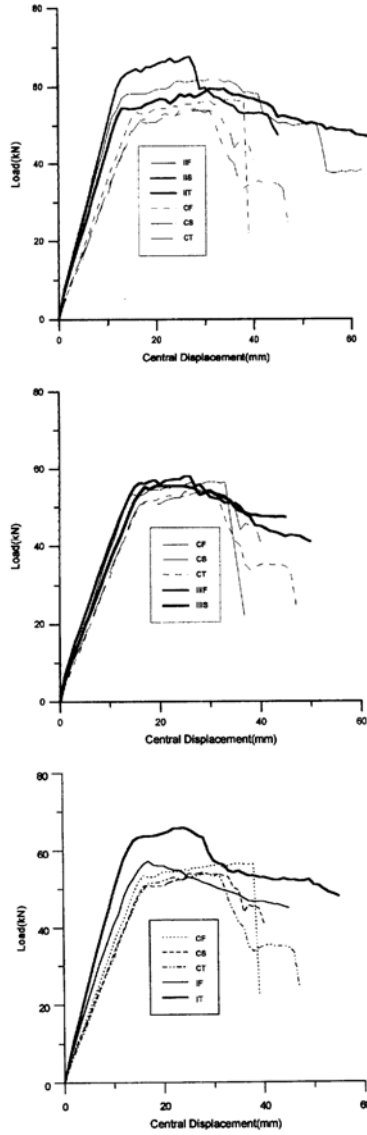
In conventionally reinforced concrete members, sufficient ductility could be achieved by making the tension steel yield before the concrete crushing. Sometimes it may be economical to use more amounts of tension steel than allowed by codes which leads to better utilization of the concrete section strength (Shah and Rangan 1970). The use of fibrous reinforced concrete in a compression zone of flexural members increases the ductility.

### **Experiments by Furlan and de Hanai (1999)**

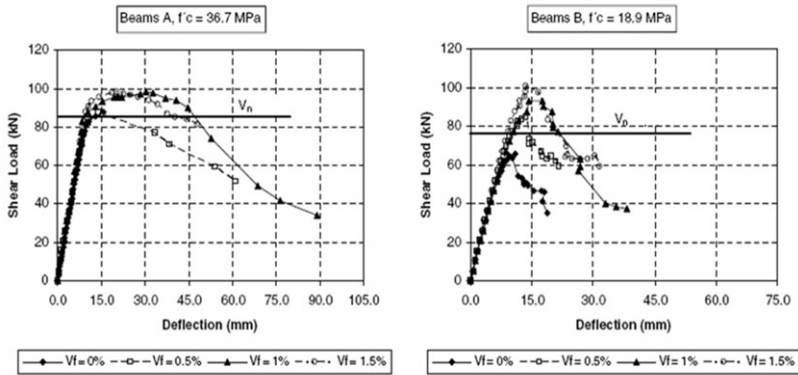
The work analyzed the effect of prestressing and fibres on the structural performance of 9 thin-walled T-section beams (length 400 mm, height 0.3 m) with reduced ratios of shear reinforcement. Two types of fibres were used: a) polypropylene, 42 mm length and 0.05 mm diameter and b) crimped steel fibre, 25.4 mm length and 0.2×2.3 mm<sup>2</sup> rectangular section. The fibre volume added to concrete was equal to 0.5% of polypropylene fibre and 1% of steel fibre. The stirrups consisted of 3.4 mm diameter wires. Longitudinal reinforcement consisted of 9.5 mm strands (seven wire prestressing strands). The prestressing force was kept approximately equal to 105 kN. The beams were tested by application of two point-loads with the shear span equal to  $4d$ . Tab.3.46 summarizes the input data from the nine beams.

Tab.3.47 and Fig.3.93 illustrate the experimental results. The addition of fibres decreased the workability of the fresh concrete, particularly in the case of polypropylene fibres which had a very high aspect ratio. The introduction of fibres increased the splitting tensile strength but it did not increase the compressive strength. It improved the shear strength, except in the beams without stirrups. Prestressing provided the same result, but with a higher intensity and regardless of shear reinforcement.

When the effect of prestressing was disregarded in the beams without stirrups, the relation between the experimental and theoretical values was close to 2.35. The difference in the beams with stirrups was slightly lower. The crack spacing in fibrous reinforced concrete beams was smaller and its development was slower. Deflections were consequently smaller. Fibres were also responsible for a larger number of inclined cracks prior to the beam collapse. Fibre effectiveness was higher in beams with stirrups. In all fibrous reinforced beams, failure was more ductile and there was the increased strength. Thus, the fibres can be considered as an equivalent of shear reinforcement. Prestressing also increased the shear strength but in a more significant manner than the fibre addition. The performance of the beam V9 confirmed the possibility of an advantageous substitution of stirrups for fibres.



**Fig. 3.87** Comparison of load-central displacement curves of concrete beams with and without steel fibres (Chunxiang and Patnaikuni 1999)



**Fig. 3.88** Strength and ductility as a function of concrete strength and volume of fibres ( $V_n$  - nominal shear strength of the reference reinforced concrete beams without fibres using the ACI 318 Code) (Juarez et al. 2007)

### Experiments by Smadi and Bani Yasin (2008)

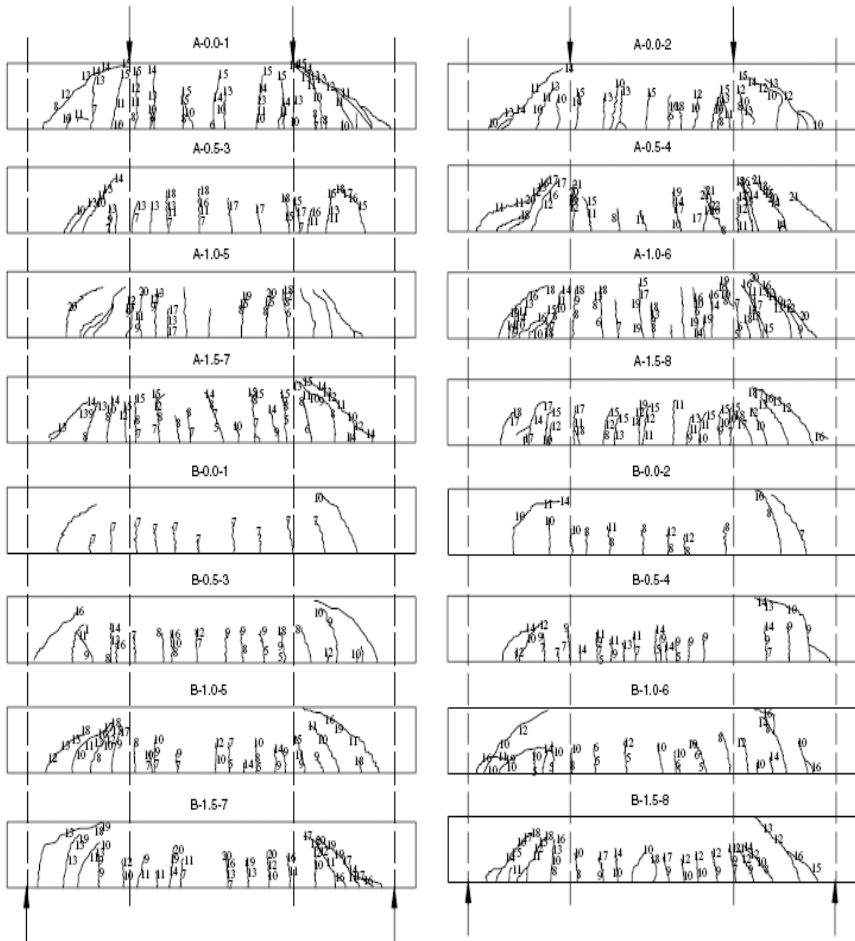
In recent years, the use of high-strength concrete in various structural elements including slabs has become popular worldwide. Flat plate slab systems, which have no beams, column capitals or drop panels, are a competitive and attractive structural system in buildings. Such system has some disadvantages, however, because of the risk of a punching shear failure at the slab-column joint. Such failure generally occurs due to a transfer of a vertical shearing force and unbalanced bending moment between the slab and column. Gravity loads mainly cause a vertical shearing force, while non-uniform gravity loads or any lateral loads due to wind or earthquake forces can produce an unbalanced bending moment. The ultimate strength of flat slab systems is governed frequently by the punching shear capacity of a connection between the slab and column. Although the use of high-strength concrete improve the shear resistance and allows higher forces to be transferred through a slab-column connection, in addition to other over all benefits, the brittleness of the system is enhanced. The additional use of steel fibres can improve the ductility of the connection, and may further increase the slab punching shear strength. The behavior of normal-strength concrete slab-column connections with or without steel fibres has been widely investigated (Ghalib 1980, Swamy and Sar 1982, Alexander and Simmonds, 1992, Harajli et al. 1995, McHarg et al. 2000). Adding fibre reinforcement appears to be a practical and easy way of increasing the punching shear capacity of slab-column connections.

**Table 3.44** Loads corresponding to crack formation and shear strength of investigated beams (Juarez et al. 2007)

Beam type	Fibre content [%]	Load at first shear crack [kN]	Load at first flexural crack [kN]	Shear failure load [kN]
A-0.0-1	0.0	32.6	32.6	87.8
A-0.0-2	0.0	46.1	46.1	91.0
A-0.5-3	0.5	46.1	30.7	90.9
A-0.5-4	0.5	46.1	30.7	92.8
A-1.0-5	1.0	61.9	46.4	98.0
A-1.0-6	1.0	51.6	30.9	90.3
A-1.5-7	1.5	51.6	30.9	96.5
A-1.5-8	1.5	56.7	36.1	97.7
-----				
B-0.0-1	0.0	30.9	30.9	65.5
B-0.0-2	0.0	30.9	36.1	63.7
B-0.5-3	0.5	36.1	20.6	85.1
B-0.5-4	0.5	41.3	20.6	74.8
B-1.0-5	1.0	51.6	25.8	93.2
B-1.0-6	1.0	46.4	20.6	90.3
B-1.5-7	1.5	46.4	30.9	100.6
B-1.5-8	1.5	51.6	30.9	98.0

A or B designates the beam group with  $f_c=36.7\text{MPa}$  and  $f_c=18.9\text{MPa}$ , respectively.





**Fig. 3.89** Cracking patterns in investigated beams (the values next to the crack represent the number of loading steps, the vertical dashed lines show the zone where the stirrups were located) (Juarez et al. 2007)

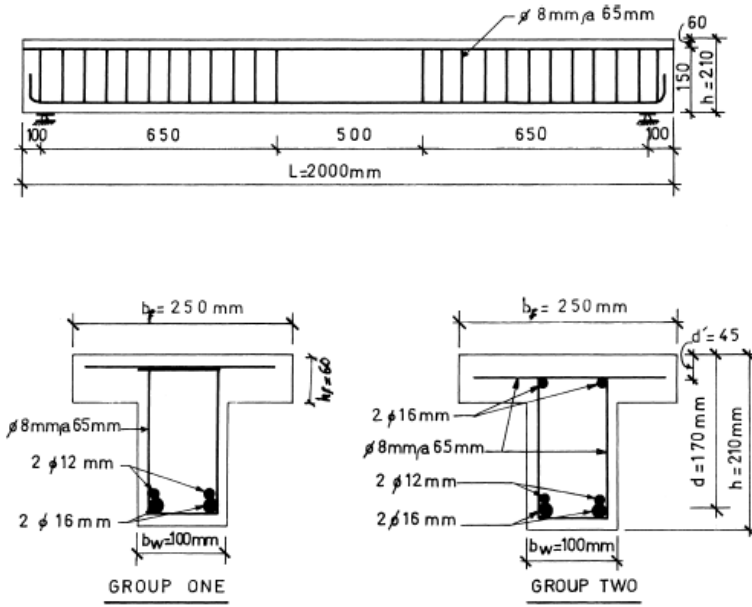


Fig. 3.90 Dimensions and reinforcement details (Abdul-Ahad and Aziz 1999)

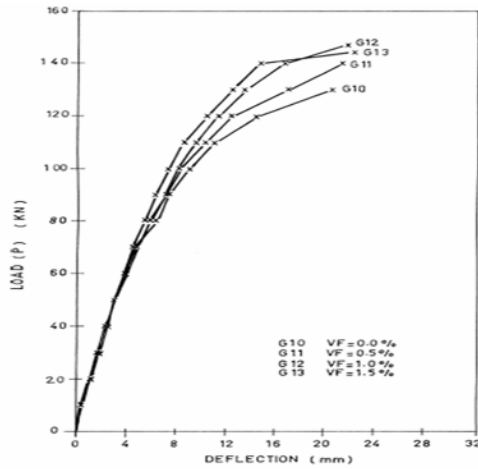
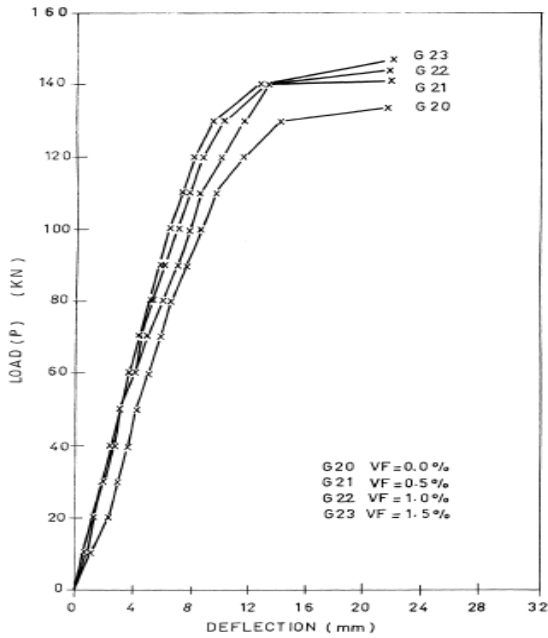


Fig. 3.91 Load-deflection relationship for group one (Abdul-Ahad and Aziz 1999)



**Fig. 3.92** Load-deflection relationship for group two (Abdul-Ahad and Aziz 1999)

A total of five normal-strength (N1–N5) and five high-strength slab specimens (H1–H5), with and without steel fibres were fabricated and tested under combinations of gravity and lateral loads. Two types of Dramix hooked steel fibres with volumetric percentages of 0.5% and 1.0% were used. The first type of fibres designated as F1, had the aspect ratio of 60 (30 mm in length and 0.5 mm diameter). The second type was designated as F2 with the aspect ratio of 75 (60 mm in length and 0.8 mm diameter). The yield strength of F1 and F2 fibres were 1172 MPa and 1100 MPa, respectively. Two sizes of reinforcing bars having diameters of 10 mm and 14 mm were used. Steel reinforcing bars had the yield strength of 468 MPa and yield strain of about 2240 micro-strain.

Ten slab-column connections, simply supported 150 mm thick and 1.5 m×1.5 m square slabs with 250 mm×250 mm column cross-sections and 650 mm height both above and below the slab were investigated (Fig.3.94).

Various material properties of the fresh and hardened concrete mixes for both normal- and high-strength slab specimens were obtained at different ages (Tab.3.48). The compressive strength of concrete was little influenced by steel fibre addition. An average increase of about 11% and 6% was observed with addition of 1.0% steel fibres by volume for normal- and high-strength concrete, respectively. Corresponding average increases of 25% and 33% were found for the splitting tensile strength, and 20% and 60% for the flexural strength, respectively.

**Table 3.45** Results of tested beams (Abdul-Ahad and Aziz 1999)

Beam nr. Fibre content [%]	Load [kN]		Mid-span deflection [mm]		Uniaxial compressive strength [MPa]	Maximum bending moment [kNm]
	First crack	Ultimate load	First crack	Ultimate load		
Group 1						
G10 (0.0%)	19.3	130.0	13	20.2	21.3	42.5
G11 (0.5%)	19.7	140.0	1.1	20.1	21.4	45.5
G12 (1.0%)	20.30	146.8	1.1	21.2	21.8	47.7
G13 (1.5%)	20.70	144.5	0.9	21.7	22.0	47.0
Group 2						
G20 (0.0%)	18.4	133.4	1.4	21.3	17.3	43.4
G21 (0.5%)	18,5	141.1	1.3	21.7	17.7	45.8
G22 (1.0%)	18.8	143.8	1.1	21.4	18.2	46.7
G23 (1.5%)	19.0	147.0	1.1	21.7	18.8	47.8

Two specimens were cast without steel fibres and subjected to pure concentrated gravity load (N1 and H1), and two were subjected to a pure unbalanced lateral moment until failure (N2 and H2). Specimens (N3, N4, and N5) and (H3, H4, and H5) were cast with 0.5% F1 steel fibres, 1.0% F1 fibres and 1.0% F2 fibres, respectively, all of which were subjected to a specified lateral moment and an increasing gravity load until failure took place. All test results are given in Tabs.3.49-3.52 and shown in Figs.3.95–3.100.

Increasing the percentage of fibres, having aspect ratio of 60, from 0.5 to 1.0 increased the ultimate load, ultimate deflection, ultimate rotation, initial stiffness, displacement ductility, and rotational ductility, by 17%, 26%, 57%, 20%, 30%, and 8%, respectively, for specimens constructed with normal-strength concrete and subjected to gravity load and moments. The corresponding increases for high-strength specimens were 5%, 8%, 25%, 16%, 34%, and 9%, respectively.

**Table 3.46** Test beam characteristics (Furlan and de Hanai 1999)

Beam	Fibre volume and type (P – polyp., S – steel)	Prestress	Geometric shear reinforcement ratio	Stirrup spacing [mm]	Shear reinforcement [cm <sup>2</sup> /m]
V1	-	-	0.225	200	0.9
V2	0.5%	-	0.225	200	0.9
V3	1% S	-	0.225	200	0.9
V4		+	0.225	200	0.9
V5	0.5%	+	0.225	200	0.9
V6	1% S	+	0.225	200	0.9
V7		+	0	-	-
V8	0.5%	+	0	-	-
V9	1% S	+	0.162	280	0.65

The use of steel fibre with a higher aspect ratio of 75 provided a better performance than that with a lower aspect ratio of 60 in terms of the ultimate load, ultimate deflection, rotation ductility, energy absorption, and initial stiffness. However, the fibres with a larger aspect ratio needed better technique during mixing to avoid balling of fibres and to ensure a homogeneous distribution in the concrete mix.

The stiffness degradation was reduced for both normal and high-strength concrete slab specimens due to the addition of steel fibres, which indicated an increase in ductility.

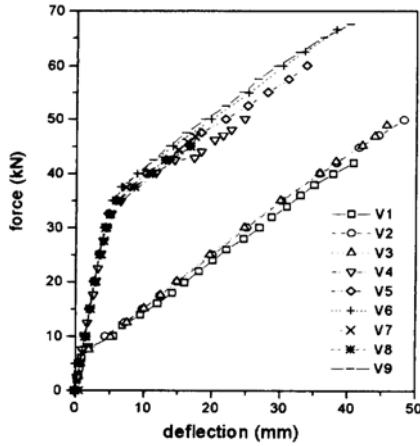
For specimens constructed with high-strength concrete, the ultimate shear strength increased by 7–21% as compared with specimens constructed with normal-strength concrete.

The ultimate deflections of high-strength specimens were larger than those of normal strength specimens with a generally longer deflection plateau before failure.

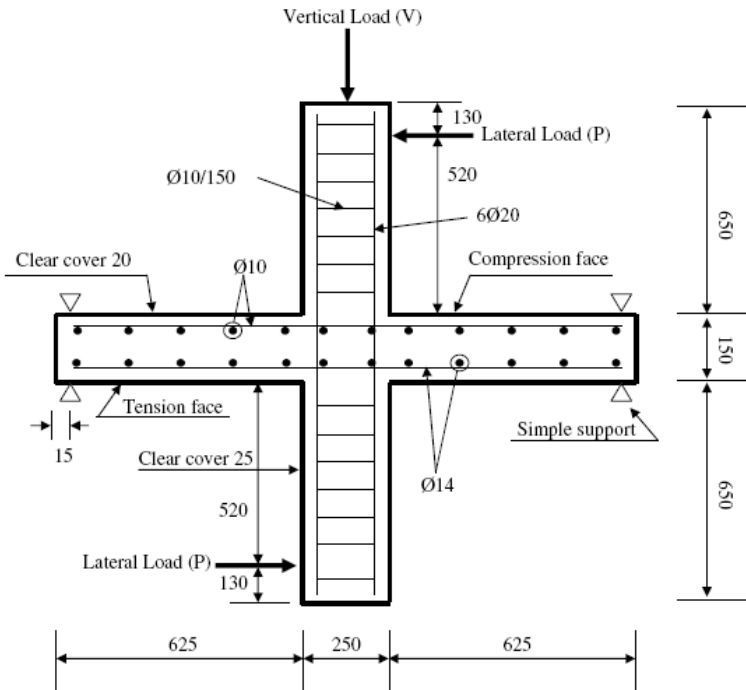
The displacement and rotation ductility ratios for high strength specimens were larger than those for normal strength by 11–64% for displacement ductility and 106–123% for rotation ductility. Their corresponding energy absorptions due to deflection and rotation were also larger by 48–150% and 93–246%, respectively.

**Table 3.47** Beam parameters at failure (Furlan and de Hanai 1999)

Beam	Uniaxial Compressive strength [MPa]	Splitting tensile strength [MPa]	Ultimate shear force $V_{max}$ [kN]
V1	48.5	3.1	42
V2	37.4	2.1	50
V3	52.8	3.6	50
V4	57.2	3.0	63.5
V5	52.1	3.2	73.5
V6	59.1	3.5	71.5
V7	52.1	2.2	47
V8	44.9	3.1	45
V9	52.3	3.4	72.5



**Fig. 3.93** Load-deflection curves in tests by Furlan and de Hanai (1999)

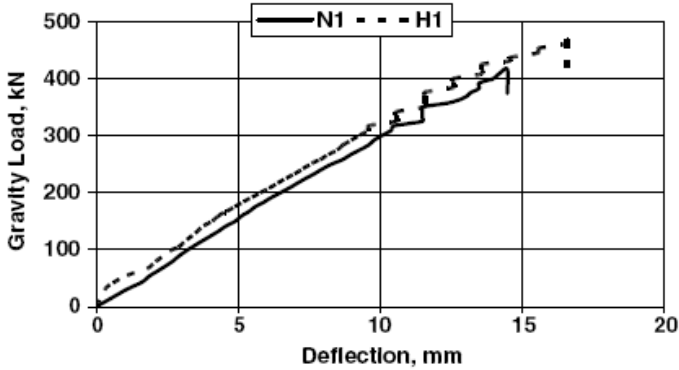


**Fig. 3.94** Cross-section of the slab-column connections (dimensions in mm) (Smadi and Bani Yasin 2000)

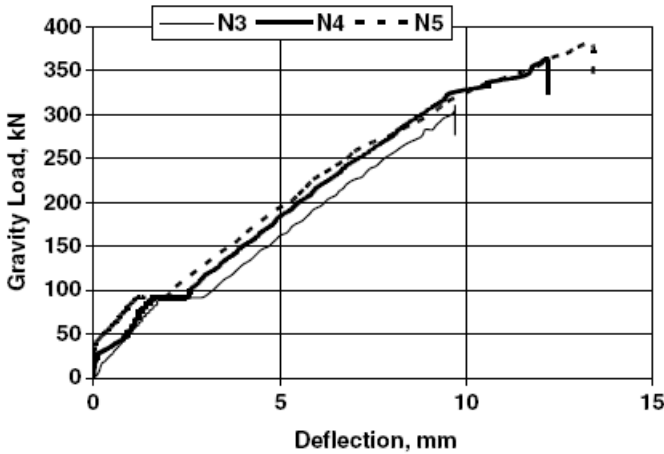
**Table 3.48** Mechanical concrete properties (Smadi and Bani Yasin 2000)

Series type, specimen size	% fibre and type	Cube compressive strength [MPa]		Splitting cylinder strength [MPa]
		7 days	28 days	
Normal strength				
N1	0	21.2	30.2	2.55
N2	0	21.7	30.7	2.49
N3	0.5 F1	23.0	32.2	2.95
N4	1.0 F1	23.5	34.1	3.20
N5	1.0 F2	23.4	33.6	3.70
High strength				
H1	0	49.9	65.7	5.51
H2	0	49.3	68.2	5.84
H3	0.5 F1	40.8	70.3	6.23
H4	1.0 F1	51.2	72.0	7.33
H5	1.0 F2	51.1	71.3	7.56





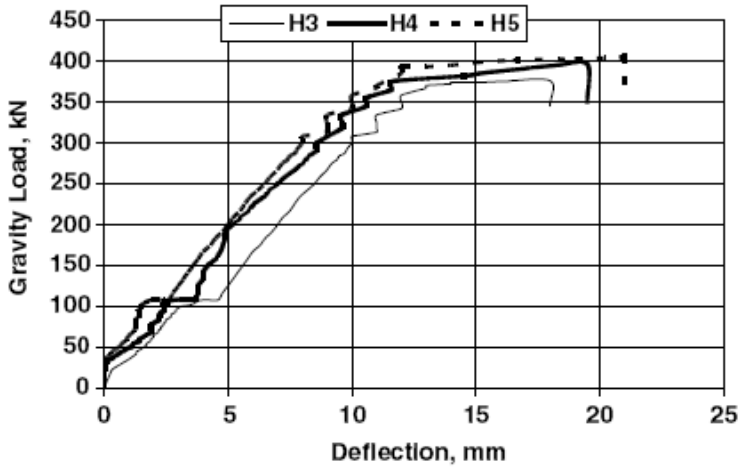
**Fig. 3.95** Load–deflection relationship for specimens N1 ( $f_c=35.6$  MPa) and H1 ( $f_c=72.6$  MPa) (gravity load only) (Smadi and Bani Yasin 2000)



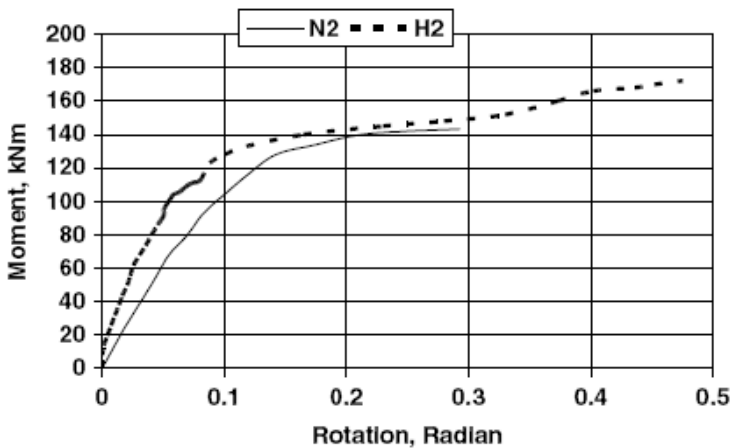
**Fig. 3.96** Load–deflection relationship for specimens N3 (0.5% F1,  $M=98.24$  kNm), N4 (1.0% F1,  $M=98.24$  kNm), and N5 (1.0% F2,  $M=101.15$  kNm) (Smadi and Bani Yasin 2000)

The cracking pattern of specimens under gravity load and moment was characterized by tangential cracks formed on a concrete tension surface on the tension side of the applied moment, and a few radial cracks formed on a compression side of the applied moment. For specimens constructed with high-strength concrete and subjected to unbalanced moment, cracks were observed to be fewer in number and narrower in width than those of normal-strength specimens. For concrete slabs without steel fibres, the cracks were wide and

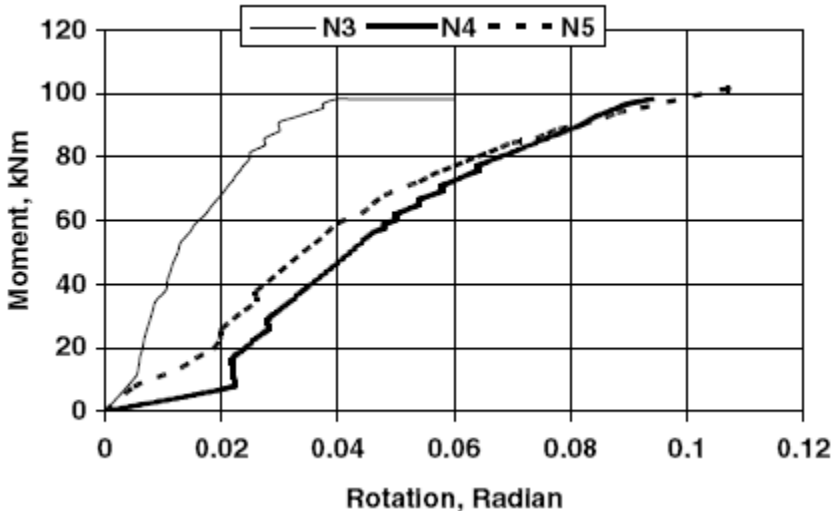
tended to branch off, whereas, in the case of slabs with steel fibres, the cracks were finer. Furthermore, the fibres restrained a propagation rate of diagonal cracks by bridging between each part of cracks. As the ratio of steel fibres increased, the number and width of cracks decreased, and ductility increased.



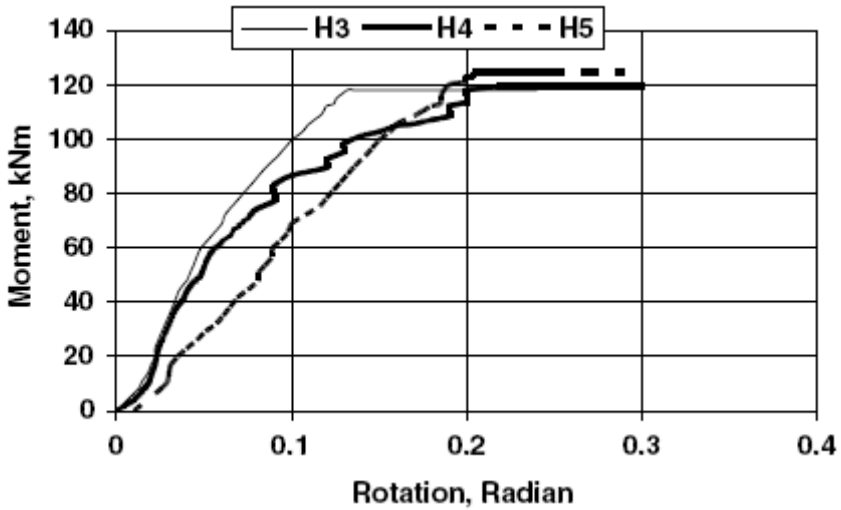
**Fig. 3.97** Load–deflection relationship for specimens H3 (0.5% F1,  $M=118.05$  kNm), H4 (1.0% F1,  $M=119.34$  kNm), and H5 (1.0% F2,  $M=124.25$  kNm) (Smadi and Bani Yasin 2000)



**Fig. 3.98** Moment–rotation relationship for specimens N2 and H2 (lateral load only) (Smadi and Bani Yasin 2000)



**Fig. 3.99** Moment–rotation relationship for specimens N3 (0.5% F1,  $M=98.24$  kNm), N4 (1.0% F1,  $M=98.24$  kNm), and N5 (1.0% F2,  $M=101.15$  kNm) (Smadi and Bani Yasin 2000)



**Fig. 3.100** Moment–rotation relationship for specimens H3 (0.5% F1,  $M=118.05$  kNm), H4 (1.0% F1,  $M=119.34$  kNm), and H5 (1.0% F2,  $M=124.25$  kNm) (Smadi and Bani Yasin 2000)

**Table 3.49** Strength and deformation measurements at yielding (Smadi and Bani Yasin 2000)

Specimen nr.	Shear force [kN]	Moment [kNm]	Deflection [mm]	Rotation [rad]
N1	252	-	7.8	-
N2	83	48	0.3	0.55
N3	134	98	3	0.009
N4	91.5	8	2.9	0.013
N5	201	29	3.0	0.014
H1	283	-	8.1	-
H2	96	80	0.7	0.04
H3	92	7	3.4	0.02
H4	192	29	3.6	0.02
H5	215	32	4.0	0.02

### Experiments by Foster and Attard (2001)

High-strength concrete has been used in many lower story columns of high-rise buildings, as well as low-rise and mid-rise buildings, bridges, and foundation piles. High-strength concrete (HSC) outperforms conventional strength concrete in terms of strength, durability, and modulus of elasticity as well as in many other material properties. However, the advantages of using HSC on columns predominantly loaded in compression are offset by what has been termed “early cover spalling” (Foster and Attard 1997). The load at which cover spalling begins is a consequence of the placement of steel ties within the column and is independent of the concrete strength. The reasons for early cover spalling not being observed in earlier studies on conventional strength concrete was due to the effect being disguised by the increase in strength due to confinement and by normal experimental variability. The event only became noticeable in the experimental data when HSC columns were tested with conventional tie detailing

arrangements, giving relatively lower increases in the columns core strength due to confinement. Previous research has shown that increases in the strength and ductility of conventional strength columns can be significantly improved by providing an effectively confined core. The increase in strength and ductility is a function of the concrete cover, concrete strength, distribution of longitudinal reinforcement and the configuration, yield strength, and spacing of the tie or spiral reinforcement. In tests on concentrically loaded HSC columns the cover concrete spalled away from the section at a load lower than the axial load capacity calculated using current building codes. After separation of the cover concrete from the section, the load dropped by 10–15%.

**Table 3.50** Strength and deformation measurements at ultimate (Smadi and Bani Yasin 2000)

Specimen nr.	Shear force [kN]	Moment [kNm]	Deflection [mm]	Rotation [rad]
N1	416	-	14.5	-
N2	83	144	1.3	0.293
N3	310	98	9.7	0.06
N4	362	98	12.2	0.094
N5	380	101	13.4	0.106
H1	468	-	16.6	-
H2	95	172	3.7	0.475
H3	376	118	18.0	0.24
H4	396	119	19.5	0.3
H5	408	124	21.0	0.29

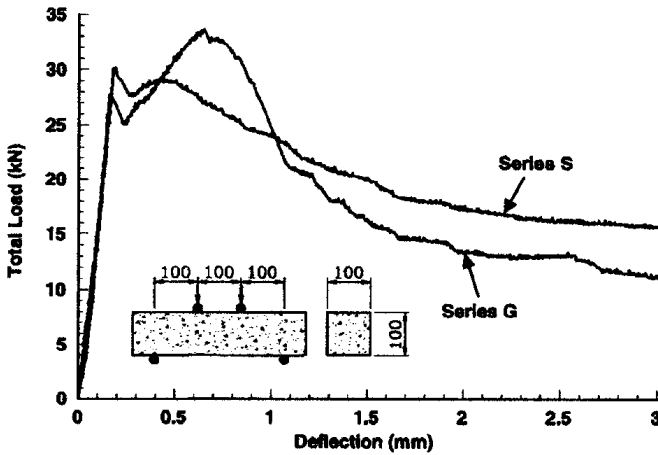
21 eccentrically loaded HSC columns were tested to study the effect of adding steel fibres into concrete. On the strength and ductility of HSC columns, of interest is the ability of the fibre reinforcement to prevent the cover spalling away from the section and to assess improvements in ductility afforded by steel fibres.

**Table 3.51** First crack load, maximum strains and modes of failure (Smadi and Bani Yasin 2000)

Specimen nr,	First crack load [kN]	Maximum steel strain (micro-strain)	Maximum concrete strain (micro-strain)	Mode of failure
N1	70.6	4800	-2400	pure punching
N2	64.9	8600	-3400	ductile punching
N3	74.7	13000	-1100	ductile punching
N4	80.2	24000	-1500	flexure
N5	78.2	25000	-3200	ductile punching
H1	79.3	6000	-3500	ductile punching
H2	82.1	11000	-3500	flexure
H3	90	16000	-2600	ductile punching
H4	94.3	29000	-3900	flexure
H5	91.3	31000	-4100	flexure

Twenty-one columns cast with high-strength fibre-reinforced concrete were tested in three series. The series A consisted of nine 155 mm square columns and the series G and S consisted of 12 200 mm square columns. The test specimens were identified by the percentage of longitudinal reinforcement, the concrete strength, the initial loading eccentricity, tie spacing, and a series identifier. For example, specimen 4HF20-60A had approximately 4% of longitudinal reinforcement, was cast with a high-strength fibre concrete, had an initial loading eccentricity of 20 mm, had a center-to-center tie spacing of 60 mm, and was tested in Series A. Details of the reinforcement arrangements and specimen dimensions are given in Fig.3.101. The cover for all specimens was 15 mm. The eccentrically loaded specimens of the series G and S were 200 mm square over the full 900 mm test region. The concentrically loaded specimens of the series G and S (specimens





**Fig. 3.102** Flexural strength of fibre concrete used in series G and S (Foster and Attard 2001)

All column specimens contained eight 12 mm diameter longitudinal bars (Y-grade) giving reinforcement ratios of 3.8% for the series A and 2.3% for series G and S. The tie arrangements for the series A consisted of 4 mm diameter bars (W-grade) spaced at 30, 60 or 120 mm centers, respectively. In the series A, full anchorage was provided to ties by welding along the lap. For the series G and S, a diamond arrangement was used for steel ties with 6 mm (W-grade) bars spaced at 50 or 100 mm centers and with 1357 end hooks used for stress development.

The experimental results are given in Figs.3.103 and 3.104 and in Tab.3.52.

The plots show that the fibre columns were able to maintain a high load capacity with increasing strain. A drop in the postpeak load for the columns with large initial eccentricities was primarily due to the second-order effects rather than due to loss of cover or confinement. A little strain development in the ties occurred until the columns were subjected to relatively high axial loads and indicated that micro-cracking of the core was controlled by fibres. In all of the specimens, the cover remained intact throughout the test, well beyond the peak load.

The test results show that when 2% (by weight) of steel fibres were introduced into the concrete mix, the cover did not spall away from the section. The columns showed a superior performance to comparable specimens cast without fibres in the mix design, particularly for post-failure ductility.



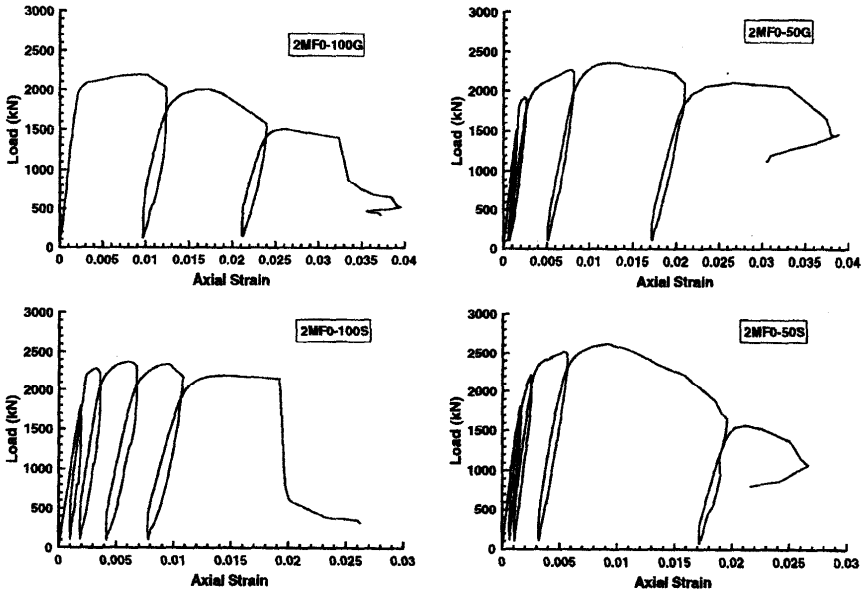


Fig. 3.103 Load versus axial strain for axially loaded columns (series G and S) (Foster and Attard 2001)

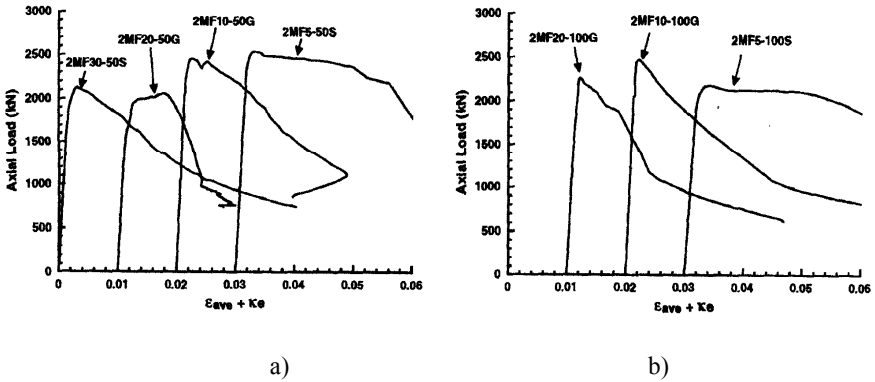


Fig. 3.104 Load versus axial strain and curvature times eccentricity for eccentrically loaded columns, specimens with tie spacing of (series G and S): a) 50 mm; and b) 100 mm (Foster and Attard 2001)

**Experiments by Campione et al. (2005a)**

The focus of the experimental research was the flexural behaviour of reinforced concrete corbels. 12 corbels having the geometry and steel reinforcement details shown in Fig.3.105 were tested in flexure. The specimens, two for each different series investigated, were made from a) plain concrete, b) fibre reinforced concrete (FRC) with hooked steel fibre 30/0.5 mm at 1% by volume percentage, c) concrete reinforced with two longitudinal bars (main bars) having a diameter of 10 mm and placed at the bottom of the beam, d) reinforced concrete with main bars and four horizontal stirrups having a diameter of 6 mm, e) reinforced concrete with main bars and externally wrapped with one ply of flexible carbon fibre reinforced sheet (CFRP) having a thickness of 0.165 mm and f) fibrous concrete with main bars (Tab.3.53).

Compressive and indirect tensile tests on cylinder specimens were carried out (Figs.3.106 and 3.107).

The addition of fibres did not produce variation in maximum uniaxial compressive strength but significantly increased the maximum strain (measured at the peak load) and improved ductility of the material, showing a less marked slope of a softening branch and more residual strength. Fibres improved the maximum splitting tensile strength and corresponding strain and produced very ductile post-peak behaviour characterized by the residual strength very close to the maximum value.

In the case of plain concrete corbels (Fig.3.108), sudden and brittle failure was observed after the first crack appeared and the ultimate load and first cracking load were practically the same. In the case of FRC corbels, a significant increase in the maximum strength was observed and the failure mode was characterized by a flexural failure mode; moreover, more ductile behaviour with high deflections and with significant residual strength values was observed.

For corbels reinforced with main steel bars and with and without transverse stirrups, shear failure was observed (Fig.3.109). When stirrups were used, more cracks were formed and they were finer and the ultimate strength measured was higher than that of corbels with main steel only. After the peak load was reached, the ductile behaviour was observed.

The resistant mechanism involved in the wrapped corbels (Fig.3.110) was also characterized by interaction phenomena at the interface between the concrete surface and the CFRP sheet. After the principal cracks in shear opened, debonding of sheet occurred at the interface with concrete. The failure mechanism observed experimentally in CFRP was in tension and in debonding.

In the case of corbels in FRC with longitudinal steel bars (Fig.3.111), the complete flexural capacity was reached and the ductile behaviour was observed.

Tab.3.54 shows the results in terms of the first cracking  $P_f$ , maximum load  $P_{max}$ , residual load  $P_u$  and the corresponding deflections.

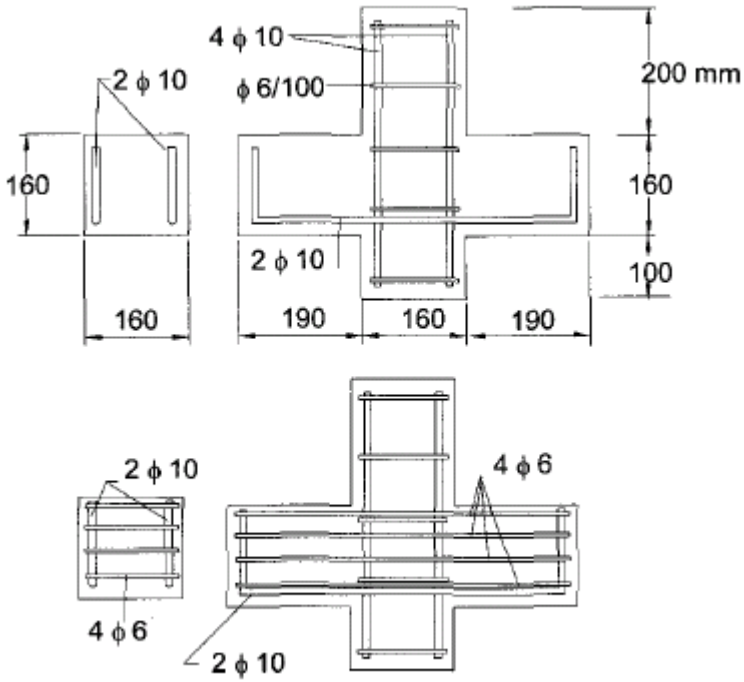
**Table 3.52** Failure loads and loading eccentricities (Foster and Attard 2001)

Specimen	Maximum axial load [kN]	Initial eccentricity [mm]	Total eccentricity at peak load [mm]	Moment at peak axial load [kNm]
4HF0-30A 2	2106	0	1.4	3
4HF0-60A	2021	0	1.9	4
4HF8-30A	1986	8	11.9	21
4HF8-60A	1648	8	13.0	24
4HF8-120A	1962	8	11.1	22
4HF20-30A	1610	20	26.3	41
4HF20-60A	1707	20	26.2	41
4HF50-30A	925	50	59.5	55
4HF50-60A	964	50	58.4	56
2MF0-50S	2612	0	2.4	6
2MF0-100S	2367	0	4.6	11
2MF5-50S	2534	5	6.9	17
2MF5-100S	2184	5	7.9	17
2MF30-50S	2123	30	38.7	82
2MF30-100S	1998	30	35.8	72
2MF0-50G	2356	0	2.1	5
2MF0-100G	2188	0	4.5	10
2MF10-50G	2450	10	12.5	30
2MF10-100G	2469	10	13.9	34
2MF20-50S	2058	20	31.9	66
2MF20-100G	2262	20	25.5	58

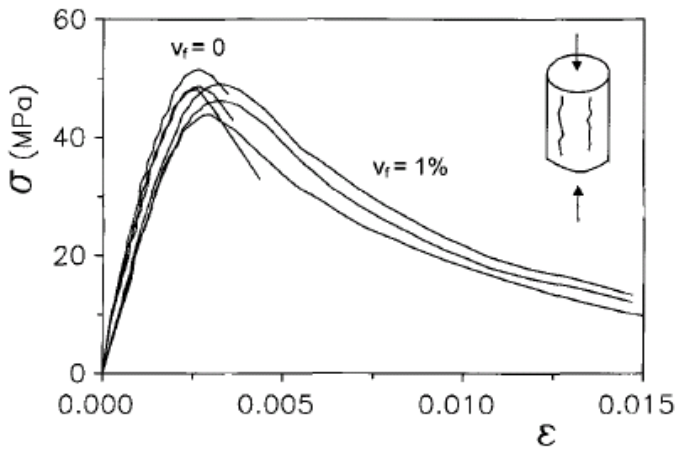
**Table 3.53** Details of corbels (Campione et al. 2005a)

Corbel type	Main bars [mm]	Transvers bars [mm]	Fibre content [%]	CFRP layer
1				
2			1.0	
3	2×10			
4	2×10	4×6		
5	2×10		1.0	
6	2×1			1

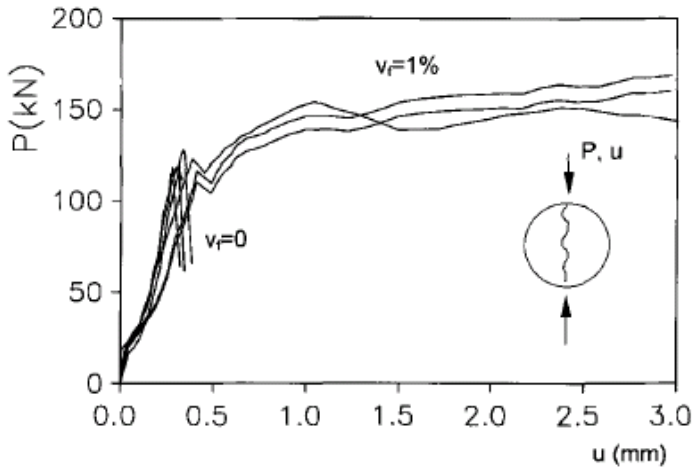
Fig.3.112 depicts the evolution of the crack pattern. In the case of corbels with main steel, the rupture was related always to the brittle failure of a compressed zone arising after the yielding of steel bars occurred. When the CFRP was used, a similar mode of failure was observed but the compressive rupture was consequent to the failure of CFRP wraps in tension. In the presence of transverse steel reinforcements, a more ductile behaviour was observed, but the flexural capacity was not completely achieved. In the case of FRC, the ductile balanced flexural failure was observed.



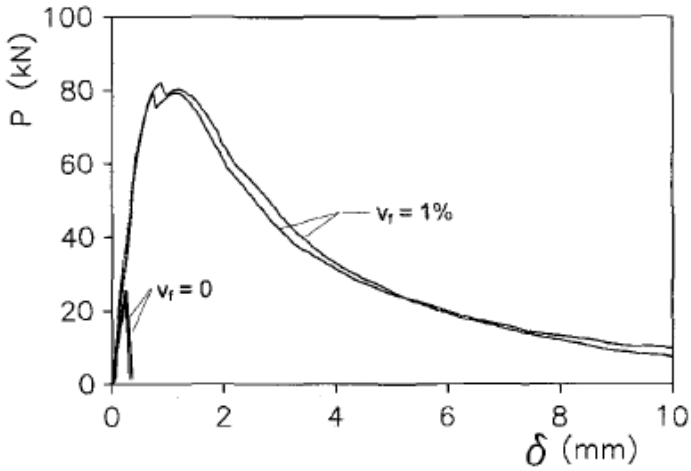
**Fig. 3.105** Geometry of corbels and details of steel reinforcement (Campione et al. 2005a)



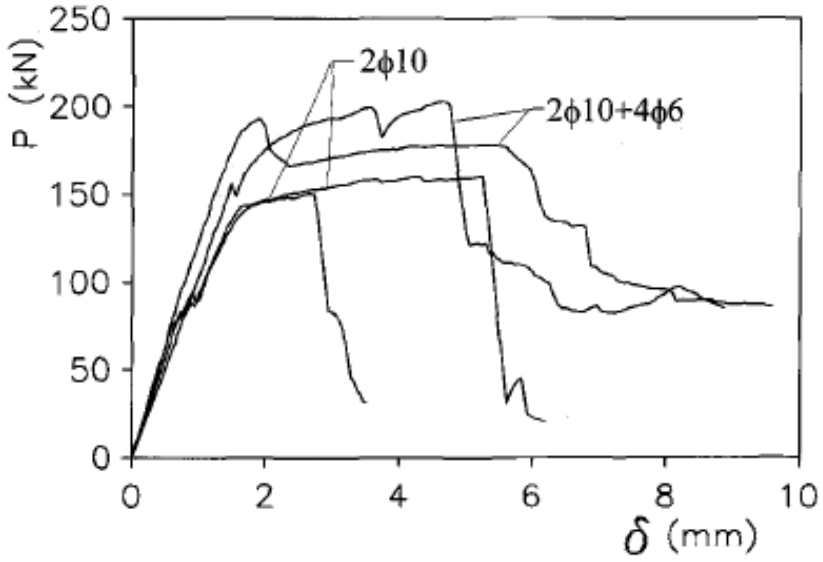
**Fig. 3.106** Stress-strain curves for concrete in compression (Campione et al. 2005a)



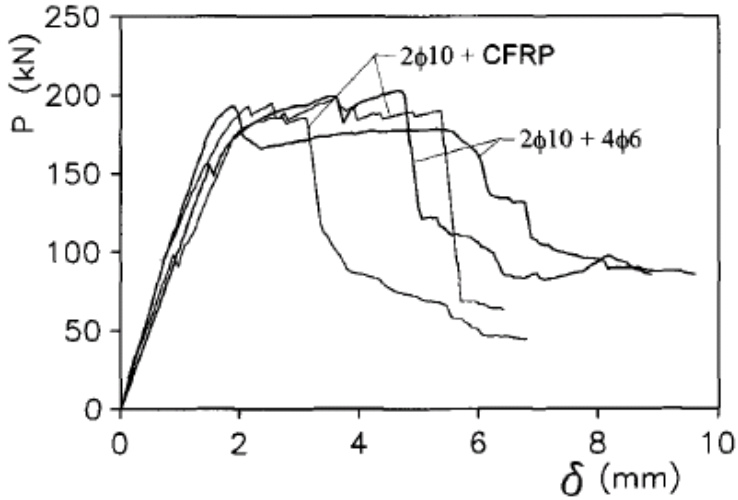
**Fig. 3.107** Load-displacement curves for concrete in tension (Campione et al. 2005a)



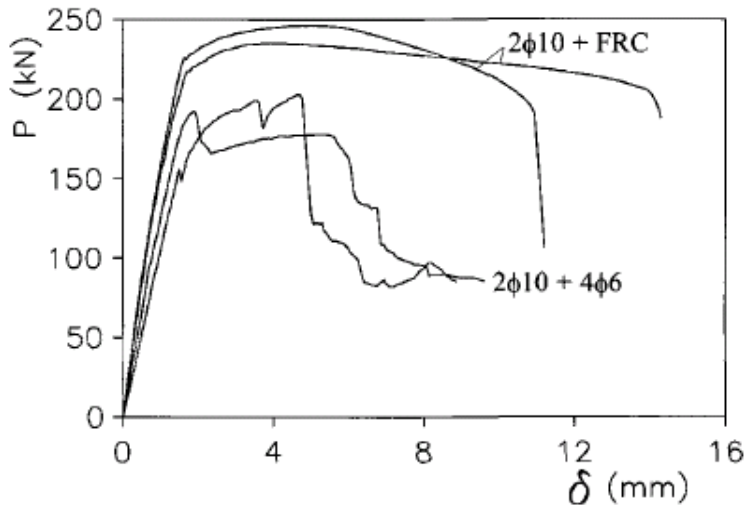
**Fig. 3.108** Load-deflection curves for corbels with and without fibres (without steel reinforcement) (Campione et al. 2005a)



**Fig. 3.109** Load-deflection curves for steel reinforced concrete corbels without fibres (Campione et al. 2005a)



**Fig. 3.110** Load-deflection curves for corbels with steel reinforcement and carbon fibre reinforced sheet CFRP (without fibres) (Campione et al. 2005a)



**Fig.3. 111** Load-deflection curves for corbels with steel reinforcements and fibre reinforced concrete FRC (Campione et al. 2005a)

**Table 3.54** Results of tests (Campione et al. 2005a)

Reinforcement of corbel	$P_f$ [kN]	$P_{max}$ [kN]	$P_u$ [kN]	$\delta_{max}$ [mm]	$\delta_u$ [mm]
2φ 10	64.5	155.2	25.95	3.93	4.27
2φ 10 + 4φ 6	60.50	197.65	85.45	3.36	5.40
2φ 10 + CFRP		192.20	93.12	3.35	4.52
2φ 10 + FRC	104.0	240.75	147.35	4.60	12.75

FRC - fibre reinforced concrete, CFRP - carbon fibre reinforced sheet.



### Experiments by Campione et al. (2005b)

The aim of the research was to investigate a local bond-slip behavior of deformed steel bars embedded in lightweight fibrous concrete under monotonic and cyclic reversal loads. The parameters investigated were: the shape and dimensions of concrete specimens, the embedded length, the percentages of fibers, and the confinement pressure acting perpendicular to the slippage direction of the bar.

Two different specimens, having geometry and dimensions shown in Fig.3.113, were used for the bond-slip tests. Squat prismatic specimens with dimensions  $170 \times 170 \times 210 \text{ mm}^3$  and slender specimens, having dimensions  $330 \times 84 \times 300 \text{ mm}^3$ , were prepared. For the squat specimen, the steel bar was embedded in a vertical position and parallel to the direction of casting, while in a slender prismatic specimen, the steel bar was embedded in a horizontal position and perpendicular to the direction of casting. The dimensions assumed for a slender concrete specimen in relation to the position of steel bars allowed one to produce a split failure type, while in the case of squat specimens, the position of steel bars in relation with the dimension of the specimen allowed one to reproduce a pull-out failure type.

To prepare the fibrous concrete, Dramix type hooked steel fibers having length  $l_f = 30 \text{ mm}$  and diameter  $\phi = 0.5 \text{ mm}$  (with aspect ratio 60) randomly distributed in the fresh concrete mixture were used. The minimum nominal tensile strength of the fibres was equal to  $1115 \text{ N/mm}^2$ . The percentage of fibers  $V_f$  by volume of 0.5%, 1% and 2% corresponded to 0.40, 0.80 and  $1.60 \text{ kN/m}^3$ .

The experimental results relative to the compressive tests, both under monotonic and cyclic loads, showed (Fig.3.114) that the presence of fibres increased lightly the maximum strength values, while it ensured better performances with respect to plain concrete (very brittle because of the nature of lightweight aggregates), especially referring to the post-peak strength and ductility resources. In tension (Fig.3.115) for both monotonic and cyclic loads, the presence of fibres in concrete ensured a better performance with respect to plain lightweight concrete both in terms of the maximum and residual strength. In particular a split tensile stress of  $2.29 \text{ MPa}$  was obtained for plain concrete with increasing up to  $4.33 \text{ MPa}$  in the case of fibrous concrete with  $V_f = 2\%$ .

Fig.3.116 shows a comparison between the bond stress–slip curves referring to pull-out tests carried out on squat and slender specimens of plain concrete for the embedded length of  $5d_b$ . The initial stiffness of the bond stress–slip curves decreased gradually from its initial large value (corresponding to chemical adhesion) to zero when approaching the maximum bond strength corresponding to a slip value of about  $1.25 \text{ mm}$  at which splitting failure with crushing cracks occurred. For further increasing slip values, the bond resistance decreased slowly and almost linearly until it approached a slip of  $6\text{--}7 \text{ mm}$ ; this value corresponded to the distance between the drowned ribbings of the embedded deformed bar. For greater slip values ( $7\text{--}10 \text{ mm}$ ) the resistance decreased very slowly and its value approached the frictional resistance

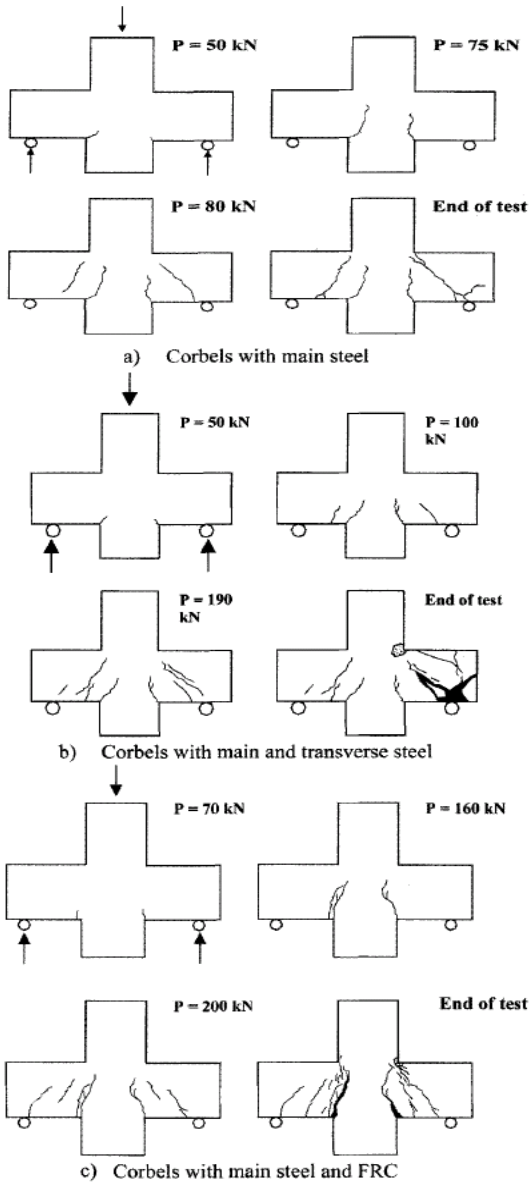
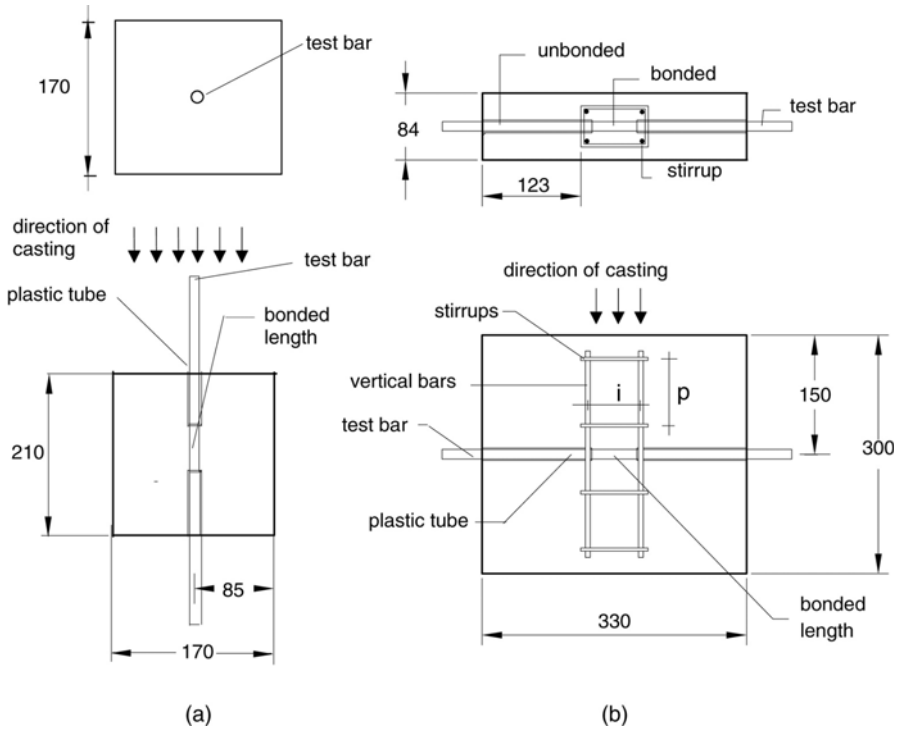


Fig. 3.112 Evolution of crack pattern for reinforced concrete (Campione et al. 2005a)

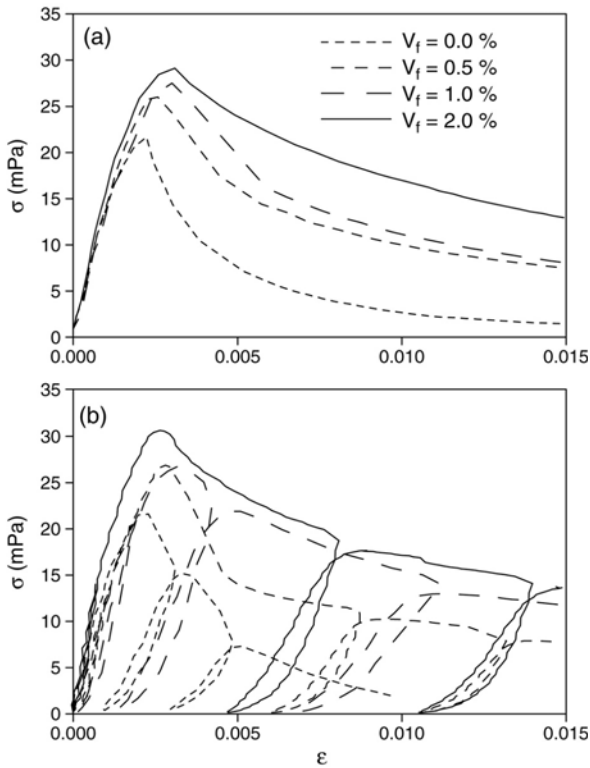


**Fig. 3.113** Geometry of test specimen: squat (a) and slender (b) (Campione et al. 2005b)

Fig.3.117 shows results relative to pull-out of longitudinal bars extracted by squat specimens with the variation in the content of fibres and for the fixed anchorage length of  $5d_b$ . From the trend of the curves it emerged that the overall behavior was quite the same as that observed for plain concrete, but the addition of fibres produced an increase in peak and residual frictional stresses and greater slippages at the peak stress and at the initial phase of the frictional behavior.

Fig.3.118 demonstrates that for slender specimens with the anchorage length of  $5d_b$ , characterized in the case of plain concrete by splitting failure, the addition of fibres did not produce a variation in the shape of the bond-slip curve, but determined an increase in the maximum strength from 8 MPa (without fibres) up to 12 MPa in the case of 1% by volume of fibres.

If the anchorage length increased (up to  $8d_b$ ), the extraction force increased and yielding of the longitudinal bar was very close as for plain concrete; the addition of fibres produced the steel yielding ensuring a better behaviour. The presence of the low confinement pressure slightly increased the maximum and residual strength with respect to specimens without confinement pressure.



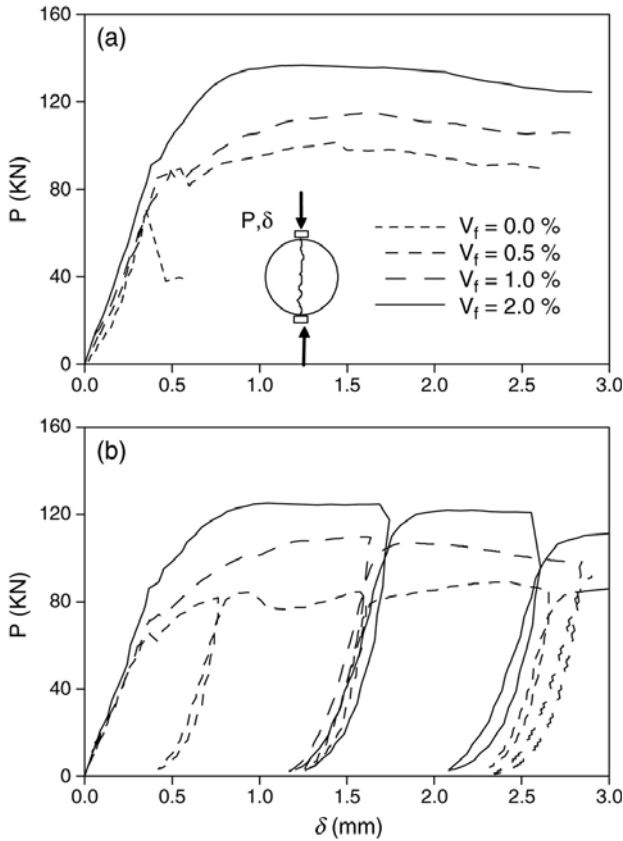
**Fig. 3.114** Stress–strain curves in compression: a) monotonic and b) cyclic (Campione et al. 2005b)

Fig.3.119 shows the cyclic stress–slip bond curves for squat specimens with the longitudinal bar embedded for  $5d_b$  and relative to the cases of plain and fibrous concrete. The envelope curves of cyclic loading approached the related monotonic curves. The unloading and reloading branches were linear.

### Experiments by Lohrmann (1999)

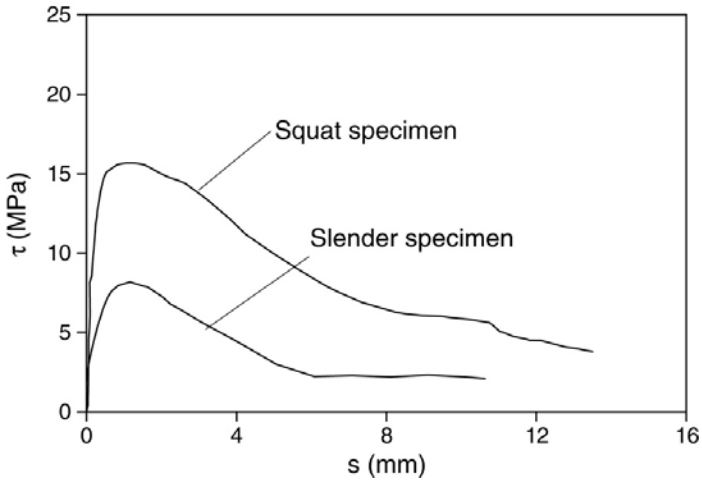
Four-point experiments were carried out with fibrous concrete beams including also longitudinal steel bars. In the first case, concrete with the maximum aggregate of 16 mm (N16) was used (the cube compressive strength was 38–41 MPa). In the second case, concrete included steel hooked fibres: Dramix 60/0.8 mm (1.2%) or steel straight fibres Wirex 40/0.6 mm (1.2%). Static, dynamic and impact tests were carried out. The dimensions of the beams were  $250 \times 250 \times 2800 \text{ mm}^3$  (the ratio

between span and height was 10)). The steel reinforcement included  $2\phi 8$  or  $2\phi 6$  at the top and  $2\phi 14$  ( $\rho=0.62\%$ ) or  $2\phi 8$  ( $\rho=0.2\%$ ) at the bottom). In turn, the shear reinforcement consisted of 24 stirrups  $\phi 6$  at distance of 100 mm and 150 mm. The impact tests were performed by means of the falling weight of 1080 kg from the height of 2.0 m-2.2 m.

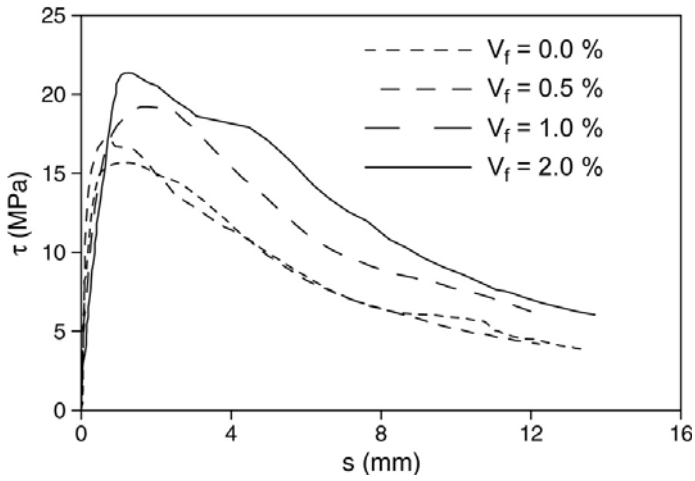


**Fig. 3.115** Load–displacement curves by split tests: a) monotonic and b) cyclic (Campione et al. 2005b)

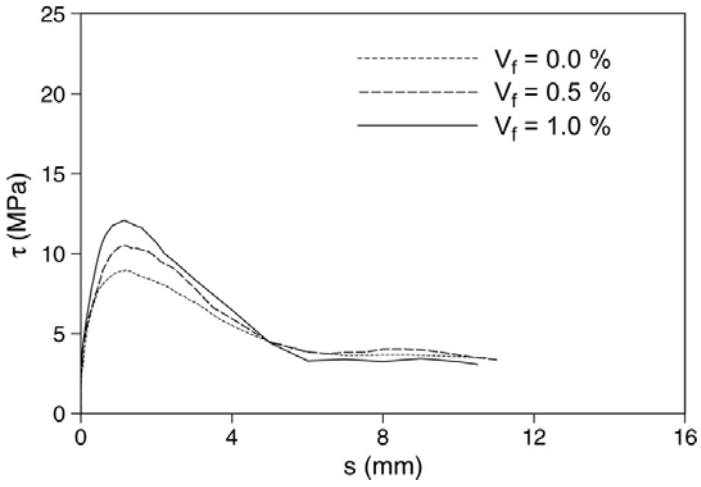
In experiments, the beam strength was higher for beams with steel fibres. Fig.3.120 demonstrates a positive effect of fibres during static experiments.



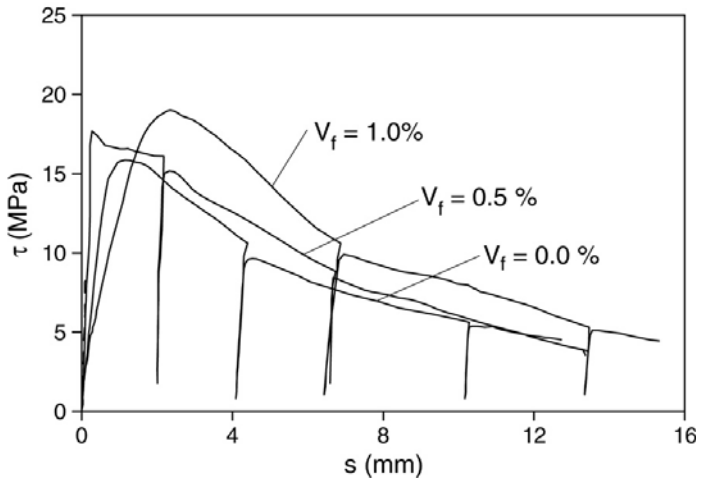
**Fig. 3.116** Bond stress–slip curves for plain lightweight concrete (Campione et al. 2005b)



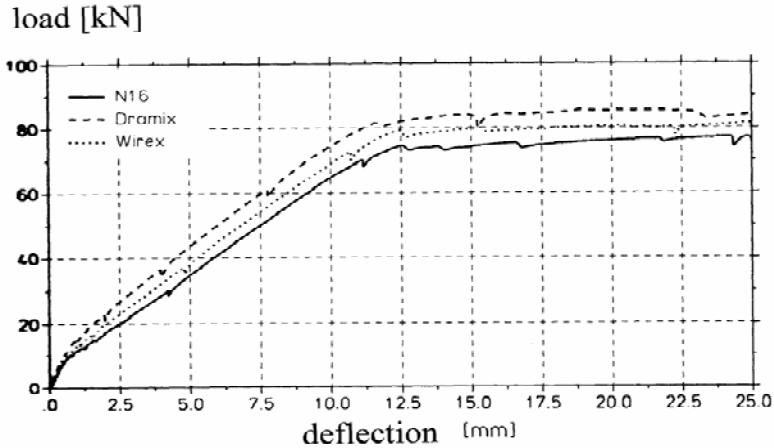
**Fig. 3.117** Bond stress–slip curves for squat fibrous specimens (Campione et al. 2005b)



**Fig. 3.118** Bond stress-slip curves for slender fibrous specimens (Campione et al. 2005b)



**Fig. 3.119** Cyclic tests on squat specimens



**Fig. 3.120** Static load-deflection curves: a) reinforced concrete beam (N16), a) reinforced concrete beam with Dramix fibre, c) a) reinforced concrete beam with Wirex fibre (Lohrmann 1999)

### 3.3 Conclusions

The following conclusions can be drawn from experimental results summarized in Sections 2 and 3.

The inclusion of steel fibres improves always the ductility (toughness) of concrete and reinforced concrete during all quasi-static and dynamic loading processes. In addition, the following properties are improved: flexural tensile strength, splitting tensile strength, first cracking strength, stiffness, toughness, durability, impact resistance, fatigue, wear strength, shock vibration resistance, freeze-thaw resistance, shrinkage and creep. Fibres limit the formation and growth of cracks by providing pinching forces at crack tips; fibres help in bridging the propagating cracks. However, concrete workability decreases, and concrete sorptivity and volumetric weight increase at the same time with a content increase of fibres. It is noticeable in the case of compression, wherein addition of fibres may not contribute to an increase of the strength due to a growth of voids. The degree of concrete improvement depends upon: size, shape, aspect ratio, volume fraction, orientation and surface characteristics of fibres, ratio between fibre length and maximum aggregate size, volume ratio between long and short fibres and concrete class. In particular, the effect of the fibre orientation is of a major importance dependent upon flow direction of concrete. Usually, both the strength and ductility of concrete and reinforced concrete specimens increase with increasing volume fraction and aspect ratio of fibres, fibre roughness and loading velocity, and increase with decreasing specimen size. The fibres hinder the crack



formation. The hooked fibres are more advantageous. Moreover, the positive effect of fibres is greater if they are inclined perpendicularly to the direction of cracks.

There exist a numerous number of experiments in particular in a quasi-static regime. However, the effect of the fibre orientation on the concrete strength and ductility has not been sufficiently studied. The same concerns a deterministic and stochastic size effect. In addition, the behavior of fibrous concrete and fibrous reinforced concrete under dynamic and impact loading needs further experimental studies.

## 4 Theoretical Models

**Abstract.** This chapter describes shortly theoretical models describing the behavior of fibrous concrete and the fracture process in plain and fibrous concrete. The models to simulate the behavior of fibrous concrete can be divided into analytical and numerical ones at macro- and meso-level.

Fracture process is a fundamental phenomenon in brittle materials (Bazant 2003). It is a major reason of damage in brittle materials under mechanical loading, contributing to a significant degradation of the material strength. It is highly complex due to a heterogeneous structure of brittle materials over many different length scales, changing e.g. in concrete from a few nanometers (hydrated cement) to the millimeters (aggregate particles). Therefore, the material heterogeneity should be taken into account when modeling the material behavior. At the meso-level, concrete can be considered as a three-phase material consisting of aggregate, cement matrix and interfacial transition zone ITZ (bond). A realistic description of a fracture process is of major importance to ensure safety of the structure and to optimize the behavior of material.

The phenomenon of propagation of a fracture process in brittle materials can be modelled with continuous and discrete models. Continuum models describing the mechanical behavior of concrete were formulated within, among others, nonlinear elasticity (Kompfner 1983, Liu et al. 1996, Palaniswamy and Shah, 1974), rate-independent plasticity (Mróz 1972, Pietruszczak et al. 1988, Menetrey and Willam 1995, Klisiński and Mróz, 1998, Bobiński and Tejchman 2004) damage theory (Dragon and Mróz 1979, di Prisco and Mazars 1996, Peerlings et al. 1998, Bobiński and Tejchman 2006a), endochronic theory (Bazant and Bhat 1976, Bazant and Shieh 1978), coupled damage and plasticity (de Borst et al. 1999, Ibrahimbegovic et al. 2003, Klisiński and Mróz 1988, Bobiński and Tejchman 2006b) and micro-plane theory (Bazant and Ozbolt 1990, Jirasek 1999). To model the thickness and spacing of strain localization properly, continuum models require an extension in the form of a characteristic length (de Borst et al. 1993). Such an extension can be done with strain gradient (Zbib and Aifantis 1989, Mühlhaus and Aifantis 1991, Peerlings et al. 1998, Chen et al. 2001, Pamin 2004), viscous (Neddleman 1988, Loret and Prevost 1990, Sluys 1992, Sluys and de Borst 1994, Lodygowski and Perzyna 1997) non-local (Bazant 1986, Pijaudier-Cabot and Bazant 1987, Chen 1999, Akkermann 2000, Bazant and Jirasek 2002, Bobiński and Tejchman 2004) and micro-polar terms (Mühlhaus 1989, Sluys 1992, Tejchman and Wu 1993, Tejchman 2008). Other numerical technique which also enables to remedy the drawbacks of a standard FE-method and to obtain

mesh-independent results during formation of cracks, is an approach allowing for a finite element formulation with a displacement discontinuity (Belytschko et al. 2001, Wells and Sluys 2001, Simone and Sluys 2004, Asferg et al. 2006) or an approach with cohesive elements representing cracks (Ortiz and Pandolfi 1999, Bobiński and Tejchman 2008). In turn, a continuous-discontinuous approach was proposed by Simo et al. (1993) and Moonen et al. (2008) which seems to be the most realistic. The enhanced continuum models were also used at meso-level of concrete (Gitman et al. 2008, Skarżyński and Tejchman 2009, 2010). Within discrete methods, the most popular ones are: classical particle DEM (Sakaguchi and Mühlhaus 1997, Donze et al. 1999, D'Addetta et al. 2002, Kozicki and Donze 2008), interface element models with constitutive laws based on non-linear fracture mechanics (Carol et al. 2001, Caballero et al. 2006) and lattice methods (Kawai 1978, Herrmann et al. 1989, Vervuurt et al. 1994, van Mier et al. 1995, Jirasek and Bazant 1995, Chung et al. 1996, Schlangen and Garboczi 1997, Lilliu and van Mier 2003, Cusatis et al. 2003, Vidya Sagar 2004, Bolander and Sukumar 2005, Yip et al. 2006, Kozicki and Tejchman 2007, 2008, Grassl and Jirasek 2008, Vorechovsky and Elias 2010). The lattice models are the simplest discrete models to simulate the development and propagation of fracture in multiphase particulate materials such as concrete consisting of a main crack with various branches, secondary cracks and micro-cracks. They allow a straightforward implementation of the material heterogeneity which is projected on a lattice and the corresponding properties are assigned to relevant lattice elements. They are composed of simple, one-dimensional mechanical elements connected on a set of nodal points that is either regularly or irregularly distributed in space. One primary justification for such models comes from a discontinuous structure of matter at a very small scale, where material can be regarded as a collection of particles held in equilibrium through forces of interaction.

In the case of lattice models, one can distinguish two main different types. In the first type model used to describe a fracture process in concrete or reinforced concrete (Vervuurt et al. 1994, van Mier et al. 1995, Schlangen and Garboczi 1997, Lilliu and van Mier 2003), each quasi-brittle material is discretized as a network of Bernoulli beams that transfer normal forces, shear forces and bending moments (Fig.4.1). Fracture is simulated by performing a linear elastic analysis up to failure under loading and removing a beam element that exceeds its tensile strength. Normal forces, shear forces and moments are calculated using a conventional simple beam theory. A special factor  $\alpha$  is used for varying the amount of bending. When this factor decreases, the compressive behavior changes from a brittle to a ductile one. The stiffness matrix is constructed for the entire lattice. The displacement vector is calculated similarly as in the conventional FEM by multiplication of the inverse global stiffness matrix with the load vector. The heterogeneity of the material is taken into account by assigning different strengths to beams (using a Gaussian or Weibull distribution) or by assuming random

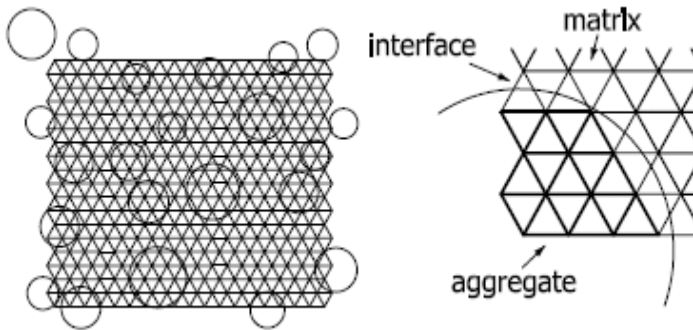
dimensions of beams and random geometry of the lattice mesh, or by mapping of different material properties to beams corresponding to the cement matrix, aggregate and interfacial transition zone (Fig.4.2) in the case of concrete. To obtain aggregate overlay in the lattice, a Fuller curve is usually chosen for the distribution of grains. The ratio between the beam height and beam length determines the Poisson's ratio. The beam length in concrete should be less than  $l_b < d_a^{min}/3$  (where  $d_a^{min}$  is the minimum aggregate diameter). The model can identify micro-cracking, crack branching, crack tortuosity and bridging which lead to a fracture process to be followed until complete failure (van Mier et al. 1995, Vidya Sagar 2004). It enables also to capture a deterministic size effect during tension (van Vliet 2000, Vidya Sagar, 2004). The advantages of this approach are simplicity and a direct insight in the fracture process on the level of the micro-structure. A complex crack patterning can be reproduced. Therein, a limited number of parameters are needed. By applying an elastic-purely brittle local fracture law at the particle level, global softening behavior is observed. The fracture process is realistically described, in particular, when the mode I failure prevails. The disadvantages of this model are the following: the results depend on the beam size and direction of loading, the response of the material is too brittle (due to the assumed brittleness of single beams), the compressed beam elements overlap each other and a big computational effort on the structure level is needed. The first disadvantage can be removed by assuming a heterogeneous structure (Schlangen and Garboczi 1997). In turn, the second drawback can be improved by 3D calculations and consideration of very small particles (Lilliu and van Mier 2003) which increase the amount of crack face bridging and the dissipated energy, and by applying a non-local approach in calculations of beam deformations (Schlangen and Garboczi 1997). In turn, the computational effort is significantly reduced by using a special version of a conjugate gradient solver (Schlangen and Garboczi 1997). In this algorithm, breaking an element and thus removing it from the lattice is a local effect, and the solution requires only a few iterations. To improve the lattice behavior in a compression regime, aggregate interlock needs to be considered.



**Fig. 4.1** Shear and normal forces and moments acting on the beam element (van Mier et al. 1995)

In the second type model (called particle model or non-linear plastic lattice model) (Jirasek and Bazant 1995, Cusatis et al. 2003, Tajima and Shirai 2006, Grassl and Jirasek 2008), lattice struts connecting adjacent particles transmit axial and shear forces and are not removed. The shear response of struts exhibits friction and cohesion, and the tensile and shear behavior are sensitive to the confining pressure (Cusatis et al. 2003). Due to that the model is suitable for the failure mode I and II. The disadvantage of the model is the fact that it uses a complex macroscopic nonlinear stress-strain relationship to describe a microscopic local behavior.

The design considerations for use of steel fibres in concrete with high and normal compressive strength in the engineering practice are summarized in the following references: ACI Committee 544 (1999), DBV-Merkblatt (1996), (2001), Deutscher Ausschuss für Stahlbeton (2005), RILEM TC 162-TDF (2001, 2003), RÖVBB (2002), The Concrete Society (2003), Henke and Empelmann (2007), Falkner (2002) .



**Fig. 4.2** Lattice of beams for concrete consisting of aggregate, cement matrix and interface (van Mier et al. 1995)

A continued development of steel fibre reinforced concrete (SFRC) has been hindered by a general lack of confidence in its design, particularly under flexural load. This is mainly due to a lack of suitable analytical design methods and appropriate material property tests that measure flexural toughness (or strength) parameters (RILEM 2001, Henke and Empelmann 2002).

Many approaches have been developed to study the behaviour of fibre reinforced concrete at different scales.

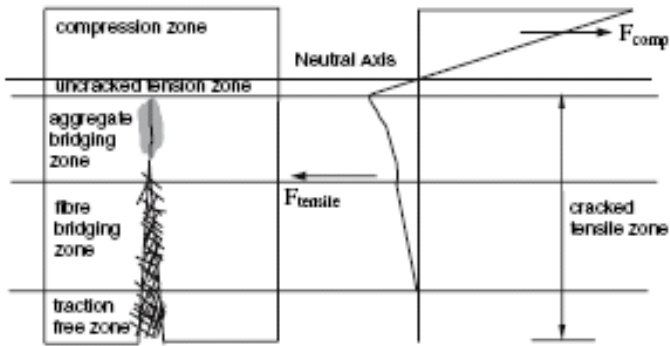
Analytical models to describe the behavior of fibrous concrete were proposed by Hillerborg (1985), Lim et al. (1987), Li et al. (1991), Kullaa (1994), Jenq and Shah (1986), Maalej and Li (1994). One proposed various stress-profiles for predicting the load-deflection behaviour of SFRC by utilising the equilibrium of

forces at the cracked section (Casanova and Rossi (1997), Armelin and Banthia 1997, RILEM 2002, Ulfkjaer et al. 1995, Henke and Empelmann 2007, Lin 1999, Altoubat et al. 2008). These models have generally adopted a semi-analytical approach, whereby failure was assumed to occur at a single crack with rigid-body motion of the two broken halves, rotating about a plastic hinge, being the dominant mechanism. The kinematics of failure was modelled using a variety of structural and fracture mechanics theories to relate crack-mouth-opening-displacement (CMOD) to mid-span deflection and the position of the neutral axis. Some authors have simplified the crack profile by assuming that the crack originates at the neutral axis (i.e.  $CMOD=0$ ) (Casanova and Rossi 1997, Amelin and Banthia 1997). Others have suggested a fictitious crack exists close to the neutral axis, whereby cracking was initiated only after the concrete tensile strength was first reached. Tensile strain-softening, according to a stress/crack-width relationship, then occurred until the critical crack width was reached (at around 0.05 mm) at which point the real crack developed (Ulfkjaer et al. 1995, Wecheratana and Shah 1983) Under compression, the concrete was assumed to behave according to a parabolic stress-strain relationship similar to those defined in most design codes. Different approaches were used to model tensile stress. These included the use of single fibre pull-out tests in combination with fibre distribution data (Armelin and Banthia 1997), theoretical (Wecheratana and Shah 1983) and experimental strain-softening relationships obtained from uniaxial tensile tests (Ulfkjaer et al. 1995).

A novel semi-analytical model based on the equilibrium of internal forces to predict the flexure behaviour of steel fibre reinforced concrete was proposed by Jones et al. (2008). The model uses a combined stress-block and strain profile approach (Figs.4.3 and 4.4). Fig.4.3 shows an idealized representation of a crack at the critical section of SFRC beam together with a corresponding stress-profile diagram. The following assumptions are made: a) failure occurs at a single crack within the middle third of a four-point loaded beam, and shearing and strain effects are negligible, b) the stresses and forces in compression and tension are as shown in Fig.4.3, c) the stresses and pull-out forces acting across the critical section are purely uniaxial, d) the beam is of homogenous material and is elastically isotropic and e) plane cross-sections remain plane.

The concrete stresses and resultant fibre pullout forces that develop at the critical section can be represented by three distinct zones: (1) compression zone; (2) an uncracked tension zone and (3) a cracked tension zone. The cracked tension zone can be further represented by three sub-zones: an aggregate bridging zone-resulting from matrix micro-cracking which initiates fibre-matrix debonding; a fibre bridging zone-in which the fibres are partially pulled out from the matrix; and a traction free zone-in which the fibres are completely pulled out from the matrix. By considering the forces across the critical section in this way, the flexural capacity of the critical section can be related to the following five

principal parameters: the uniaxial compressive stress–strain relationship, the uniaxial tensile stress–strain relationship, the single fibre pull-out load versus crack-width relationship, the number, distribution, embedment lengths and orientations of fibres bridging the cracked section, the strain and crack-width profiles of uncracked and cracked sections respectively in relation to the mid-span beam deflection. If relationships for these parameters can be established, then the shape and magnitude of the stress-block diagram can be predicted for a given beam deflection. Thus, providing the internal force equilibrium of the section is satisfied, the flexural moment capacity of the beam can be computed for a given beam deflection.

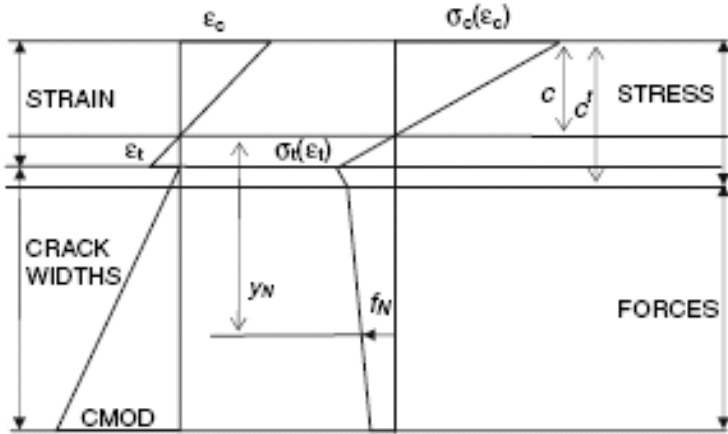


**Fig. 4.3** Schematic representation at the cracked section of steel fibre reinforced concrete beam under flexural loading ( $F_{comp}$  – resultant compressive force,  $F_{tensile}$  – resultant tensile force) (Jones et al. 2008)

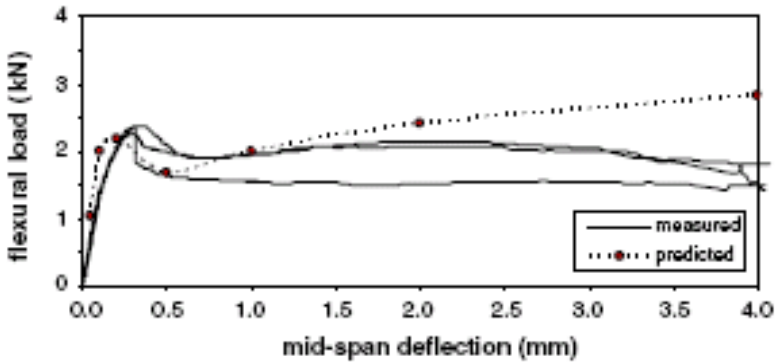
Comparisons between the predicted load-deflection responses, derived from the model, and those obtained experimentally from flexural toughness beam tests for a selection of the beams investigated are shown in Figs.4.5–4.8.

On the meso scale, discrete truss models have been used (Bolander and Saito 1997, van Hauwaert and van Mier 1998, Leite et al. 2004, Cusatis et al. 2010) to study the material behavior where multiple individual fibres were explicitly modeled in specimens.

In turn, on the macro scale, finite element computations were used on the basis of different constitutive models (Al-Taan and Ezzadeen 1995, Lohrmann 1999, Kooiman et al. 2000, Peng and Meyer 2000, Stamm 2002, Suwada and Fukuyama 2006, Beghini et al. 2007, Billington 2010, Gödde and Mark 2010). An approach to the prediction of the torsional behaviour of steel fibre reinforced concrete has been presented by Karayannis (1995) by solving the governing equation of torsion by taking into account stress-strain laws for fibre-concrete under direct tension.

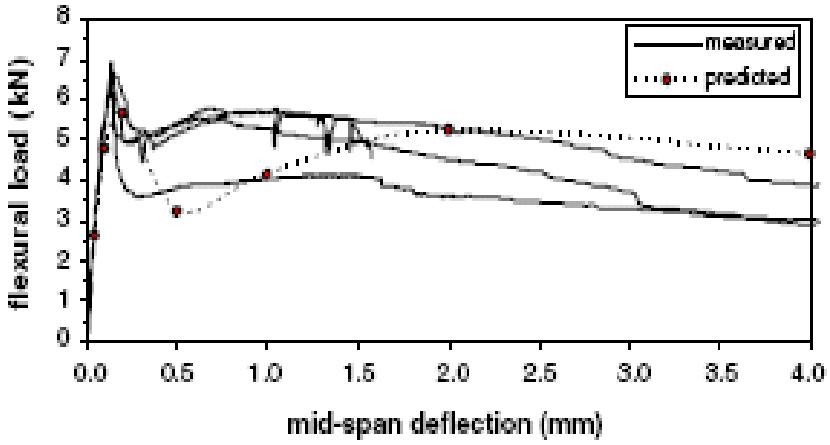


**Fig. 4.4** Schematic representation of the stress-strain and force/crack-width blocks acting across the cracked section ( $f_N$  – force carried by each of the  $N$  individual fibres bridging the cracked tensile zone,  $\sigma_c$  - compressive normal stress,  $\sigma_t$  - tensile normal stress,  $c$  – height of compressive zone,  $c'$  – height of uncracked zone) (Jones et al. 2008)

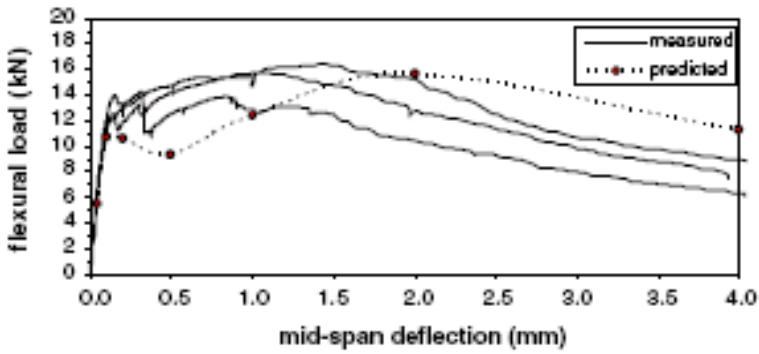


**Fig. 4.5** Comparison between predicted and measured response - 50x100 mm<sup>2</sup> cast beam, 40 kg/m<sup>3</sup> (probabilistic fibre pull-out curve) (Jones et al. 2008)

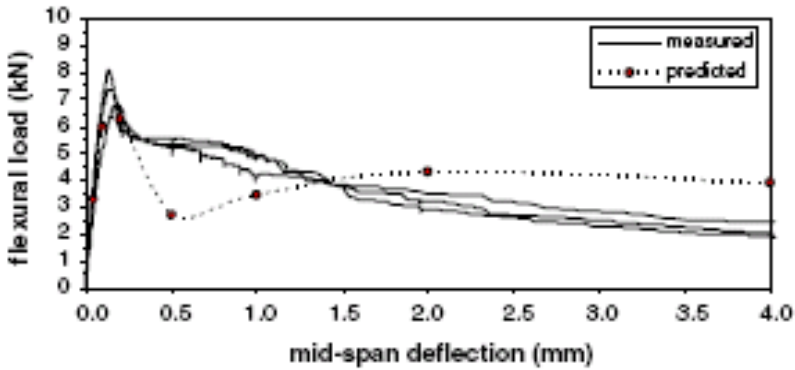




**Fig. 4.6** Comparison between predicted and measured response -  $75 \times 100 \text{ mm}^2$  cast beam,  $40 \text{ kg/m}^3$  (probabilistic fibre pull-out curve) (Jones et al. 2008)



**Fig. 4.7** Comparison between predicted and measured response -  $100 \times 100 \text{ mm}^2$  cast beam,  $80 \text{ kg/m}^3$  (probabilistic fibre pull-out curve) (Jones et al. 2008)



**Fig. 4.8** Comparison between predicted and measured response -  $75 \times 125 \text{ mm}^2$  sprayed beam,  $26 \text{ kg/m}^3$  (probabilistic fibre pull-out curve) (Jones et al. 2008)

Recently, a numerical continuum approach (in the context of FEM) was proposed by Radtke et al. (2008, 2009, 2010) wherein the existing continuum approach enhanced by a characteristic length of micro-structure to model concrete failure was combined with a discrete representation of fibres by adding extra nodal forces at fibre ends which were equal to forces measured during the pull-out of a fibre from a matrix specimen. Thus, instead of explicitly modelling fibres, only reaction forces from the fibre to the matrix were considered. The model has proven to be able to represent characteristic features of fibre reinforced concrete as ductile behaviour, strain hardening and multiple cracking.

In turn, Chuang and Ulm (2002), and Kabele (2007) used a multiscale framework for modeling of fracture in high performance fibre reinforced cementitious composites (which linked analytical and computational models covering scales from micro- to macro-level).

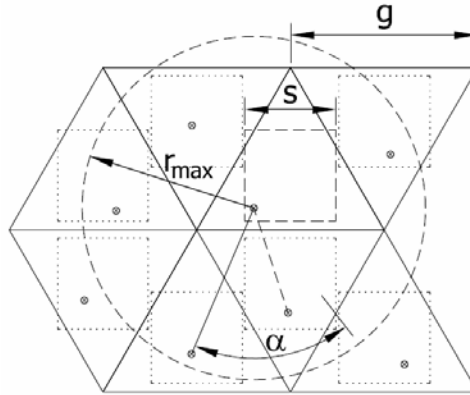


## 5 Lattice Discrete Model

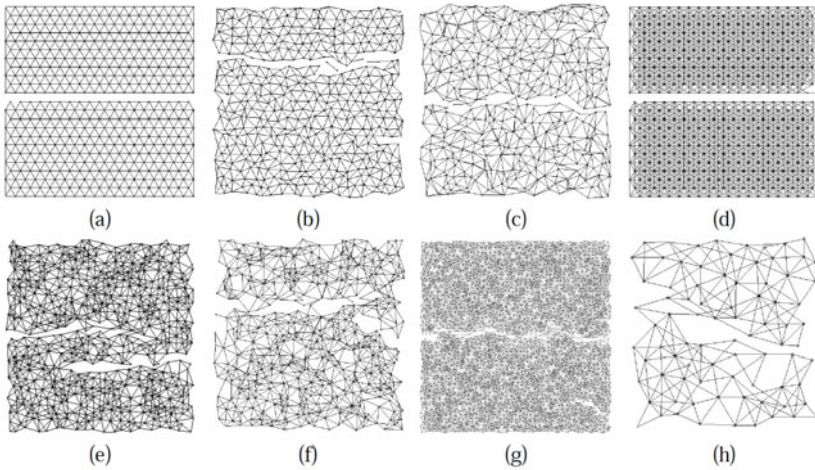
**Abstract.** The chapter describes a novel discrete lattice model taking material micro-structure into account to simulate fracture in plain and fibrous concrete. Numerical results on the basis of a discrete lattice model are demonstrated for different quasi-static boundary value problems involving a fracture process in plain concrete and fibrous concrete. Numerical results are qualitatively compared with corresponding laboratory tests. Results of detailed parametric studies are demonstrated.

A lattice model takes into account material micro-structure at meso-level (van Mier et al. 1995). In our linear and irregular lattice model (Kozicki and Tejchman 2007b, 2008, 2010, Kozicki and Donze 2008), a quasi-brittle material was discretized in the form of a 3D tetrahedral grid or a 2D triangular grid of lines. The distribution of rods was assumed to be completely random using a Voronoi's construction scheme (Fig.5.1) or a Delaunay's construction scheme (Fig.5.2). In the first case, a triangular grid was created in the material with a side dimension equal to  $g$ . In each triangle of the grid, additional interior squares were assumed with an area of  $s \times s$ . Next, one point was selected at random within these interior squares. Later, all points inside the squares were connected with the neighboring ones within a distance of  $r_{max}$  to create a non-uniform mesh of rod elements (Figs.5.2d-5.2h), where the maximum element length was  $r_{max}$  (e.g.  $r_{max}=2g$ ), the minimum element length was  $r_{min}$  (e.g.  $r_{min}=0.1 \times g$  for  $s=0.6 \times g$ ) and the minimum angle between elements was assumed to be  $\alpha$  (e.g.  $\alpha=20^\circ$ ). A uniform triangular mesh could be obtained with the parameter  $s=0 \times g$  (Fig.5.2a). Using this grid generation method, the elements could cross each other in two-dimensional calculations (similarly as in the paper by Burt and Dougill 1977) but they did not intersect each other in a three-dimensional analysis.

In a Delaunay's construction scheme, a tetrahedral grid of nodes was first created in the material with a side dimension equal to  $g$ . Then each node was randomly displaced by a 3D vector of a random magnitude  $\leq s$ . The nodes randomized in this way were connected with each other. Thus, each edge in the Delaunay mesh formed a lattice (Figs.5.2a-5.2c). A uniform tetrahedral mesh could be obtained with the parameter  $s=0$  (Fig.5.2a). The model needs 2 parameters ( $g$  and  $s$ ) to randomly distribute elements in the lattice. In the calculations, we assumed mainly  $g=1-2$  mm and  $s=0.6g$ .



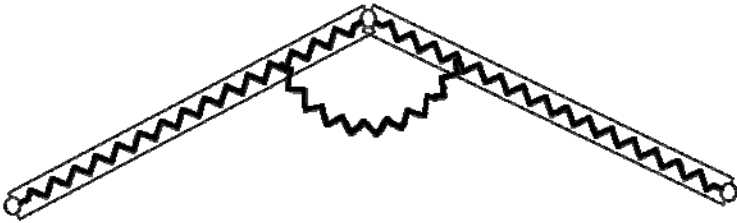
**Fig. 5.1** Scheme to assume a non-uniform distribution of rod elements in the 2D lattice ( $s$  - size of interior squares,  $r_{max}$  - maximum rod length,  $\alpha$  - minimum angle between two rods,  $g$  - size of triangular grid) (Kozicki and Tejehman 2007b)



**Fig. 5.2** Deformed 2D lattice using different generation methods and generation parameters: a)  $g=0.005$  m,  $s=0$ , Delaunay's scheme, b)  $g=0.005$  m,  $s=0.6g$ , Delaunay's scheme, c)  $g=0.005$  m,  $s=1.2g$ , Delaunay's scheme, d) Voronoi's scheme  $g=0.005$  m,  $s=0$ ,  $r_{max}=1.9g$ ,  $\alpha=20^\circ$ , e) Voronoi's scheme  $g=0.005$  m,  $s=0.6g$ ,  $r_{max}=1.9g$ ,  $\alpha=20^\circ$ , f) Voronoi's scheme  $g=0.005$  m,  $s=1.2g$ ,  $r_{max}=1.9g$ ,  $\alpha=20^\circ$ , g) Voronoi's scheme  $g=0.002$  m,  $s=0.6g$ ,  $r_{max}=1.9g$ ,  $\alpha=20^\circ$ , h) Voronoi's scheme  $g=0.012$  m,  $s=0.6g$ ,  $r_{max}=1.9g$ ,  $\alpha=20^\circ$  (Kozicki and Tejehman 2007b)

The lattice rods in the 2D model possessed the longitudinal stiffness described by the parameter  $k_l$  (which controlled the changes of the element length). The nodal springs had the bending stiffness described by the parameter  $k_b$  (which controlled the changes of the angle between elements). In the 3D model, the nodal springs had also the parameter  $k_t$  (which controlled the torsion between elements, i.e. angle in the plane perpendicular to the plane formed by two rods connected with a node). Thus, the rods had separate springs to represent bending and torsion.

Our novel lattice model (Kozicki and Tejchman 2007b, 2008) differs from classical lattice models (Schlangen and Garboczi 1997) composed of beams connected by non-flexible nodes in that it consists of rods with flexible nodes and longitudinal deformability, rotating in the form of a rigid body rotation (Fig.5.3). Thus, shearing, bending and torsion are represented by a change of the angle between rod elements connected by angular springs. This quasi-static model is of a kinematic type. The 2D calculations of rod displacements are carried out on the basis of the consideration of successive geometrical changes of rods due to translation, rotation and normal and bending deformation. Thus, the global stiffness matrix is not needed to be built and the calculation method has a purely explicit character. In spite of necessity of the application of small displacement increments (what is the inherent property of explicit numerical procedures), the computation time is significantly reduced as compared to implicit solutions (e.g. the computation time of 3D uniaxial extension (specimen  $10 \times 10 \times 10 \text{ cm}^3$ ) with 1'400'000 rod elements is about 90 hours on PC 3.5GHz). In addition, in contrast to the lattice beam model by Schlangen and Garboczi (1997), the torsion in three-dimensional simulations is included as well.



**Fig. 5.3** The rods connected by angular springs (the rods do not bend) (Kozicki and Tejchman 2006)

The displacement of the center of each rod was calculated as the average displacement of two end nodes of the rod element from the previous iteration step

$${}_i\Delta\vec{X} = \frac{{}_i^A\Delta\vec{X} + {}_i^B\Delta\vec{X}}{2}, \quad (5.1)$$

wherein  ${}^A \Delta \vec{X}$  and  ${}^B \Delta \vec{X}$  – displacement of the end nodes A and B in the rod element  $i$ , respectively. The displacement vector  ${}^j \Delta \vec{X}$  of each element node in the 3D model was obtained by averaging the displacements of the end of elements attached to this node caused by translation, rotation, normal, bending and torsional deformation (Fig.5.4)

$${}^j \Delta \vec{X} = \sum_i \frac{{}_i \Delta \vec{W} + {}_i \Delta \vec{R}}{{}^j n_{sum}} + \frac{\sum_i \frac{1}{{}_i d_{init}} ({}_i \Delta \vec{D} {}_i k_l + {}_i \Delta \vec{B} {}_i k_b + {}_i \Delta \vec{T} {}_i k_t)}{\sum_i \frac{1}{{}_i d_{init}} ({}_i k_l + {}_i k_b + {}_i k_t)}, \quad (5.2)$$

wherein:  ${}^j \Delta \vec{X}$  – resultant node displacement,  ${}_i \Delta \vec{W}$  – node displacement due to the rod translation,  ${}_i \Delta \vec{R}$  – node displacement due to the rod rotation,  ${}_i \Delta \vec{D}$  – node displacement due to the change of the rod length,  ${}_i \Delta \vec{B}$  – node displacement due to the change of the bending angle between rods,  ${}_i \Delta \vec{T}$  – node displacement due to the change of the torsional angle between rods,  $i$  – successive rod number connected with the node  $j$ ,  $j$  – node number,  ${}^j n_{sum}$  – number of rods attached to the node  $j$  and  ${}_i d_{init}$  – initial rod length  $i$ . The node displacements were calculated successively during each calculation step beginning first from elements along boundaries subject to prescribed displacements. The normal strain  $\varepsilon$ , shear angle  $\gamma$  and bending angle  $\chi$  in rods are equal to (Fig.5.5)

$$\varepsilon = \frac{d - d_o}{d_o}, \quad \gamma = \frac{\alpha^A + \alpha^B}{2} \quad \text{and} \quad \chi = \frac{\alpha^A - \alpha^B}{2}, \quad (5.3)$$

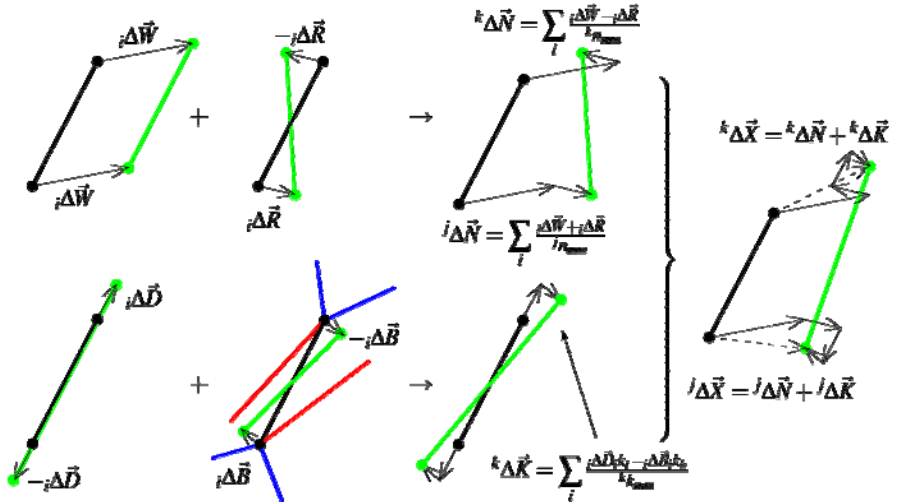
where  $d$  – current rod length,  $d_o$  – initial rod length. The normal stress, shear stress and moment are respectively

$$\sigma = \varepsilon k_l E, \quad \tau = \gamma k_b G \quad \text{and} \quad m = \chi k_b G d^2. \quad (5.4)$$

Thus, the resultant vertical force  $F$  in a selected specimen's cross-section area  $A$  was determined with the aid of the corresponding normal strain  $\varepsilon$ , shear strain  $\gamma$ , stiffness parameters  $k_l$ ,  $k_b$ , modulus of elasticity  $E$ , shear modulus  $G$  and specimen's cross-section area  $A$  (Fig.5.5)

$$F = A \sum_n (k_l \varepsilon E + k_b \gamma G), \quad (5.5)$$

where the sum is extended over all rods  $n$  that intersect a selected specimen's cross-section. By applying Eqs.5.2 and 5.5, the equilibrium of forces was obtained in each node (what required always about 10 iterations).



**Fig. 5.4** General scheme to calculate rod displacements in the 2D lattice (Kozicki and Tejchman 2007b)

Each rod was removed from the lattice if the threshold local tensile rod normal strain  $\varepsilon_{min}$  was exceeded. All presented numerical calculations were strain-controlled. On the basis of initial calculations, the critical global strain increment expressed as

$$\Delta\varepsilon_{crit}^{gl} = (l_r \varepsilon_{min}) / \Delta l, \quad (5.6)$$

where  $l_r$  - average rod length,  $\varepsilon_{min}$  - threshold local tensile strain,  $\Delta l$  - vertical displacement increment of the specimen edge, should be larger than 500-1000 in a single calculation step to obtain a negligible effect (about 2-4%) of the strain



increment on numerical results of stresses (Fig.5.41). It means that minimum 500-1000 iterations were required to remove a single rod. If this condition was not preserved (in particular for tension), both the crack shape and crack direction depended on the strain increment.

The ratio between the mean rod length  $l_r$  and the smallest specimen size  $h$  had to be at least 1/100-1/50 ( $l_r/h \leq 1/100-1/50$ ) in 2D (Fig.5.40) and 1/66-1/33 ( $l_r/h \leq 1/66-1/33$ ) in 3D specimens to obtain a negligible effect (about 2%-4%) of the rod length on stress results.

The node displacement due to the rod translation  ${}_i\Delta\vec{W}$  was calculated by subtracting the previous rod's position  ${}_i\vec{X}_{prev}$  from the current one  ${}_i\vec{X}$

$${}_i\Delta\vec{W} = {}_i\vec{X} - {}_i\vec{X}_{prev}, \quad (5.7)$$

The node displacement  ${}_i\Delta\vec{R}$  due to the rod rotation was computed from the rotational difference  ${}_i\Delta\overset{\circ}{q}$  between the current rod orientation  ${}_i\overset{\circ}{q}$  and its previous orientation  ${}_i\overset{\circ}{q}_{prev}$  (both expressed as the unit quaternion  $\overset{\circ}{q} = a + bi + cj + dk$ ). The real numbers  $a$ ,  $b$ ,  $c$  and  $d$  satisfy the equation  $a^2 + b^2 + c^2 + d^2 = 1$  and  $i$ ,  $j$  and  $k$  are the imaginary numbers satisfying the equation ( $i^2 = j^2 = k^2 = ijk = -1$ )

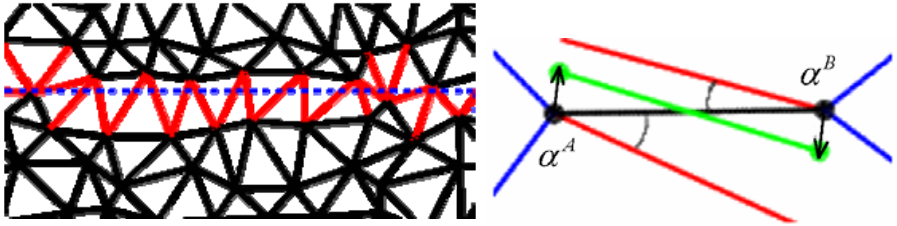
$${}_i\Delta\overset{\circ}{q} = {}_i\overset{\circ}{q} \cdot \left( {}_i\overset{\circ}{q}_{prev} \right)^{-1}, \quad (5.8)$$

$${}_i\Delta\vec{R} = {}_i\Delta\overset{\circ}{q} \cdot {}_i\vec{h} \cdot \left( {}_i\Delta\overset{\circ}{q} \right)^{-1} - {}_i\vec{h}, \quad (5.9)$$

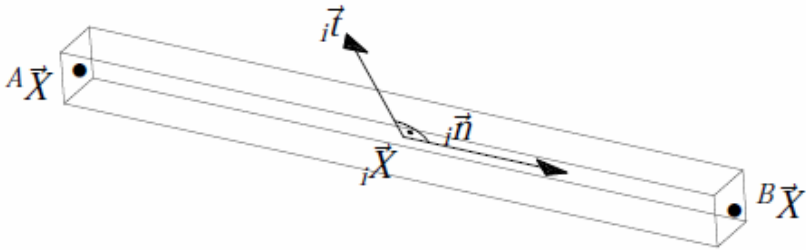
where  $\vec{h}$  is the rod half-length vector from the rod center towards its end. The value of  ${}_i\overset{\circ}{q}$  was calculated in a local coordinate system using the matrix  $\mathbf{R}$

$${}_i\overset{\circ}{q} = {}_i\overset{\circ}{q} [ {}_i\vec{n} \quad {}_i\vec{t} \quad {}_i\vec{n} \times {}_i\vec{t} ] = \overset{\circ}{q}(\mathbf{R}), \quad (5.10)$$

where the normal  ${}_i\vec{n}$  and perpendicular  ${}_i\vec{t}$  vectors are shown in Fig.5.6.



**Fig. 5.5** Calculation of cross-sectional force ( $\varepsilon$  and  $\gamma$  are projected on normal direction of cross-section plane - dotted) (Kozicki and Teichman 2007b)



**Fig. 5.6** Local coordinate system for a single rod (Kozicki 2007)

The quaternion-vector-quaternion multiplication in Eq.5.9 denotes a rotation of a vector by a quaternion (a conversion of a vector  $\vec{h}$  to a quaternion), where three imaginary coefficients  $b, c, d$  are the coordinates  $x, y, z$  of the vector (Shoemaker 1985). The real part of the resulting quaternion is zero, while its imaginary coefficients are the coordinates of the rotated vector. This approach is faster than using the usual rotation matrix because it reduces twice the number of operations. In addition, a quaternion requires a smaller memory footprint (4 floats versus 9 floats for a matrix) and does not suffer both a singularity problem as an Euler representation of rotation or a matrix skew problem due to the accumulation of numerical errors. The quaternion can be computed from the rotation matrix  $\mathbf{R}$ , e.g. as follows

$${}^o q(\mathbf{R}) = \begin{cases} a = \pm \frac{1}{2} \sqrt{1 + \mathbf{R}_{11} + \mathbf{R}_{22} + \mathbf{R}_{33}} \\ b = \frac{1}{4a} (\mathbf{R}_{23} - \mathbf{R}_{32}) \\ c = \frac{1}{4a} (\mathbf{R}_{31} - \mathbf{R}_{13}) \\ d = \frac{1}{4a} (\mathbf{R}_{12} - \mathbf{R}_{21}) \end{cases} . \quad (5.11)$$

The node displacement  ${}_i \Delta \vec{D}$  due to the change of the rod length was obtained by multiplying the rod normal vector  ${}_i \vec{n}$  by the rod length difference

$${}_i \Delta \vec{D} = {}_i \vec{n} \cdot ({}_i d - {}_i d_{init}), \quad (5.12)$$

where  ${}_i d$  and  ${}_i d_{init}$  are the current and initial length of the rod  $i$ , respectively.

The node displacement  ${}_i \Delta \vec{B}$  due to the angle change between rods was determined from

$${}_i \Delta \vec{B} = {}_i \overset{o}{B} \cdot ({}_i d \cdot {}_i \vec{n}) \left( {}_i \overset{o}{B} \right)^{-1} - {}_i d \cdot {}_i \vec{n}, \quad (5.13)$$

where the quaternion  ${}_i \overset{o}{B}$  was a product of the bending (angular) change between the rod and other connected rods divided by the rod number  ${}_i b_{sum}$

$${}_i \overset{o}{B} = \prod_j \overset{o}{B}^j \left( \vec{p}^j, \frac{\Delta \alpha^j}{{}_i b_{sum}} \right), \quad (5.14)$$

wherein the index  $j$  refers to all angular springs connected with the rod  $i$ . A temporary quaternion  $\overset{o}{B}^j$  was built with the axis  $\vec{p}^j$  orthogonal to the plane formed by two rods connected by the angular spring  $j$  and the angle

$\Delta\alpha^j \in \langle -\pi, \pi \rangle$  between them. To obtain the quaternion  $\overset{o}{B}^j$  from a rotational axis and a rotation angle, the following formula was applied

$$\overset{o}{B}^j(\vec{p}^j(x, y, z), \Delta\alpha^j) = \begin{cases} a = \cos\left(\frac{\Delta\alpha^j}{2}\right) \\ b = \sin\left(\frac{\Delta\alpha^j}{2}\right) \cdot x \\ c = \sin\left(\frac{\Delta\alpha^j}{2}\right) \cdot y \\ d = \sin\left(\frac{\Delta\alpha^j}{2}\right) \cdot z \end{cases} \quad (5.15)$$

The node displacement  ${}_i\Delta\vec{T}$  due to the torsion between two neighboring rods was calculated from

$${}_i\Delta\vec{T} = {}_i\overset{o}{T} \cdot ({}_i d \cdot {}_i \vec{n}) \left( {}_i\overset{o}{T} \right)^{-1} - {}_i d \cdot {}_i \vec{n} \quad (5.16)$$

where the quaternion  ${}_i\overset{o}{T}$  was a product of the twisting angular change  $\vartheta^j$  and torsional angular change  $\omega^j$  between the rod and other connected rods divided by the rod number  ${}_i b_{sum}$

$${}_i\overset{o}{T} = \prod_j {}_i\overset{o}{T}^j \left( \vec{n}^j, \frac{\vartheta^j - \omega^j}{{}_i b_{sum}} \right), \quad (5.17)$$

wherein the index  $j$  refers to all angular springs connected with the rod  $i$ . A temporary quaternion  $\overset{o}{T}^j$  was built from the axis  $\vec{n}^j$  of other rods and a mean value of the torsional and twisting angle (as in Eq.5.14).

The calculation method of the resultant node displacement (Eq.5.2) is shown below on the example of a simple frame composed of 4 rods during one prescribed displacement increment (Fig.5.8). The nodes ‘3’ and ‘5’ are fixed and the node ‘1’ is assumed to displace to the point with the new coordinates (0.58, 1.42). The

displacement vectors of the node ‘2’ in rods 1, 2 and 3 are:  ${}_1\vec{W} = (0.09, -0.04)$ ,  ${}_2\vec{W} = (0.0, 0.0)$ ,  ${}_3\vec{W} = (0.0, 0.0)$ ,  ${}_1\vec{R} = (-0.065, -0.012)$ ,  ${}_2\vec{R} = (0.0, 0.0)$ ,

$\vec{R}_3^2 = (0.0, 0.0)$ ,  $\vec{D}_1^2 = (0.035, -0.131)$ ,  $\vec{D}_2^2 = (0.0, 0.0)$ ,  $\vec{D}_3^2 = (0.0, 0.0)$ ,  
 $\vec{B}_1^2 = (0.124, 0.044)$ ,  $\vec{B}_2^2 = (0.44, -0.064)$ ,  $\vec{B}_3^2 = (-0.006, 0.041)$ , respectively  
 (with the rotation angle of the node '2':  $\vec{\Delta\varphi}_1^2 = -8.9^\circ$  (rod 1),  $\vec{\Delta\varphi}_1^2 = -4.45^\circ$  (rod  
 2) and  $\vec{\Delta\varphi}_1^2 = -2.97^\circ$  (rod 3)). For the stiffness parameters  $k_b=0.6$  and  $k_t=1.0$ , the  
 resultant displacement vector of the node '2' (Eq.5.2) is equal to

$$\begin{aligned}
 \Delta X^2 &= \frac{1}{3} (\vec{W}_1^2 + \vec{W}_2^2 + \vec{W}_3^2 + \vec{R}_1^2 + \vec{R}_2^2 + \vec{R}_3^2) + \\
 &+ \frac{(\vec{k}_1^2 \vec{D}_1^2 + \vec{k}_2^2 \vec{D}_2^2 + \vec{k}_3^2 \vec{D}_3^2 + \vec{k}_b^2 \vec{B}_1^2 + \vec{k}_b^2 \vec{B}_2^2 + \vec{k}_b^2 \vec{B}_3^2)}{(\vec{k}_1^2 + \vec{k}_2^2 + \vec{k}_3^2 + \vec{k}_b^2 + \vec{k}_b^2 + \vec{k}_b^2)} = \\
 &= \frac{1}{3} (0.09, -0.04) + (0, 0) + (0, 0) + (-0.065, -0.012) + (0, 0) + (0, 0) + \\
 &+ \frac{[(0.035, -0.131) + (0, 0) + (0, 0)] \times 1.0 + [(-0.124, 0.044) + (0.44, -0.064) + (0.006, 0.041)] \times 0.6}{1.0 + 1.0 + 1.0 + 0.6 + 0.6 + 0.6} = \\
 &= (0.037, -0.042),
 \end{aligned} \tag{5.18}$$

and the new coordinates of the node '2' are (0.837, 0.558). In turn, the  
 displacement vectors of the node '4' in the rods 3 and 4 are:  $\vec{W}_3^4 = (0.0, 0.0)$ ,  
 $\vec{W}_4^4 = (0.0, 0.0)$ ,  $\vec{R}_4^4 = (0.0, 0.0)$ ,  $\vec{D}_3^4 = (0.0, 0.0)$ ,  $\vec{D}_4^4 = (0.0, 0.0)$ ,  $\vec{B}_3^4 = (-$   
 $0.006, -0.041)$  and  $\vec{B}_4^4 = (0.0, 0.0)$ , respectively (with the rotation angle of the  
 node '4':  $\vec{\Delta\varphi}_3^4 = -2.97^\circ$  (rod 3),  $\vec{\Delta\varphi}_4^4 = 2.97^\circ$  (rod 4)). The resultant  
 displacement vector of the node '4' is equal to

$$\begin{aligned}
 \vec{\Delta X}^4 &= \frac{1}{2} (\vec{W}_3^4 + \vec{W}_4^4 + \vec{R}_3^4 + \vec{R}_4^4) + \\
 &+ \left( \frac{{}^4k_1 {}^4D_3 + {}^4k_1 {}^4D_4 + {}^4k_b {}^4B_3 + {}^4k_b {}^4B_4}{{}^4k_1 + {}^4k_1 + {}^4k_b + {}^4k_b} \right) = \\
 &= \frac{1}{2} (0.0, 0.0) + (0, 0) + (0, 0) + (0, 0) + \\
 &\left( \frac{[(0, 0)] \times 1.0 + [(-0.006, -0.041) + (0.0, 0.0)] \times 0.6}{1.0 + 1.0 + 0.6 + 0.6} \right) = \\
 &= (-0.001, -0.007),
 \end{aligned}
 \tag{5.19}$$

and the new coordinates of the node '4' are (1.599, 0.493).

A block diagram of the calculation algorithm is shown in Fig.5.8.

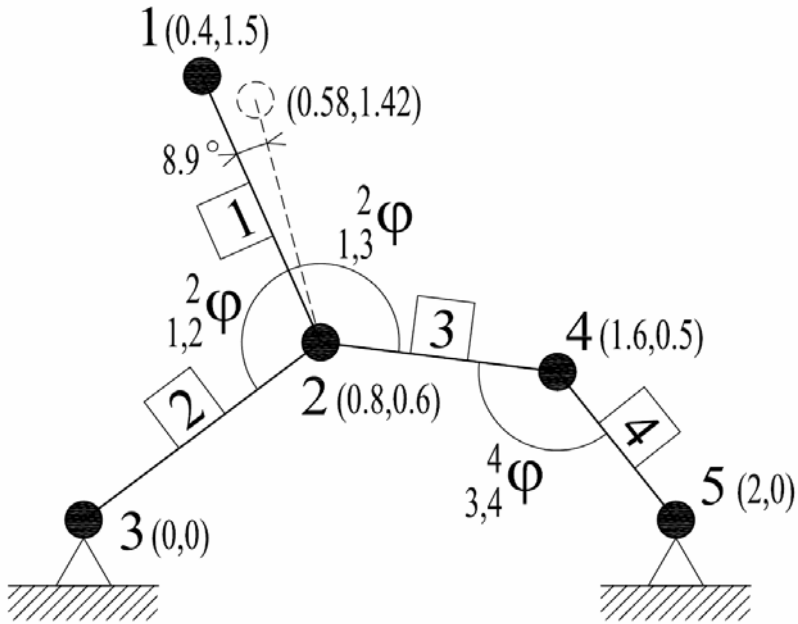
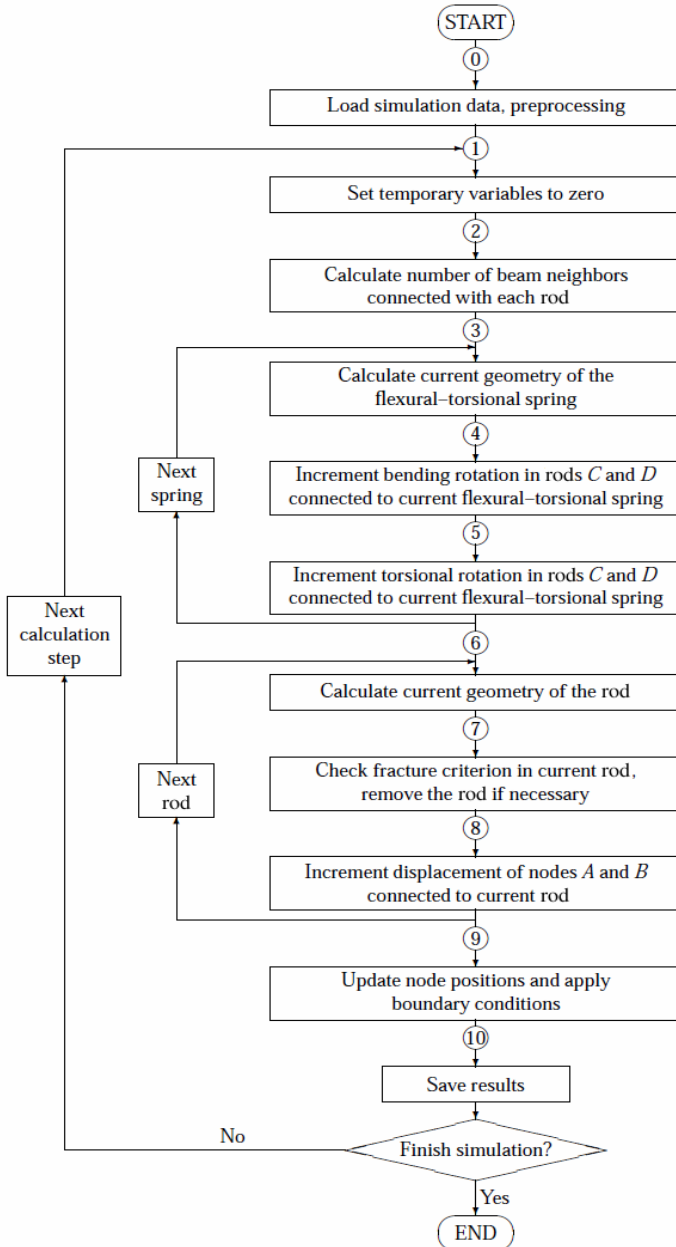


Fig. 5.7 A simplified frame composed of 4 rods (Kozicki 2007)



**Fig. 5.8** Block diagram for calculation algorithm (Kozicki 2007)

## 5.1 Simulations of Fracture Process in Plain Concrete

### One-Phase Material

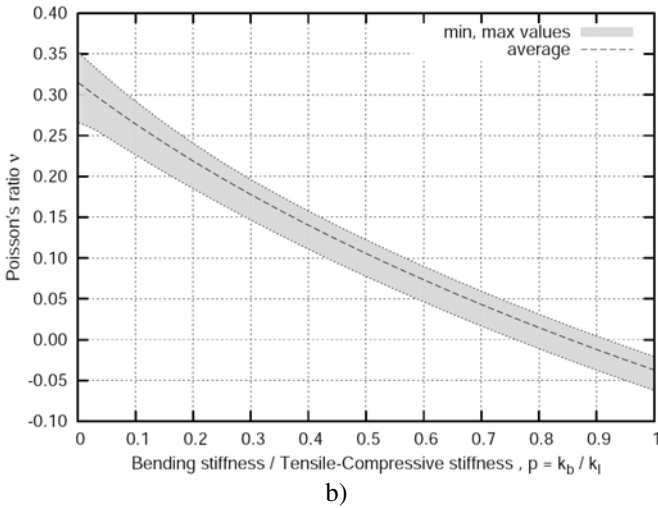
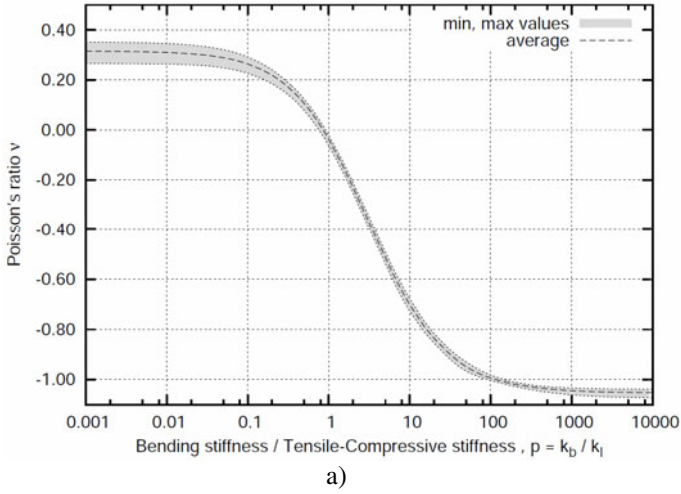
The 2D calculations with a simplified one-phase brittle material were carried out with the specimen of the size  $100 \times 100 \text{ mm}^2$  ( $b \times h$ ), composed of 20'000 rods distributed non-uniformly ( $\alpha=20$ ,  $s=0.6g$ ,  $g=l_r=1.5 \text{ mm}$ ,  $r_{\max}=2g$ ). The minimum element length was about  $l_r^{\min}=0.6 \text{ mm}$  and the maximum one was about  $l_r^{\max}=3 \text{ mm}$ . The modulus of elasticity of all elements was assumed to be  $E=20 \text{ GPa}$ . The following strain increments were assumed on the basis of initial calculations: 0.000032% (uniaxial compression) and 0.000004% (uniaxial tension). Smaller strain increments only insignificantly influenced the results. The computation time with 20'000 elements was about 10 hours using PC 3.6 GHz.

Our lattice model allows one to describe the different Poisson's ratio as a function of the stiffness ratio  $p=k_t/k_c$ . Figure 5.9 presents the change of the Poisson's ratio versus  $p$  during uniaxial compression and uniaxial tension of a specimen with smooth horizontal edges at the beginning of a deformation process (the rods were not removed). If the stiffness ratio  $p=0.1$ , the Poisson's ratio was 0.23 (the value realistic for concrete). In turn, if the ratio  $p>1$ , the Poisson's ratio became negative (with the smallest value approximately equal to  $\nu=-1.0$  at  $p=10000$ ). The behavior of rods with values of  $p$  approaching zero corresponds obviously to that of simple bars (Kozicki and Tejchman 2003, 2006).

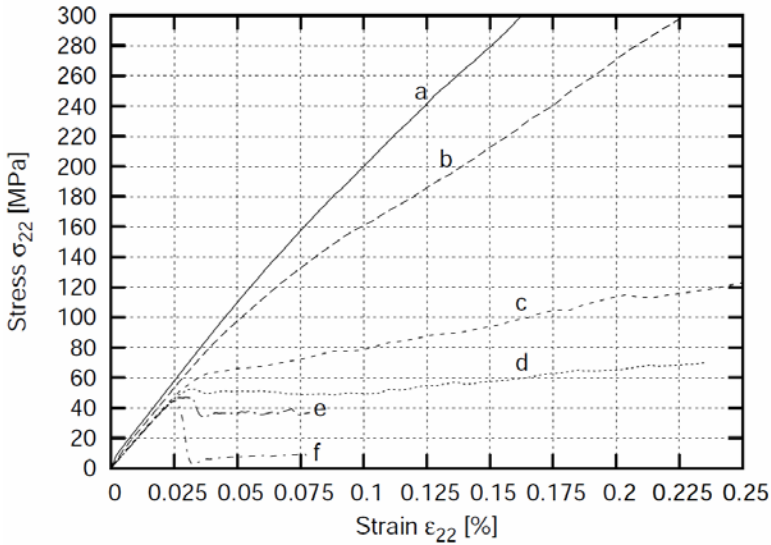
The effect of the stiffness ratio  $p$  on the evolution of the global stress-strain curve  $\sigma-\varepsilon$  (vertical normal stress versus the vertical strain) and crack propagation in a specimen during uniaxial compression with smooth edges is shown in Figs.5.10 and 5.11 for  $\varepsilon_{\min}=0.02\%$  ( $\sigma=P/b$ ,  $\varepsilon=u_2/h$ ;  $P$  - global vertical force,  $u_2$  - vertical displacement of the top edge). The strength and ductility (ratio between the energy consumed after and before the peak) increase with increasing stiffness ratio  $p$ . The material becomes elastic for  $p>0.6$ , quasi-brittle for  $0.025>p>0.01$  and brittle for  $p=0.001$  ( $\varepsilon=0.3\%$ ). In the last case, the vertical global strain corresponding to the material strength is about 0.03%. The cracks are predominantly vertical (parallel to the loading direction) if  $p>0.2$  (Fig.5.11a). In the case of  $p<0.1$ , the dominant cracks are more inclined (Figs.5.11b and 5.11c).

The results of uniaxial tension in a specimen with a small notch at mid-height of the left side and smooth horizontal edges are demonstrated in Figs.5.12, 5.14a and 5.15 for the case of  $\varepsilon_{\min}=0.02\%$ . The material behaves in the elastic-purely brittle way (Fig.5.12). The strength increases with increasing  $p$ , and the brittleness increases with decreasing  $p$ . The overall vertical strain corresponding to the peak stress values is about 0.005-0.007% (thus it is smaller than the local  $\varepsilon_{\min}$ ). The crack pattern practically does not depend on  $p$  (Figs.5.14a and 5.15).

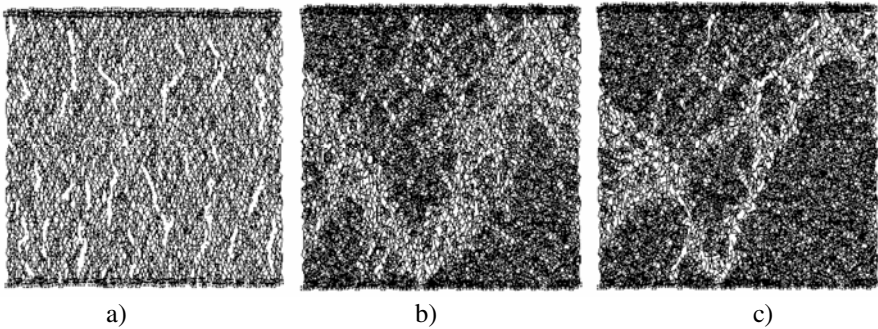




**Fig. 5.9** Influence of ratio between bending and longitudinal stiffness  $p=k_b/k_l$  on Poisson's ratio  $\nu$  during uniaxial compression and extension of one-phase specimen with smooth edges: a) for  $0.0001 \leq p \leq 10000$  (using semi-logarithmic scale), b) for  $0 \leq p \leq 1$  (Kozicki and Tejchman 2007b)



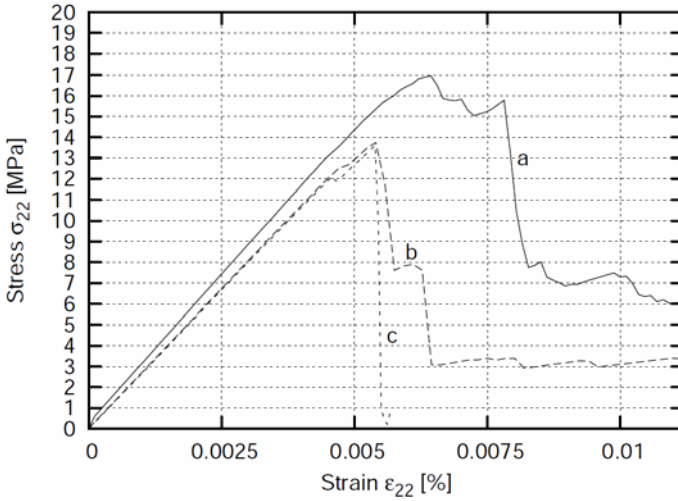
**Fig. 5.10** Effect of ratio  $p=k_b/k_l$  between bending stiffness and longitudinal stiffness on stress-strain curve during uniaxial compression of one-phase specimen with smooth edges (rods were removed when local  $\epsilon_{min}=0.02\%$ ): a)  $p=0.6$ , b)  $p=0.3$ , c)  $p=0.06$ , d)  $p=0.025$ , e)  $p=0.01$ , f)  $p=0.001$  ( $\sigma_{22}$  - vertical normal stress,  $\epsilon_{22}$  - vertical normal strain) (Kozicki and Tejchman 2007b)



**Fig. 5.11** Effect of ratio  $p$  between bending and longitudinal stiffness on crack pattern during uniaxial compression of one-phase specimen with smooth edges (rods were removed when local  $\epsilon_{min}=0.02\%$ ): a)  $p=0.3$ , b)  $p=0.01$ , c)  $p=0.001$  (Kozicki and Tejchman 2007b)

The main crack is always initiated at the notch and then propagates almost horizontally through the specimen. The ratio of the flexural to axial stiffness  $p$  has an inverse effect during compressive fracture as the bending factor  $\alpha$  used in a conventional beam lattice model (Lilliu and van Mier 2003). The compressive

behavior changes namely from brittle to ductile when  $p$  increases ( $\alpha$  decreases). During tensile fracture, the ratio factor  $p$  slightly affects the material behavior.



**Fig. 5.12** Effect of ratio stiffness  $p=k_r/k_b$  on stress-strain curve during uniaxial extension (rods were removed when local  $\epsilon_{min}=0.02\%$ ): a)  $p=0.3$ , b)  $p=0.025$ , c)  $p=0.001$  ( $\sigma_{22}$  - vertical normal stress,  $\epsilon_{22}$  - vertical normal strain) (Kozicki and Tejchman 2007b)

The results of uniaxial tension with a too large rod length of 5 mm ( $l_r/h=1/20$  with  $h=100$  mm) show that a regular mesh ( $s=0 \times g$  using a Delaunay's mesh generation method of Fig.5.2) causes the most brittle material response. An irregular mesh using a Delaunay's generation method ( $s=1.2g$ , Fig.5.2) contributes to a less brittle behavior. The effect of the mesh irregularity is smaller when a Voronoi's method is used. A mesh with a big cell size ( $g=0.012$  m, Fig.5.2) induces the most ductile behavior (each jump on a softening curve corresponds to a removal of a single rod). An increase of the parameter  $\alpha$  and a decrease of the parameter  $r_{max}$  (Voronoi's method) increase brittleness and reduce strain corresponding to strength.

To decrease material brittleness in calculations, which is too large in 2D one-phase material as compared to experiments (van Vliet 2000), and to obtain results totally independent of the rod length, a non-local approach (Bazant and Jirasek 2002) was used (Kozicki and Tejchman 2006). In our calculations, the normal strain in each rod was assumed to be non-local

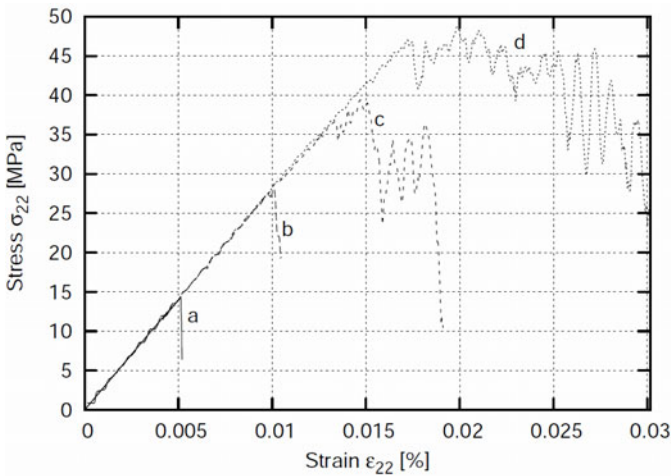
$$\bar{\epsilon} = \frac{\sum \omega(r) \epsilon(x_k + r) l \cos \alpha}{\sum \omega(r) l \cos \alpha}, \quad (5.20)$$

where  $x_k$  – the global coordinates of the element,  $\omega$  - the weighting function,  $r$  – the distance between the mid-point of the element and the mid-points of other neighboring elements,  $l$  - the rod length and  $\alpha$  - the angle between rods. In general, it is required that the weighting function should not alter a uniform field which means that it must satisfy the normalizing condition (Bazant and Jirasek 2002). Therefore, as a weighting function  $\omega(r)$  in Eq.5.19, a Gauss distribution function for 2D problems was used

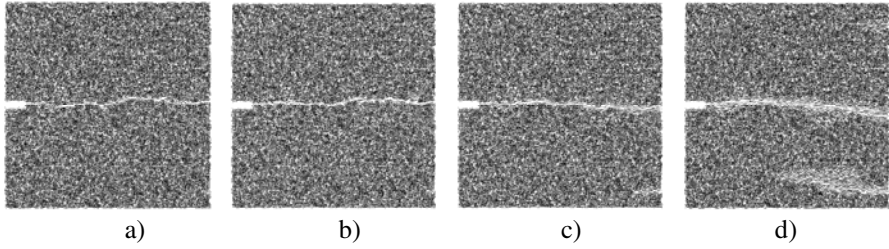
$$\omega = \frac{1}{l_c \sqrt{\pi}} e^{-(r/l_c)^2}, \quad (5.21)$$

wherein the parameter  $l_c$  is a characteristic length of micro-structure. The averaging in Eq.5.20 is restricted to a small representative area around each material point (the influence of points at the distance of  $r=3l_c$  is only of 0.01%).

Figures 5.13 and 5.14 demonstrate the results for a non-local approach during uniaxial tension with the different values of  $l_c$  ( $l_c=0 \times g$ ,  $1 \times g$ ;  $2 \times g$  and  $3 \times g$ ). The results show that the strength, normal strain corresponding to the peak and material ductility increase with increasing  $l_c$ . Therein, the computation time increased by the factor 3-5 (depending on the size of a non-local region connected with  $l_c$ ).



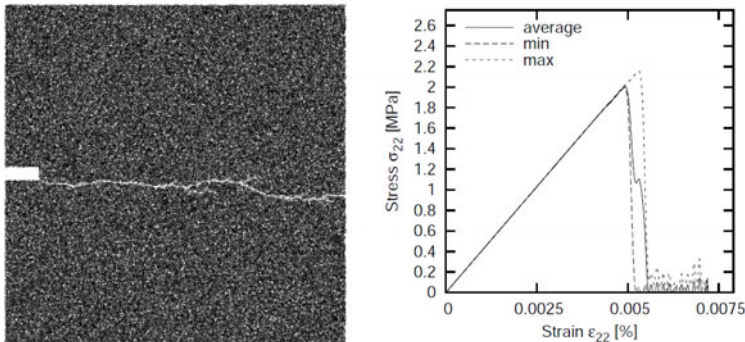
**Fig. 5.13** Effect of the characteristic length on the stress-strain curve ( $p=0.6$ , specimen  $100 \times 100 \text{ mm}^2$ ): a)  $l_c=0$  (local approach), b)  $l_c=g$ , c)  $l_c=2g$ , d)  $l_c=3g$  (non-local approach,  $\sigma_{22}$  - vertical normal stress,  $\epsilon_{22}$  - vertical normal strain) (Kozicki and Tejchman 2007b)



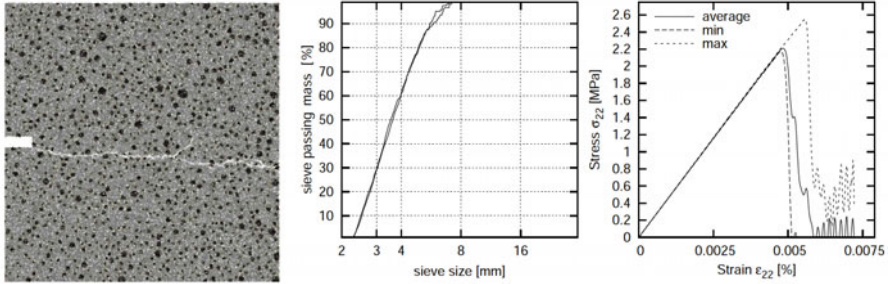
**Fig. 5.14** Effect of characteristic length  $l_c$  on fracture process (rods were removed when local  $\varepsilon_{22}=0.02\%$ ,  $p=0.6$ ): a)  $l_c=0$  (local approach), b)  $l_c=g$ , c)  $l_c=2g$ , d)  $l_c=3g$  (non-local approach) (Kozicki and Teichman 2007b)

## Two-Phase Material

Figures 5.16 and 5.17 show the effect of the aggregate on the fracture behavior of 2D specimens under uniaxial extension (without interfacial transition zones). The 2D calculations were carried out with a specimen size of  $200 \times 200 \text{ mm}^2$  ( $b \times h$ ) composed of 180'000 elements distributed non-uniformly ( $\alpha=20^\circ$ ,  $s=0.6g$ ,  $g=l_r=1.0 \text{ mm}$ ,  $r_{max}=2g$ ,  $l_r/h=1/200$ ). The minimum element length was about 0.3 mm and the maximum one was about 2 mm. The moduli of elasticity were:  $E=60 \text{ GPa}$  (aggregate) and  $E=20 \text{ GPa}$  (cement matrix), respectively (van Mier et al. 1995) which can be directly measured in laboratory tests. The ratio between the bending and longitudinal stiffness was assumed according to Fig.5.9 to obtain a realistic Poisson's ratio. The ratios between the parameters  $k_l$  and  $\varepsilon_{min}$  for the cement matrix and aggregate were assumed on the basis of ratios between the moduli of elasticity and tensile strengths, respectively, assumed by van Mier et al. (1995).



**Fig. 5.15** 2D specimen subject to uniaxial extension (one-phase material with critical local strain of  $\varepsilon_{min}=0.02\%$ ):  $p=0.7$  ( $k_l=0.1$ ) (Kozicki and Teichman 2007b)



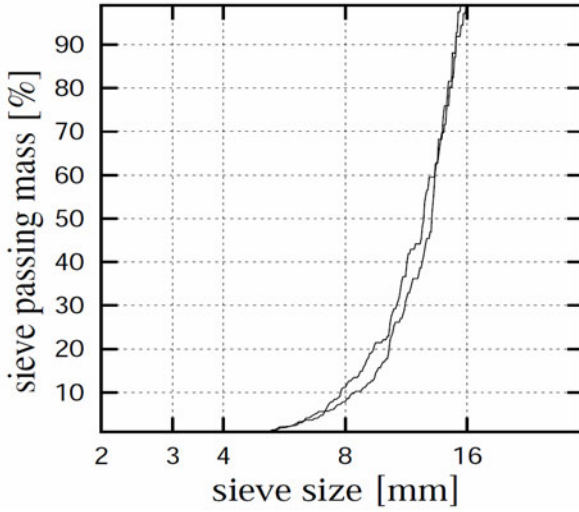
**Fig. 5.16** 2D specimen subject to uniaxial extension (two-phase material) with cement matrix:  $p_m=k_f/k_l=0.7$  (with  $k_l=0.1$  and local  $\epsilon_{min}=0.02\%$ ) and aggregate:  $p_a=k_f/k_l=0.7$  (with  $k_l=0.3$  and local  $\epsilon_{min}=0.0133\%$ ) (Kozicki and Tejchman 2007b)

The parameter  $k_l$  and  $\epsilon_{min}$  were calibrated on the basis of a uniaxial tension test to obtain a good match between theoretical and experimental results. One choose  $p_m=k_f/k_l=0.7$  (with  $k_l=0.1$ ) and  $\epsilon_{min}=0.02\%$  in the cement matrix, and  $p_a=k_f/k_l=0.7$  (with  $k_l=0.3$ ) and  $\epsilon_{min}=0.0133\%$  in the aggregate (for  $l_f=1$  mm). The particle distribution curve for aggregate is shown in Fig.5.17 with the mean aggregate diameter of  $d_{50}=3.5$  mm. The aggregate volume density was taken as 50%. The computation time was about 15 hours using the processor AMD 4600+.

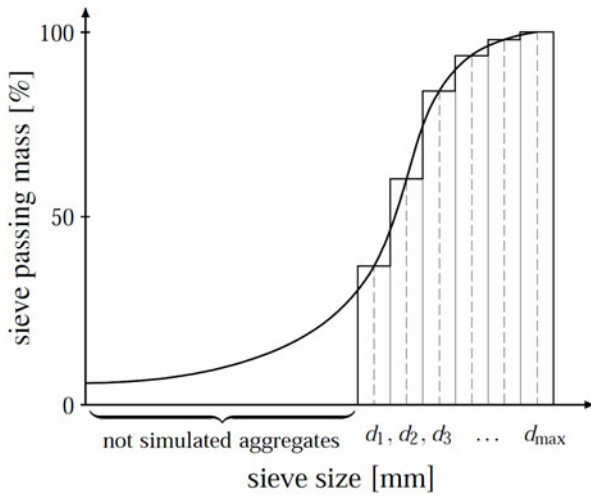
The aggregate distribution was generated following the method given by Cusatis et al. 2003, and Eckardt and Könke 2006). First, a grading curve was chosen (Fig.5.17). Next, the specified numbers of particles with defined diameters were generated according to this curve (Fig.5.18). Finally, the spheres describing aggregates were randomly placed in the specimen preserving the particle density and a certain mutual minimum distance (van Mier et al. 1995)

$$D_p > 1.1 \frac{D_1 + D_2}{2}, \quad (5.22)$$

where  $D_p$  is the distance between two neighboring particle centers and  $D_1$  and  $D_2$  are the diameters of these two particles. The results of the uniaxial tensile test in Fig.5.16 show evidently that the presence of aggregate without interfacial zones does not significantly affect the load-displacement curve in concrete which remains still too brittle as compared to experiments with concrete specimens (van Vliet and van Mier 1996, van Vliet 2000). The overall vertical strain  $\epsilon_{22}$  corresponding to the peak is about 4 times smaller than the assumed local  $\epsilon_{22}$  of cement matrix, and 10 times too large as compared to experiments (van Vliet 2000).



**Fig. 5.17** Aggregate sieve curve with  $d_{50}=12$  mm (prescribed and calculated) (Kozicki and Tejchman 2007b)

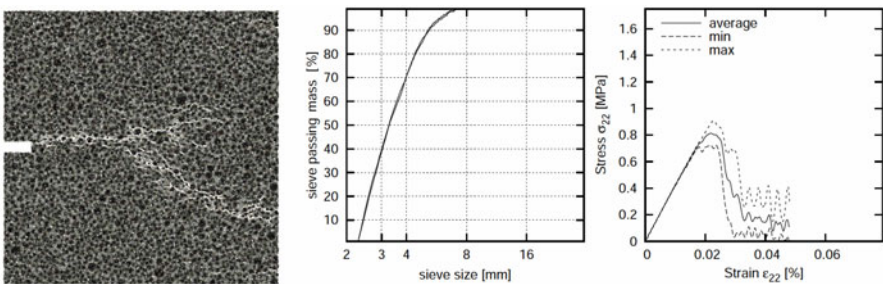


**Fig. 5.18** Approximation of the grading curve with discrete number of aggregate sizes (Cusatis et al. 2003)



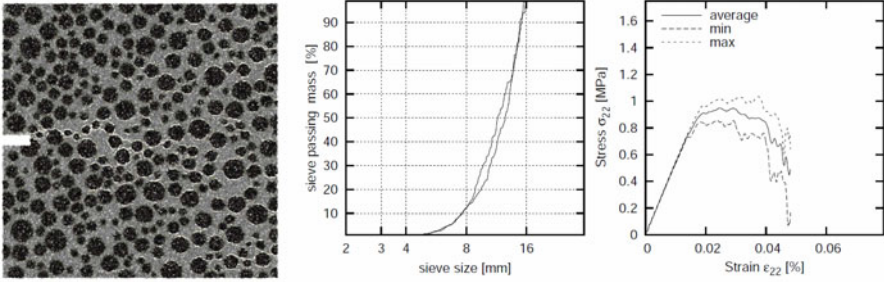
### Three-Phase Material

Figures 5.19-5.22 present the results concerning a square concrete specimen considered as a three-phase material at meso-scale. The 2D calculations were carried out mainly with a specimen size of  $200 \times 200 \text{ mm}^2$  ( $b \times h$ ) composed of 180'000 rods distributed non-uniformly ( $\alpha=20^\circ$ ,  $s=0.6g$ ,  $g=l_r=1.0 \text{ mm}$ ,  $r_{max}=2g$ ,  $l_r/h=1/200$ ). The minimum element length was about  $l_r^{min}=0.3 \text{ mm}$  and the maximum one was about  $l_r^{max}=2.0 \text{ mm}$ . The assumed material parameters are given in Tab.5.1 with the torsional stiffness parameter  $k_t$  assumed to be equal to the bending stiffness parameter  $k_b$ . The simulations with a smaller  $l_r$  did not influence the results, however greatly increased the computation time. Although the width of the interfacial transition zone between aggregate and cement matrix is only about  $50 \mu\text{m}=0.05 \text{ mm}$  (He et al. 2009), the interface is commonly regarded as a weak link in determining both the mechanical and transport properties of cement-based composites. The role of ITZ is especially important when considering concretes where the volume fractions of inclusions are high in the range 60% to 75% of the total material volume. Therefore, we also assumed that the weakest phase was bond between aggregate and cement matrix. The material parameters for the interface were assumed following van Mier et al. (1995). The parameters for the aggregate and cement matrix were chosen as for a two-phase material. The aggregate density was assumed to be 25% or 50%, respectively. The mean aggregate diameter  $d_{50}$  was taken as 3.5 mm for the aggregate size of the range 2-8 mm and 12 mm for the aggregate size of the range 2-16 mm. Five different simulations were performed for each random case. The interfacial aggregate zones ITZ were added by assigning different properties to those rods only which connected directly the aggregate with cement matrix. Thus, the ITZ thickness was varying with its mean value equal to the mean rod length  $l_r=1 \text{ mm}$ .



**Fig. 5.19** 2D concrete specimen subject to uniaxial extension (three-phase material), aggregate area percentage 50%, mean aggregate diameter  $d_{50}=3.5 \text{ mm}$ , material parameters as in Tab.5.1 ( $\sigma_{22}$  - vertical normal stress,  $\epsilon_{22}$  - vertical normal strain) (Kozicki and Teichman 2007b)





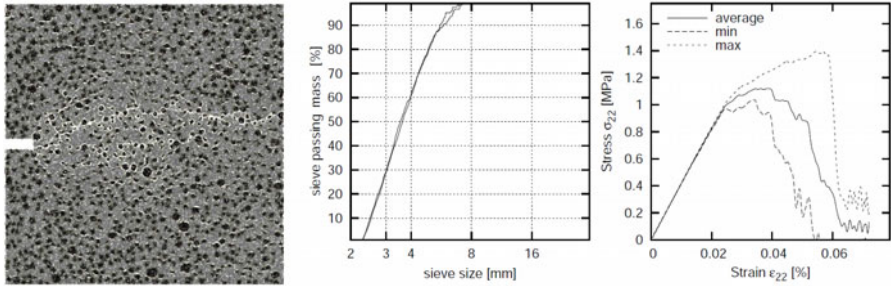
**Fig. 5.20** 2D concrete specimen subject to uniaxial extension (three-phase material), aggregate area percentage 50%, mean aggregate diameter  $d_{50}=12$  mm, material parameters as in Tab.5.1 ( $\sigma_{22}$  - vertical normal stress,  $\epsilon_{22}$  - vertical normal strain) (Kozicki and Teichman 2007b)

The effect of a stochastic distribution of rods in the lattice on the load-displacement curve is pronounced. The strength and pre-peak nonlinearity decrease with increasing aggregate density and decreasing mean aggregate diameter. In turn, the material ductility increases when the particle density increases. The vertical strain corresponding to the peak increases with decreasing particle density. At the low particle content, de-bonding occurs extensively near the isolated aggregates (most of the fractured elements are in bonds). This micro-cracking is responsible for a nonlinear behavior in the pre-peak part of the stress-strain diagram. Next, after the peak, the fracture process progressively spreads through the entire specimen in the form of a macro-crack linking de-bonded aggregates in lines. With increasing number of aggregates, the fraction of bond elements increases and de-bonding prevails. At the high particle density, percolation of bond zones occurs, and the condition for macro-crack nucleation and growth occurs early in the loading history. The material becomes significantly weaker (since the interface strength is the weakest component of the system) and the pre-peak nonlinearity does not appear. Since the amount of aggregates is large, the cracks cannot propagate in long lines. Instead of this, several discontinuous macro-cracks propagate in a tortuous manner. The cracks overlap and form branches. As a result, the material ductility grows after the peak.

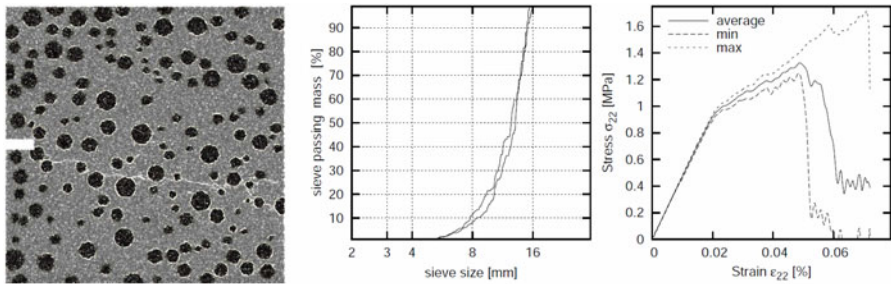
All curves with consideration of interfacial transition zones resemble qualitatively the experimental curves for real concrete (van Vliet 2000). The uniaxial tensile strength changes between 0.7-1.7 MPa. The scatter of the material strength increases with decreasing particle density due to the larger possibility at the choice of the propagation way. The vertical strain corresponding to the peak varies between 0.02%-0.06%.

Figure 5.23 shows the number of rods removed during each iteration under uniaxial tension with the sieve curve, particle content and average rod length as in Fig.5.19 and the specimen size of  $10 \times 10$  cm<sup>2</sup>. The maximum number of iterations

was about 50'000. The maximum number of rods simultaneously reaching the threshold tensile strain in a single iteration was about 7.



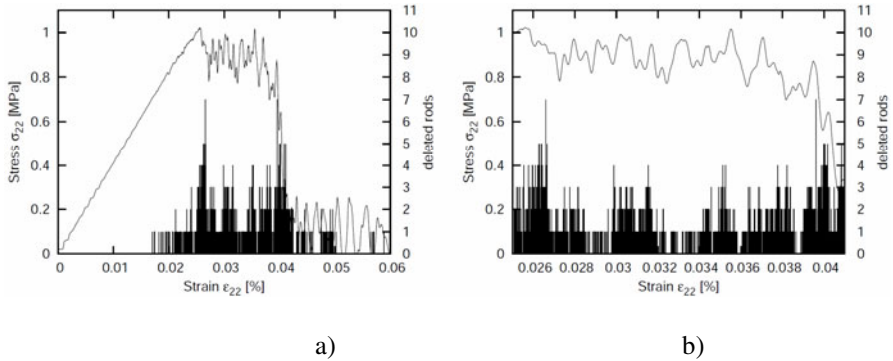
**Fig. 5.21** 2D concrete specimen subject to uniaxial extension (three-phase material), aggregate area percentage 25%, mean aggregate diameter  $d_{50}=3.5$  mm, material parameters as in Tab.5.1 ( $\sigma_{22}$  - vertical normal stress,  $\epsilon_{22}$  - vertical normal strain) (Kozicki and Tejchman 2007b)



**Fig. 5.22** 2D concrete specimen subject to uniaxial extension (three-phase material), aggregate area percentage 25%, mean aggregate diameter  $d_{50}=12$  mm, material parameters as in Tab.5.1 ( $\sigma_{22}$  - vertical normal stress,  $\epsilon_{22}$  - vertical normal strain) (Kozicki and Tejchman 2007b)

**Table 5.1** Parameters used in calculations with three-phase material (Kozicki and Tejchman 2007b)

Phase	Modulus of elasticity $E$ [GPa]	$k_i$	$p=k_i/k_i$	threshold local strain $\epsilon_{min}$ [%]
Cement matrix	20	0.010	0.7	0.2
Aggregate	60	0.030	0.7	0.133
Interface bond	14	0.007	0.7	0.05

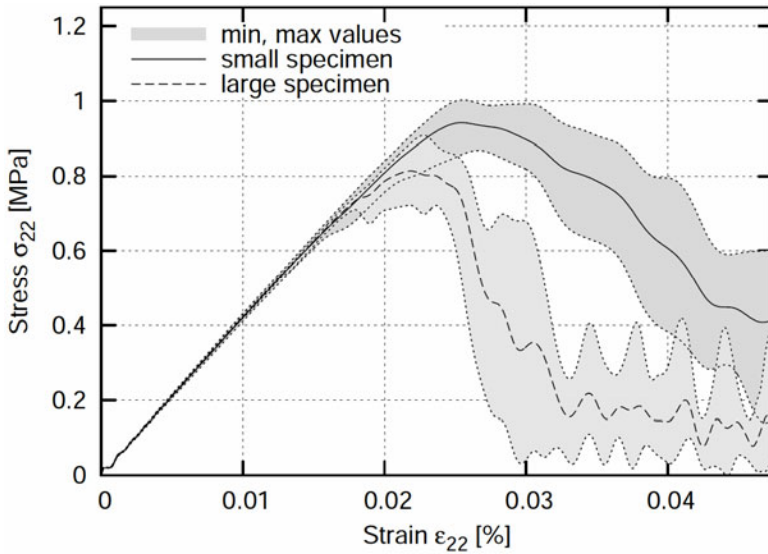


**Fig. 5.23** Stress–strain curve for uniaxial extension and the number of rods removed in each iteration: a) entire curve, b) curve in the range of  $\varepsilon_{22}=0.025\div 0.041$  ( $\sigma_{22}$  – vertical normal stress,  $\varepsilon_{22}$  – vertical normal strain) (Kozicki and Tejchman 2007b)

Finally, Figures 5.24 and 5.26 show a deterministic size effect during uniaxial tension (with the grading curve of Fig.5.19,  $l_r=1$  mm). Several numerical simulations were carried out with two different rectangular concrete specimens:  $10\times 10$  cm<sup>2</sup> and  $20\times 20$  cm<sup>2</sup> using the same rod distribution for each specimen. The results show that the material strength and ductility increase with decreasing specimen size as in the experiments (Fig.5.24) while the crack pattern remains similar (Fig.5.26). In turn, the fracture energy decreases. The obtained results from numerical experiments for uniaxial tension are only qualitatively in agreement with experimental results given by and van Vliet (2000), Lilliu and van Mier (2003), van Mier and van Vliet (2003 (Fig.5.25). They cannot be directly compared with each other due to the lack of the information on the concrete micro-structure (aggregate density, aggregate size, aggregate roughness, thickness of contact zones) in experiments.

Figure 5.27a shows schematically a shear-extension test to obtain a mixed-mode of a fracture (Nooru-Mohamed 1992). This test is frequently used as a benchmark test to check the ability of constitutive models to simulate curved cracks (Gasser and Holzapfel 2006). A double-notched prism (200 mm $\times$ 200 mm $\times$ 50 mm) with two 25 mm deep notches was loaded first in shear and then in tension. Various proportional and non-proportional loading paths were followed by controlling both displacement and load (Nooru-Mohamed 1992). First, the horizontal shear force  $F_S$  was increased up to a certain value, while the vertical tensile force  $F_T$  was kept zero. Afterwards, the horizontal force  $F_S$  was kept constant, while the tensile force  $F_T$  was applied under a displacement control until the specimen failed completely. In experiments, the horizontal force  $F_S$  was kept

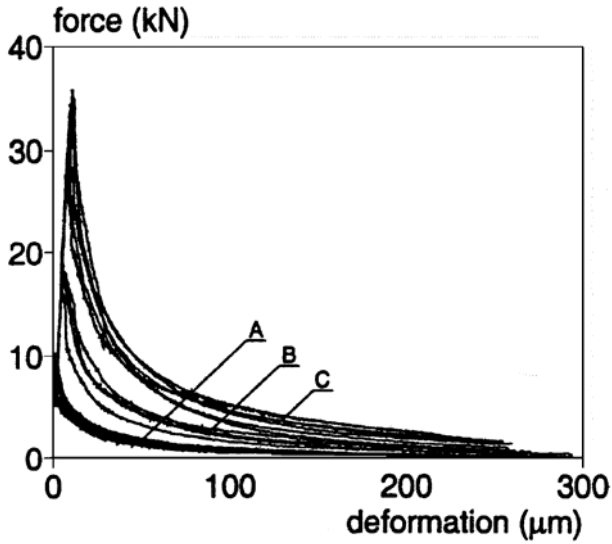
constant at  $F_S=5 \text{ kN} \approx F_{S,max}/6$ ,  $F_S=10 \text{ kN} \approx F_{S,max}/3$  and  $F_S=27.38 \text{ kN} = F_{S,max}$ , where  $F_{S,max}$  is the maximum force that the specimen could sustain in the absence of a tensile force. Because of a specific loading protocol, the principal stresses rotated during a test resulting in two curvilinear cracks, whose curvature depended upon  $F_S$ . The experimental cracks during a loading path with  $F_S=F_{S,max}$  is demonstrated in Figure 5.27b. If the force  $F_S$  becomes smaller with respect to  $F_{S,max}$ , the main cracks are more flat.



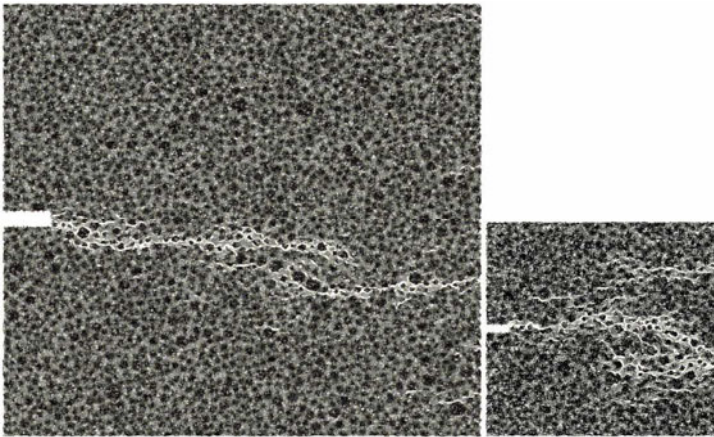
**Fig. 5.24** Deterministic size effect for 2D concrete specimens subject to uniaxial extension with sizes  $10 \times 10 \text{ cm}^2$  (small specimen) and  $20 \times 20 \text{ cm}^2$  (large specimen), aggregate area percentage 50%, mean aggregate diameter  $d_{50}=3.5 \text{ mm}$ , material parameters as in Tab.5.1 (Kozicki and Tejchman 2007b)

In the calculations, a different value of the stiffness parameter  $k_b$  was used both in compression ( $k_{b,compression}$ ) and in tension ( $k_{b,tension}$ ) (Fig.5.28a) to obtain numerical outcomes of the crack curvature more close to experimental ones. For the sake of simplicity, we assumed the same ratio of  $p=k_b/k_l$  ( $p_{compression}=0.2$  and  $p_{tension}=0.6$ ) for all concrete phases ( $p_m=p_a=p_b$ ). The chosen ratio  $p$  resulted in the following Poisson's ratio: 0.22 (uniaxial compression) and 0.07 (uniaxial tension) (Figs.5.9 and 5.28b).

All material parameters are listed in Table 5.2 for a one-phase material and in Table 5.3 for a three-phase material.

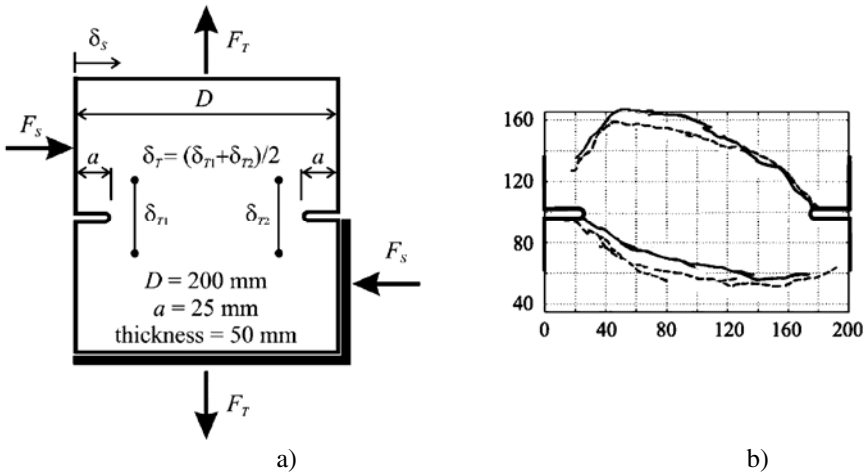


**Fig. 5.25** Experimental force-deformation diagram for 3 different dog-bone shaped specimens  $h \times b$ : A)  $75 \times 50 \text{ mm}^2$ , B)  $150 \times 75 \text{ mm}^2$ , C)  $300 \times 200 \text{ mm}^2$  ( $h$  - height,  $b$  - width) (van Vliet 2000)

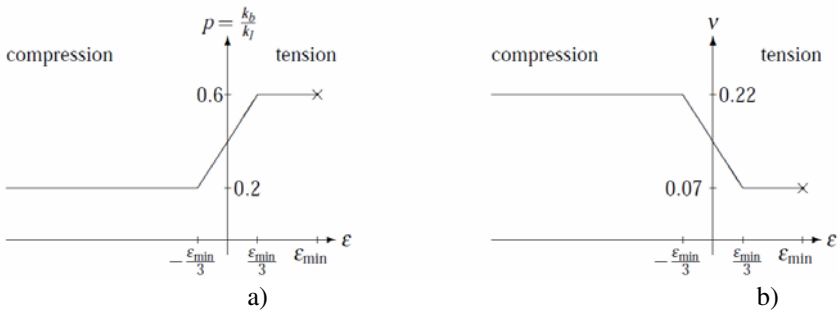


**Fig. 5.26** Calculated fracture in 2 concrete specimens of different size:  $20 \times 20 \text{ cm}^2$  and  $10 \times 10 \text{ cm}^2$  (Kozicki and Tejchman 2007b)

Figure 5.29 shows the 2D results where concrete was modeled as a one-phase (Tab.5.2) and a three-phase material (Tab.5.3) using different values of the ratio  $p$ . The specimen included 50'000 elements with a mean rod length  $l_r = 1.0 \text{ mm}$ .



**Fig. 5.27** Shear-extension test: a) test description (schematically), b) experimental crack pattern (Nooru-Mohamed 1992)

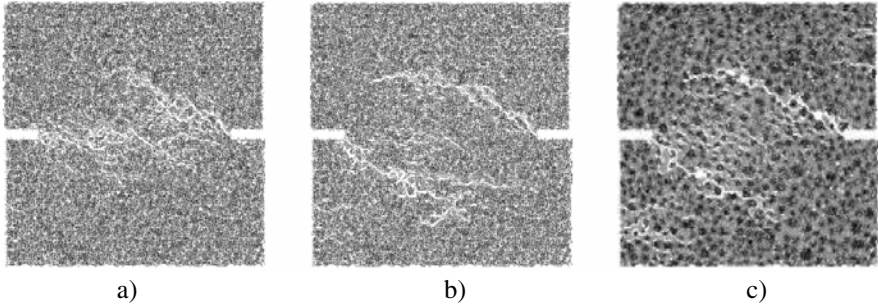


**Fig. 5.28** Shear-extension test: a) assumed change of ratio  $p=k_b/k_l$ , b) resulting Poisson's ratio of the lattice versus strain  $\epsilon_{min}$  (Kozicki and Tejchman 2008)

The results indicate that the ratio  $=k_b/k_l$  has a significant influence on the inclination of the main curved cracks. For  $p=0$  (Fig.5.29a), the cracks are too flat, and the material behavior corresponds to that composed of pure rods. When  $p=0.6$ , a correct shape of 2 main cracks is generated (Fig5.29) for both a one-phase and a three-phase material.

Figure 5.30 demonstrates the effect of the horizontal force  $F_s$  on the crack pattern changing between  $0.3F_{s,max}$  and  $F_{s,max}$  (with parameters as in Tab.5.3: three-phase material,  $p_{compression}=0.2$ ,  $p_{tension}=0.6$ ). The calculated cracks of Figs.5.30b and 5.30f correspond well to those for the experimental loading paths (Nooru-Mohamed 1992). Similarly, as in the experiments, the inclination angle of

curved cracks decreases with decreasing  $F_s$ . Figure 5.31 shows a comparison between the calculated and experimental normal force  $F_T$ . The calculated force is too large.



**Fig. 5.29** Fracture in specimen during shear-extension test: a) one-phase material with  $p=0$ , b) one-phase material with  $p=0.6$ , c) three-phase material with  $p=0.6$  for all phases (Kozicki and Teichman 2008)

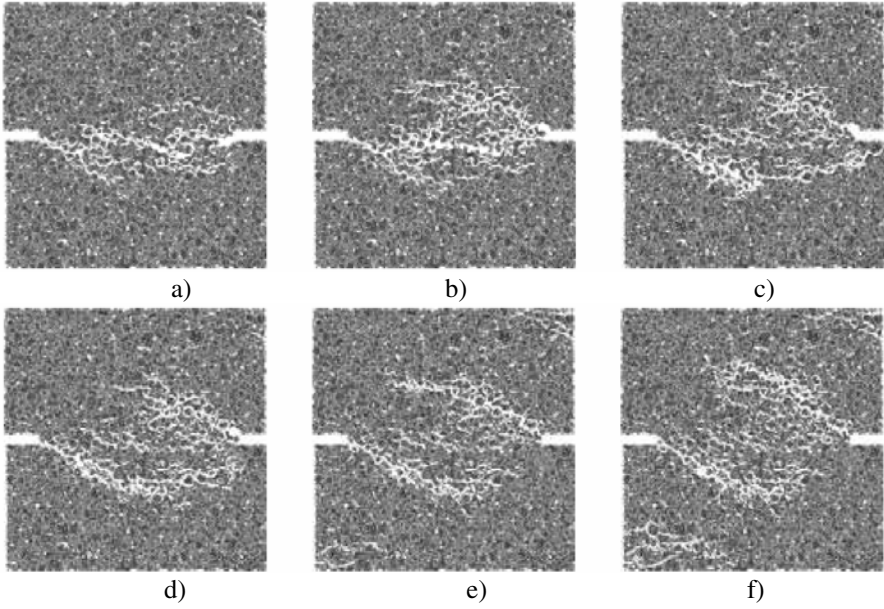
**Table 5.2** Material parameters used in calculations (one-phase material) (Kozicki and Teichman 2008)

	Modulus of elasticity $E$ [GPa]	$p_{tension}$	$p_{compression}$	$k_l$	Threshold local strain $\epsilon_{min}$ [%]
One-phase Material	20	0.6	0.2	0.01	0.2

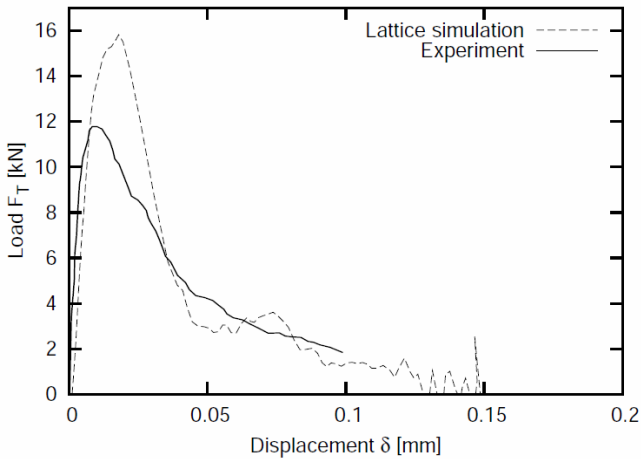
**Table 5.3** Material parameters used in calculations (three-phase material,  $k_l=k_b$ ) (Kozicki and Teichman 2008)

	Modulus of elasticity $E$ [GPa]	$p_{tension}$	$p_{compression}$	$k_l$	Threshold local strain $\epsilon_{min}$ [%]
Cement matrix	20	0.6	0.2	0.01	0.2
Aggregate	60	0.6	0.2	0.03	0.133
Interface bond	14	0.6	0.2	0.007	0.05





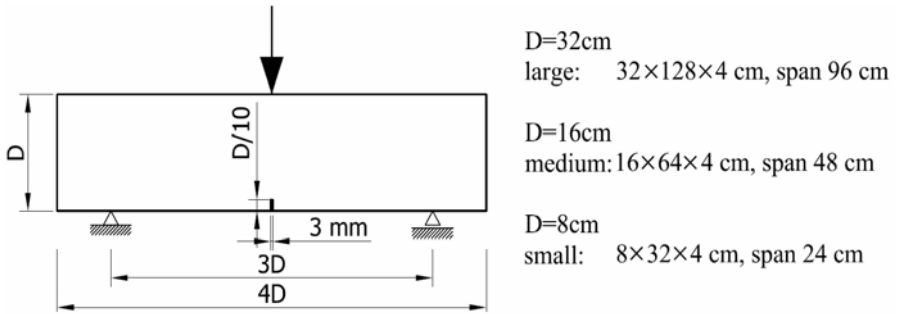
**Fig. 5.30** Fracture in specimen during shear–extension test for different values of horizontal force  $F_S$  in three-phase material: a)  $F_S=0.3F_{S,max}$ , b)  $F_S=0.35F_{S,max}$ , c)  $F_S=0.38F_{S,max}$ , d)  $F_S=0.5F_{S,max}$ , e)  $F_S=0.75F_{S,max}$ , f)  $F_S=F_{S,max}=26$  kN (Kozicki and Tejchman 2008)



**Fig. 5.31** Shear-extension test: comparison between 2D simulation (Kozicki and Tejchman 2008) and experiment by Nooru-Mohamed (1992) with two very curved cracks



The 2D simulations of three-point bending were compared with the results of own model tests (Kozicki and Tejchman 2007a) performed with 18 notched concrete beams of a different size under three-point bending (with free beam ends). Figure 5.32 shows the geometry of 3 geometrically similar concrete beams with a different cross-section and the same depth of 40 mm (the same geometry was assumed in laboratory experiments by Le Bellego et al. 2003). The beam height  $D$  was 80 mm (small-size beam), 160 mm (medium-size beam) and 320 mm (large-size beam), respectively. A notch of the depth of  $D/10$  mm and thickness of 3 mm was placed in the middle of the beam bottom. The beam deformation was induced by a vertical displacement prescribed at the mid-span with a rate of 0.01 mm/min. The concrete composition consisted of 70% gravel, 17% cement and 7% water using ordinary Portland cement and aggregate with a mean grain diameter of  $d_{50}=2.0$  mm. During experiments, load-deflection curves were registered and a fracture zone width was measured with a displacement gauge placed above the notch (Kozicki and Tejchman 2007a).

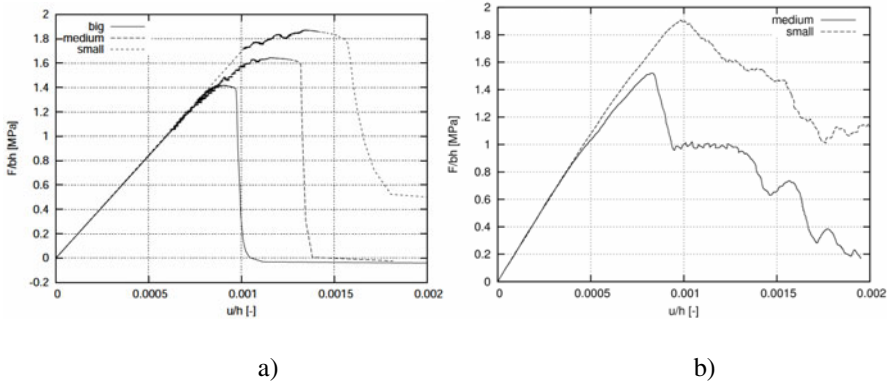


**Fig. 5.32** Geometry of concrete beams subjected to three-point bending (Kozicki and Tejchman 2007a)

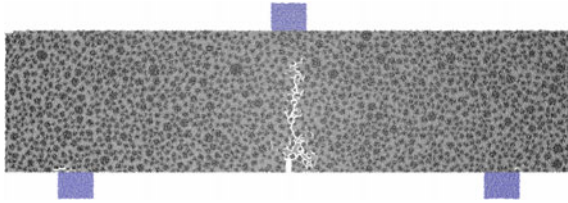
Figure 5.33 presents the experimental load-displacement curves compared with the calculated ones. In turn, Figs.5.34 and 5.35 demonstrate a crack pattern for a medium- and small-size beam. The 2D calculations were carried out with 200'000 rods with a mean length of  $l_r=1.0$  mm.

The ultimate vertical forces (Fig.5.33b) and crack patterns (Figs.5.34 and 5.35) are in a qualitative agreement with the experimental curves. The initial stiffness is also similar as in the experiment. Evident discrepancies between experiments and numerical results occur after the peak. It is due to difficulties related to the force measurement in our experiment after the peak against the beam deflection (Kozicki and Tejchman 2007a). The larger the beam, the smaller is the strength

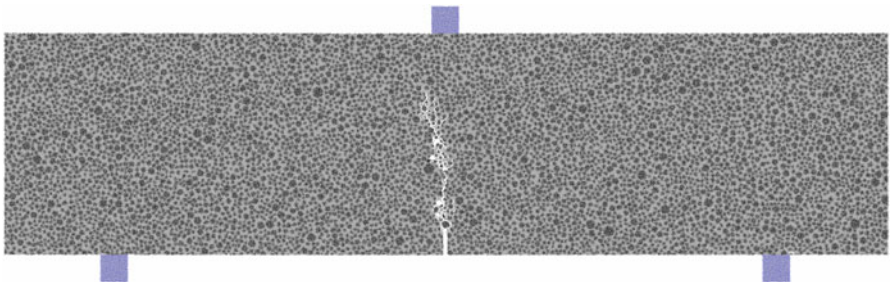
and the larger the brittleness. A main non-symmetric crack obviously occurs directly above the notch.



**Fig. 5.33** Load-displacement curves ( $u$  – beam deflection,  $b$  – beam depth,  $h$  – beam height): a) experimental nominal strength versus normalized deflection  $u/h$ , b) calculated nominal strength versus normalized deflection  $u/h$  (Kozicki and Tejchman 2008)

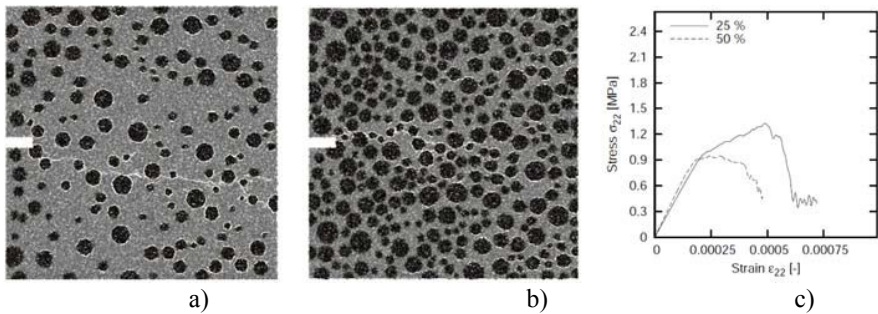


**Fig. 5.34** Calculated crack pattern during three-point bending (small-size beam) (Kozicki and Tejchman 2008)

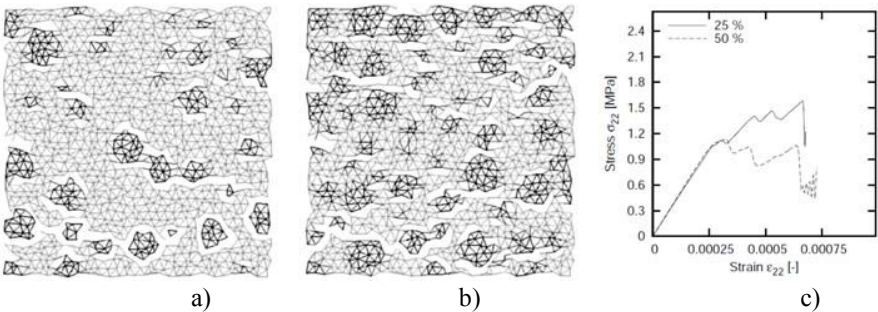


**Fig. 5.35** Calculated crack pattern during three-point bending (medium-size beam) (Kozicki and Tejchman 2008)

Figures 5.36-5.39 demonstrate the results of comparative 2D and 3D simulations with a square (2D simulation) and cubic (3D simulation) concrete specimen represented as a three-phase material with the material parameters of Tab.5.3. The 2D calculations were carried out with a specimen size of  $10 \times 10 \text{ cm}^2$  ( $b \times h$ ) including 50'000 elements with a mean rod length  $l_r=1 \text{ mm}$  ( $l_r/h=1/100$ ) (Fig.5.36) and 6'000 elements with a mean rod length  $l_r=3 \text{ mm}$  ( $l_r/h=1/33$ ) (Fig.5.37), which were non-uniformly distributed. The calculations lasted from 1 up to 4 hours using PC 3.6 GHz. In turn, the 3D calculations were performed with a specimen size of  $10 \times 10 \times 10 \text{ cm}^3$  including 400'000 elements with an average length equal to  $l_r=3 \text{ mm}$  (Fig.5.38) and distributed non-uniformly ( $l_r/h=1/33$ ). In this case, the calculations took 1 day. The torsional stiffness parameter  $k_t$  was again equal to the bending stiffness parameter  $k_b$ .



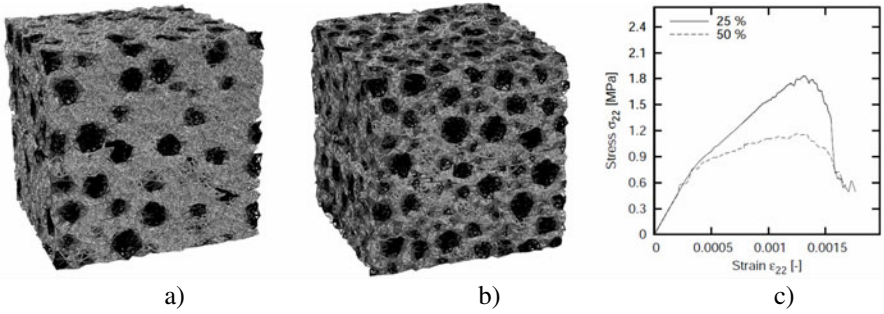
**Fig. 5.36** 2D concrete specimen subject to uniaxial extension with average element length of  $l_r=1.0 \text{ mm}$  ( $l_r/h=1/100$ ): a) aggregate density 25%, b) aggregate density 50%, c) stress-strain curve ( $\sigma_{22}$  - vertical normal stress,  $\epsilon_{22}$  - vertical normal strain) (Kozicki and Tejchman 2008)



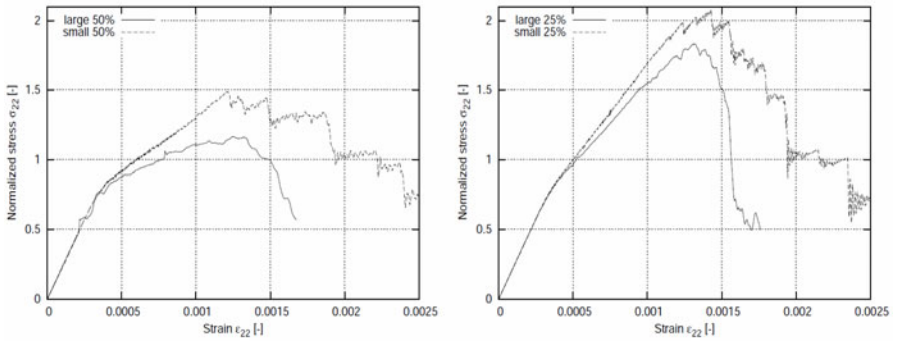
**Fig. 5.37** 2D concrete specimen subject to uniaxial extension with average element length of  $l_r=3.0 \text{ mm}$  ( $l_r/h=1/33$ ): a) aggregate density 25%, b) aggregate density 50%, c) stress-strain curve ( $\sigma_{22}$  - vertical normal stress,  $\epsilon_{22}$  - vertical normal strain) (Kozicki and Tejchman 2008)

The numerical results demonstrate that the material ductility increases with increasing aggregate density. The vertical strain corresponding to the peak increases with decreasing particle density. It varies between 0.0002–0.0006. At the low particle content, de-bonding occurs extensively near the isolated aggregates (most of fractured elements are in bonds). It is caused by the fact that the interface has the lowest strength. This micro-cracking is responsible for the non-linear behavior in the pre-peak part of the stress-strain diagram. Next, after the peak, the fracture process progressively spreads through the entire specimen in the form of a macro-crack linking de-bonded aggregates in lines. With increasing number of aggregates, the fraction of bond elements increases and de-bonding prevails. At the high particle density, percolation of bond zones occurs, and the condition for macro-crack nucleation and growth occurs early in the loading history. The material becomes significantly weaker (since the interface strength is the weakest component of the system) and the pre-peak non-linearity does not appear. Since the number of aggregates is large, the cracks cannot propagate in long lines. Instead of this, several discontinuous macro-cracks propagate in a tortuous way. The cracks overlap and form branches. As a result, the material ductility grows after the peak. All curves with consideration of interfacial transition zones resemble qualitatively the experimental curves for real concrete specimens (van Vliet 2000). The uniaxial tensile strength changes between 0.9–1.7 MPa. The scatter of the material strength increases with decreasing particle density due to a larger possibility at the choice of the propagation way. The 3D results (Fig.5.38) with a mean rod length of 3 mm are qualitatively similar to 2D results with a mean rod length of 1 mm owing to that in both simulations a large amount of rods was used. In 3D simulations, the tensile strength is higher by 10-20% and the vertical strain corresponding to the peak is almost 3 times larger. In turn, the 3D results are completely different than 2D results with the same average element length of 3 mm, since the number of rods in 2D simulation is simply too small to properly describe a fracture process (less branching and bridging in the crack pattern is expected). Each local instability on the stress-strain curve (expressed by a "zig-zag" behavior) corresponds to the removal of damaged rods. A similar behavior also occurs in 3D specimens with a small aggregate content (Fig.5.39a).

Figure 5.39 shows the calculated size effect in two 3D cubic specimens:  $5 \times 5 \times 5 \text{ cm}^3$  and  $10 \times 10 \times 10 \text{ cm}^3$  (with an average rod length of  $l_r=3 \text{ mm}$ ,  $l_r/h=1/33-1/17$  and material parameters from Tab.5.3). The specimens had 50'000 (smaller specimen) and 400'000 rods (larger specimen), respectively. The larger the specimen, the smaller is the strength and the larger is the brittleness. The obtained outcome of the size effect for uniaxial tension is qualitatively in agreement with experiments (van Vliet 2000).



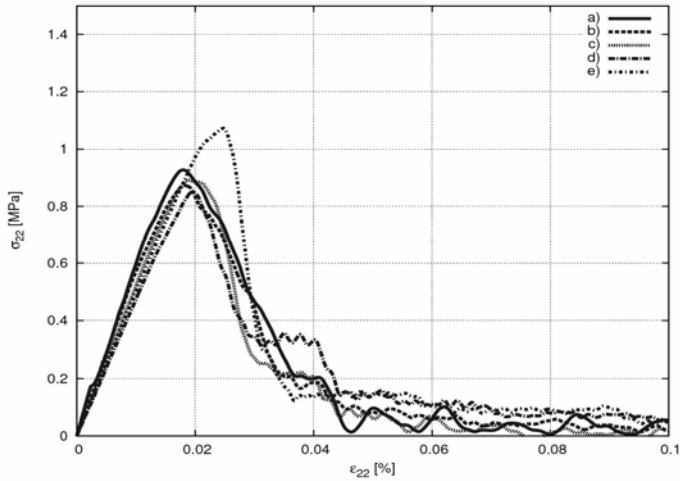
**Fig. 5.38** 3D concrete specimen subject to uniaxial extension with average rod length of  $l_r=3$  mm ( $l_r/h=1/33$ ): a) aggregate density 25%, b) aggregate density 50%, c) stress-strain curve ( $\sigma_{22}$  - vertical normal stress,  $\epsilon_{22}$  - vertical normal strain) (Kozicki and Tejchman 2008)



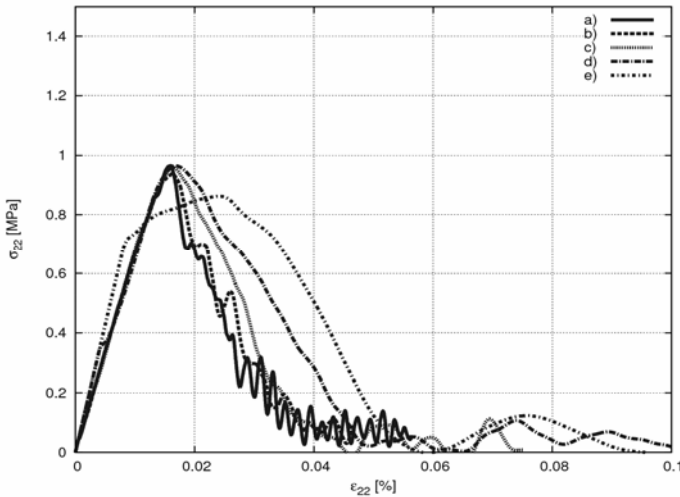
**Fig. 5.39** Size effect obtained for 3D specimens  $10 \times 10 \times 10$  cm<sup>3</sup> (lower curve) and  $5 \times 5 \times 5$  cm<sup>3</sup> (upper curve) with average rod length of  $l_r=3$  mm and aggregate density 50% (a) and 25% (b) ( $\sigma_{22}$  - vertical normal stress,  $\epsilon_{22}$  - vertical normal strain) (Kozicki and Tejchman 2008)

Finally, Figs.5.40 and 5.41 show the effect of the mean rod length  $g=l_r$  and global critical strain increment  $\Delta \epsilon_{crit}^{gl}$  (Eq.5.6) on the mean stress-strain curve during uniaxial tension of a notched concrete three-phase specimen of  $20 \times 20 \times 20$  cm<sup>3</sup>. 5 different simulations were performed for each different  $l_r$ . The same rod distribution was assumed for the different  $\Delta \epsilon_{crit}^{gl}$ .

The stress-strain curves for  $l_r=1-4$  mm ( $l_r/h=1/200-1/50$ ) and for  $\Delta \epsilon_{crit}^{gl}=500-2000$  are similar.



**Fig. 5.40** Effect of mean rod length  $l_f$  on mean stress-strain curve during uniaxial tension ( $\Delta \varepsilon_{crit}^{gl}=500$ , specimen  $20 \times 20 \times 20 \text{ cm}^3$ ): a)  $l_f=1.0 \text{ mm}$ , b)  $l_f=2.0 \text{ mm}$ , c)  $l_f=3.0 \text{ mm}$ , d)  $l_f=4.0 \text{ mm}$ , e)  $l_f=5.0 \text{ mm}$  ( $\sigma_{22}$  - vertical normal stress,  $\varepsilon_{22}$  - vertical normal strain)



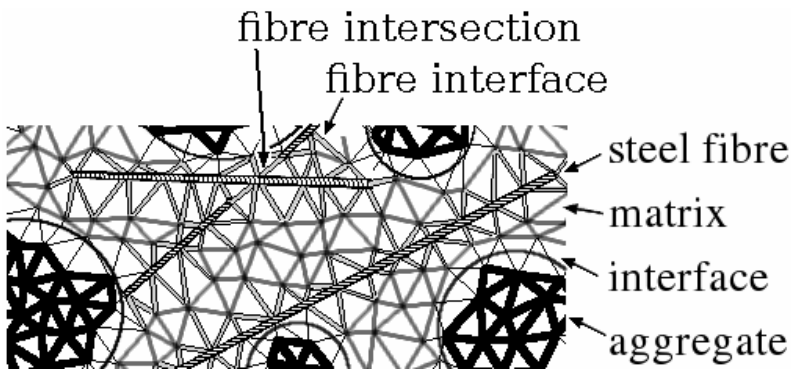
**Fig. 5.41** Effect of critical global strain increment  $\Delta \varepsilon_{crit}^{gl}$  on mean stress-strain curve during uniaxial tension ( $l_f=1.0 \text{ mm}$ ,  $20 \times 20 \times 20 \text{ cm}^3$ ): a)  $\Delta \varepsilon_{crit}^{gl}=2000$ , b)  $\Delta \varepsilon_{crit}^{gl}=1000$ , c)  $\Delta \varepsilon_{crit}^{gl}=500$ , d)  $\Delta \varepsilon_{crit}^{gl}=250$ , e)  $\Delta \varepsilon_{crit}^{gl}=100$  ( $\sigma_{22}$  - vertical normal stress,  $\varepsilon_{22}$  - vertical normal strain)

## 5.2 Simulations of Fracture Process in Fibrous Concrete

The discrete calculations of uniaxial tension and three-point bending were performed with fibrous concrete specimens using a lattice model. The effect of straight steel fibres only was investigated. Due to the lack of information concerning micro-structure of concrete and distribution of fibres, the results were compared qualitatively with the corresponding experiments only (Section 3.1.1). In calculations, non-local terms (Eqs.5.19 and 5.20) were not considered.

In the 2D and 3D discrete calculations, different properties were prescribed to lattice elements to simulate the concrete behaviour composed of aggregate, cement matrix, fibres, bond between aggregate and cement matrix, and bond between fibres and cement matrix (Fig.5.42, Tab.5.4).

The interfacial cement matrix-aggregate zones were distinguished by assigning different properties to rods which connected directly the aggregate with the cement matrix (their mean width was  $g=1$  mm or  $g=2$  mm). In turn, the interfacial cement matrix-fibre zones were distinguished by assigning different properties to rods which connected directly the steel fibres with the cement matrix or two different fibres (their mean width was also  $g=1$  mm or  $g=2$  mm). The width of interfaces connecting the aggregate and fibres with the cement matrix was thus varying and equal always to the rod length connecting the corresponding concrete phases.



**Fig. 5.42** Lattice composed of rods to model five phases of concrete: fibres, aggregate, cement matrix and interfaces between aggregate and cement matrix and between fibres and cement matrix (Kozicki and Tejchman 2010)

The mean aggregate diameter was assumed to be  $d_{50}=12$  mm. The aggregate volume or aggregate area percentage was assumed to be 60%. The fibre volume was  $V_f=0.0\%$  (plain concrete),  $V_f=0.15\%$  and  $V_f=1.5\%$ , respectively in 3D simulations. In turn, the fibre area was in 2D analyses:  $A_f=0.0\%$  (plain concrete),

$A_f = 0.15\%$  and  $A_f = 1.5\%$ . The minimum rod length was 0.2-0.4 mm and the maximum one was 2-4 mm ( $l_r = 1.0$  mm or  $l_r = 2.0$  mm on average) in 2D calculations. In 3D calculation, the minimum rod length was 1.2 mm and the maximum one was 4 mm ( $l_r = 2$  mm on average). The size of the 2D concrete specimens was  $5 \times 5$  cm<sup>2</sup>,  $10 \times 10$  cm<sup>2</sup> and  $20 \times 20$  cm<sup>2</sup>, respectively ( $l_r/h = 1/50$ - $1/200$  with  $l_r = 1$  mm,  $l_r/h = 1/25$ - $1/100$  with  $l_r = 2$  mm). In turn, the size of the 3D concrete specimens was  $5 \times 5 \times 5$  cm<sup>3</sup> or  $10 \times 10 \times 10$  cm<sup>3</sup> ( $l_r/h = 1/25$ - $1/100$ ). The number of rods was 170'000 (3D specimen  $5 \times 5 \times 5$  cm<sup>3</sup>), 1'400'000 (3D specimen  $10 \times 10 \times 10$  cm<sup>3</sup>), 8'000 (2D specimen  $5 \times 5$  cm<sup>2</sup>), 36'000 (2D specimen  $10 \times 10$  cm<sup>2</sup>) and 140'000 (specimen  $20 \times 20$  cm<sup>2</sup>), respectively. A length of straight steel fibres changed between  $l_f = 10$  mm and  $l_f = 60$  mm. The mean fibre width  $b_f$  (2D simulations) or fibre diameter  $d_f$  (3D simulations) corresponded exactly to the grid parameter  $g$  equal to the mean rod length  $g = l_r = 1$  mm or  $g = l_r = 2$  mm.

Table 5.4 includes the material parameters assumed in all phases for numerical 2D and 3D analyses (on the basis of the data for plain concrete from Table 5.3). We again assumed that the weakest phase was bond between aggregate and cement matrix. In the case of the cement matrix-fibre interface, the different interface strength was taken into account by changing the threshold local tensile strain  $\varepsilon_{min}$  (Tab.5.4) (with the values of  $E$  and  $p$  in the cement matrix-fibre interface as in the cement matrix-aggregate interface). The torsional stiffness parameter was always  $k_t = k_b$  in all phases ( $k_b$  - bending stiffness parameter). A different value of the ratio  $p$  in tension and compression (Tab.5.4) influences the crack shape during a mixed shear-extension mode (Tab.5.3, Figs.5.29-5.30) and during compression (Kozicki 2007). For pure extension, a different ratio  $p$  in tension and compression has no effect on results.

We considered the following 4 cases in calculations:

- A) no interface between fibres and cement matrix (interfacial properties were the same as for the cement matrix),
- B) the strength of the cement matrix-fibre interface was smaller than the strength of cement matrix-aggregate interface (threshold local tensile strain in the cement matrix-fibre interface was  $\varepsilon_{min} = 0.025\%$ ),
- C) the strength of the cement matrix-fibre interface was equal to the strength of cement matrix-aggregate interface ( $\varepsilon_{min} = 0.05\%$ ),
- D) the strength of the cement matrix-fibre interface was stronger than the strength of cement matrix-aggregate interface ( $\varepsilon_{min} = 0.1\%$ ,  $\varepsilon_{min} = 0.5\%$ ,  $\varepsilon_{min} = 1.0\%$ ).

The material parameters for rigid steel fibres were chosen as follows (Tab.5.4):  $E = 160$  GPa,  $p = 0.6$  (tension) and  $p = 0.2$  (compression),  $k_t = 0.08$  and  $\varepsilon_{min} = 90\%$ .

During an initial process of forming of a 3D fibrous concrete specimen (Fig.5.43), steel fibres were first distributed at random positions within the specimen. Next, a so-called iterative repulsion algorithm was used. Each steel fibre was described with 20 points (it was divided into 19 equal parts) and each sphere was represented by a single point. The fibre points were subjected to repulsion from other fibre points and specimen boundaries inversely proportional to the squared distance between two points. As a result, a random distribution of



fibres in the entire specimen was obtained. Next, the number of spheres with a different diameter was calculated according to Figs.5.17 and 5.18 to fit a prescribed granulometric curve. The spheres were inserted at random positions into a concrete specimen by ignoring fibre and sphere overlaps. Afterwards, a repulsion procedure was again used, if an overlap was detected (sphere to sphere or sphere to fibre) in order to satisfy Eq.5.22. This quasi-static algorithm simulated a process of sphere compaction up to the aggregate volume of 60%-70%.

**Table 5.4** Material parameters used in 2D and 3D calculations of fibrous concrete at meso-scale with  $k_t=k_b$  (Kozicki and Tejchman 2010)

Concrete Phase	Modulus of elasticity $E$ [GPa]	Stiffness ratio $p=k_t/k_l$ (tension)	Stiffness ratio $p=k_t/k_l$ (compression)	Stiffness parameter $k_l$	Threshold local tensile strain $\epsilon_{min}$ [%]	Cement matrix-fibre interface type
Cement matrix	20	0.6	0.2	0.01	0.2	A)-D)
Aggregate inclusions	60	0.6	0.2	0.03	0.133	A)-D)
Cement matrix-aggregate interface	14	0.6	0.2	0.007	0.05	A)-D)
Cement matrix-fibre interface	20	0.6	0.2	0.01	0.2	A)
	14	0.6	0.2	0.007	0.025	B)
	14	0.6	0.2	0.007	0.05	C)
	14	0.6	0.2	0.007	0.1	D)
	14	0.6	0.2	0.007	0.5	D)
	14	0.6	0.2	0.007	1.0	D)
Steel fibres	160	0.6	0.2	0.08	90	A)-D)

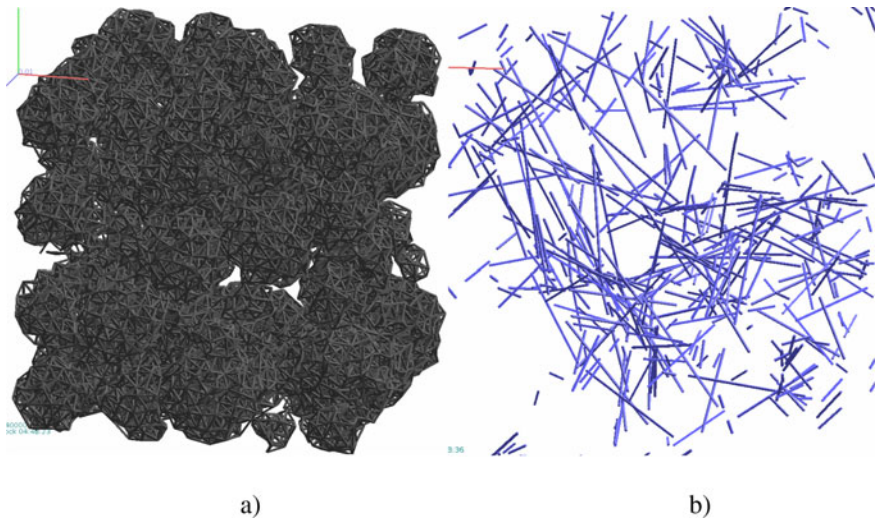
In 2D calculations, the fibres could intersect with each other (Fig.5.42). If two fibres cross each other, then one of them was split into two parts (Fig.5.42).

### 5.2.1 Two-Dimensional Simulations of Uniaxial Extension

#### Effect of Fibrous Bond Strength

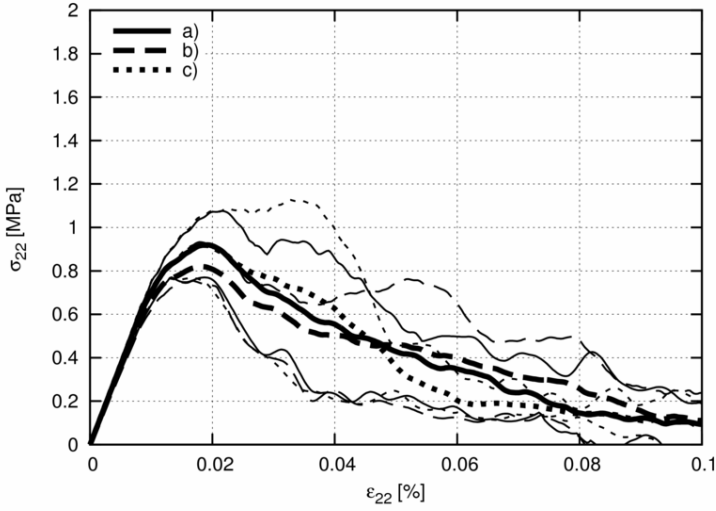
The results of stress-strain curves during quasi-static uniaxial tension with 3 different notched rectangular fibrous concrete specimen sizes ( $5 \times 5 \text{ cm}^2$ ,  $10 \times 10 \text{ cm}^2$  and  $20 \times 20 \text{ cm}^2$ ) with smooth horizontal edges are shown in Figs.5.44-5.49 by assuming the varying threshold local tensile strain  $\epsilon_{min}$  in the cement matrix-fibre

interface ( $\varepsilon_{min}=0.025\%-1.0\%$ ) (Tab.5.4) and two different contents of fibres in concrete:  $A_f=0.15\%$  and  $A_f=1.5\%$ . Five stochastic simulations were performed for each case. Therefore, for each case with the different  $\varepsilon_{min}$ , the mean curves and the scatters of results around the mean curves are demonstrated. The fibre length was  $l_f=2.0$  cm. In turn, the mean rod length was  $l_r=1.0$  mm ( $b_f=1.0$  mm) or  $l_r=2.0$  mm ( $b_f=2.0$  mm). The same initial distribution of all concrete components was assumed for the same specimen size and different strain  $\varepsilon_{min}$ . The development of the calculated deformation is demonstrated in Fig.5.50 for 3 different specimen sizes:  $5\times 5$  cm<sup>2</sup>,  $10\times 10$  cm<sup>2</sup> and  $20\times 20$  cm<sup>2</sup> (with  $\varepsilon_{min}=0.5\%$  and  $A_f=1.5\%$ ). In turn, Figs.5.51-5.53 present the final crack pattern in fibrous concrete specimens at the vertical normal strain of  $\varepsilon_{22}=0.08\%$ .

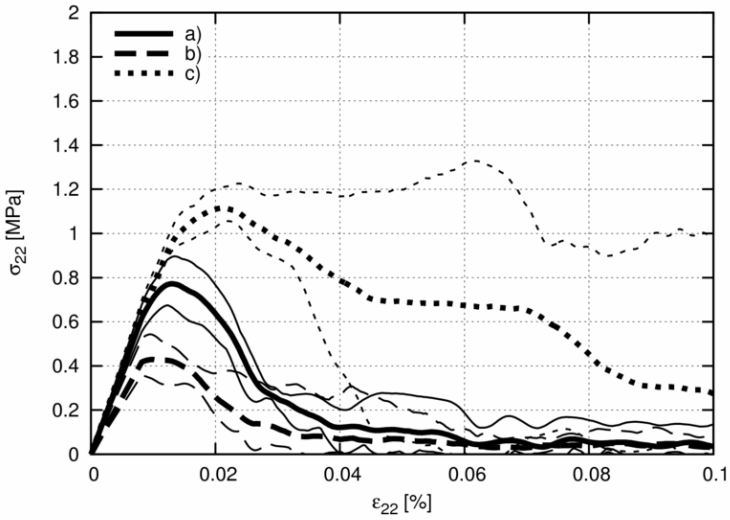


**Fig. 5.43** Fibrous concrete 3D specimen  $5\times 5\times 5$  cm<sup>3</sup> with 1.5% fibre volume: spatial distribution of aggregate (a) and steel fibres (b)

The results show that both strength and ductility of fibrous concrete increase if the cement matrix-fibre interface is stronger than the cement matrix-aggregate interface, i.e. for  $\varepsilon_{min}\geq 0.1\%$  in the cement matrix-fibre interface. All further discrete simulations were carried out with strain  $\varepsilon_{min}=0.5\%$  in the cement matrix-fibre bond.

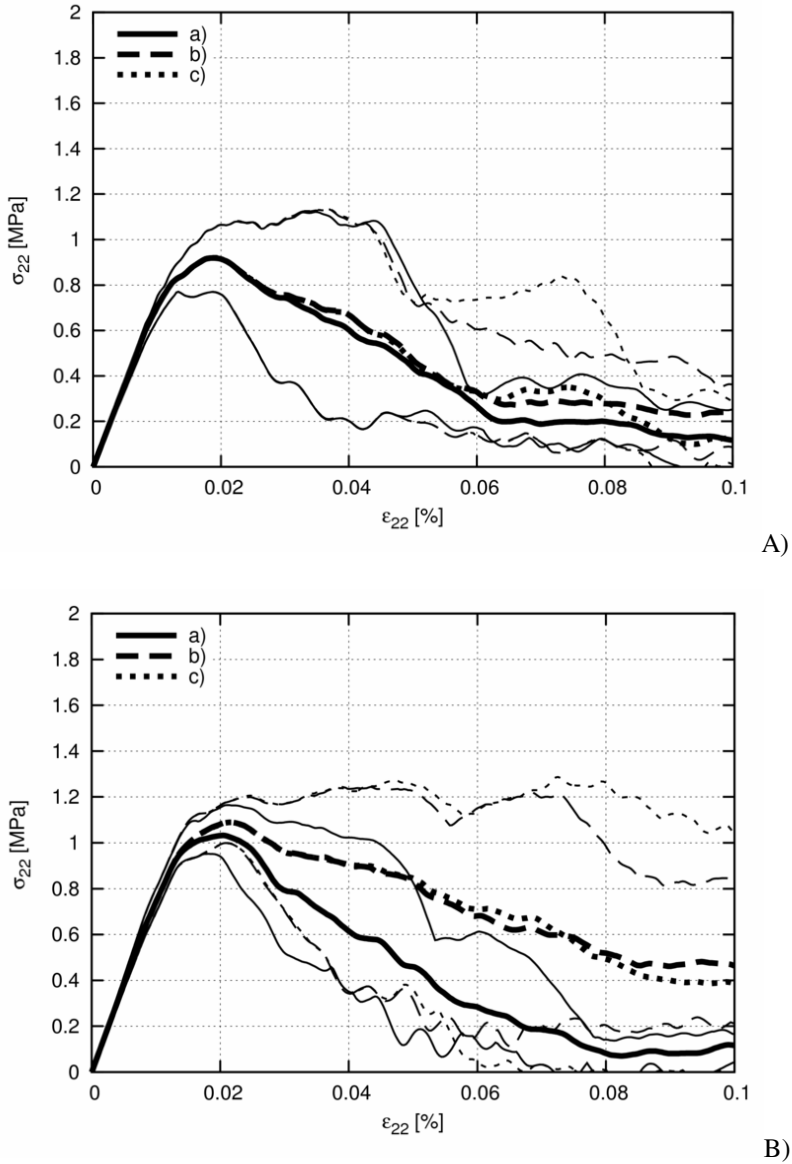


A)

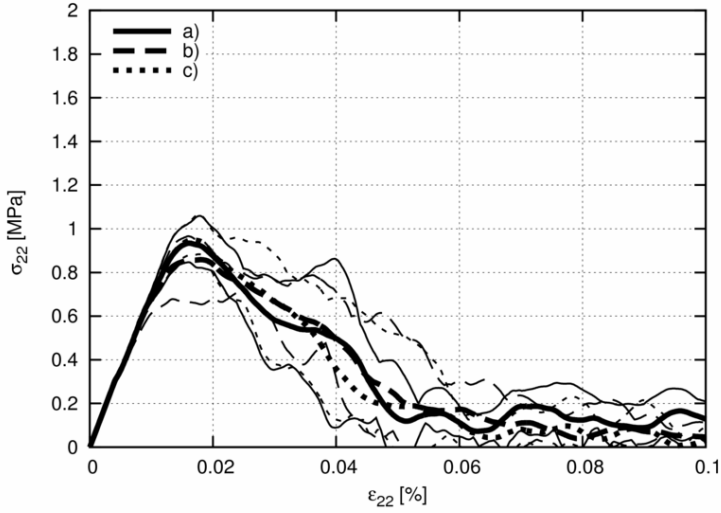


B)

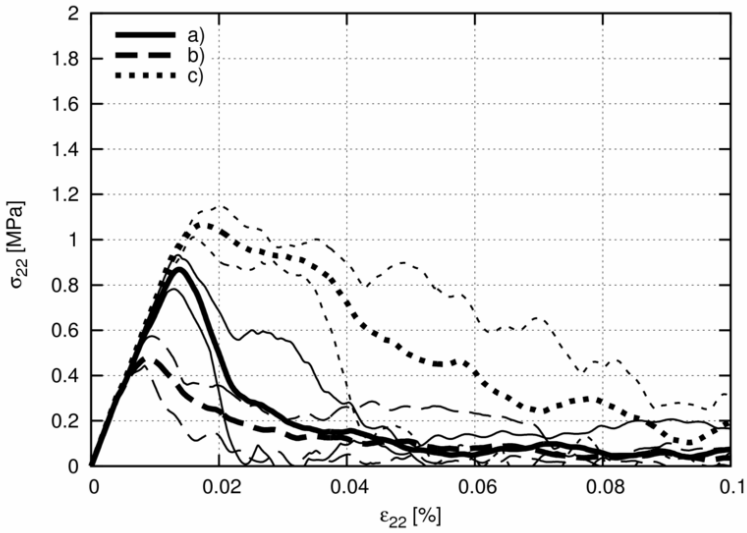
**Fig. 5.44** Calculated stress-strain curves for 2D notched fibrous concrete specimens subjected to uniaxial extension for different  $\varepsilon_{min}$  (specimen  $5 \times 5 \text{ cm}^2$ ,  $l_f=2 \text{ cm}$ ,  $l_r=1 \text{ mm}$ ,  $l_r/h=1/50$ ): a)  $\varepsilon_{min}=0.05\%$ , b)  $\varepsilon_{min}=0.025\%$ , c) no cement matrix-fibre interface, A)  $A_f=0.15\%$ , B)  $A_f=1.5\%$  ( $\sigma_{22}$  – vertical normal stress,  $\varepsilon_{22}$  – vertical normal strain)



**Fig. 5.45** Calculated stress-strain curves for 2D notched fibrous concrete specimens subjected to uniaxial extension for different  $\varepsilon_{min}$  (specimen  $5 \times 5$  cm,  $l_f = 2$  cm,  $l_i = 1$  mm,  $l_f/h = 1/50$ ): a)  $\varepsilon_{min} = 0.1\%$ , b)  $\varepsilon_{min} = 0.5\%$ , c)  $\varepsilon_{min} = 1.0\%$ , A)  $A_f = 0.15\%$ , B)  $A_f = 1.5\%$  ( $\sigma_{22}$  – vertical normal stress,  $\varepsilon_{22}$  – vertical normal strain)

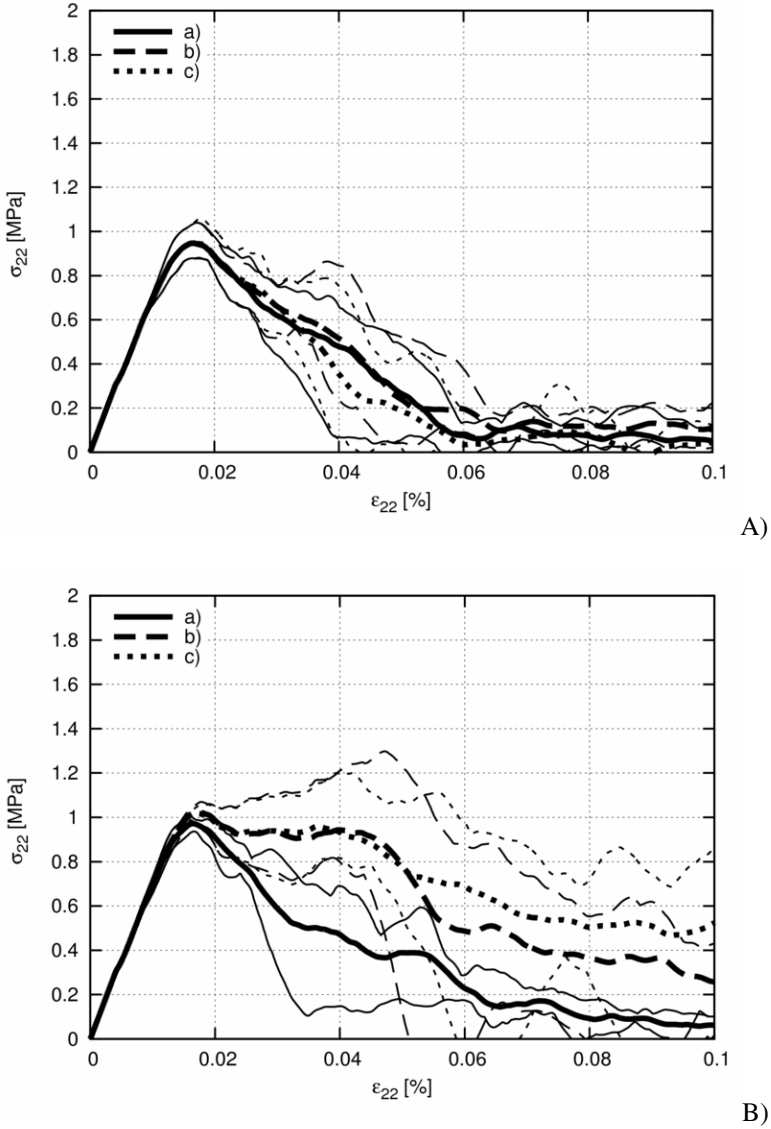


A)

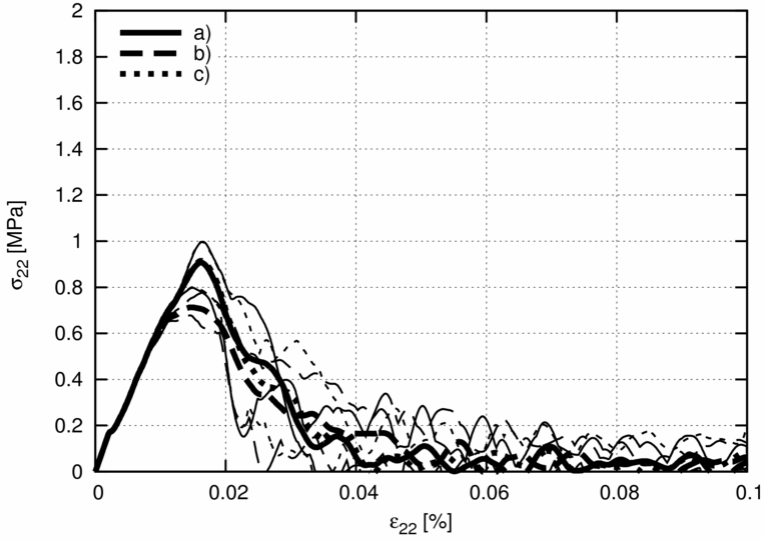


B)

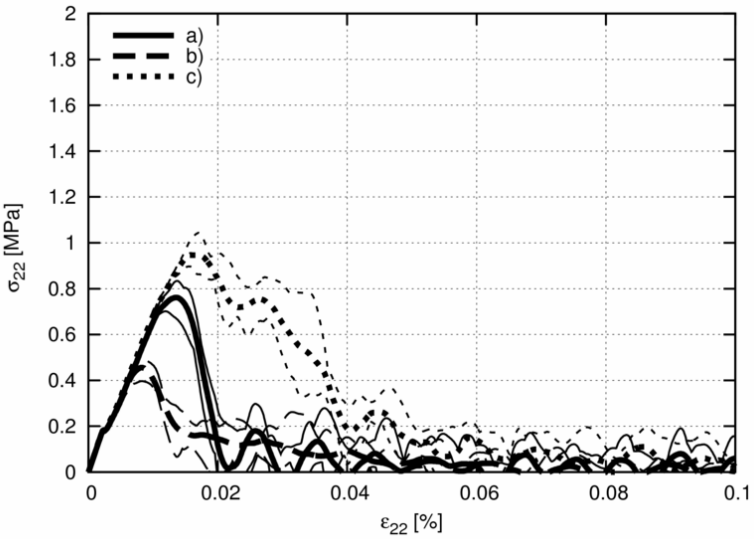
**Fig. 5.46** Calculated stress-strain curves for 2D notched fibrous concrete specimens subjected to uniaxial extension for different  $\varepsilon_{min}$  (specimen  $10 \times 10 \text{ cm}^2$ ,  $l_f=2 \text{ cm}$ ,  $l_r=1 \text{ mm}$ ,  $l_r/h=1/100$ ): a)  $\varepsilon_{min}=0.05\%$ , b)  $\varepsilon_{min}=0.025\%$ , c) no cement matrix-fibre interface, A)  $A_f=0.15\%$ , B)  $A_f=1.5\%$  ( $\sigma_{22}$  – vertical normal stress,  $\varepsilon_{22}$  – vertical normal strain)



**Fig. 5.47** Calculated stress-strain curves for 2D notched fibrous concrete specimens subjected to uniaxial extension for different  $\varepsilon_{min}$  (specimen  $10 \times 10 \text{ cm}^2$ ,  $l_f = 2 \text{ cm}$ ,  $l_f = 1 \text{ mm}$ ,  $l_f/h = 1/100$ ): a)  $\varepsilon_{min} = 0.1\%$ , b)  $\varepsilon_{min} = 0.5\%$ , c)  $\varepsilon_{min} = 1.0\%$ , A)  $A_f = 0.15\%$ , B)  $A_f = 1.5\%$  ( $\sigma_{22}$  – vertical normal stress,  $\varepsilon_{22}$  – vertical normal strain)

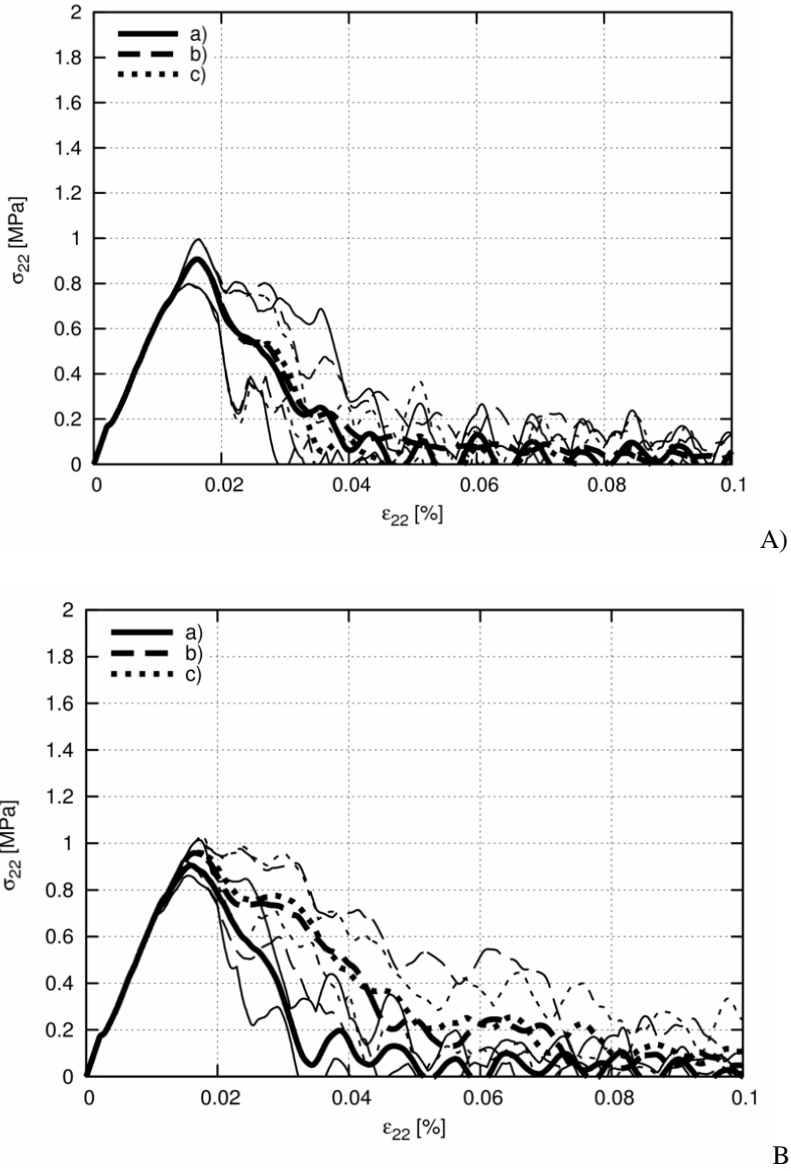


A)



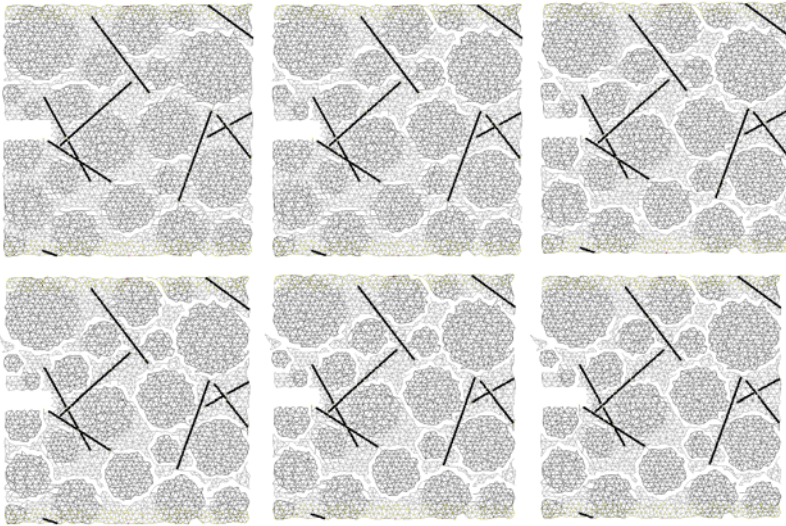
B)

**Fig. 5.48** Calculated stress-strain curves for 2D notched fibrous concrete specimens subjected to uniaxial extension for different  $\epsilon_{min}$  (specimen  $20 \times 20 \text{ cm}^2$ ,  $l_f = 2 \text{ cm}$ ,  $l_f = 1 \text{ mm}$ ,  $l_f/h = 1/200$ ): a)  $\epsilon_{min} = 0.05\%$ , b)  $\epsilon_{min} = 0.025\%$ , c) no cement matrix-fibre interface ( $\sigma_{22}$  - vertical normal stress,  $\epsilon_{22}$  - vertical normal strain), A)  $A_f = 0.15\%$ , B)  $A_f = 1.5\%$

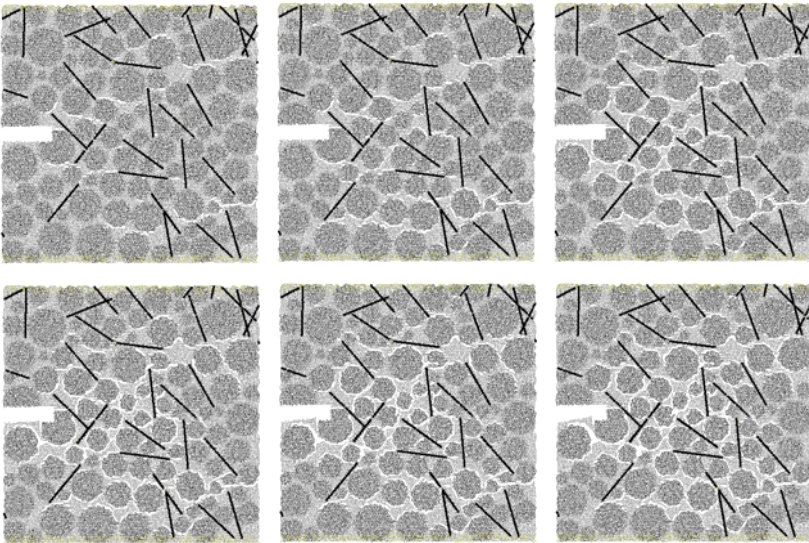


**Fig. 5.49** Calculated stress-strain curves for 2D notched fibrous concrete specimens subjected to uniaxial extension for different  $\varepsilon_{min}$  (specimen  $20 \times 20 \text{ cm}^2$ ,  $l_f=2 \text{ cm}$ ,  $l_r=1 \text{ mm}$ ,  $l_r/h=1/200$ ): a)  $\varepsilon_{min}=0.1\%$ , b)  $\varepsilon_{min}=0.5\%$ , c)  $\varepsilon_{min}=1.0\%$ , A)  $A_f=0.15\%$ , B)  $A_f=1.5\%$  ( $\sigma_{22}$  - vertical normal stress,  $\varepsilon_{22}$  - vertical normal strain)





A)



B)

**Fig. 5.50** 2D notched fibrous concrete specimen subjected to uniaxial extension: evolution of calculated crack pattern ( $\epsilon_{min}=0.5\%$ ,  $l_f=2$  cm,  $A_f=1.5\%$ ,  $l_f=1$  mm): A) specimen  $5\times 5$  cm<sup>2</sup>, B) specimen  $10\times 10$  cm<sup>2</sup>, C) specimen  $20\times 20$  cm<sup>2</sup>

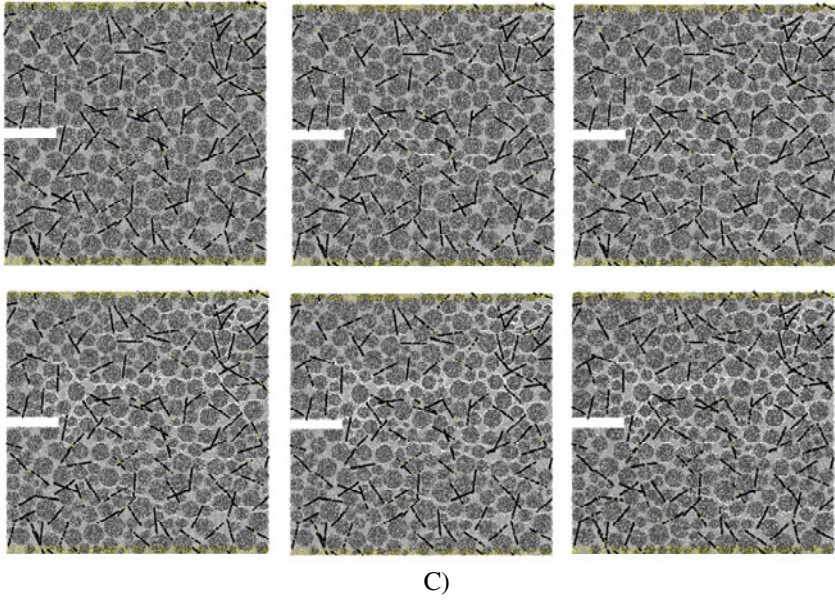
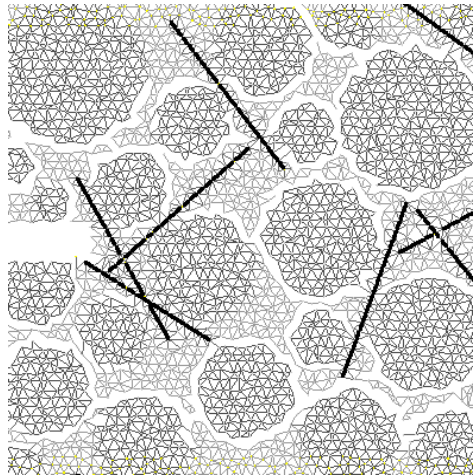
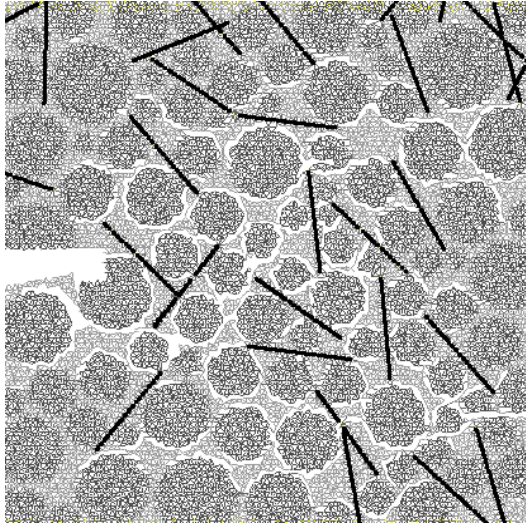


Fig. 5.50 (continued)

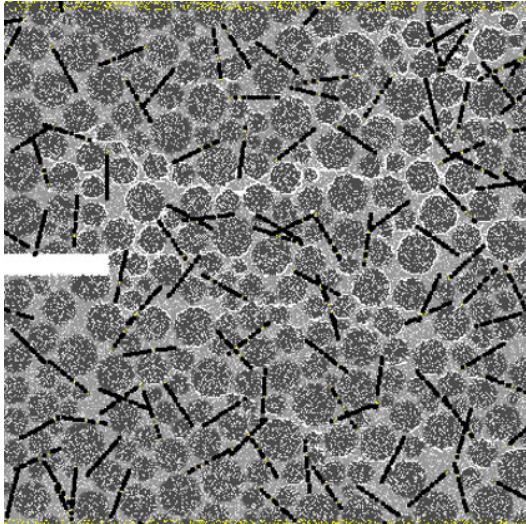


**Fig. 5.51** Calculated crack pattern in post-peak region in 2D notched fibrous concrete specimen subjected to uniaxial extension ( $\epsilon_{min}=0.5\%$ ,  $l_j=2$  cm,  $A_f=1.5\%$ ,  $l_f=1$  mm, specimen  $5\times 5$  cm<sup>2</sup>,  $\epsilon_{22}=0.08$  %)





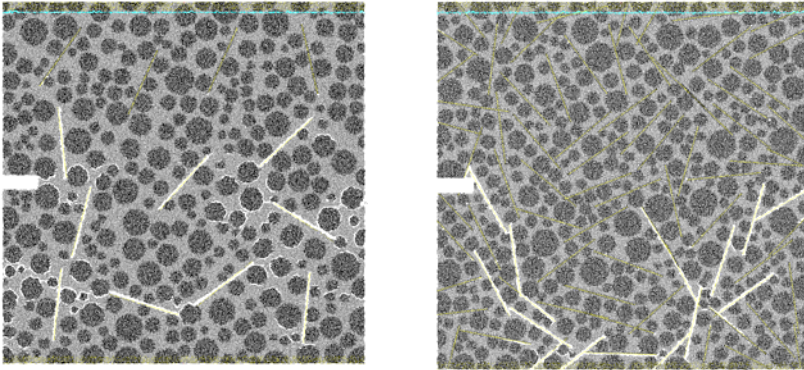
**Fig. 5.52** Calculated crack pattern in post-peak region in 2D notched fibrous concrete specimen subjected to uniaxial extension ( $\epsilon_{min}=0.5\%$ ,  $l_f=2$  cm,  $A_f=1.5\%$ ,  $l_f=1$  mm, specimen  $10\times 10$  cm<sup>2</sup>,  $\epsilon_{22}=0.08$  %)



**Fig. 5.53** Calculated crack pattern in post-peak region in 2D notched fibrous concrete specimen subjected to uniaxial extension ( $\epsilon_{min}=0.5\%$ ,  $l_f=2$  cm,  $A_f=1.5\%$ ,  $l_f=1$  mm, specimen  $20\times 20$  cm<sup>2</sup>,  $\epsilon_{22}=0.08$  %)

Due to a high particle density of 60% (Figs.5.50-5.53), percolation of bond zones occurs early in the loading history due to the fact that the interface between the cement matrix and aggregate is the weakest component of the system and cracks are created along aggregates. The cracks are obviously initiated in the region of the notch. Since the number of aggregates is relatively large, several discontinuous macro-cracks propagate in a tortuous way between fibres. The cracks overlap and form branches. The way propagation of cracks is clearly enhanced by the presence of steel fibres which delay their development.

If the cement matrix-fibre interface is weaker than the cement matrix-aggregate interface ( $\varepsilon_{min} < 0.05\%$ ), both material strength and ductility are smaller than in plain concrete due to the fact that cracks are created in interfaces along fibres which act as imperfections to promote them (Fig.5.54).



**Fig. 5.54** Two 2D notched fibrous concrete specimens subjected to uniaxial extension with steel fibres: calculated crack pattern with cement matrix-fibre interface weaker than cement matrix-aggregate interface (case 'B' of Tab.5.4)

In the case of the lack of the cement matrix-fibre interface, both the material strength and ductility are also higher in fibrous concrete than in plain concrete due to the different  $k_l$  and  $E$  as compared to the cement matrix-aggregate interface (Tab.5.4). However, the presence of the cement matrix-fibre interface with the different threshold local normal strain  $\varepsilon_{min}$  allows us to control the evolution of the stress-strain curve.

### Effect of Fibre Presence

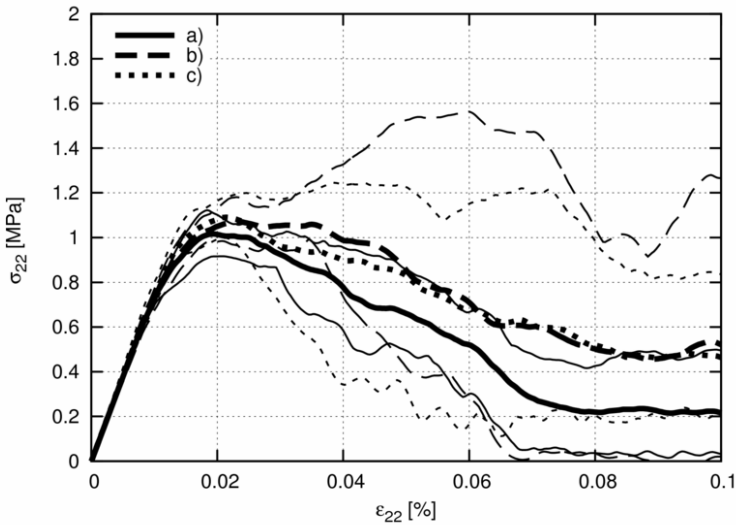
The effect of fibres on the behavior of plain concrete is demonstrated for 3 different fibrous concrete specimen sizes ( $\varepsilon_{min}=0.5\%$ ,  $A_f=1.5\%$ ,  $l_f=1-2$  cm,  $l_r=1.0$  mm)

in Fig.5.55. Presented are as usually three stress-strain curves: minimum, mean and maximum for each case.

As in the experiments (Shah and Rangan 1971, Bentur and Mindess 1990), both the material strength and ductility increase with increasing fibre volume depending strongly on a stochastic fibre distribution. However, the strength increase is rather small. The mean tensile strength  $f_t$  increases, namely, from 0.85-1.0 MPa (plain concrete) up to  $f_t=0.95-1.1$  MPa ( $A_f=1.5\%$ ).

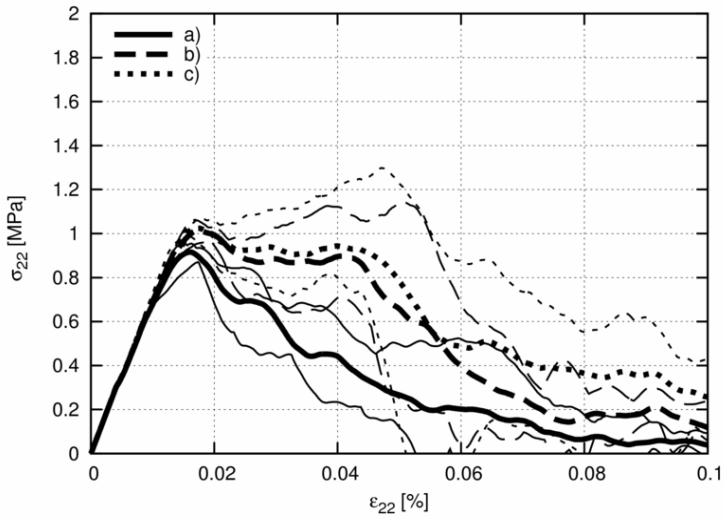
### Effect of Specimen Size

The results of stress-strain curves during quasi-static uniaxial tension with notched rectangular fibrous concrete specimens  $5\times 5$  cm<sup>2</sup>,  $10\times 10$  cm<sup>2</sup> and  $20\times 20$  cm<sup>2</sup> with smooth horizontal edges are shown in Figs.5.56 and 5.57 ( $\epsilon_{min}=0.5\%$ ,  $l_f=2$  cm) for three different contents of fibres in concrete:  $A_f=0.0\%$  (plain concrete)  $A_f=0.15\%$  and  $A_f=1.5\%$ , and two different mean rod lengths  $l_r=1.0$  mm and  $l_r=2.0$  mm. Presented are again three stress-strain curves: the minimum, mean and maximum one.

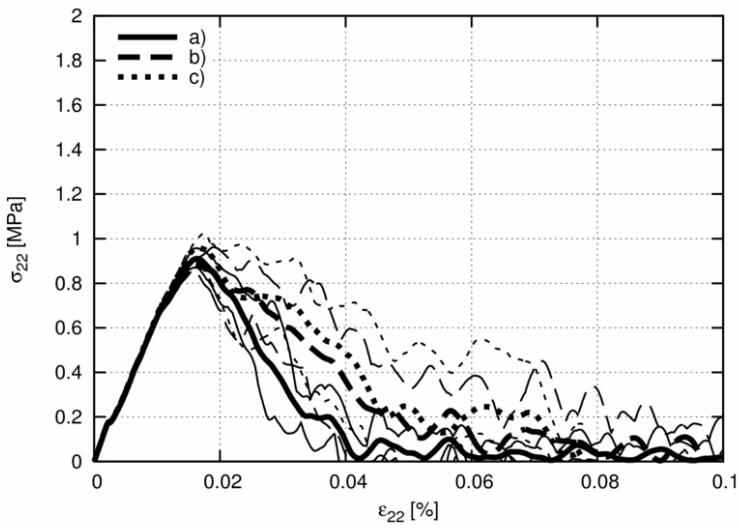


A)

**Fig. 5.55** Calculated stress-strain curves for 2D notched fibrous concrete specimens subjected to uniaxial extension ( $\epsilon_{min}=0.5\%$ ,  $A_f=1.5\%$ ,  $l_r=1$  mm): a) plain concrete, b) fibrous concrete with  $l_f=1$  cm, c) fibrous concrete with  $l_f=2$  cm, A) specimen  $5\times 5$  cm<sup>2</sup>, B) specimen  $10\times 10$  cm<sup>2</sup>, C) specimen  $20\times 20$  cm<sup>2</sup> ( $\sigma_{22}$  – vertical normal stress,  $\epsilon_{22}$  – vertical normal strain)

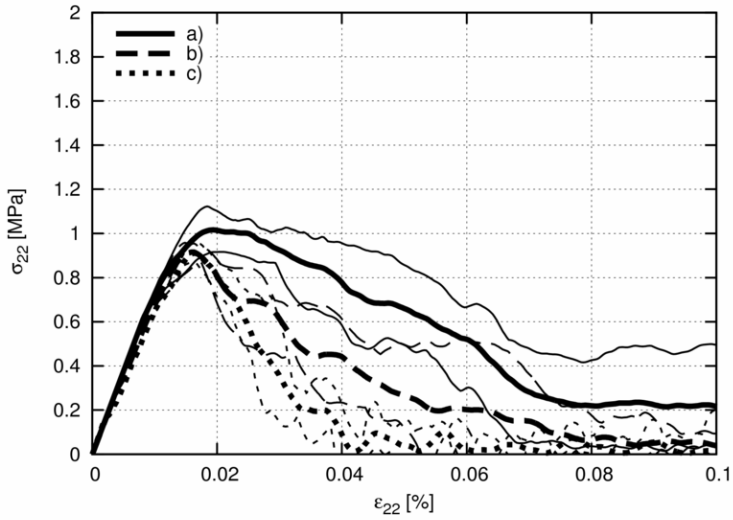


B)

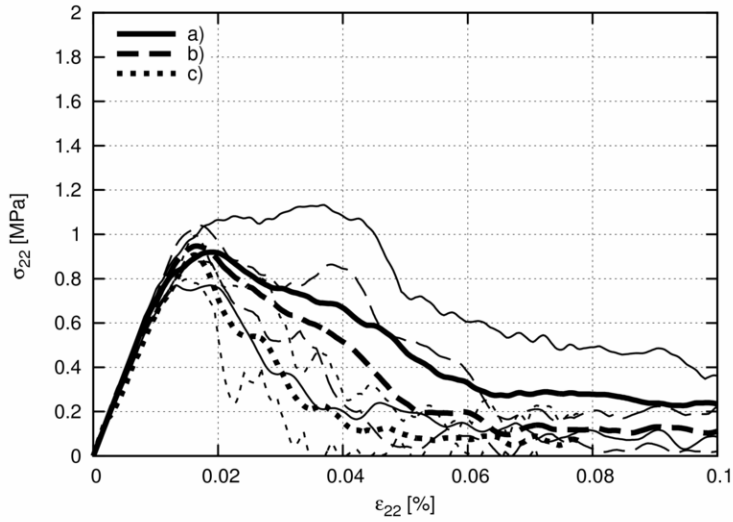


C)

Fig. 5.55 (continued)

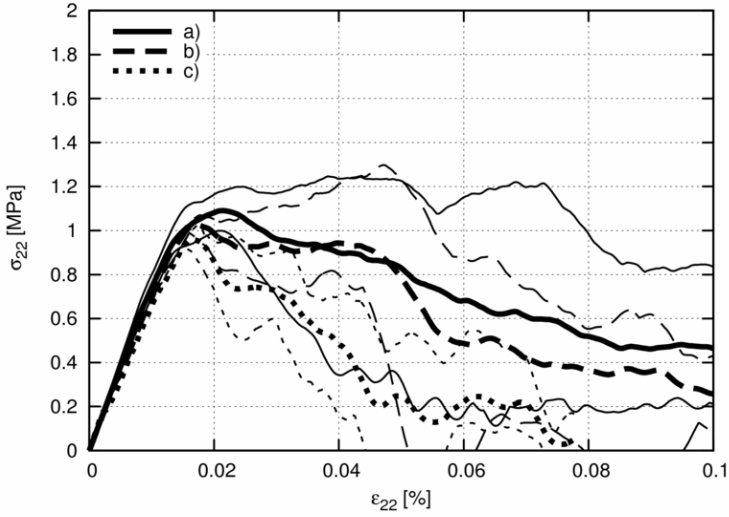


A)



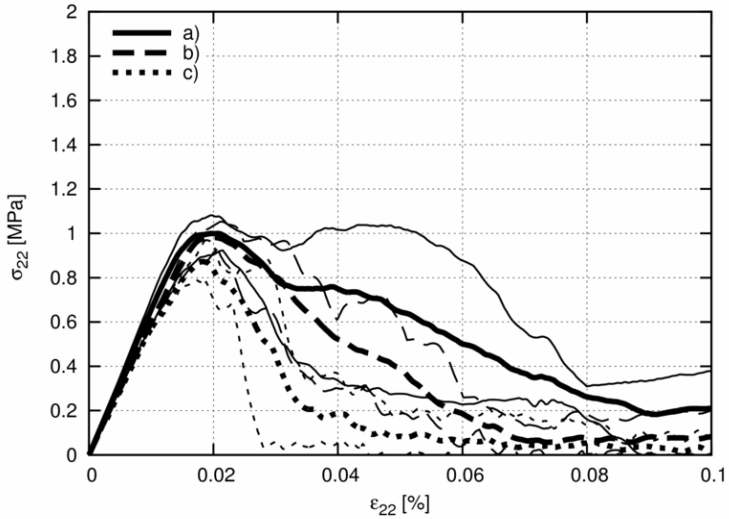
B)

**Fig. 5.56** Calculated stress-strain curves for 2D notched fibrous concrete specimens subjected to uniaxial extension ( $l_f=1$  mm,  $\varepsilon_{min}=0.5\%$ ): a) specimen  $5\times 5$  cm<sup>2</sup>, b) specimen  $10\times 10$  cm<sup>2</sup>, c) specimen  $20\times 20$  cm<sup>2</sup>, A)  $A_f=0\%$ , B)  $A_f=0.15\%$ , C)  $A_f=1.5\%$  ( $\sigma_{22}$  – vertical normal stress,  $\varepsilon_{22}$  – vertical normal strain)



C)

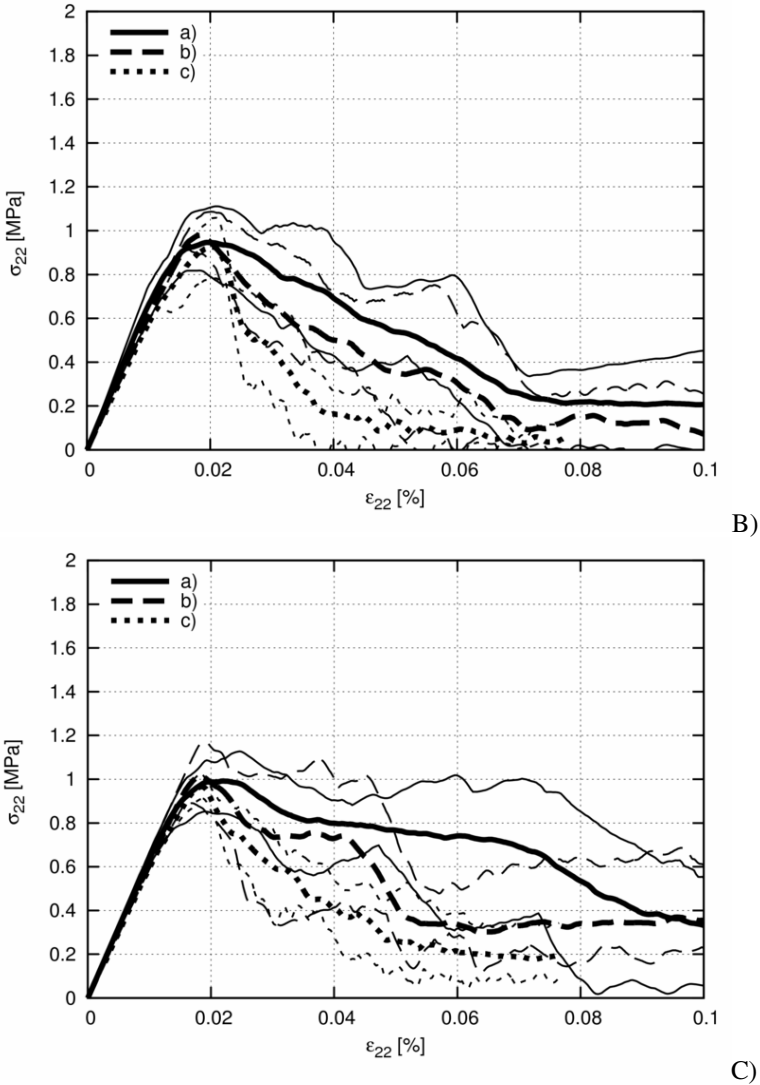
Fig. 5.56 (continued)



A)

Fig. 5.57 Calculated stress-strain curves for 2D notched fibrous concrete specimens subjected to uniaxial extension ( $l_r=2$  mm,  $\epsilon_{min}=0.5\%$ ): a) specimen  $5\times 5$  cm<sup>2</sup>, b) specimen  $10\times 10$  cm<sup>2</sup>, c) specimen  $20\times 20$  cm<sup>2</sup>, A)  $A_f=0\%$ , B)  $A_f=0.15\%$ , C)  $A_f=1.5\%$  ( $\sigma_{22}$  – vertical normal stress,  $\epsilon_{22}$  – vertical normal strain)





**Fig. 57** (continued)

The results show that both strength and ductility of plain and fibrous concrete increase with decreasing specimen size. Thus, a size effect was realistically modelled (Balendran 2002, Ward and Li 1990, Lin 1999). The mean tensile strength is about  $f_t=0.85\text{-}1.0$  MPa ( $A_f=0.0\%$ ),  $f_t=0.85\text{-}0.9$  MPa ( $A_f=0.15\%$ ) and  $f_t=0.95\text{-}1.1$  MPa ( $A_f=1.5\%$ ).

### Effect of Location Direction of Fibres

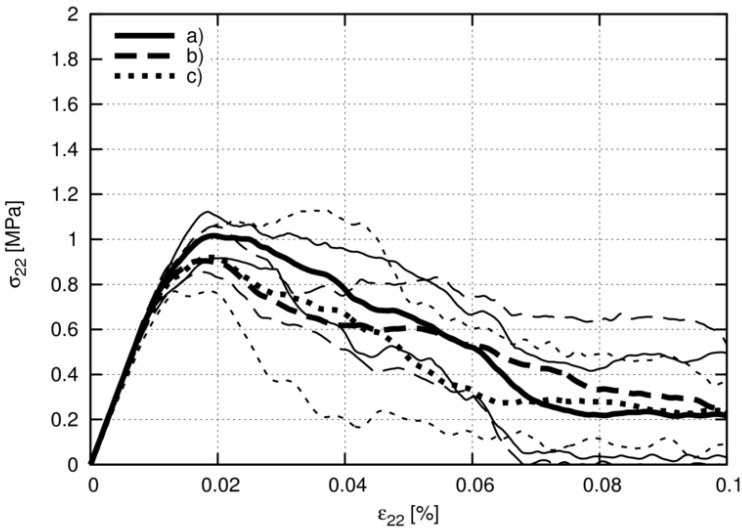
Figures 5.58-5.61 show the effect of the location direction of fibres, which were distributed in 3 different fibrous concrete specimens at random, vertically and horizontally. 5 simulations were again performed for each case. Presented are again three stress-strain curves: minimum, mean and maximum one, respectively. The results show that the strength and ductility are the highest if fibres are vertically oriented and weaker if fibres are horizontally oriented as compared to their stochastic orientation.

### Effect of Fibre Length

The effect of the fibre length on the stress-strain curve during uniaxial tension is demonstrated in Fig.5.62 for 3 different fibrous concrete specimens. The fibre length was 2 cm, 4 cm and 6 cm, respectively ( $\epsilon_{min}=0.5\%$  in the cement matrix-fibre interface).

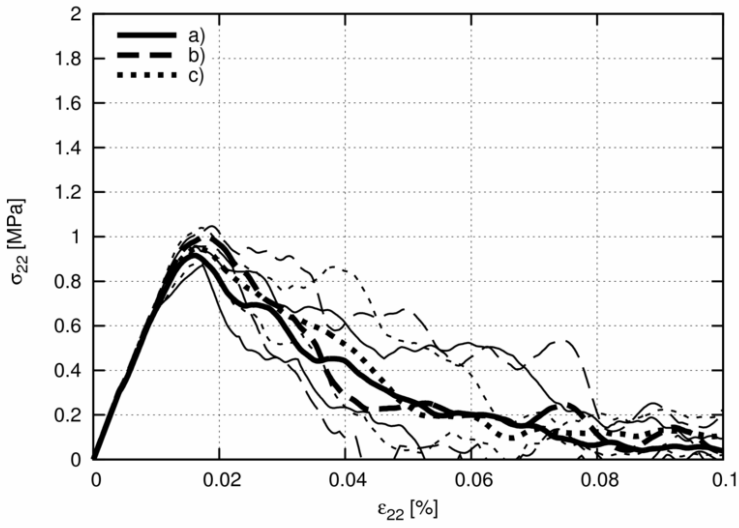
The calculated strength and ductility do not increase with increasing fibre length as in the experiments (Ward and Li 1990). Thus, the effect of the fibre distribution is stronger than the effect of the fibre length.

Finally, Fig.5.63 shows the evolution of deformation for 2 different specimen sizes  $5 \times 5 \text{ cm}^2$  and  $20 \times 20 \text{ cm}^2$  with  $l_f=2.0 \text{ cm}$  and  $l_f=1 \text{ cm} - 6 \text{ cm}$  ( $\epsilon_{min}=0.25\% - 0.5\%$ ,  $A_f=1.5\%$ ).

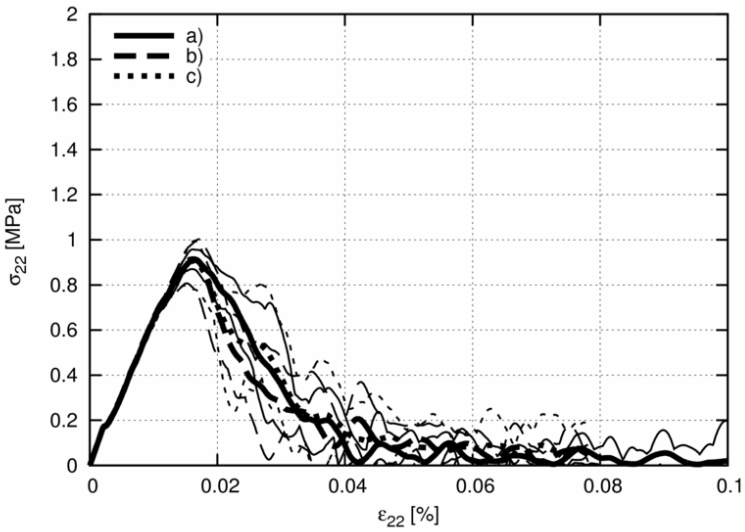


A)

**Fig. 5.58** Calculated stress-strain curves for 2D notched fibrous concrete specimens subjected to uniaxial extension ( $\epsilon_{min}=0.5\%$ ,  $A_f=0.15\%$ ,  $l_f=2 \text{ cm}$ ,  $l_r=1 \text{ mm}$ ): a) plain concrete, b) fibres vertically placed, c) fibres randomly placed, A) specimen  $5 \times 5 \text{ cm}^2$ , B) specimen  $10 \times 10 \text{ cm}^2$ , C) specimen  $20 \times 20 \text{ cm}^2$  ( $\sigma_{22}$  - vertical normal stress,  $\epsilon_{22}$  - vertical normal strain)

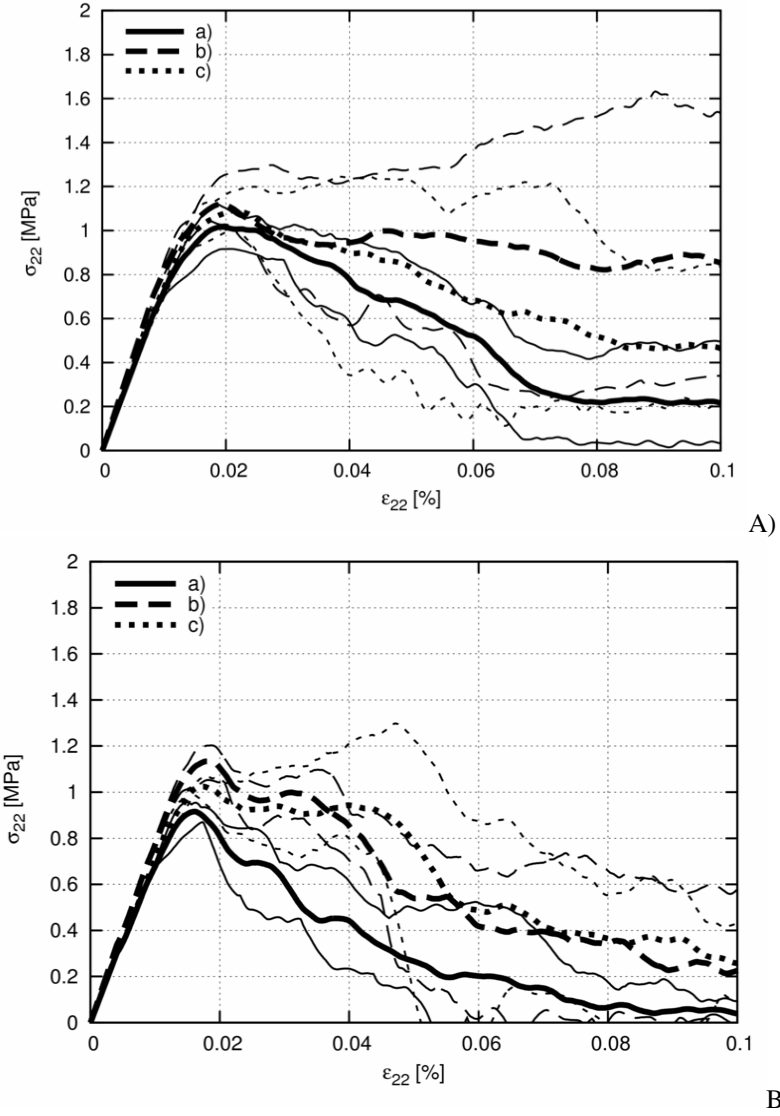


B)



C)

Fig. 5.58 (continued)



**Fig. 5.59** Calculated stress-strain curves for 2D notched fibrous concrete specimens subjected to uniaxial extension ( $\epsilon_{min}=0.5\%$ ,  $A_f=1.5\%$ ,  $l_f=2$  cm,  $l_r=1$  mm): a) plain concrete, b) fibres vertically placed, c) fibres randomly placed, A) specimen  $5\times 5$  cm<sup>2</sup>, B) specimen  $10\times 10$  cm<sup>2</sup>, C) specimen  $20\times 20$  cm<sup>2</sup> ( $\sigma_{22}$  – vertical normal stress,  $\epsilon_{22}$  - vertical normal strain)

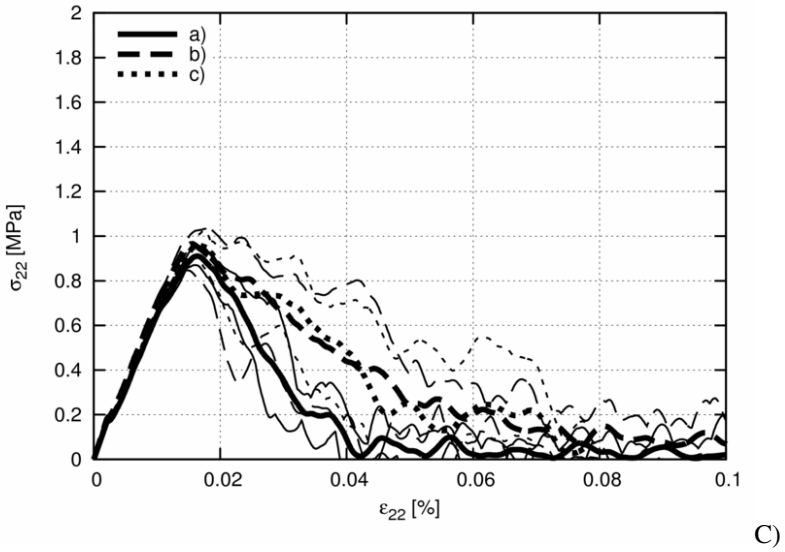


Fig. 5.59 (continued)

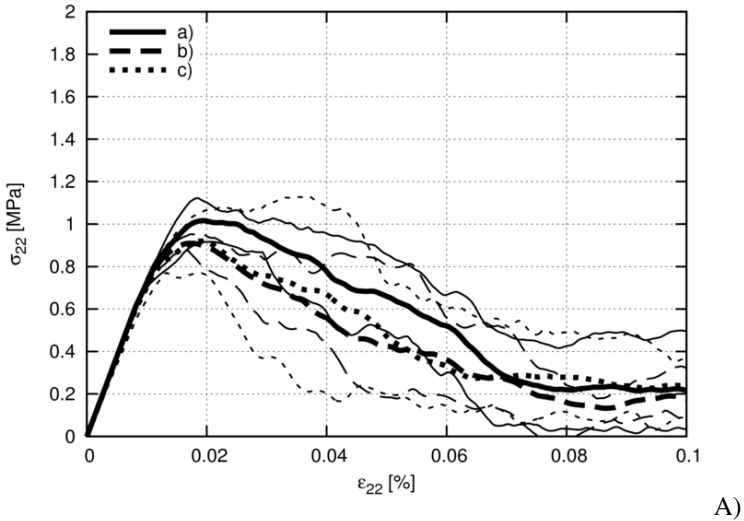


Fig. 5.60 Calculated stress-strain curves for 2D notched fibrous concrete specimens subjected to uniaxial extension ( $\epsilon_{min}=0.5\%$ ,  $A_f=0.15\%$ ,  $l_f=2$  cm,  $l_r=1$  mm): a) plain concrete, b) fibres horizontally placed, c) fibres randomly placed, A) specimen  $5 \times 5$  cm<sup>2</sup>, B) specimen  $10 \times 10$  cm<sup>2</sup>, C) specimen  $20 \times 20$  cm<sup>2</sup> ( $\sigma_{22}$  – vertical normal stress,  $\epsilon_{22}$  - vertical normal strain)

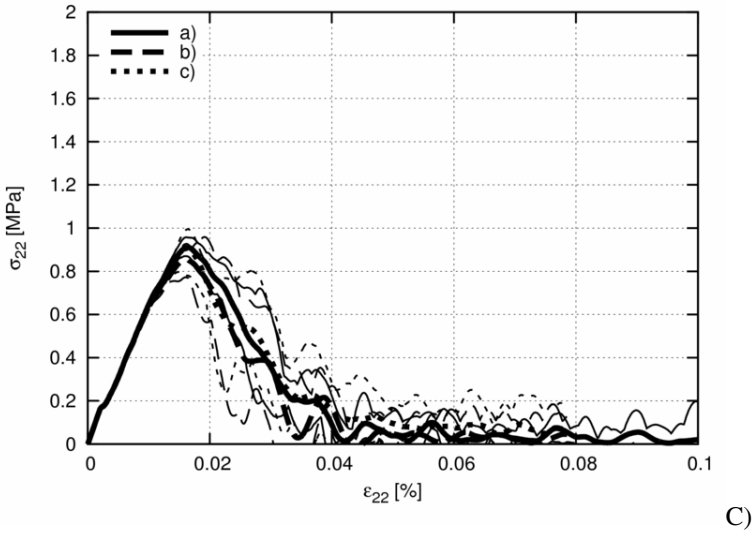
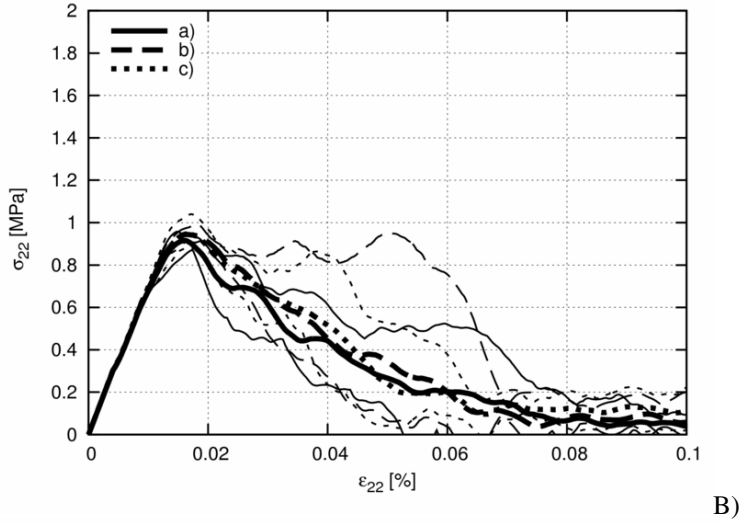
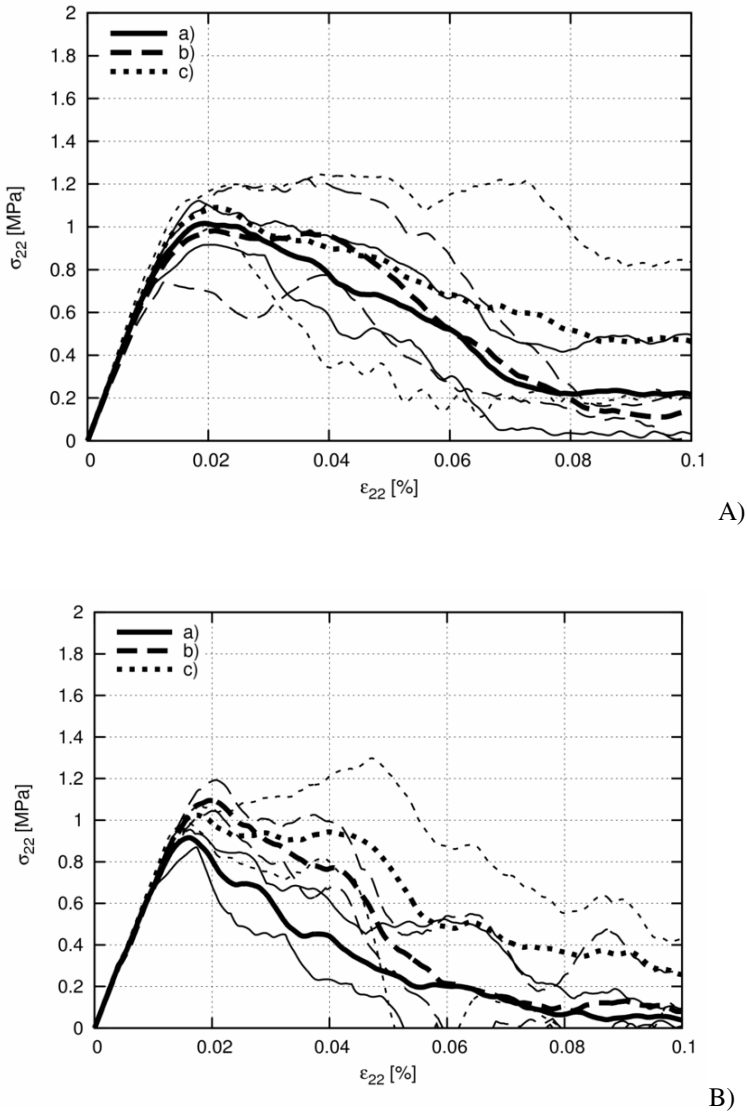


Fig. 5.60 (continued)



**Fig. 5.61** Calculated stress-strain curves for 2D notched fibrous concrete specimens subjected to uniaxial extension ( $\epsilon_{min}=0.5\%$ ,  $A_f=1.5\%$ ,  $l_f=2$  cm,  $l_r=1.0$  mm): a) plain concrete, b) fibres horizontally placed, c) fibres randomly placed, A) specimen  $5\times 5$  cm<sup>2</sup>, B) specimen  $10\times 10$  cm<sup>2</sup>, C) specimen  $20\times 20$  cm<sup>2</sup> ( $\sigma_{22}$  – vertical normal stress,  $\epsilon_{22}$  – vertical normal strain)

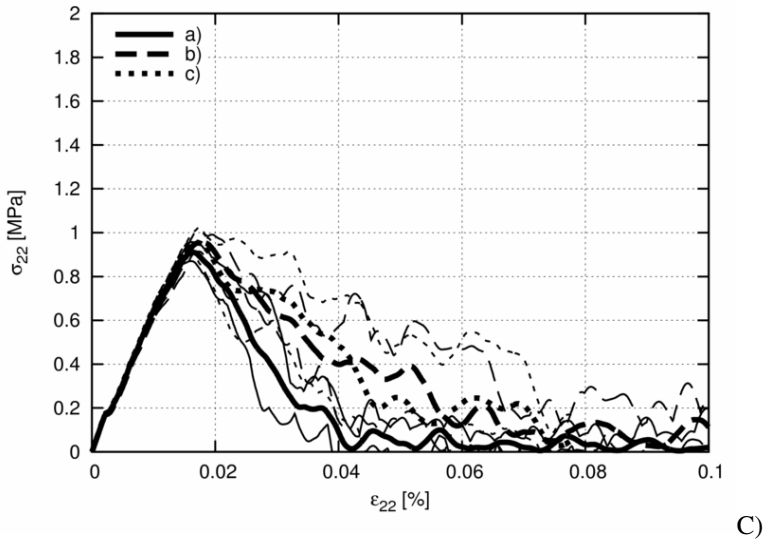


Fig. 5.61 (continued)

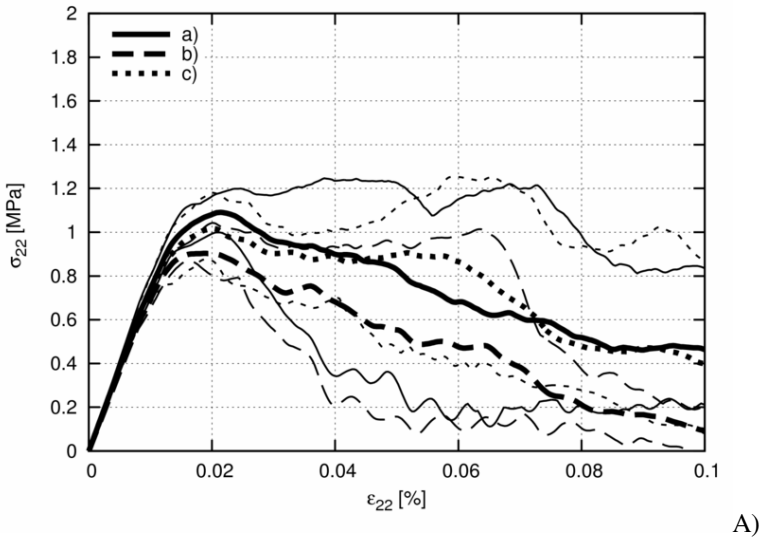
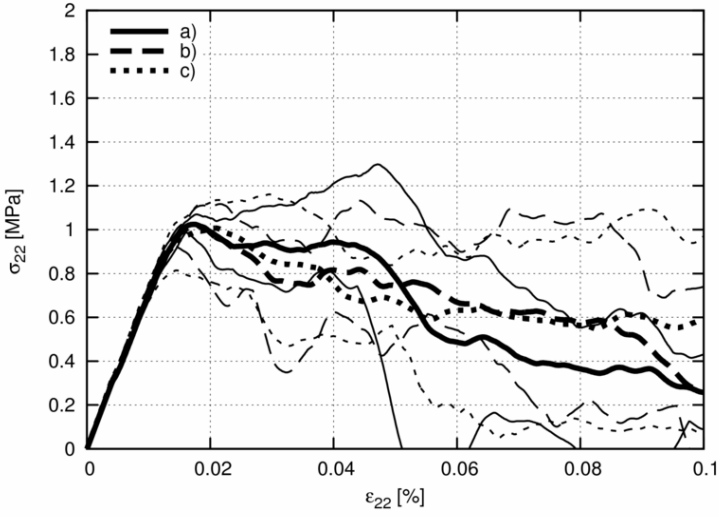
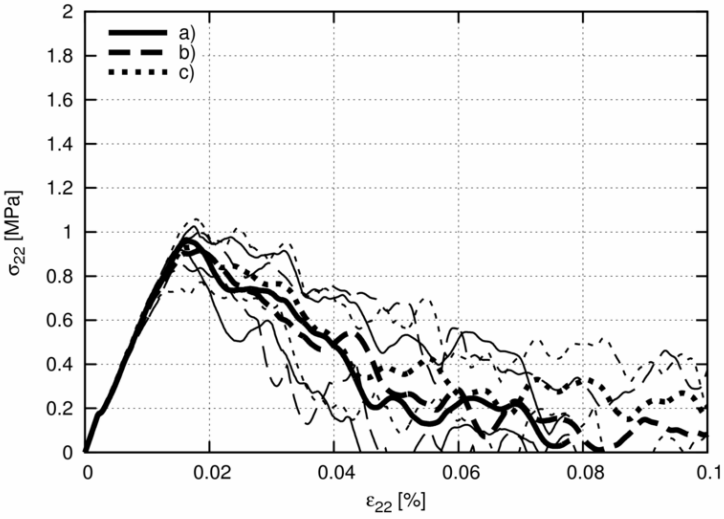


Fig. 5.62 Calculated stress-strain curves for 2D notched fibrous concrete specimens subjected to uniaxial extension ( $\epsilon_{min}=0.5\%$ ,  $A_f=1.5\%$ ,  $l_r=1.0$  mm): a)  $l_f=2$  cm, b)  $l_f=4$  cm, c)  $l_f=6$  cm, A) specimen  $5\times 5$  cm<sup>2</sup>, B) specimen  $10\times 10$  cm<sup>2</sup>, C) specimen  $20\times 20$  cm<sup>2</sup> ( $\sigma_{22}$  – vertical normal stress,  $\epsilon_{22}$  – vertical normal strain)



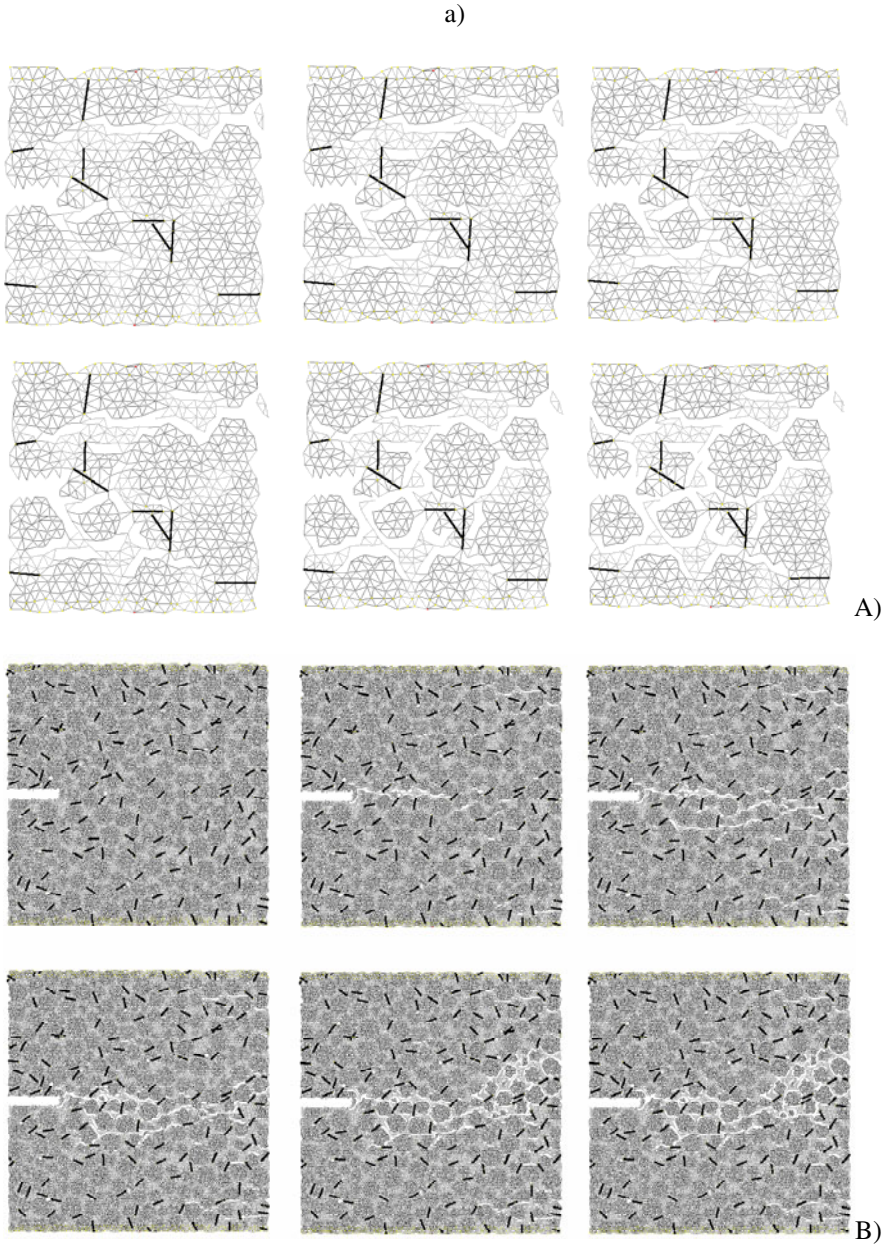


B)

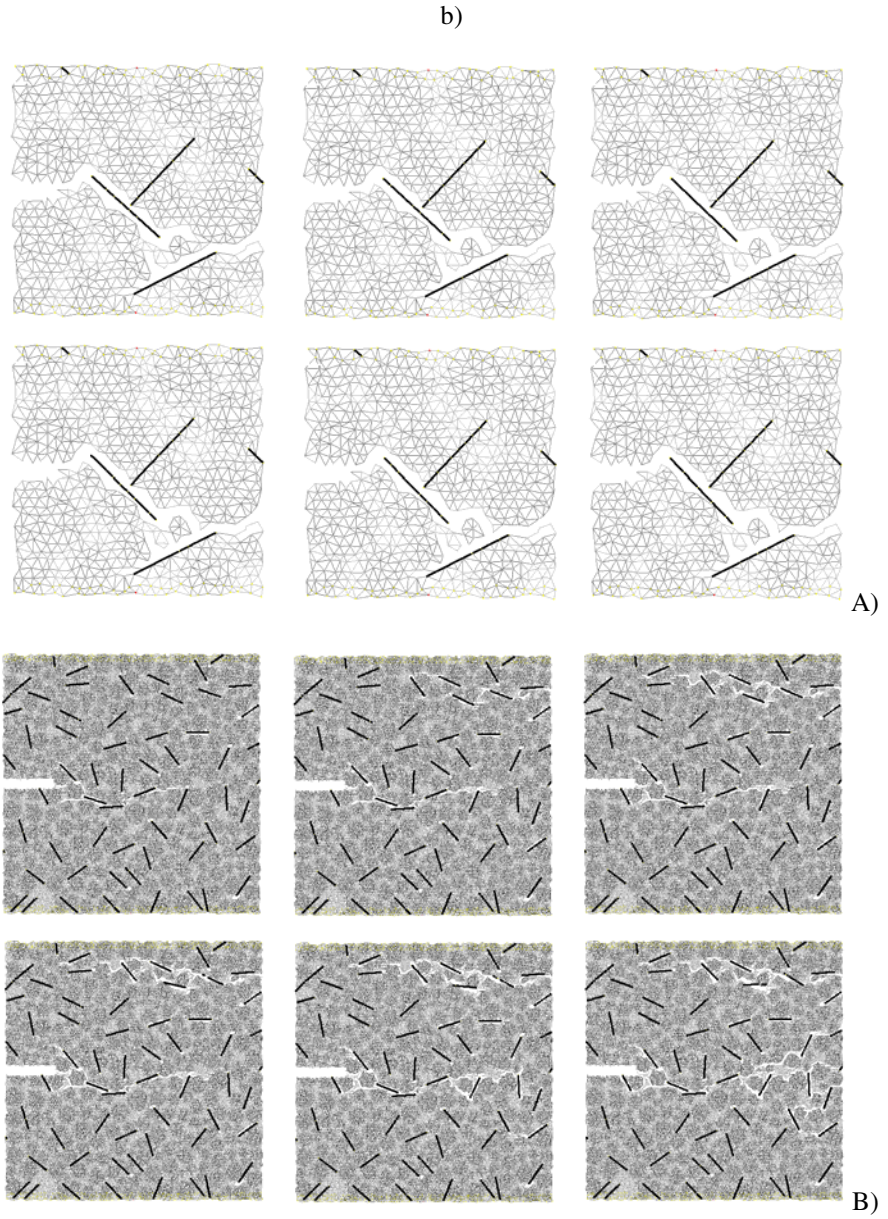


C)

Fig. 5.62 (continued)



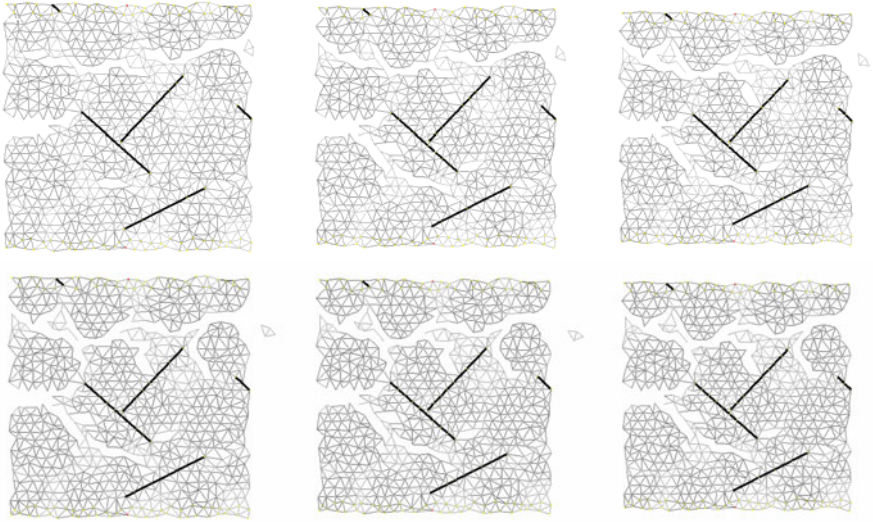
**Fig. 5.63** 2D notched fibrous concrete specimen subjected to uniaxial extension: evolution of calculated crack pattern ( $l_f=2.0$  mm,  $A_f=1.5\%$ ): a)  $\varepsilon_{min}=0.5\%$ ,  $l_f=1$  cm, b)  $\varepsilon_{min}=0.25\%$ ,  $l_f=2$  cm, c)  $\varepsilon_{min}=0.5\%$ ,  $l_f=2$  cm, d)  $\varepsilon_{min}=0.5\%$ ,  $l_f=6$  cm, A) specimen  $5\times 5$  cm<sup>2</sup>, B) specimen  $20\times 20$  cm<sup>2</sup> (note that specimens are not proportionally scaled)



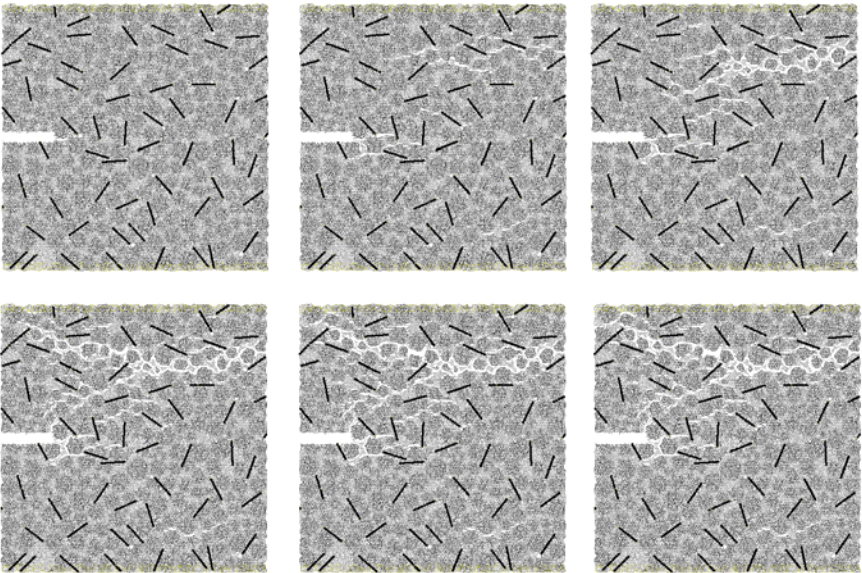
**Fig. 5.63** (continued)



c)

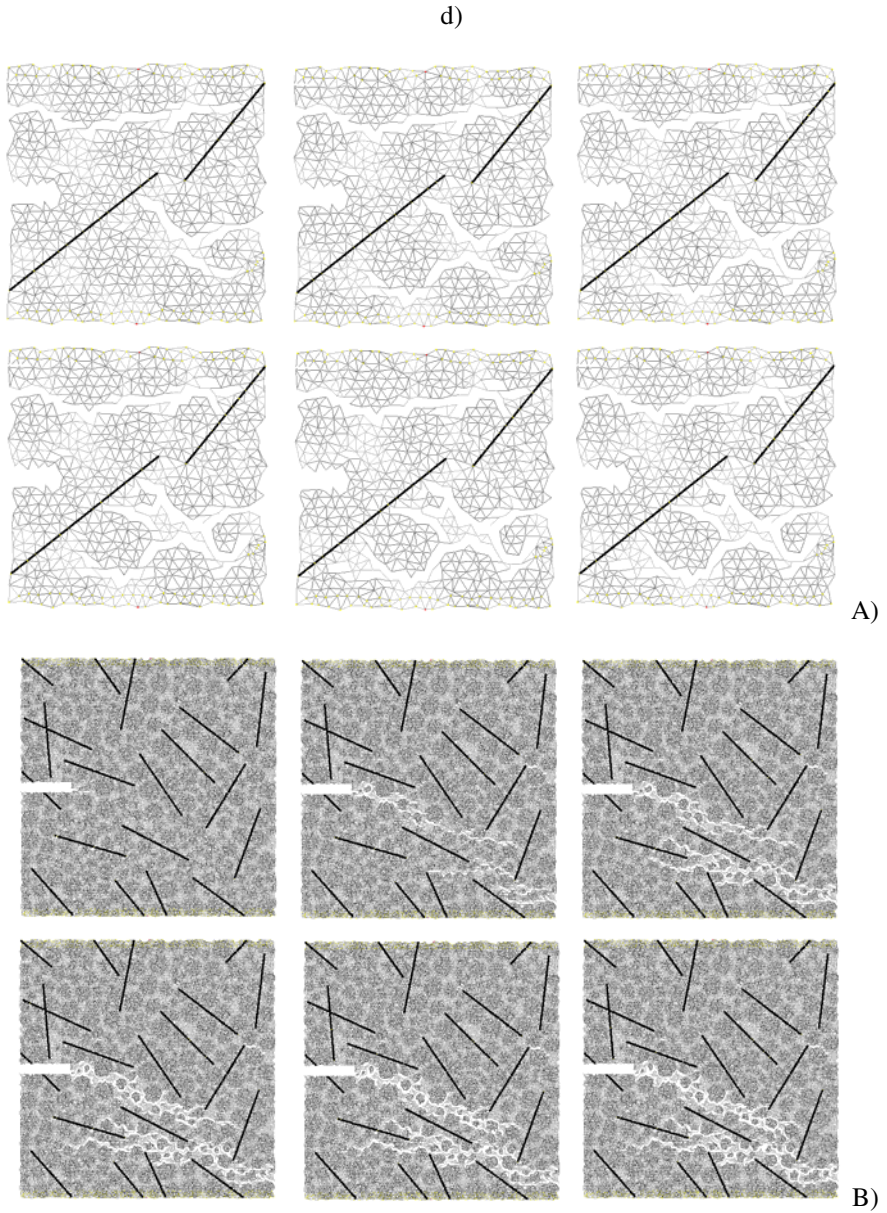


A)



B)

Fig. 5.63 (continued)



**Fig. 5.63** (continued)

The results of Fig.5.63 show clearly that the propagation of cracks is hindered by the presence of fibres independently of  $l_f$ . In the case of threshold strain  $\varepsilon_{min}=0.25\%$  (Fig.5.63b), the cement matrix-fibre interfaces act as imperfections and contribute to the occurrence of dominant cracks.

Similarly as in the experiments (Lin 1999), the concrete specimen becomes the strongest as compared to plain concrete when the fibres are oriented vertically, i.e. they are parallel to the loading direction (perpendicular to the direction of dominant horizontal cracks). The material becomes also the most ductile.

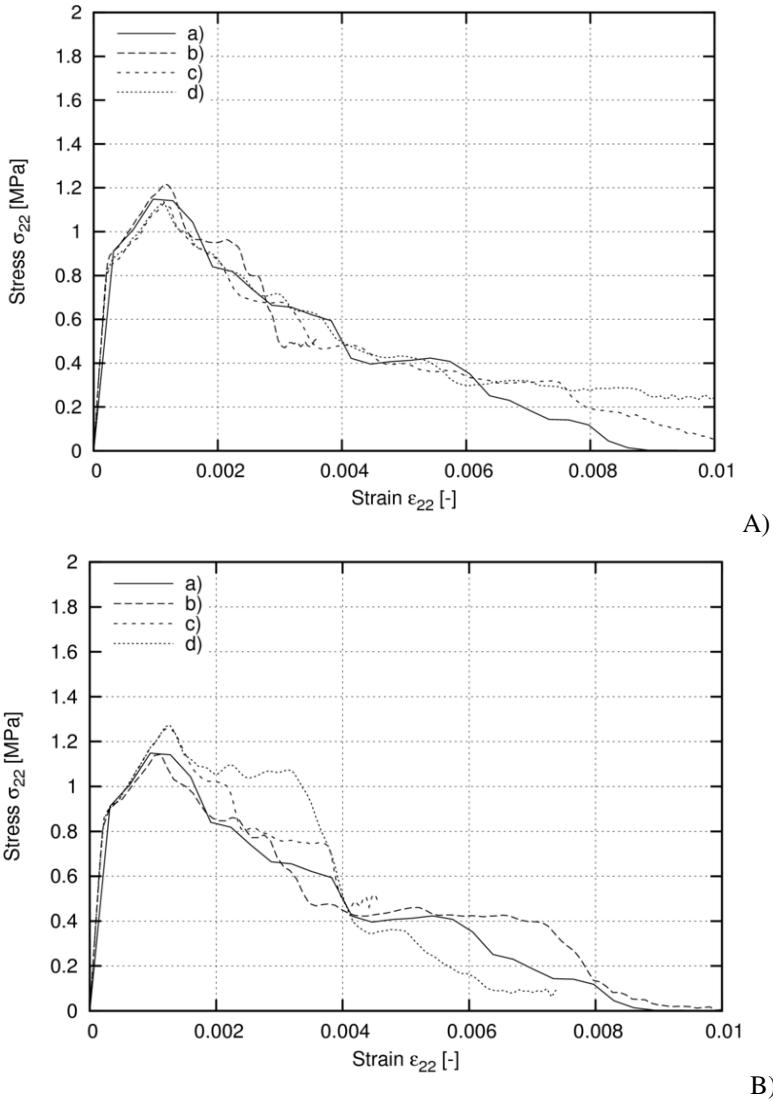
## 5.2.2 Three-Dimensional Simulations of Uniaxial Extension

### Effect of Fibrous Bond Strength and Fibre Volume

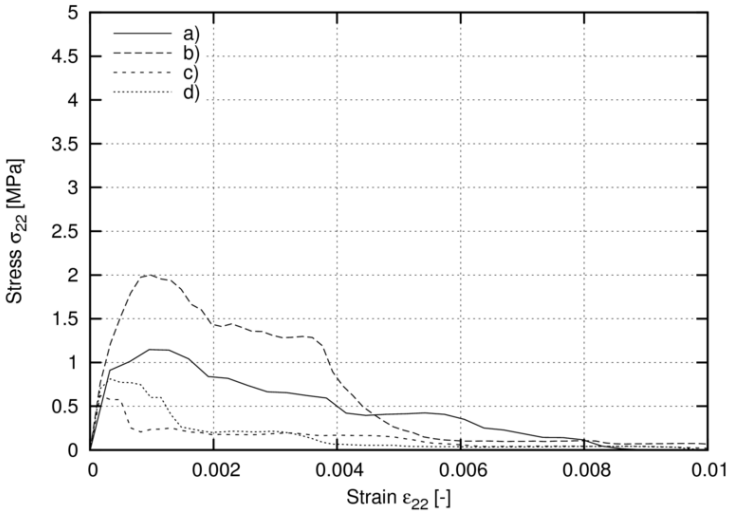
The results of stress-strain curves during quasi-static uniaxial tension with a notched rectangular fibrous concrete specimen  $5 \times 5 \times 5 \text{ cm}^3$  with smooth horizontal edges are shown in Figs.5.64 and 5.65 by assuming the varying threshold local tensile strain  $\varepsilon_{min}$  in the cement matrix-fibre interface ( $\varepsilon_{min}=0.025\%-1.0\%$ ) (Tab.5.4) and two different volumetric contents of straight steel fibres in the concrete mass:  $V_f=0.15\%$  and  $V_f=1.5\%$ . Five stochastic simulations were performed for each case. For each case with the different  $\varepsilon_{min}$ , the mean curves are demonstrated. The fibre length was  $l_f=2.0 \text{ cm}$  ( $d_f=2 \text{ mm}$ ,  $l_f=2.0 \text{ mm}$ ,  $l_f/h=1/25$ ). The same initial distribution of all concrete components was always assumed for each  $\varepsilon_{min}$ . The evolution of fracture in the specimen is demonstrated in Figs.5.66 and 5.67.

Similarly as in 2D simulations, both the strength and ductility of fibrous concrete are improved (in particular with  $V_f=1.50\%$ ) if the cement matrix-fibre interface is stronger than the cement matrix-aggregate interface, i.e. for  $\varepsilon_{th}>0.1\%$  (in this case, both the strength and ductility grow with increasing  $\varepsilon_{min}$ ). The dependence of the tensile strength and area under the stress-strain curve on  $\varepsilon_{min}$  is linear with  $V_f=0.15\%$  and parabolic with  $V_f=1.50\%$ . Further discrete simulations were carried out with the threshold strain  $\varepsilon_{min}=0.5\%$  in the cement matrix-fibre interface. As in the splitting tension and bending experiments by Schnüttgen (1981), Ward and Lin (1990), and Chenkui and Guofan (1995), both the strength and ductility clearly increase with increasing fibre volume. The mean tensile strength  $f_t$  increases from 1.15 MPa (plain concrete) up to  $f_t=1.25 \text{ MPa}$  (fibrous concrete with  $V_f=0.15\%$ ) and even up to  $f_t=2.6 \text{ MPa}$  (fibrous concrete with  $V_f=1.5\%$ ) with  $\varepsilon_{min}=0.5\%$ .

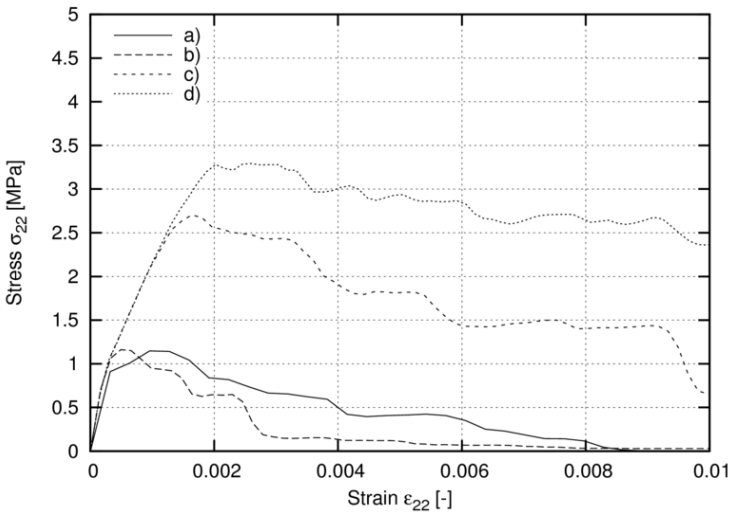
The 3D fracture process develops similarly as in 2D specimens. Since the interface between cement matrix and aggregate is the weakest component of the system, cracks are again created along aggregates. Cracks do not propagate in long lines due to a large number of aggregates. Instead of this, several discontinuous curved macro-cracks propagate in a tortuous manner. The crack propagation is evidently enhanced by the presence of steel fibres which delay their development. As compared to 2D simulations, the fracture process is more complex with more branched strongly curved micro-cracks (significantly more rods break in 3D analyses). Pronounced non-linearity appears in the pre-peak regime.



**Fig. 5.64** Calculated stress-strain curve for 3D notched concrete specimen  $5 \times 5 \times 5 \text{ cm}^3$  subjected to uniaxial extension with  $V_f=0.15\%$  volume content of fibres for different cement matrix-fibre interface strength: A) a) plain concrete, b) no cement matrix-fibre interface, c) cement matrix-fibre interface with  $\epsilon_{min}=0.025\%$ , d) cement matrix-fibre interface with  $\epsilon_{min}=0.05\%$ , B) a) plain concrete, b) cement matrix-fibre interface with  $\epsilon_{min}=0.1\%$ , c) cement matrix-fibre interface with  $\epsilon_{min}=0.5\%$ , d) cement matrix-fibre interface with  $\epsilon_{min}=1.0\%$  ( $\sigma_{22}$  – vertical normal stress,  $\epsilon_{22}$  - vertical normal strain)



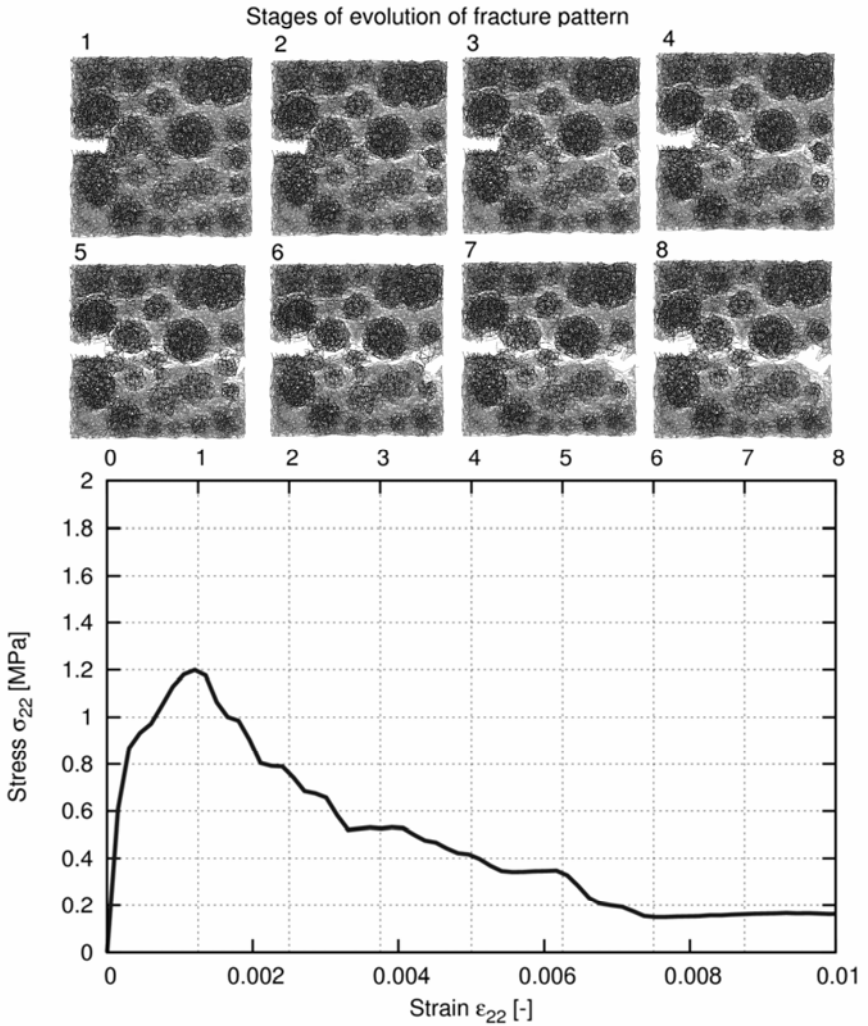
A)



B)

**Fig. 5.65** Calculated stress-strain curve for 3D notched concrete specimen  $5 \times 5 \times 5$  cm<sup>3</sup> subjected to uniaxial extension with  $V_f = 1.5\%$  volume content of fibres for different cement matrix-fibre interface strength: A) a) plain concrete, b) no cement matrix-fibre interface, c) cement matrix-fibre interface with  $\epsilon_{min} = 0.025\%$ , d) cement matrix-fibre interface with  $\epsilon_{min} = 0.05\%$ , B) a) plain concrete, b) cement matrix-fibre interface with  $\epsilon_{min} = 0.1\%$ , c) cement matrix-fibre interface with  $\epsilon_{min} = 0.5\%$ , d) cement matrix-fibre interface with  $\epsilon_{min} = 1.0\%$  ( $\sigma_{22}$  – vertical normal stress,  $\epsilon_{22}$  - vertical normal strain)





**Fig. 5.66** Deformed specimen with crack pattern in notched fibrous concrete specimen  $5 \times 5 \times 5 \text{ cm}^3$  subjected to uniaxial extension: a) 2D deformation process in the mid-section of 1 cm thick in different stages of stress-strain curve (stage number given at the top), b) deformed 3D specimen with distinguished aggregates at peak (stage '1',  $\epsilon_{22}=0.001$ ), c) deformed 3D specimen with distinguished steel fibres at peak (stage '1',  $\epsilon_{22}=0.001$ ) (cement matrix-fibre interface with  $\epsilon_{min}=0.5\%$ , fibre volume  $V_f=0.15\%$ )

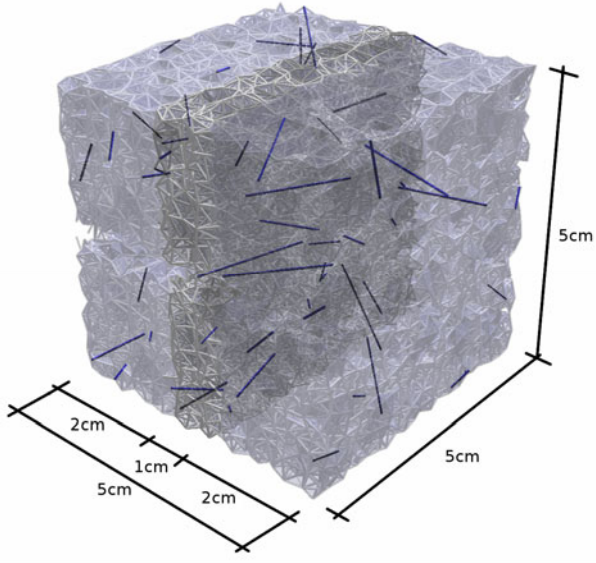
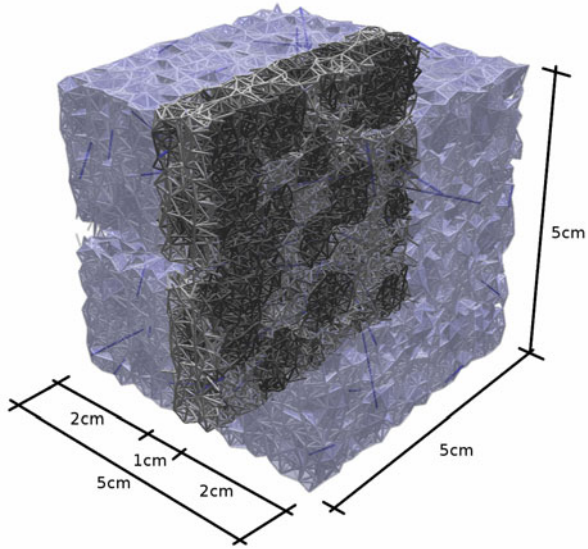
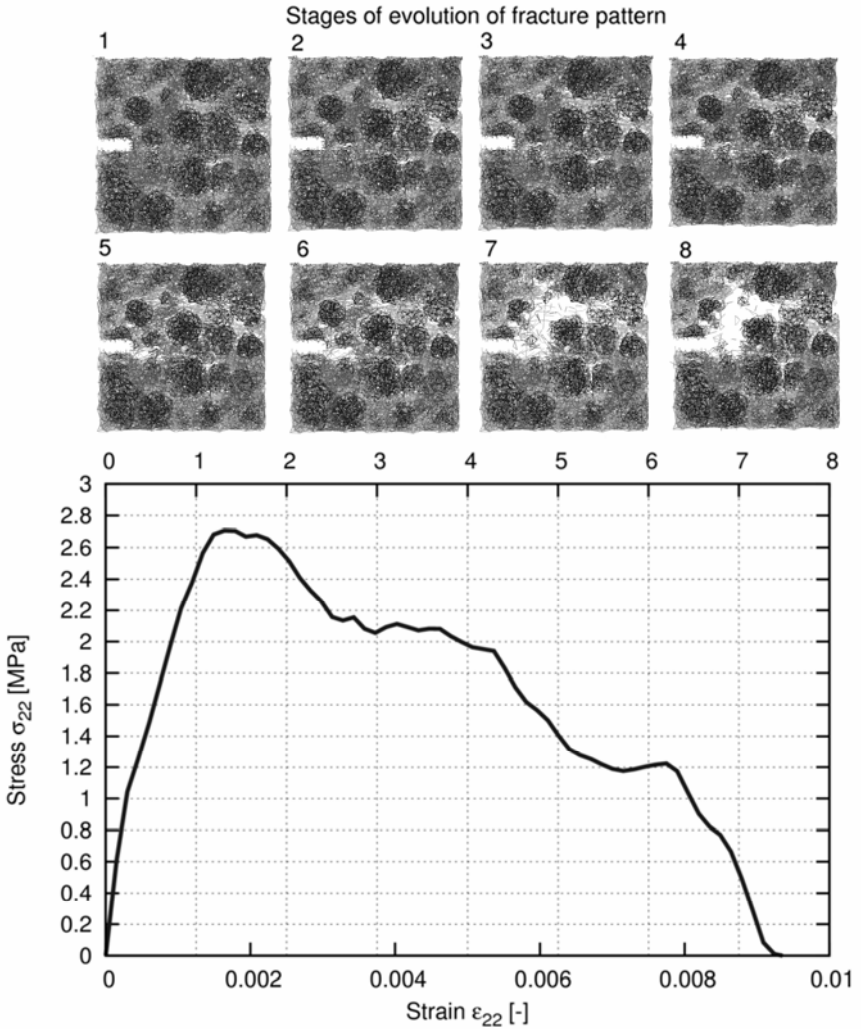


Fig. 5.56 (continued)



**Fig. 5.67** Deformed specimen with crack pattern in notched fibrous concrete specimen  $5 \times 5 \times 5 \text{ cm}^3$  subjected to uniaxial extension: a) 2D deformation process in the mid-section of 1 cm thick in different stages of stress-strain curve (stage number given at the top), b) deformed 3D specimen with distinguished aggregates at peak (stage '1',  $\epsilon_{22}=0.001$ ), c) deformed 3D specimen with distinguished steel fibres at peak (stage '1',  $\epsilon_{22}=0.001$ ) (cement matrix-fibre interface with  $\epsilon_{min}=0.5\%$ , fibre volume  $V_f=1.5\%$ )

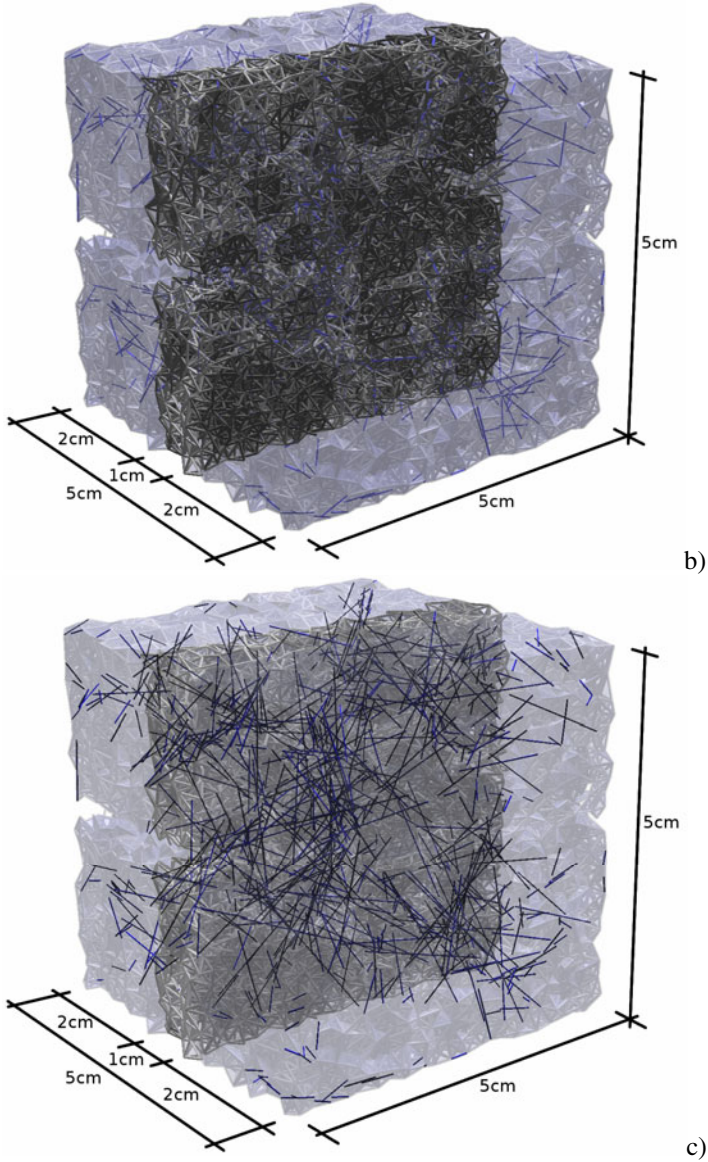


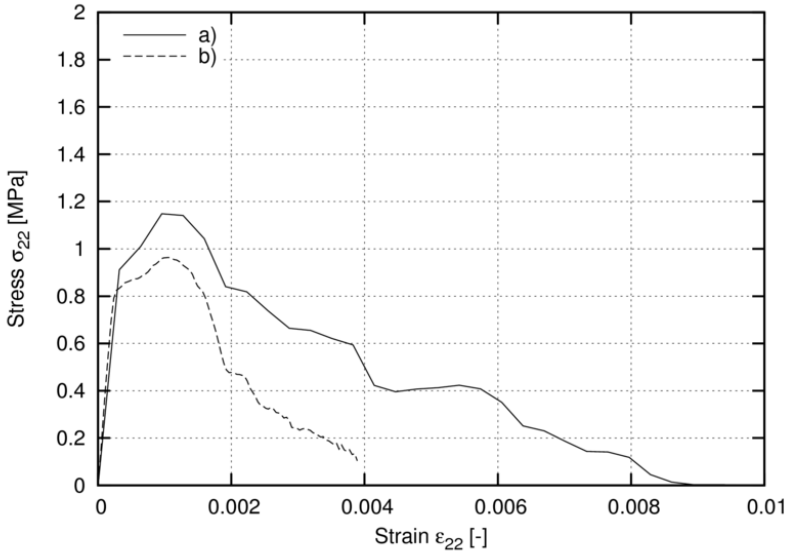
Fig. 5.67 (continued)

As in 2D analyses (Fig.5.54), if the cement matrix-fibre interface is weaker than the cement matrix-aggregate interface ( $\epsilon_{min} < 0.05\%$ ), both material strength and ductility are smaller than in plain concrete due to the fact that cracks are created along fibres which act as imperfections. In the case of the lack of the cement matrix-fibre interface, both material strength and ductility are also higher in fibrous concrete than in plain concrete (due to the different  $k_l$  and  $E$  as compared to the cement matrix-aggregate interface, Tab.5.4).

### Effect of Specimen Size

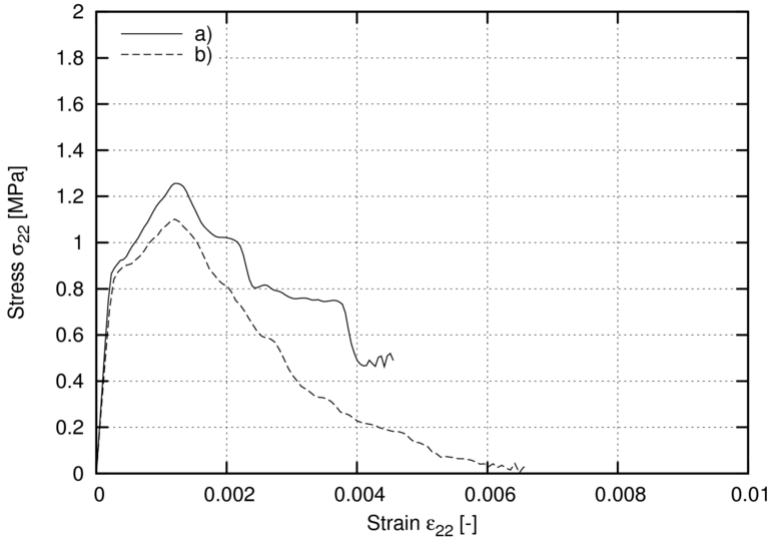
The results of mean stress-strain curves during quasi-static uniaxial tension with notched rectangular fibrous concrete specimens  $5 \times 5 \times 5 \text{ cm}^3$  and  $10 \times 10 \times 10 \text{ cm}^3$  with smooth horizontal edges are shown in Fig.5.68 ( $\epsilon_{min} = 0.5\%$ ,  $l_f = 2 \text{ cm}$ ) for three different volumetric contents of fibres in concrete:  $V_f = 0.0\%$  (plain concrete),  $V_f = 0.15\%$  and  $V_f = 1.5\%$ .

The results show that both the strength and ductility of fibrous concrete (similarly as in concrete, Bazant and Planas 1998) linearly increase with decreasing specimen size causing an evident size effect. The mean tensile strength is about  $f_t = 0.9\text{--}1.15 \text{ MPa}$  ( $V_f = 0.0\%$ ),  $f_t = 1.15\text{--}1.25 \text{ MPa}$  ( $V_f = 0.15\%$ ) and  $f_t = 2.4\text{--}2.6 \text{ MPa}$  ( $V_f = 1.5\%$ ). The size effect is slightly stronger in a plain concrete specimen than in a fibrous one. The numerical results are in agreement with size effect

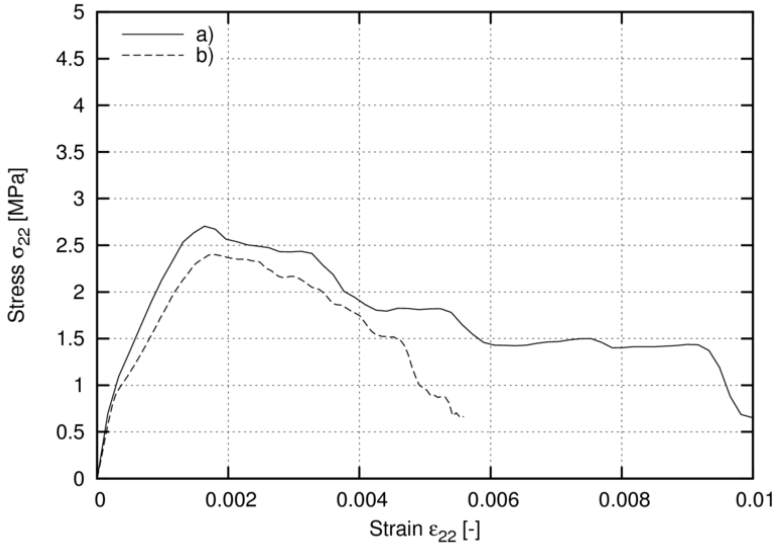


A)

**Fig. 5.68** Calculated stress-strain curves for 3D notched concrete specimen  $5 \times 5 \times 5 \text{ cm}^3$  (a) and  $10 \times 10 \times 10 \text{ cm}^3$  (b) subjected to uniaxial extension ( $\epsilon_{min} = 0.5\%$ ,  $l_f = 2 \text{ cm}$ ,  $l_r = 2 \text{ mm}$ ,  $l_r/h = 1/50\text{--}1/25$ ): A) fibre volume  $V_f = 0.0\%$ , B) fibre volume  $V_f = 0.15\%$ , C) fibre volume  $V_f = 1.5\%$  ( $\sigma_{22}$  – vertical normal stress,  $\epsilon_{22}$  – vertical normal strain)



B)



C)

Fig. 5.68 (continued)

model experiments on fibrous concrete during bending (Ward and Li 1990, Lin 1999, Balendran et al. 2001) and during splitting tension (Balendran et al. 2001). The calculated 3D size effect is similar as this in 2D simulations.

The tensile strength and area under the stress-strain curve increase linearly with increasing fibre volume what is in good accordance with experimental results by Ward and Li (1990), Campione et al. 2005, Altun et al. 2007 and Mohammadi et al. 2008. In the experiments by Chenkui and Guofan (1995), this dependence was more parabolic.

### Effect of Distribution of Fibres

Figures 5.69-5.71 depict the effect of the direction and location of fibres. The effect of an entirely random distribution of steel fibres is demonstrated in Fig.5.69 for five different simulations (specimen  $5 \times 5 \times 5 \text{ cm}^3$ ,  $\varepsilon_{min}=0.5\%$ ,  $V_f=0.15\%$  and  $V_f=1.5\%$ ,  $l_f=2.0 \text{ cm}$ ). Presented are three stress-strain curves: minimum, mean and maximum with the scatter region, respectively. Next, a mean stress-strain curve from stochastic simulations was compared with the mean ones from specimens where fibres were solely oriented horizontally (Figs.5.70Ab and 5.71Ab) or solely oriented vertically (Fig.5.70Bb and 5.71Bb).

The effect of a stochastic distribution of fibres on the stress-strain curve grows with increasing fibre volume. The fibrous specimen is stronger if the fibres are vertically oriented (stronger by 25%), and weaker if the fibres are horizontally oriented (weaker by 10%) as compared to their stochastic orientation (mean stochastic tensile strength was  $f_t=2.6 \text{ MPa}$  at  $V_f=1.5\%$ ). If the fibres are horizontally oriented, the strength's increase is by 100% as compared to plain concrete, and if the fibres are vertically oriented, the strength's growth is by 200% as compared to plain concrete (at  $V_f=1.5\%$ ). The strength increases from 2.4 MPa (horizontally oriented fibres) up to 3.2 MPa (vertically oriented fibres) at  $V_f=1.5\%$ . The dependence of the strength and area under the stress-strain curve on the fibre orientation is linear what is in agreement with splitting tension tests by Lin (1999) and Lohrmann (1999).

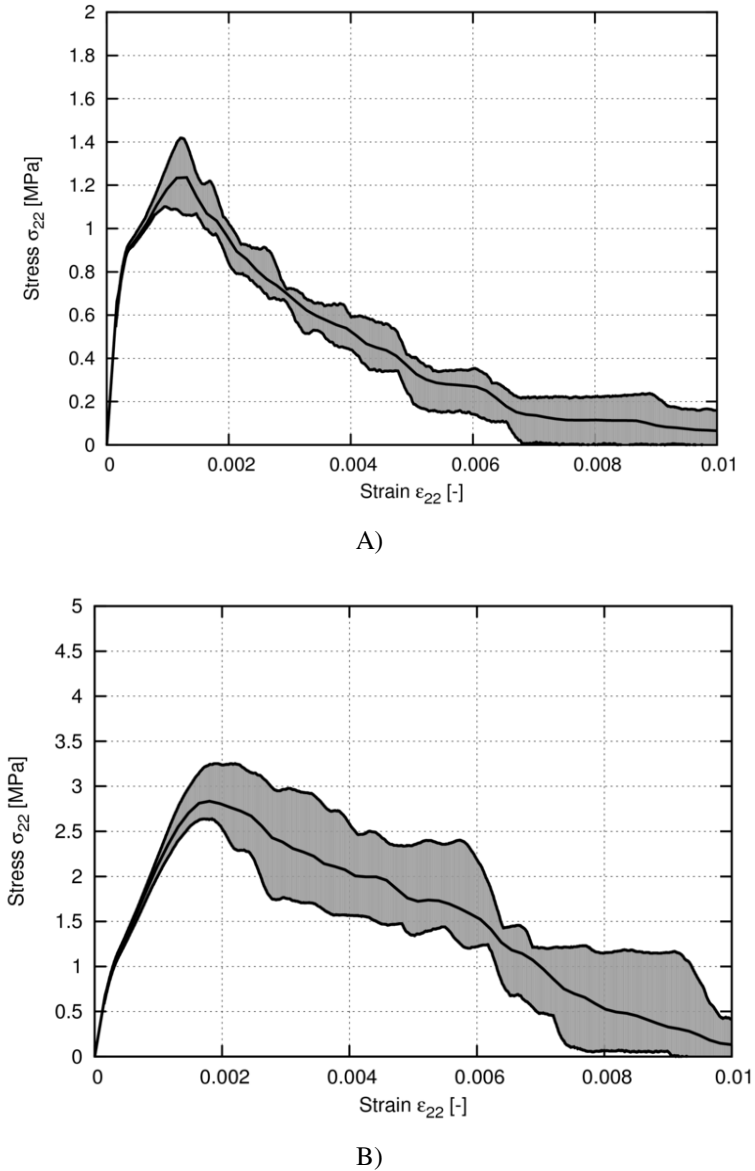
### Effect of Fibre Length

The effect of the fibre length on the mean stress-strain curves during uniaxial tension is demonstrated in Fig.5.72 in the fibrous concrete specimen  $5 \times 5 \times 5 \text{ cm}^3$  and  $10 \times 10 \times 10 \text{ cm}^3$ , respectively. The fibre length was 1 cm, 2 cm, 4 cm and 6 cm, respectively ( $\varepsilon_{min}=0.5\%$  in the cement matrix-fibre interface).

In contrast to 2D outcomes, the strength and ductility increase with increasing fibre length independently of the specimen size (the effect is stronger with a higher fibre volume). The increase of the strength and ductility with the fibre length is linear as in experiments by Gopalaratnam and Shah (1985), Ward and Li (1990) and Mohammadi et al. (2008).

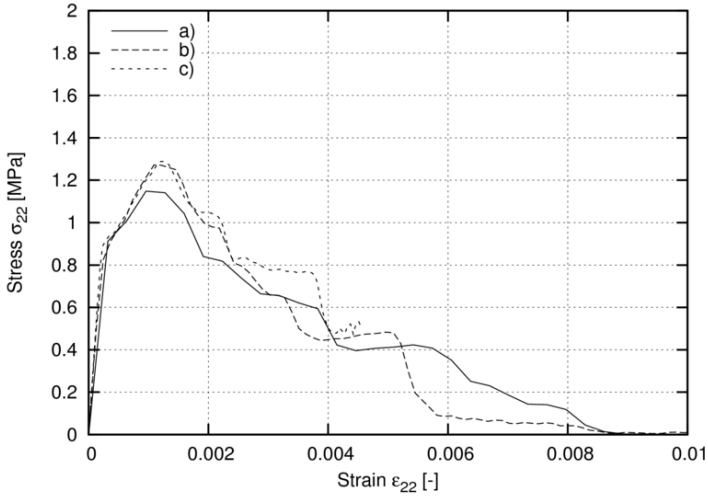
Figure 5.73 shows the number of damaged rods removed during each iteration for 3D uniaxial tension test in the specimen of  $5 \times 5 \times 5 \text{ cm}^3$ . The number of all iterations was about 50'000. The maximum number of rods simultaneously reaching the critical tensile strain in a single iteration was higher with a smaller content of steel fibres than with a higher one, i.e. 6 ( $V_f=1.5\%$ ) and 14 ( $V_f=0.15\%$ ), respectively.

Finally, Figs.5.74 and 5.75 shows the effect of the simulation type on the calculated stress-strain curves. Compared were the mean stress-strain curves from 2D simulations with the mean rod length  $l_f=1$  mm and those from 3D simulations with  $l_f=2$  mm.

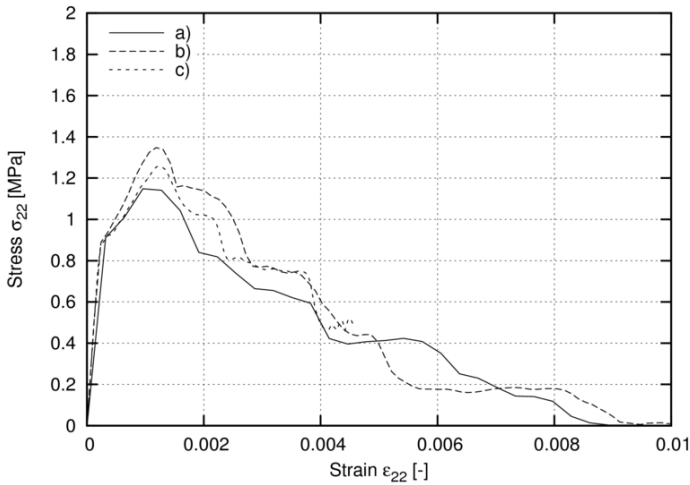


**Fig. 5.69** Calculated stress-strain curves for 3D notched fibrous concrete specimen  $5 \times 5 \times 5$  cm<sup>3</sup> subjected to uniaxial extension ( $\epsilon_{min}=0.5\%$ ,  $l_f=2$  cm,  $l_f/h=1/25$ ) for different 5 stochastic distributions of steel fibres: A)  $V_f=0.15\%$ , B)  $V_f=1.5\%$  ( $\sigma_{22}$  – vertical normal stress,  $\epsilon_{22}$  – vertical normal strain)



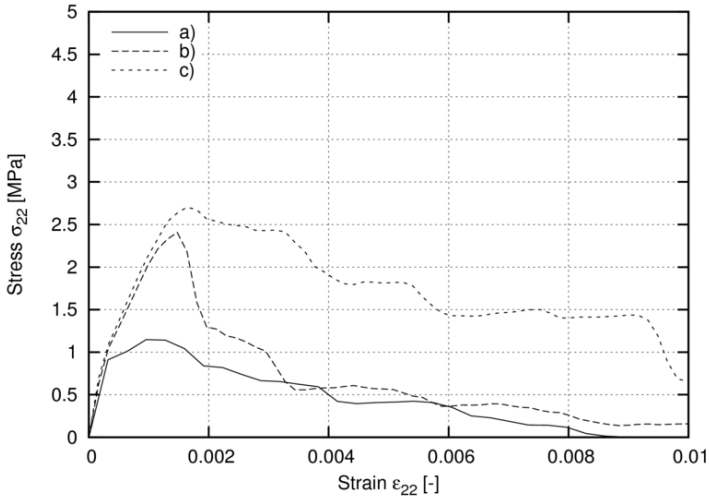


A)

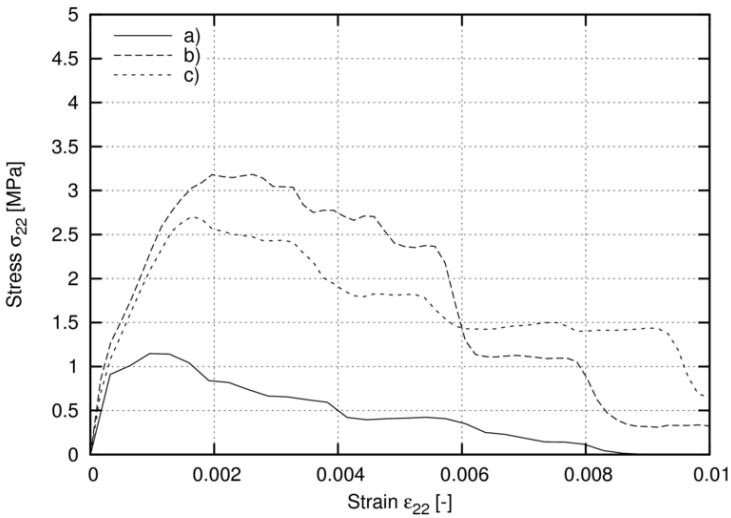


B)

**Fig. 5.70** Calculated stress-strain curves for 3D notched concrete specimen  $5 \times 5 \times 5 \text{ cm}^3$  subjected to uniaxial extension with  $V_f = 0.15\%$  volume amount of fibres for different fibre orientation ( $\epsilon_{min} = 0.5\%$ ,  $l_f = 2 \text{ cm}$ ,  $l_f = 2.0 \text{ mm}$ ,  $l_f/h = 1/25$ ): A) a) plain concrete, b) fibres oriented horizontally, c) fibres distributed stochastically, B) a) plain concrete, b) fibres oriented vertically, c) fibres distributed stochastically ( $\sigma_{22}$  - vertical normal stress,  $\epsilon_{22}$  - vertical normal strain)

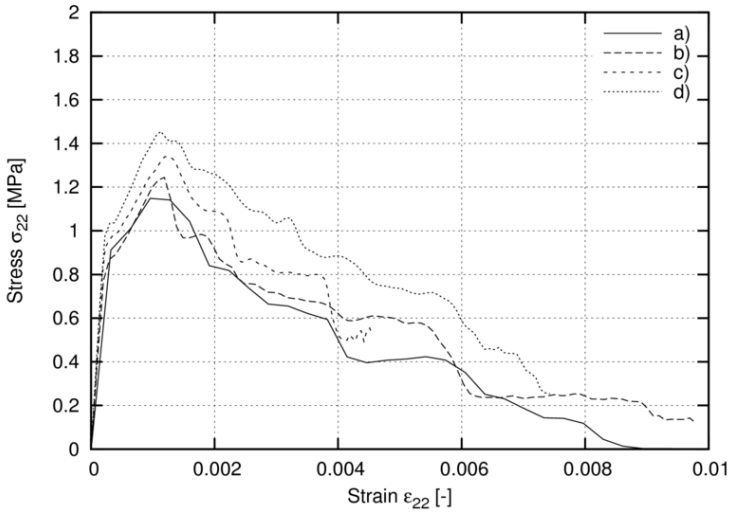


A)

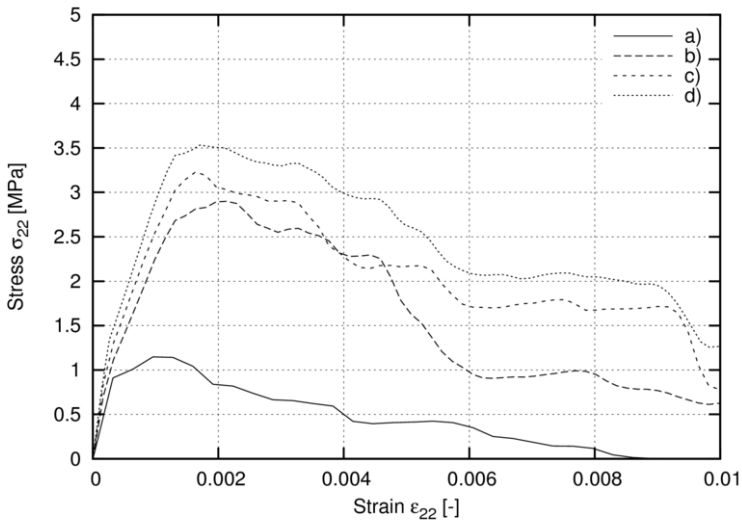


B)

**Fig. 5.71** Calculated stress-strain curves for 3D notched concrete specimen  $5 \times 5 \times 5 \text{ cm}^3$  subjected to uniaxial extension with  $V_f = 1.5\%$  volume amount of fibres for different fibre orientation ( $\epsilon_{min} = 0.5\%$ ,  $l_f = 2.0 \text{ mm}$ ,  $l_f = 2 \text{ cm}$ ): A) a) plain concrete, b) fibres oriented horizontally, c) fibres distributed stochastically, B) a) plain concrete, b) fibres oriented vertically, c) fibres distributed stochastically ( $\sigma_{22}$  – vertical normal stress,  $\epsilon_{22}$  – vertical normal strain)

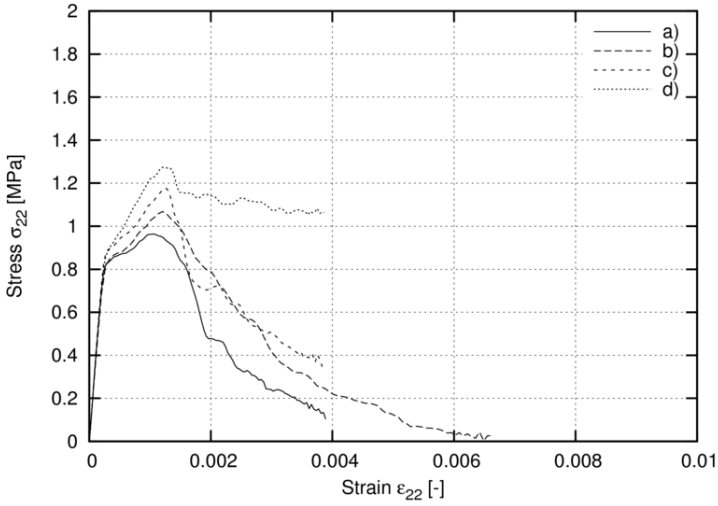


A)

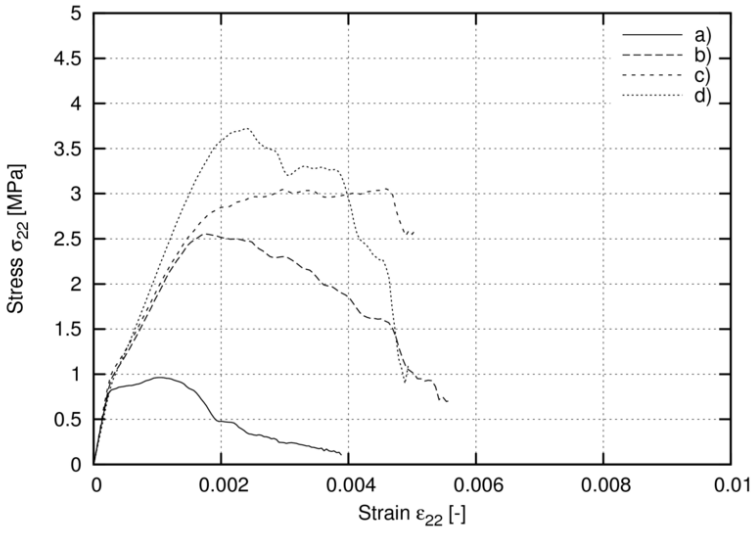


B)

**Fig. 5.72** Calculated stress-strain curves for 3D notched fibrous concrete specimens subjected to uniaxial extension ( $\epsilon_{min}=0.5\%$ ) for different lengths of steel fibres  $l_f$ : A) specimen  $5 \times 5 \times 5 \text{ cm}^3$ : a) plain concrete, b)  $V_f=0.15\%$ ,  $l_f=1 \text{ cm}$ , c)  $V_f=0.15\%$ ,  $l_f=2 \text{ cm}$ , d)  $V_f=0.15\%$ ,  $l_f=4 \text{ cm}$ , B) specimen  $5 \times 5 \times 5 \text{ cm}^3$ : a) plain concrete, b)  $V_f=1.5\%$ ,  $l_f=1 \text{ cm}$ , c)  $V_f=1.5\%$ ,  $l_f=2 \text{ cm}$ , d)  $V_f=1.5\%$ ,  $l_f=4 \text{ cm}$ , C) specimen  $10 \times 10 \times 10 \text{ cm}^3$ : a) plain concrete, b)  $V_f=0.15\%$ ,  $l_f=2 \text{ cm}$ , c)  $V_f=0.15\%$ ,  $l_f=4 \text{ cm}$ , d)  $V_f=0.15\%$ ,  $l_f=6 \text{ cm}$ , D) specimen  $10 \times 10 \times 10 \text{ cm}^3$ : a) plain concrete, b)  $V_f=1.5\%$ ,  $l_f=2 \text{ cm}$ , c)  $V_f=1.5\%$ ,  $l_f=4 \text{ cm}$ , d)  $V_f=1.5\%$ ,  $l_f=6 \text{ cm}$  ( $\sigma_{22}$  – vertical normal stress,  $\epsilon_{22}$  – vertical normal strain)

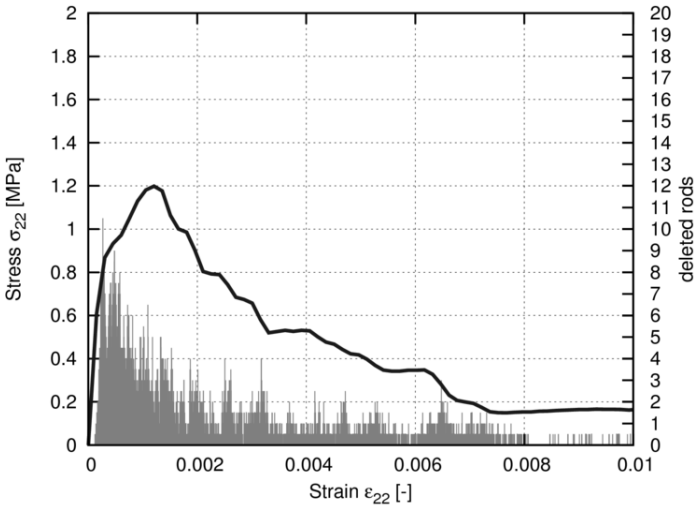


C)

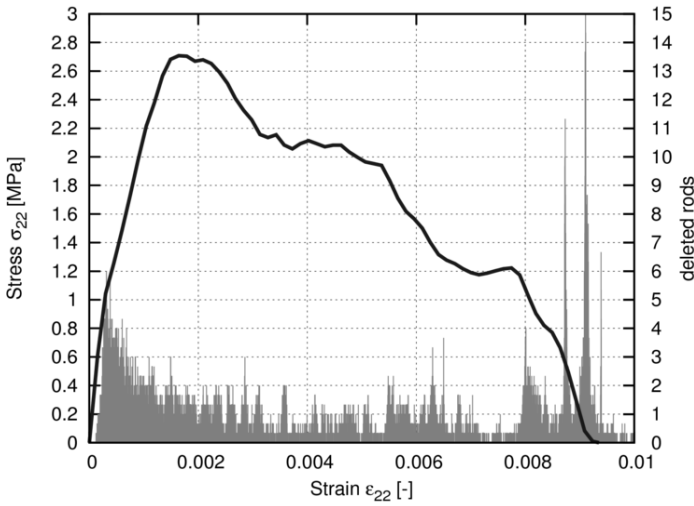


D)

Fig. 5.72 (continued)

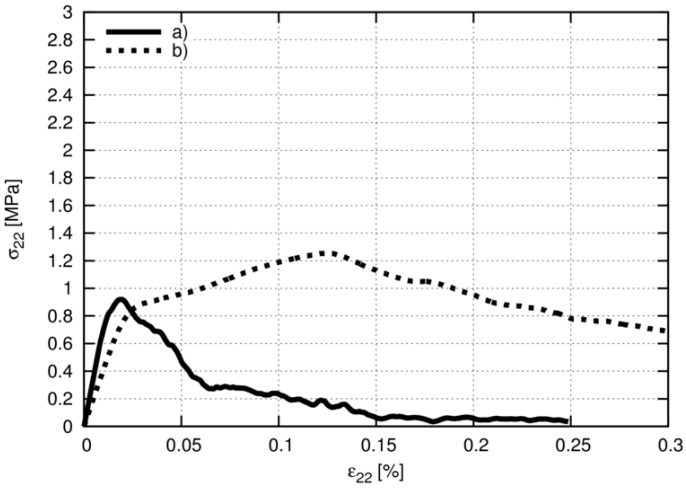


A)

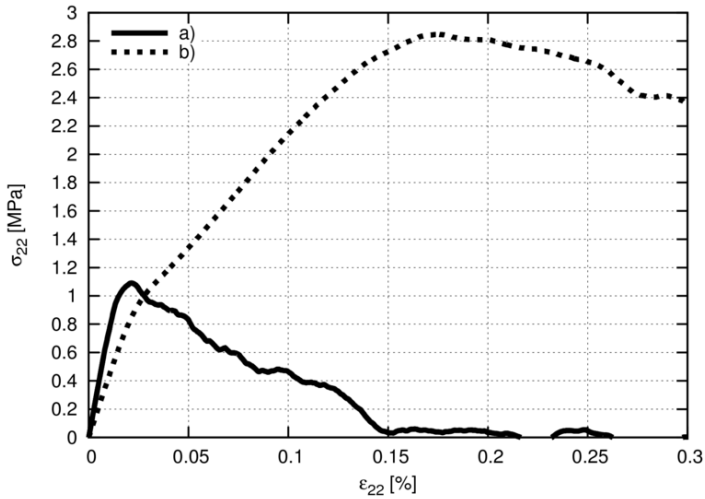


B)

**Fig. 5.73** Stress-strain curve for uniaxial extension for 3D notched fibrous concrete specimen  $5 \times 5 \times 5 \text{ cm}^3$  and the number of damaged rods removed in each iteration ( $\epsilon_{\min} = 0.5\%$ ,  $l_f = 2 \text{ cm}$ ,  $l_r = 2.0 \text{ mm}$ ): A)  $V_f = 0.15\%$ , B)  $V_f = 1.5\%$  ( $\sigma_{22}$  – vertical normal stress,  $\epsilon_{22}$  – vertical normal strain)

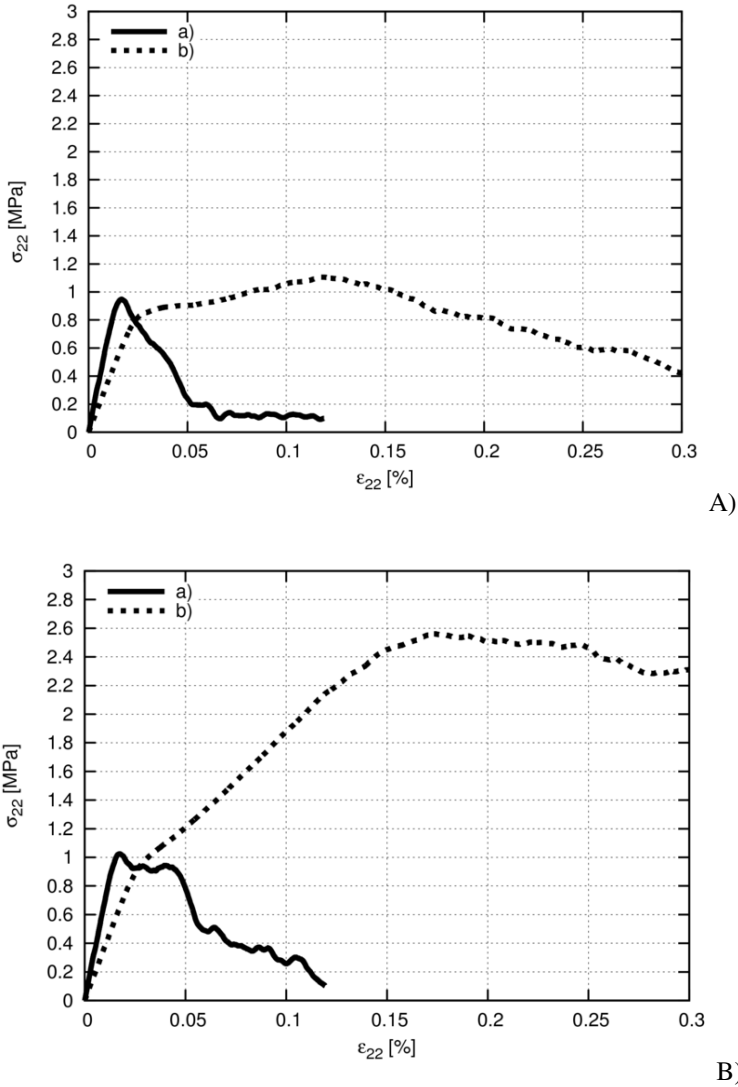


A)



B)

**Fig. 5.74** Calculated mean stress-strain curves for notched fibrous concrete specimens subjected to uniaxial extension ( $\varepsilon_{min}=0.5\%$ ): a) 2D simulations, specimen  $5 \times 5 \text{ cm}^2$ ,  $l_f=1 \text{ mm}$ ,  $l_f/h=1/50$ , b) 3D simulations, specimen  $5 \times 5 \times 5 \text{ cm}^3$ ,  $l_f=2 \text{ mm}$ ,  $l_f/h=1/25$ , A)  $A_f=V_f=0.15\%$ , B)  $A_f=V_f=1.5\%$  ( $\sigma_{22}$  – vertical normal stress,  $\varepsilon_{22}$  – vertical normal strain)

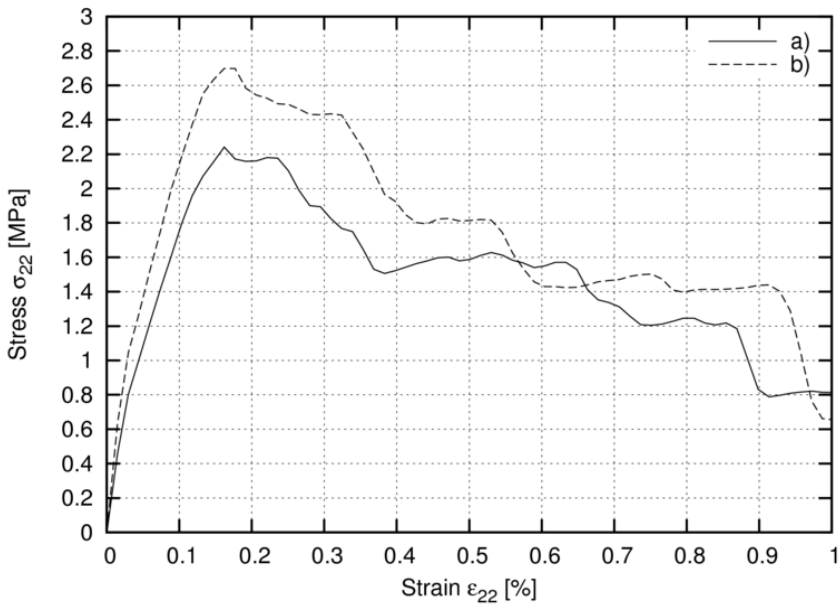


**Fig. 5.75** Calculated mean stress-strain curves for notched concrete specimens subjected to uniaxial extension ( $\varepsilon_{min}=0.5\%$ ): a) 2D simulations, specimen  $10 \times 10 \text{ cm}^2$ ,  $l_f=1 \text{ mm}$ ,  $l_f/h=1/100$ , b) 3D simulations, specimen  $10 \times 10 \times 10 \text{ cm}^3$ ,  $l_f=2 \text{ mm}$ ,  $l_f/h=1/50$ , A)  $A_j=V_j=0.15\%$ , B)  $A_j=V_j=1.5\%$  ( $\sigma_{22}$  – vertical normal stress,  $\varepsilon_{22}$  – vertical normal strain)

The results show that the difference between 2D and 3D discrete analyses is pronounced. The material behavior in the 3D model is significantly stronger and more ductile. The fracture energy is significantly higher in 3D simulations because: a) more fibres can be placed in the volumetric unit as in the area unit with the same fibre length, b) more rods break in 3D simulations what requires more energy, c) the crack propagation way is longer in 3D computations since the cracks are more curved and propagate in a more tortuous manner and d) torsion is taken into account in 3D analyses. The vertical normal strain corresponding to the peak on the stress-strain curve is also higher in 3D analyses.

### Effect of Torsion

The 3D results with a fibrous concrete specimen ( $V_f=1.5\%$ ,  $l_f=2$  cm) are demonstrated in Fig.5.76. One assumed the torsional stiffness parameter  $k_t=0$  or  $k_t=k_b$  ( $k_b$  - bending stiffness parameter). The material strength is obviously higher when the torsional stiffness is taken into account.



**Fig. 5.76** Calculated stress-strain curves for 3D notched fibrous concrete specimens subjected to uniaxial extension ( $\epsilon_{min}=0.5\%$ ,  $l_r=2$  mm, specimen  $5\times 5\times 5$  cm<sup>3</sup>,  $l_r/h=1/25$ ): a)  $k_t=0$ , b)  $k_t=k_t$  ( $V_f=1.5\%$ ,  $l_f=2$  cm,  $\sigma_{22}$  - vertical normal stress,  $\epsilon_{22}$  - vertical normal strain,  $k_t$  - torsional stiffness parameter,  $k_b$  - bending stiffness parameter)



### 5.2.3 Two-Dimensional Simulations of Three-Point Bending

Figures 5.77-5.78 show the 2D results for a small-size and medium-size beam of Fig.5.32 with ( $\epsilon_{min}=0.5\%$  in the fibrous bond) and without steel fibres. The aggregate area percentage was assumed to be 50%. The fibre area was 2.25%. The minimum rod length was 0.2 mm and the maximum one was 2 mm ( $l_f=1.0$  mm in average). One assumed the fibre length  $l_f=2$  cm.

Both the strength and ductility increase with increasing number of fibres (Fig.5.77). As in the case of uniaxial tension, steel fibres prohibit the development of vertical cracks (Figs.5.78 and 5.79). The scatter of results with respect to load-displacement evolutions is again relatively large what indicates that the effect of the fibre orientation is of major importance.

## 5.3 Conclusions

The following conclusions can be drawn from numerical results of fibrous concrete specimens with our lattice model, where individual straight steel fibres were explicitly modeled in the irregular lattice:

Strength and ductility of fibrous concrete specimens increase with increasing number of fibres during uniaxial extension if the strength of the cement matrix-fibre interface is equal or higher than the strength of the cement matrix-aggregate interfacial zones. In this case, the crack propagation is delayed by the presence of steel fibres. Both the strength and ductility of fibrous concrete strongly depend on cement matrix-fibre bond strength (they grow with increasing cement matrix-fibre bond strength).

The orientation of fibres very strongly influences strength and failure of the material. The effectivity of fibrous concrete significantly increases, if fibres are located perpendicularly to the cracks' direction.

Strength and ductility of fibrous concrete specimens increase with increasing fibre length.

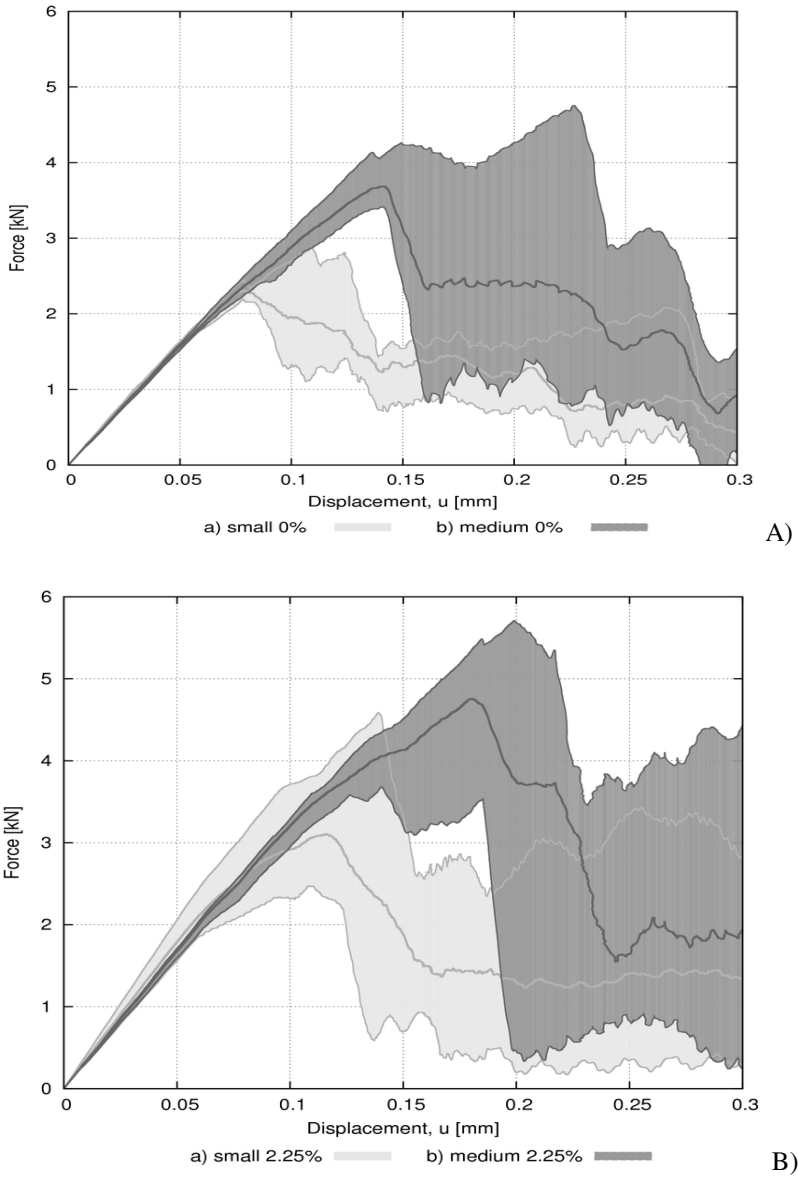
A deterministic size effect occurs in fibrous concrete specimen, i.e. strength and ductility increase with decreasing specimen size.

The specimen strength and toughness are higher when the torsional stiffness is taken into account.

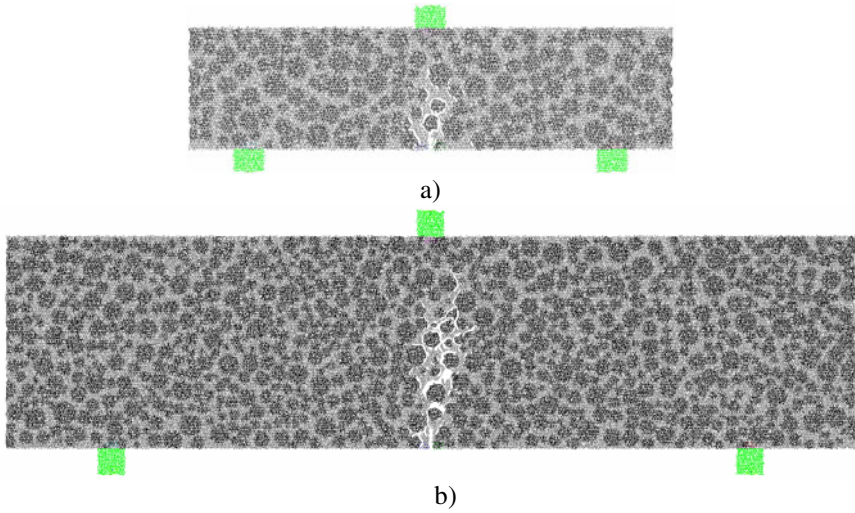
The 3D results significantly differ from the 2D results (as in plain concrete). The effect of fibres appears to be significantly stronger in 3D simulations than in 2D ones. The scatter of results is also larger in 3D simulations. To obtain similar 2D and 3D results, a different calibration procedure has to be performed. A fracture process is significantly more complex in 3D specimens, i.e. more branched and tortuous micro-cracks are created.

The specimen strength is higher when the torsional stiffness is taken into account.

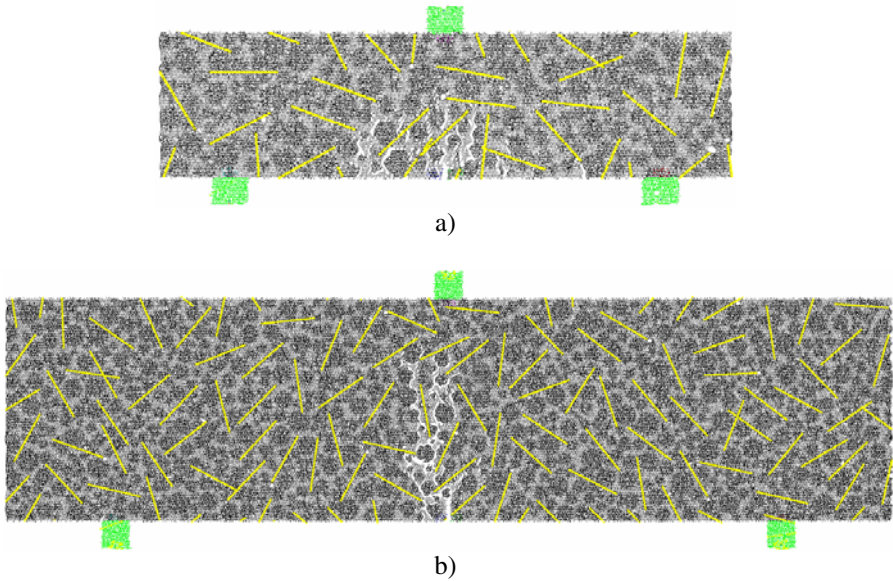
A non-local approach can totally eliminate the effect of the rod length on results. However, it significantly increases the computation time. Thus, it is more efficient to use a rod length small enough.



**Fig. 5.77** Load-displacement curves ( $u$  – beam deflection) for a 2D concrete small-size and medium-size beam of Fig 5.32 subject to three-point bending: A) beams without steel fibres, B) beams with 2.25% steel fibres



**Fig. 5.78** Calculated 2D crack pattern during three-point bending without steel fibres: a) small-size beam, b) medium-size beam



**Fig. 5.79** Calculated 2D crack pattern during three-point bending with 2.25% steel fibres: a) small-size beam, b) medium-size beam

## 6 Epilogue

The book deals with a fracture process in plain concrete and in fibrous concrete elements including straight steel fibres. The experimental results of numerous tests described in the scientific literature and the numerical results obtained with a novel discrete lattice model were presented.

The following main conclusions can be drawn from experimental results summarized in Section 3.

Plain concrete specimens fail catastrophically by a single crack. On the contrary, fibre-reinforced concrete specimens, even those with a small fibre volume fraction, retain post-cracking ability to carry out loads. The inclusion of steel fibres improves the following properties of concrete under quasi-static and dynamic loading: flexural tensile strength, splitting tensile strength, ductility, first cracking strength, toughness (energy absorption capacity), stiffness, durability, impact resistance, fatigue, wear strength, shock vibration resistance, crack width, freeze-thaw resistance, shrinkage and creep since fibres limit the formation and growth of cracks by providing pinching forces at crack tips (they help in bridging the propagating cracks). The most important positive property is an increase of material ductility. However, concrete workability decreases, and both concrete sorptivity and volumetric weight increase at the same time with an increase of fibres. It is noticeable in the case of compression, wherein addition of fibres may not contribute to an increase of strength due to a growth of voids. The degree of concrete improvement depends upon: size, shape, anchorage, aspect ratio, volume fraction, orientation and surface roughness of fibres, ratio between fibre length and maximum aggregate size, volume ratio between long and short fibres and concrete class. In particular, the effect of the fibre orientation is of a major importance dependent upon flow direction of concrete against the casting direction. The positive effect is greater if more fibres are inclined perpendicularly to the direction of cracks.

The following basic conclusions can be drawn from 2D and 3D numerical quasi-static results with a discrete lattice model to describe the behaviour of plain concrete and fibrous concrete with individual fibres distributed at random and explicitly modeled (Section 5).

An irregular lattice model is a simple discrete approach to the fracture behavior in heterogeneous quasi-brittle materials. By using an elastic-purely brittle local

fracture law at the particle level of the material, global softening behavior is obtained. The heterogeneous 3D-lattice model for fibrous concrete used in the book requires 5 material parameters for each of five phases: cement matrix, aggregate, fibres, cement matrix-fibre interface and cement matrix-aggregate interface (which can be calibrated with a uniaxial extension test) and 2 grid parameters (when using Delaunay's method) or 4 grid parameters (when using a Voronoi's scheme) related to the distribution of rods in a lattice

The obtained results of crack patterns and stress-strain curves for plain concrete during uniaxial tension, uniaxial compression, three-point bending and combined shear-extension are realistic. A quantitative comparison of numerical results with corresponding ones is not possible due to the lack of the detailed information on concrete micro-structure of specimens used in experiments (aggregate density, aggregate roughness, aggregate distribution curve, contact zone thickness).

The particle density and distribution of weak bond zones have a significant effect on the plain concrete behavior. Both strength and pre-peak non-linearity decrease with increasing aggregate density and decreasing mean aggregate diameter during uniaxial tension. The material ductility increases when the aggregate density increases. The vertical strain corresponding to the peak increases with decreasing particle density. At the low particle content, de-bonding occurs extensively near the isolated aggregates. At the high particle density, percolation of bond zones occurs, and the condition for macro-crack nucleation and growth takes place. The pre-peak non-linearity cannot be ignored at low particle density. The macro-crack process occurs before the maximum load. The stress-strain curves are strongly affected by a stochastic distribution of rods in a lattice. The rod number and strain increment have also a significant effect on results. To obtain realistic results, the ratio between the rod length and the smallest specimen size has to be at least 1/100-1/50 in 2D and 1/66-1/33 in 3D specimens. About 500-1000 iterations are needed to remove a single element. The results of 3D simulations are only qualitatively the same as the corresponding 2D ones. The tensile strength and vertical strain related to the peak on the load-displacement curve are significantly larger in 3D simulations than in 2D ones using the same parameters. The advantage of our quasi-static lattice model lies in its explicit character. Thus, a large number of rod elements can be taken into account when using parallelized computers as compared to implicit lattice models. To entirely eliminate the effect of a rod length on results, a non-local approach can be used.

Both strength and ductility of fibrous concrete specimens including straight steel fibres increase with increasing number and length of fibres during uniaxial extension and three-point bending if the stiffness of the cement matrix-fibre interface is higher than the stiffness of cement matrix-aggregate interfacial zones. In this case, the crack propagation is delayed by the presence of steel fibres. The effectivity of fibrous concrete significantly increases if fibres are located perpendicularly to the direction of cracks. The orientation of fibres strongly influences strength and failure of the material (it is the most dominating factor in

fibrous concrete). A significant deterministic size effect also occurs in fibrous concrete (as in plain concrete), i.e. strength and ductility increase with decreasing specimen size. The effect of steel fibres is stronger in 3D analyses. The 3D fracture process is more complex than in 2D specimens due to occurrence significantly more branched and tortuous cracks. The 3D results are more realistic than the corresponding 2D results as compared to laboratory experiments.

The calculations with a lattice model will be continued. Further calibration studies will be performed to obtain a quantitative agreement with experiments by taking into account the real micro-structure of fibrous concrete specimens. The effect of the material heterogeneity and fibre distribution will be carefully investigated. The possibility of a crack closure will be considered. A two-scale model will be used linking a lattice model with a continuum elastic-plastic model wherein the first model will be restricted to the damaged and fractured part of the concrete specimen only. In addition, inertial forces will be taken into account during dynamic calculations.

**Acknowledgment.** Scientific research has been carried out as a part of the Project: “Innovative resources and effective methods of safety improvement and durability of buildings and transport infrastructure in the sustainable development” financed by the European Union. The second author thanks also Foundation for Polish Science and Gdansk University of Technology for their financial support when preparing the book.

## References

- Abdul-Ahad, R.B., Aziz, O.Q.: Flexural strength of reinforced concrete T-beams with steel fibers. *Cement and Concrete Composites* 21, 263–268 (1999)
- ACI Committee 544, Design considerations for steel fiber reinforced concrete. *ACI Manual of Concrete Practice* part 5, 544.4R-1–544.4R-18 (1999)
- Akkermann, J.: Rotationsverhalten von Stahlbeton-Rahmenecken. Dissertation, Universität Fridericiana zu Karlsruhe, Karlsruhe (2000)
- Alavizadeh-Farhang, A.: Plain and steel fibre reinforced concrete beams subjected to combined mechanical and thermal loading. PhD Thesis, Royal Institute of Technology, Stockholm, Sweden (1999)
- Alexander, S.D.B., Simmonds, S.H.: Punching shear tests of concrete slab-column joints containing fiber reinforcement. *ACI Struct. J.* 89(4), 425–432 (1992)
- Al-Taan, S.A., Al-Feel, J.R.: Evaluation of shear strength of fibre reinforced concrete beams. *Cement and Concrete Composites* 12, 87–94 (1990)
- Al-Taan, S.A., Ezzadeen, N.A.: Flexural analysis of reinforced fibrous concrete members using the finite element method. *Computers and Structures* 56(6), 1065–1072 (1995)
- Altoubat, S.A., Roesler, J.R., Lange, D.A., Rieder, K.-A.: Simplified method for concrete pavement design with discrete structural fibers. *Construction and Building Materials* 22, 384–393 (2008)
- Altun, F., Haktanir, T., Ari, K.: Effects of steel fiber addition on mechanical properties of concrete and RC beams. *Construction and Building Materials* 21, 654–661 (2007)

- Armelin, H.S., Bantia, B.: Predicting the flexural postcracking performance of steel fiber reinforced concrete from the pullout of single fibers. *ACI Materials Journal* 94(1), 18–31 (1997)
- Asferg, P.N., Poulsen, P.N., Nielsen, L.O.: Modelling of crack propagation in concrete applying the XFEM. In: Meschke, G., de Borst, R., Mang, H., Bicanic, N. (eds.) *Computational Modelling of Concrete Structures, EURO-C*, pp. 33–42. Taylor and Francis, Abington (2006)
- Ashour, S.A., Hasanain, G.S., Wafa, F.F.: Shear behavior of high-strength fiber reinforced concrete beams. *ACI Struct. J.* 89(2), 176–184 (1992)
- ASTM C1018-97 Standard test method for flexural toughness and first-crack strength of fiber-reinforced concrete (1997)
- Atis, C.D.: High volume fly ash abrasion resistant concrete. *J. Mater. Civil Eng.* 14(3), 274–277 (2002)
- Atis, C.D.: High-volume fly ash concrete with high strength and low drying shrinkage. *J. Mater. Civil Eng.* 15(4), 153–156 (2003)
- Atis, C.D.: Carbonation-porosity-strength model for fly ash concrete. *J. Mater Civil Eng.* 16(1), 91–94 (2004)
- Atis, C.D., Karahan, O.: Properties of steel fiber reinforced fly ash concrete. *Construction and Building Materials* 23(1), 392–399 (2009)
- Balaguru, P., Shah, S.P.: *Fiber reinforced cement composites*. McGraw-Hill, USA (1992)
- Balaguru, P., Foden, A.: Properties of fiber reinforced structural lightweight concrete. *ACI Materials Journal* 93(1), 63–78 (1996)
- Baledran, R.V., Zhou, F.P., Nadeem, A., Leung, A.Y.T.: Influence of steel fibres on strength and ductility of normal and lightweight high strength concrete. *Building and Environment* 37, 1361–1367 (2002)
- Bantia, N.: A Study of some factors affecting the fibre-matrix bond in steel fibre. *Can. J. Civil Eng.* 17(4), 610–620 (1990)
- Bazant, Z.P., Bhat, P.D.: Endochronic theory of inelasticity and failure of concrete. *ASCE Journal of Engineering Mechanics* 102, 701–722 (1976)
- Bazant, Z.P., Shieh, C.L.: Endochronic model for nonlinear triaxial behaviour of concrete. *Nucl. Engng. Des.* 47, 305–315 (1978)
- Bazant, Z.P.: Mechanics of distributed cracking. *Appl. Mech. Rev.* 26, 675–705 (1986)
- Bazant, Z.P., Ozbolt, J.: Non-local microplane model for fracture, damage and size effect in structures. *ASCE Journal of Engineering Mechanics* 116, 2485–2505 (1990)
- Bazant, Z.P., Schell, W.F.: Fatigue fracture of high-strength concrete and size effect. *ACI Mater. J.* 5, 472–478 (1993)
- Bazant, Z.P., Jirasek, M.: Nonlocal integral formulations of plasticity and damage: survey of progress. *J. Engng. Mech.* 128(11), 1119–1149 (2002)
- Bazant, Z.P.: *Scaling of structural strength*. Hermes-Penton, London (2003)
- Beghini, A., Bazant, Z.P., Zhou, Y., Gouirand, O., Caner, F.C.: Microplane model M5f for multiaxial behaviour and fracture of fibre-reinforced concrete. *J. Engng. Mech.* 133(1), 66–75 (2007)
- Belytschko, T., Moes, N., Usui, S., Parimi, C.: Arbitrary discontinuities in finite elements. *International Journal for Numerical Methods in Engineering* 50(4), 993–1013 (2001)
- Bentur, A., Mindess, S.: *Fiber reinforced cementitious composites*. Elsevier Applied Science, New York (1990)

- Billington, S.L.: Alternative approaches to simulating the performance of ductile fibre-reinforced cement-based materials in structural applications. In: Bicanic, N., de Borst, R., Mang, H., Meschke, G. (eds.) *Computational Modelling of Concrete Structures*, pp. 15–29. Taylor and Francis, Abington (2010)
- Bobiński, J., Tejchman, J.: Numerical simulations of localization of deformation in quasi-brittle materials within non-local softening plasticity. *Computers and Concrete* 4, 433–455 (2004)
- Bobiński, J., Tejchman, J.: Modelling of concrete behaviour with a non-local continuum damage approach. *Archives of Hydro-Engineering and Environmental Mechanics* 52(2), 85–102 (2005)
- Bobiński, J., Tejchman, J.: Modelling of size effects in concrete using elasto-plasticity with non-local softening. *Archives of Civil Engineering* 52(1), 7–35 (2006a)
- Bobiński, J., Tejchman, J.: Modelling of strain localization in quasi-brittle materials with coupled elasto-plastic-damage model. *J. Theoretical and Applied Mechanics* 44(4), 767–782 (2006b)
- Bobiński, J., Tejchman, J.: Quasi-static crack propagation in concrete with cohesive elements under mixed-mode conditions. In: Schrefler, B.A., Perego, U. (eds.) *Proc. 8th World Congress on Computational Mechanics WCCM 2008*, Venice, vol. 30.06-4.06, pp. 6–4 (2008)
- Bolander, J.E., Saito, S.: Discrete modeling of short-fiber reinforcement in cementitious composites. *Adv. Cem. Based Mater.* 6, 76–86 (1997)
- Bolander, J.E., Sukumar, N.: Irregular lattice model for quasi-static crack propagation. *Phys. Rev. B* 71, 94106 (2005)
- Bonzel, J., Dahms, J.: Schlagfestigkeit von faserbewehrten Beton. *Beton* 31 (1981)
- Bonzel, J., Schmidt, M.: Verteilung und Orientierung von Stahlfasern im Beton und ihrer Einfluss auf die Eigenschaften von Stahlfaserbeton. *Betontechnische Berichte* (1984)
- Bui, H.D.: Failure mechanics of fibre-reinforced concrete and pre-damage structures. Brite-Euram Project, P-89-3275, Task Report 3, EDF, Paris (1991)
- Burt, N.J., Dougill, J.W.: Progressive failure in a model heterogeneous medium. *ASCE Journal of Engineering Mechanics* 103, 365–376 (1977)
- Caballero, A., Carol, I., Lopez, C.M.: New results in 3d meso-mechanical analysis of concrete specimens using interface elements. In: Meschke, G., de Borst, R., Mang, H., Bicanic, N. (eds.) *Computational Modelling of Concrete Structures, EURO-C*, pp. 43–52. Taylor and Francis, Abington (2006)
- Cachim, P.B.: Experimental and numerical analysis of the behaviour of structural concrete under fatigue loading with applications to concrete pavements. PhD Thesis, Faculty of Engineering of the University of Porto (1999)
- Cachim, P.B., Figueiras, J.A., Pereira, P.A.A.: Fatigue behavior of fiber-reinforced concrete in compression. *Cement & Concrete Composites* 24, 211–217 (2002)
- Campione, G., Mendola, L.L., Papia, M.: Flexural behaviour of concrete corbels containing steel fibers or wrapped with FRP sheets. *Materials and Structures* 38, 617–625 (2005a)
- Campione, G., Cucchiara, C., La Mendola, L., Papia, M.: Steel-concrete bond in lightweight fiber reinforced concrete under monotonic and cyclic actions. *Engineering Structures* 27, 881–890 (2005b)
- Canova, P., Rossi, P., Schaller, I.: Can steel fibers replace transverse reinforcements in reinforced concrete beams. *ACI Materials Journal* 94(5), 341–354 (1997)
- Carol, I., López, C.M., Roa, O.: Micromechanical analysis of quasi-brittle materials using fracture-based interface elements. *Int. J. Numer. Methods Eng.* 52, 193–215 (2001)



- Casanova, P., Rossi, P.: Analysis and design of steel fibre reinforced concrete beams. *ACI Structural Journal* 94(5), 595–602 (1997)
- Chang, D.I., Chai, W.K.: Flexural fracture and fatigue behavior of steel-fiber-reinforced concrete structures. *Nucl. Eng. Des.* 156, 201–207 (1995)
- Chen, E.: Non-local effects on dynamic damage accumulation in brittle solids, I. *J. Num. Anal. Meth. Geomech.* 23, 1–21 (1999)
- Chen, J., Yuan, H., Kalkhof, D.: A nonlocal damage model for elastoplastic materials based on gradient plasticity theory, Report Nr. 01-13, Paul Scherrer Institut., 1, 13, 1-130 (2001)
- Chenkui, H., Guofan, Z.: Properties of steel fibre reinforced concrete containing larger coarse aggregate. *Cement and Concrete Composite* 17, 199–206 (1995)
- Chunxiang, Q., Patnaikuni, I.: Properties of high strength fiber-reinforced concrete beams in bending. *Cement and Concrete Composites* 21, 73–81 (1999)
- Cornelissen, H.A.W.: Fatigue failure of concrete in tension. *Heron* 29(4), 68 (1984)
- Chuang, E., Ulm, F.-J.: Two-phase composite model for high performance cementitious composites. *J. Engineering Mechanics* 128(12), 1314–1323 (2002)
- Chung, J.W., Ross, A., Hosson, J.T.M.: Fracture of disordered three-dimensional spring networks: a computer simulation technology. *Physical Review B* 54(21), 15095–15100 (1996)
- Cusatis, G., Bazant, Z.P., Cedolin, L.: Confinement-shear lattice model for concrete damage in tension and compression: I. theory. *ASCE Journal of Engineering Mechanics* 129(12), 1439–1448 (2003)
- Cusatis, G., Schauffert, E.A., Pelessone, D., O’Daniel, J.L., Marangi, P., Stacchini, M., Savoia, M.: Lattice discrete particle model for fiber reinforced concrete with application to the numerical simulation of armoring systems. In: Bicanic, N., de Borst, R., Mang, H., Meschke, G. (eds.) *Computational Modelling of Concrete Structures*, pp. 291–300. Taylor and Francis, Abington (2010)
- D’Addetta, G.A., Kun, F., Ramm, E.: In: the application of a discrete model to the fracture process of cohesive granular materials. *Granular Matter* 4, 77–90 (2002)
- David, A.F., Naaman, A.E.: Stress-strain properties of fiber reinforced mortar in compression. *ACI Materials Journal* 475–483 (1985)
- DBV-Merkblatt: Technologie des Stahlfaserbetons und Stahlfaserspritzbetons (1996a)
- DBV-Merkblatt: Grundlagen zur Bemessung von Industriefußböden aus Stahlfaserbeton (1996b)
- DBV-Merkblatt: Stahlfaserbeton (2001)
- de Borst, R., Sluys, L.J., Mühlhaus, H.-B., Pamin, J.: Fundamental issues in finite element analyses of localization of deformation. *Engineering Computations* 10, 99–121 (1993)
- de Borst, R., Pamin, J., Geers, M.: On coupled gradient-dependent plasticity and damage theories with a view to localization analysis. *European Journal of Mechanics A/Solids* 18(6), 939–962 (1999)
- Deutscher Ausschuss für Stahlbeton (DAfStB): Richtlinie Stahlfaserbeton (22. und 23. Entwurf). Ergänzung zu DIN 1045-1, Teile 1-4 (Dezember 2005)
- Ding, Y., Kusterle, W.: Compressive stress-strain relationship of steel fibre-reinforced concrete at early age. *Cement and Concrete Research* 30, 1573–1579 (2000)
- di Prisco, M., Mazars, J.: Crush-crack - a non-local damage model for concrete. *Mechanics of Cohesive-Frictional Materials*, 321–347 (1996)
- Do, M.T., Chaallal, O., Aitcin, P.C.: Fatigue behavior of high performance concrete. *J. Mater. Civil Eng.* 5(1), 96–111 (1993)

- Donze, F.V., Magnier, S.A., Daudeville, L., Mariotti, C.: Numerical study of compressive behaviour of concrete at high strain rates, *Journal for Engineering Mechanics* 1154-1163 (1999)
- Dragon, A., Mróz, Z.: A continuum model for plastic-brittle behaviour of rock and concrete. *Int. Journ. Eng. Science* 17, 121–137 (1979)
- Dupont, D., Vandewalle, L.: Bending capacity of steel fibre reinforced (SFRC) beams. In: *Proc. Int. Congress on Challenges of Concrete Construction*, Dundee, pp. 81–90 (2002)
- Eckardt, S., Könke, C.: Simulation of damage in concrete structures using multiscale models. In: Meschke, G., de Borst, R., Mang, H., Bicanic, N. (eds.) *Computational Modelling of Concrete Structures*, EURO-C, pp. 77–83. Taylor and Francis, Abington (2006)
- Eibl, J., Bischoff, P.H., Bachman, G.: Failure mechanism of fibre-reinforced concrete and predamaged structures. Task Report – Brite Euram P-89-3275, Universität Karlsruhe (1991)
- Falkner, H., Henke, V.: *Stahlfaserbeton- konstruktive Anwendungen*. *Beton- und Stahlbetonbau* 95(10), 597–606 (2000)
- Falkner, H.: *Stahlfaserbeton – ein unberechenbares Material?* Bauseminar 2002. Braunschweig 164, 1–612 (2002)
- Foster, S. J., and Attard, M. M. Experimental tests on eccentrically loaded high strength concrete columns. *ACI Struct. J.* 94(3), 2295–2303 (1997)
- Foster, S. J. and Attard, M. M. Strength and ductility of fiber-reinforced high-strength concrete columns. *Journal of Structural Engineering* 127, 1 (2001)
- Frosch, R.J.: Behavior of large-scale reinforced concrete beams minimum shear reinforcement. *ACI Struct. J.* 97(6), 814–820 (2000)
- Furlan, S., de Hanai, J.: Shear behaviour of fiber reinforced concrete beams. *Cement and Concrete Composites* 19(4), 359–366 (1997)
- Furlan Jr., S.F., de Hanai, J.B.: Prestressed fiber reinforced concrete beams with reduced ratios of shear reinforcement. *Cement and Concrete Composites* 21, 213–221 (1999)
- Ganesan, N., Shivananda, K.P.: Spacing and width of cracks in polymer modified steel fibre reinforced concrete flexural members. In: *Proc. Int. Congress on Challenges of Concrete Construction*, Dundee, pp. 244–253 (2002)
- Gao, L., Hsu, T.C.C.: Fatigue of concrete under uniaxial compression cyclic loading. *ACI Mater. J.* 95(5), 575–581 (1998)
- Gasser, T.C., Holzzapfel, G.A.: 3d crack opening in unreinforced concrete. a two-step algorithm for tracking 3d crack paths. *Computer Methods in Applied Mechanics and Engineering* 195, 5198–5219 (2006)
- Ghalib, M.A.: Moment capacity of steel fiber reinforced small concrete slabs. *ACI Materials J.* 77(4), 247–257 (1980)
- Gitman, I.M., Askes, H., Sluys, L.J.: Coupled-volume multi-scale modelling of quasi-brittle material. *European Journal of Mechanics A/Solids* 27, 302–327 (2008)
- Glinicki, M.: Dimensioning of industrial floors of fibrous concrete with steel fibres (in polish). In: *Conference Warsztat pracy projektanta konstrukcji*, vol. IV, pp. 35–47 (2004)
- Gopalaratnam, V.S., Shah, S.P.: Strength deformation and fracture toughness of fiber cement composites at different rates of flexural loading. In: Shah, S.P., Skarendahl, A. (eds.) *US-Sweden Joint Seminar*, pp. 299–331. Elsevier, Amsterdam (1985)
- Gopalaratnam, V.S., Shah, S.P., Baton, G.B., Criswell, M.E., Ramaksishran, V., Wecharatara, M.: Fracture toughness of fiber reinforced concrete. *ACI Mater. J.* 88(4), 339–353 (1991)

- Gödde, L., Mark, P.: Numerical modeling of failure mechanisms and redistributions effects in steel fibre reinforced concrete slabs. In: Bicanic, N., de Borst, R., Mang, H., Meschke, G. (eds.) *Computational Modelling of Concrete Structures*, pp. 611–621. Taylor and Francis, Abington (2010)
- Granju, J.K., Ringot, E.: Amorphous iron fiber reinforced concretes and mortars, comparison of the fiber arrangement. *Acta Stereol.* 8, 579–584 (1989)
- Grassl, P., Jirasek, M.: Meso-mechanically motivated nonlocal models for modelling of the fracture process zone in quasi-brittle materials. In: Schrefler, B.A., Perego, U. (eds.) *Proc. 8th World Congress on Computational Mechanics WCCM8*, Venice, vol. 30.06-4.06 (2008)
- Grübl, P., Weigler, H., Karl, S.: *Beton, Arten, Herstellung und Eigenschaften*, vol. 2. Auflage, Ernst & Sohn, Berlin (2001)
- Grünewald, S.: Performance-based design of selfcompacting fibre reinforced concrete. Ph.D. Thesis, Delft University of Technology (2004)
- Grzybowski, M., Meyer, C.: Damage accumulation in concrete with and without fiber reinforcement. *ACI Mater. J.* 90(6), 594–604 (1993)
- Haktanir, T., Air, K., Altun, F., Karahan, O.: A comparative experimental investigation of concrete, reinforced concrete and steel-fibre concrete pipes under three-edge-bearing test. *Construction and Building Materials* 21, 1702–1708 (2007)
- Harajli, M.H., Maalouf, D., Khatib, H.: Effect of fibers on the punching shear strength of slab–column connections. *Cem. Concr. Res.* 17, 161–170 (1995)
- Hartman, T.: Steel fiber reinforced concrete. PhD Thesis, Royal Institute of Technology, Stockholm, Sweden, 38 (1999)
- He, H., Guo, Z., Stroeven, P., Stroeven, M., Sluys, L.: J. Influence of Particle Packing on Elastic Properties of Concrete. In: *Ist International Conference on Computational Technologies in Concrete Structures CTCS 2009*, Jeju, Korea, May 24–27 (2009)
- Henke, V., Empelmann, M.: Rissbreitenberechnung bei Kombibewehrung. *Beton- und Stahlbetonbau* 102(2), 66–79 (2007)
- Herrmann, H.J., Hansen, A., Roux, S.: Fracture of disordered elastic lattices in two dimensions. *Physical Rev. B* 39, 637–647 (1989)
- Hillerborg, A.: Determination and significance of the fracture toughness of steel fibre concrete. In: Shah, S.P. (ed.) *Proc. Steel Fiber Concrete US-Sweden Joint Seminar* (1983)
- Hilsdorf, H.K., Brameshuber, W., Kottas, R.: Abschlussbericht zum Forschungsvorhaben Weiterentwicklung und Optimierung der Materialeigenschaften faserbewehrten Betons und Spritzfaserbetons als Stabilisierungselemente der Felssicherung. Universität Karlsruhe (1985)
- Horii, H., Shin, H.C., Pallemwatta, T.M.: Mechanism of fatigue crack growth in concrete. *Cem. Concr. Compos.* 14, 83–89 (1992)
- Horszczaruk, E.: Wear abrasion model of cement concretes (in polish). Monograph. Szczecin University of Technology, Szczecin (2008)
- Höcker, T.: Einfluß von Stahlfasern auf das Verschleißverhalten von Betonen unter extremen Betriebsbedingungen in Bunkern von Abfallbehandlungsanlagen. *DafSfb*, Heft 488, Beuth Verlag (1996)
- Hsu, T.C.C.: Fatigue of plain concrete. *ACI Materials J.* 78, 292–305 (1981)
- Iman, M., Vandewalle, L., Mortelmans, F., Vanemert, D.: Shear domain of fibre-reinforced high strength concrete beams. *Engineering Structures* 9 (1997)
- Ibrahimbegovic, A., Markovic, D., Gatuing, F.: Constitutive model of coupled damage-plasticity and its finite element implementation. *Eur. J. Finite Elem.* 12(4), 381–405 (2003)

- JCI-S-002-003 Standard. Method of test for load-displacement curve of fiber reinforced concrete by use of notched beam (2003)
- Jenq, Y.S., Shah, S.P.: Application of two parameter fracture model to concrete and fiber reinforced concrete. In: Wittmann, F.H. (ed.) *Fracture Toughness and Fracture Energy of Concrete*. Elsevier, Amsterdam (1986)
- Jirasek, M., Bazant, Z.P.: Particle model for quasi-brittle fracture and application to sea ice. *J. Eng. Mech.* 121(9), 1016–1025 (1995)
- Jirasek, M.: Comments on microplane theory. In: Pijaudier-Cabot, G., Bittnar, Z., Gerard, B. (eds.) *Mechanics of quasi-brittle materials and structures*, pp. 55–77. Hermes Science Publications (1999)
- Johnston, C.D., Zemp, R.W.: Flexural fatigue performance of steel fiber reinforced concrete-influence of fiber content, aspect ratio, and type. *ACI Mater. J.* 88(4), 374–383 (1991)
- Jones, P.A., Austin, S.A., And Robins, P.J.: Predicting the flexural load-deflection response of steel fibre reinforced concrete from strain, crack-width, fibre pull-out and distribution data. *Materials and Structures* 41, 449–463 (2008)
- Juarez, C., Valdez, P., Duran, A., Sobolev, K.: The diagonal tension behavior of fiber reinforced concrete beams. *Cement & Concrete Composites* 29, 402–408 (2007)
- Jun, Z., Stang, H.: Fatigue performance in flexure of fiber reinforced concrete. *ACI Mater. J.* 95(1), 58–67 (1998)
- Kabele, P.: Multiscale framework for modeling of fracture in high performance fiber reinforced cementitious composites. *Engineering Fracture Mechanics* 74, 194–209 (2007)
- Karayannis, C.G.: A numerical approach to steel fibre reinforced concrete under torsion. *Structural and Engineering Review* 7(2), 83–91 (1995)
- Kawai, T.: New discrete models and their application to seismic response analysis of structure. *Nuclear Engineering and Design* 48, 207–229 (1978)
- Khuntia, M., Stojadinovic, B.: Shear strength of reinforced concrete beams without transverse reinforcement. *ACI Struct. J.* 98(5), 648–656 (2001)
- Klisiński, M., Mróz, Z.: Description of anelastic deformations and damage for concrete (in polish). Technical University of Poznań, 193 (1988)
- Kooiman, A.G.: Modelling steel fibre reinforced concrete for structural design. Ph.D. Thesis, TU Delft (2000)
- Kolluru, S.V., O'Neil, E.F., Popovics, J.S., Shah, S.P.: Crack propagation in flexural fatigue of concrete. *J. Eng. Mech.* 126(9), 891–898 (2000)
- Komlos, K., Babal, B., Nürnbergerova: Hybrid fibre-reinforced concrete under repeated loading. *Nuclear Engineering and Design* 156, 195–200 (1995)
- Kompfner, T.A.: Ein finites Elementmodell für die geometrisch und physikalisch nicht-lineare Berechnung von Stahlbetonschalen. PhD Thesis, University of Stuttgart, Germany (1983)
- Kozicki, J., Tejchman, J.: Discrete methods to describe the behaviour of quasi-brittle and granular materials. In: *Electronic Proceedings of 16th Engineering Mechanics Conference ASCE, University of Washington, Seattle, USA, July 16-18*, pp. 1–10 (2003)
- Kozicki, J., Tejchman, J.: 2D lattice model for fracture in brittle materials. *Archives of Hydro-Engineering and Environmental Mechanics* 53(2), 71–88 (2006)
- Kozicki, J.: Application of discrete models to describe the fracture process in brittle materials. PhD Thesis, Gdańsk University of Technology (2007)
- Kozicki, J., Tejchman, J.: Experimental investigations of strain localization in concrete using Digital Image Correlation (DIC) technique. *Archives of Hydro-Engineering and Environmental Mechanics* 54(1), 3–24 (2007a)

- Kozicki, J., Tejchman, J.: Effect of aggregate structure on fracture process in concrete using 2D lattice model. *Archives of Mechanics* 59(4-5), 1–20 (2007b)
- Kozicki, J., Tejchman, J.: Modelling of fracture processes in concrete using a novel lattice model. *Granular Matter* 10(5), 377–388 (2008)
- Kozicki, J.F.V., Donzé, F.V.: A new open-source software developed for numerical simulations using discrete modeling methods. *Comput. Methods Appl. Mech. Engrg.* 197, 4429–4443 (2008)
- Kozicki, J. and Tejchman, J.: Effect of steel fibres on concrete behavior in 2D and 3D simulations using lattice model. *Archive of Mechanics* (submitted, 2010).
- Krstulovic-Opara, N., Haghayeghi, A.R., Haidar, M., Krauss, P.D.: Use of conventional and high-performance steel-fiber reinforced concrete for bridge deck overlays. *ACI Mater. J.* 92(6), 669–677 (1995)
- Kulaa, J.: Fibre-reinforced concrete under uniaxial tensile loading. *Nordic Concrete Research* 14, 77–90 (1994)
- Kwak, K.H., Suh, J., Hsu, T.C.T.: Shear-fatigue behavior of steel fiber reinforced concrete beams. *ACI Struct. J.* 88(2), 155–160 (1991)
- Kwan, A.K.H., Ng, I.Y.T.: Adding steel fibres to improve shock vibration resistance of concrete. *Magazine of Concrete Research* 59(8), 587–597 (2007)
- Le Bellego, C., Dube, J.F., Pijaudier-Cabot, G., Gerard, B.: Calibration of nonlocal damage model from size effect tests. *European Journal of Mechanics A/Solids* 22, 33–46 (2003)
- Leite, J.P.B., Slowik, V., Mihashi, H.: Computer simulation of fracture processes of concrete using mesolevel models of lattice structures. *Cem. Concr. Res.* 34(6), 1025–1033 (2004)
- Lee, M.K., Barr, B.I.G.: An overview of the fatigue behaviour of plain and fibre reinforced concrete. *Cement & Concrete Composites* 26, 299–305 (2004)
- Li, V. C., Wang, Y. J. and Backers, S. A micromechanical model of tension-softening and bridging toughening of short random fiber reinforced brittle matrix composites. *J. Mech. Phys. Solids*, 39( 5), 607-625 (1991)
- Li, V. C., H., Horii, H., Kabele, P., Kanda, T. and Lim, Y. M. Repair and retrofit with engineered cementitious composites. *Engineering Fracture Mechanics* 65, 317-334 (2000)
- Lilliu, G., van Mier, J.G.M.: 3d lattice type fracture model for concrete. *Engineering Fracture Mechanics* 70, 927–941 (2003)
- Lim, T.Y., Paramaivam, P., Lee, S.L.: Analytical model for tensile behaviour of steel-fibre concrete. *ACI Materials Journal* (1987)
- Lim, D.H., Oh, B.H.: Experimental and theoretical investigation on the shear of steel fibre reinforced concrete beams. *Engineering Structures* 21, 937–944 (1999)
- Lin, Y.-Z.: *Tragverhalten von Stahlfaserbeton*, Deutscher Ausschuss für Stahlbeton, Heft 494, Berlin, Beuth Verlag GmbH (1999)
- Linsel, S.: *Magnetische Positionierung von Stahlfasern in zementösen Medien*. PhD. Thesis, Technische Universität Berlin (2005)
- Lodygowski, T., Perzyna, P.: Numerical modelling of localized fracture of inelastic solids in dynamic loading process. *Int. J. Num. Meth. Eng.* 40(22), 4137–4158 (1997)
- Liu, T.C.Y., Nilson, A.H., Slate, F.O.: Biaxial stress-strain relationships for concrete. *ASCE Journal of Engineering Mechanics* 103, 423–439 (1996)
- Lohrmann, G.: *Faserbeton unter hoher Dehngeschwindigkeit*. PhD Thesis, University of Karlsruhe, 33 (1999)
- Loret, B., Prevost, J.H.: Dynamic strain localisation in elasto-visco-plastic solids, Part 1. General formulation and one-dimensional examples. *Comp. Appl. Mech. Eng.* 83, 247–273 (1990)

- Maalej, M., Li, V.: Flexural strength of fiber cementitious composites. *Journal of Materials in Civil Engineering* 6, 5 (1994)
- Mangat, P.S., Azari, M.M.: A theory for the creep of steel fiber reinforced cement matrices under compression. *Journal of Materials Science* 20, 1119–1133 (1985)
- Mangat, P.S., Azari, M.M.: Shrinkage of steel fiber reinforced cement composites. *Mat. Struct.* 21, 163–171 (1988)
- Mansur, M.A., Ong, K.C.G., Paramisivam, P.: Shear strength fibrous concrete beams without stirrups. *Journal of Structural Engineering* 12(9), 2066–2079 (1986)
- Markovic, I.: High-performance hybrid-fibre concrete. Ph.D. Thesis, Delft University of Technology (2006)
- McHarg, P.J., Cook, W.D., Mitchell, D., Yoon, Y.S.: Benefits of concentrated slab reinforcement and steel fibers on performance of slab–column connections. *ACI Struct. J.* 97(2), 225–234 (2000)
- Menetrey, P., Willam, K.J.: Triaxial failure criterion for concrete and its generalization. *ACI Structural Journal*, 311–318 (1995)
- Mindes, S., Banthia, N., Bentur, A.: The response of reinforced concrete beams with a fibre concrete matrix to impact loading. *Int. J. of Cement Composites and Lightweight Concrete* 8(3), 165–170 (1986)
- Mirsayah, A.A., Banthia, N.: Shear strength of steel fiber-reinforced concrete. *ACI Struct. J.* 99(5), 473–479 (2002)
- Mohammadi, Y., Singh, S.P., Kaushik, S.K.: Properties of steel fibrous concrete containing mixed fibres in fresh and hardened state. *Construction and Building Materials* 22, 956–965 (2008)
- Moonen, P., Carmeliet, J., Sluys, L.J.: A continuous-discontinuous approach to simulate fracture processes. *Philosophical Magazine* 88, 3281–3298 (2008)
- Morris, A.D., Garrett, G.G.: A comparative study of the static and fatigue behaviour of plain and steel fibre reinforced mortar in compression and direct tension. *Int. J. Cem. Compos. Lightweight Concr.* 3(2), 73–91 (1981)
- Mróz, Z.: Mathematical models of inelastic concrete behaviour, pp. 47–72. University Waterloo Press, Waterloo (1972)
- Mühlhaus, H.-B.: Application of Cosserat theory in numerical solutions of limit load problems. *Ing. Arch.* 59, 124–137 (1989)
- Mühlhaus, H.-B., Aifantis, E.C.: A variational principle for gradient plasticity. *Int. J. Solids Structures* 28, 845–858 (1991)
- Naaman, A.E., Hammoud, H.: Fatigue characteristics of high performance fiber-reinforced concrete. *Cem. Concr. Compos.* 20, 353–363 (1998)
- Nammur, G.G., Naaman, A.E.: Strain rate effects of tensile properties of fiber reinforced concrete. In: Mindess, S., Shah, S.P. (eds.) *Symposia Proceedeengs Cement-based composites – strain rate effects on fracture*, Pittsburgh, vol. 64, pp. 97–118 (1986)
- Narayaman, R., Darwish, I.Y.S.: Shear in mortar beams containing fibers and fly-ash. *ACI Structural Journal* 114(1), 84–102 (1988)
- Neddleman, A.: Material rate dependence and mesh sensitivity in localization problems. *Comp. Meths. Appl. Mech. Eng.* 67, 69–85 (1988)
- Neville, A.M.: Properties of concrete, pp. 628–645. Pitmann Publishing Ltd., Great Britain (1994)
- Noghabai, K.: Beams of fibrous concrete in shear and bending: experiment and model. *J. Struct. Eng.* 126(2), 243–251 (2000)
- Nooru-Mohamed. M.: Mixed mode fracture of concrete: an experimental approach. Ph.D Thesis, Delft University of Technology (1992)

- Oh, B.H.: Fatigue-life distributions of concrete for various stress levels. *ACI Mater. J.* 88(2), 122–128 (1991)
- Ong, K.C.G., Basheerkhan, M., Paramasivam, P.: Resistance of fibre concrete slabs to low velocity projectile impact. *Cement and Concrete Composites* 21(5-6), 391–401 (1999)
- Ortiz, N., Pandolfi, A.: Finite-deformation irreversible cohesive elements for three-dimensional crack-propagation analysis. *Int. Journal for Numerical Methods in Engineering* 44, 1267–1282 (1999)
- Padmarajaiah, S.K., Ramaswamy, A.: Behavior of fiber-reinforced prestressed and reinforced high-strength concrete beams subjected to shear. *ACI Struct. J.* 98(5), 752–761 (2001)
- Paine, K.A., Elliott, K.S., Peaston, C.H.: Flexural toughness as a measure of shear strength and ductility of prestressed fibre reinforced concrete beams. In: *Proc. Int. Congress on Challenges of Concrete Construction, Dundee*, pp. 200–212 (2002)
- Palaniswamy, R., Shah, S.P.: Fracture and stress-strain relationship of concrete under triaxial compression. *ASCE Journal of Engineering Mechanics* 100, 901–916 (1974)
- Pamin, J.: Gradient-enhanced continuum models: formulation, discretization and applications. Monograph, Cracow University of Technology (2004)
- Pamin, J., de Borst, R.: Simulation of crack spacing using a reinforced concrete model with an internal length parameter. *Arch. App. Mech.* 68(9), 613–625 (1998)
- Paskova, T., Meyer, C.: Low-cycle fatigue of plain and fiber-reinforced concrete. *ACI Mater. J.* 94(4), 273–285 (1997)
- Peerlings, R.H., de Borst, R., Brekelmans, W.A.M., Geers, M.G.D.: Gradient enhanced damage modelling of concrete fracture. *Mechanics of Cohesive-Frictional Materials* 3, 323–342 (1998)
- Peng, X., Meyer, C.: A continuum damage mechanics model for concrete reinforced with randomly distributed short fibres. *Comput. Struct.* 78, 505–515 (2000)
- Pietruszczak, S., Jiang, J., Mirza, F.A.: An elastoplastic constitutive model for concrete. *Int. J. Solids Structures* 24(7), 705–722 (1988)
- Pijaudier-Cabot, G., Bazant, Z.: Nonlocal damage theory. *ASCE Journal of Engineering Mechanics* 113, 1512–1533 (1987)
- Pompo, A., Stupak, P.R., Nicolais, L., Marchese, B.: Analysis of steel fibre pull-out from a cement matrix using video photography. *Cement and Concrete Composites* 18, 3–8 (1996)
- Radtke, F.K.F., Simone, A., Sluys, L.J.: An efficient computational model for fibre reinforced concrete incorporating information from multiple scales. In: Schrefler, B.A., Perego, U. (eds.) *Proc. 8th. World Congress on Computational Mechanics WCCM8, Venice*, 30.06–4.06 (2008)
- Radtke, F., Simone, A., Sluys, L.J.: A computational model for failure in fibre reinforced concrete including the influence of discrete fibre distributions. In: *Proc. 1st Int. Conf. Computational Technologies in Concrete Structures, CTCS 2009*, pp. 767–781 (2009)
- Radtke, F., Simone, A., Sluys, L.J.: A computational model for failure analysis of fibre reinforced concrete with discrete treatment of fibres. *Engng. Fracture Mech.* 77, 597–620 (2010)
- Rafeeq, A.S., Gupta, A., Krishnamoorthy, S.: Influence of steel fibers in fatigue resistance of concrete in direct compression. *J. Mater. Civil Eng.* 12(2), 172–179 (2000)
- Ramakrishnan, V., Lokvik, B.J.: Flexural fatigue strength of fiber reinforced concretes. In: Reinhardt, H.W., Naaman, A.E. (eds.) *High Performance Fiber Reinforced Cement Composites: Proceedings of the International RILEM/ACI Workshop*, pp. 271–287. E&FN SPON, London (1992)

- Redon, C., Chermant, J.-L.: Damage mechanics applied to concrete reinforced with amorphous cast iron fibers, concrete subjected to compression. *Cement and Concrete Composites* 21, 197–204 (1999)
- RILEM TC 162-TDF. Test and design methods for steel fibre reinforced concrete – uniaxial tension test for steel fibre reinforced concrete. *Mater. Struct.* 34(1), 3–6 (2001)
- RILEM TC 162-TDF, Test and design methods for steel fibre reinforced concrete sigma-epsilon-design method. *Materials and Structures* 36(262), 560–567 (2003)
- Robins, P.J., Austin, S.A., Jones, P.A.: Spatial distribution of steel fibres in sprayed and cast concrete. *Magazine of Concrete Research* 55(3), 225–235 (2003)
- Roesler, J.R., Lange, D.A., Altoubat, S.A., Rieder, K.-A., Ulreich, G.R.: Fracture of plain and fiber-reinforced concrete slabs under monotonic loading. *ASCE J. Mater. Civil Eng.* 6(5), 452–460 (2004)
- RÖVBB Richtlinie der Österreichischen Vereinigung für Beton und Bautechnik, Faserbeton, Wien (2002)
- Saito, M.: Characteristics of microcracking in concrete under static and repeated tensile loading. *Cement Concrete Research* 17, 211–218 (1987)
- Sakaguchi, H., Mühlhaus, H.-B.: Mesh free modelling of failure and localisation in brittle materials. In: Asaoka, A., Adachi, T., Oka, F. (eds.) *Deformation and Progressive Failure in Geomechanics*, pp. 15–21 (1997)
- SCA Swedish Concrete Association, Stålfiberbetong – rekommendationer för konstruktion, utförande och provning (1997)
- Schlangen, E., Garboczi, E.J.: Fracture simulations of concrete using lattice models: computational aspects. *Engineering Fracture Mechanics* 57, 319–332 (1997)
- Schnütgen, B.: Bemessung von Stahlfaserbeton und ihre Problematik, vol. 37. Ruhr-Universität Bochum (1981)
- Schnütgen, B., Teutsch, M.: Beonbauwerke aus Stahlfaserbeton beim Umgang mit umweltgefährdenden Stoffen. *Beton- und Stahlbetonbau* 96(7), 451–457 (2001)
- Schönlin, K.: Ein Verfahren zur Ermittlung der Orientierung und Menge der Fasern im faserbewehrten Beton. Diplomarbeit, Universität Karlsruhe (1983)
- Schulz, M.: Einsatz von Stahlfaserbeton beim Bau von Schrottplätzen. *Stahlfaserbeton – ein unberechenbares Material?* Bauseminar, Braunschweig 164, 47–63 (2002)
- Sendeckyj, G.P.: Constant life diagrams-a historical review. *Int. J. Fatigue* 23, 347–353 (2001)
- Shah, S.P., Rangan, B.V.: Effect of reinforcements of ductility of concrete. In: *ASCE Proc.*, vol. 96(ST6), pp. 1167–1183 (1970)
- Shah, S.P., Rangan, B.V.: Fiber reinforced concrete properties. *ACI Journal* 68(2), 126–135 (1971)
- Shah, S.P.: Fiber reinforced concrete. *Am. Concr. Inst.* 12(3), 81–82 (1990)
- Shah, S.P., Ouyang, C.: Mechanical behaviour of fiber-reinforced cement-based composites. *Journal of the American Ceramic Society* 74(11), 2227–2238 (1991)
- Shaheen, E., Shrive, N.G.: Cyclic loading and fracture mechanics of Ductal concrete. *Int. J. Fract.* 148, 251–260 (2007)
- Shin, S.W., Oh, J.G., Ghosh, S.K.: Shear behavior of laboratory-sized high strength concrete beams reinforced with bars and steel fibers, SP-142-10. American Concrete Institute, 181–200 (1994)
- Shi, X.P., Fwa, T.F., Tan, S.A.: Flexural fatigue strength of plain concrete. *ACI Mater. J.* 90(5), 435–440 (1993)
- Shoemake, K.: Quaternion calculus and fast animation. SIGGRAPH course notes (1985)



- Simo, J.C., Oliver, J., Armero, F.: An analysis of strong discontinuities induced by strain-softening in rate-independent inelastic solids. *Computational Mechanics* 12, 277–296 (1993)
- Simone, A., Sluys, L.J.: The use of displacement discontinuities in a rate-dependent medium. *Computer Methods in Applied Mechanics and Engineering* 193, 3015–3033 (2004)
- Singh, S.P., Kaushik, S.K.: Flexural fatigue life distributions and failure probability of steel fibrous concrete. *ACI Mater. J.* 297(6), 658–667 (2000)
- Sivakumar, A., Santhanam, M.: A quantitative study on the plastic shrinkage cracking in high strength hybrid fibre reinforced concrete. *Cement & Concrete Composites* 29, 575–581 (2007a)
- Sivakumar, A., Santhanam, M.: Mechanical properties of high strength concrete reinforced with metallic and non-metallic fibres. *Cement and Concrete Composites* 29, 603–608 (2007b)
- Skarżyński, Ł., Tejchman, J.: Mesoscopic modelling of strain localization in concrete. *Archives of Civil Engineering* LV 4, 521–540 (2009)
- Skarżyński, Ł., Tejchman, J.: Calculations of fracture process zones on meso-scale in notched concrete beams subjected to three-point bending. *European Journal of Mechanics / A Solids* 29, 746–760 (2010)
- Sluys, L.: Wave propagation, localisation and dispersion in softening solids, PhD thesis. Delft University of Technology (1992)
- Sluys, L., de Borst, R.: Dispersive properties of gradient and rate-dependent media. *Mech. Mater.* 183, 131–149 (1994)
- Smadi, M.M., Bani Yasin, I.S.: Behavior of high-strength fibrous concrete slab-column connections under gravity and lateral loads. *Construction and Building Materials* 22, 1863–1873 (2008)
- Song, P.S., Hwang, S., Sheu, B.C.: Statistical evaluation for impact resistance of steel-fibre-reinforced concretes. *Magazine of Concrete Research* 56(8), 437–442 (2004)
- Soroushian, P., Lee, C.D.: Distribution and orientation of fibers in steel fiber reinforced concrete. *ACI Materials Journal* 87, 5 (1990)
- Soulioti, D.V., Barkoula, N.M., Paipetis, A., Matikas, T. E.: Effects of fibre geometry and volume fraction on the flexural behaviour of steel-fibre reinforced concrete. *Strain* (in print, 2010)
- Spadea, G., Bencardino, F.: Behavior of fiber-reinforced concrete beams under cyclic loading. *J. Struct. Eng.* 123(5), 660–668 (1997)
- Stamm, M.: Schädigungsevolution von Stahlfaserbeton. *Beton und Stahlbetonbau* 97(2), 365–371 (2002)
- Stähli, P., Custer, R., van Mier, J.G.M.: On flow properties, fibre distribution, fibre orientation and flexural behaviour of FRC. *Materials and Structures* 41, 189–196 (2008)
- Stroeven, P., Shah, S.P.: Use of radiography-image analysis for steel fibre reinforced concrete. In: *Testing and Test Methods of Fiber Content Cement Composites*. RILEM Symposium. Construction Press Ltd. (1978)
- Suaris, W., Shah, S.P.: Strain rate effects in fibre-reinforced concrete subjected to impact and impulsive loading. *Composites* 13, 153–159 (1982)
- Suaris, W., Shah, S.P.: Test methods for impact resistance of fiber reinforced concrete. In: Hoff, G.C. (ed.) *Proceedings of an International Symposium on Fiber Reinforced Concrete*, American Concrete Institute, Detroit, vol. ACI SP-81, pp. 247–265 (1984)
- Su, E.C.M., Hsu, T.C.C.: Biaxial compression fatigue and discontinuity of concrete. *ACI Mater. J.* 3, 78–188 (1988)

- Sun, W., Janming, G.: A study on the fatigue performance of SFRC. In: Proc. on Research on SFRC, pp. 49–60. Dalian University of Technology, China (1990)
- Sun, W., Gao, J., Yan, Y.: Study of the fatigue of steel fiber reinforced concrete. *ACI Materials Journal* 5, 217–225 (1992)
- Suwada, H., Fukuyama, H.: Nonlinear finite element analysis on shear failure of structural elements HPRCC. *J. Advanced Cement Technology* 4(11), 45–57 (2006)
- Swamy, R.N., Stavrides, H.: Influence of fiber reinforcement on restrained shrinkage and cracking. *ACI J.*, 443–460 (1979)
- Swamy, R.N., Sar, A.: Punching shear behavior of reinforced slab–column connections made with steel fiber concrete. *ACI J. Proc.* 79(5), 392–406 (1982)
- Swamy, R.N., Bahla, H.M.: The effectiveness of steel fibres as shear reinforcement. *Concrete International*, 35–40 (1985)
- Swamy, R.N., Jones, R., Chiam, T.P.: Influence of steel fibers on the shear resistance of lightweight concrete I-beams. *ACI Struct. J.* 90(1), 103–114 (1993)
- Szumigała, E., Jasiczek, J., Zieliński, K.: Cemeticious concretes with steel fibres – characteristics and own experiments (in polish), *Industrial floors*, Adiment Polska, Poznań, pp. 81–100 (2001)
- Tajima, K., Shirai, N.: Numerical prediction of crack width in reinforced concrete beams by particle model. In: Meschke, G., de Borst, R., Mang, H., Bicanic, N. (eds.) *Computational Modelling of Concrete Structures, EURO-C*, pp. 221–230. Taylor and Francis, Abington (2006)
- Tan, K.H., Murugappan, K., Paramasivam, P.: Shear behavior of fiber reinforced concrete beams. *ACI Struct. J.* 90(1), 3–11 (1993)
- Tan, K.H., Paramasivam, P., Murugappan, K.: Steel fibers as shear reinforcement in partially prestressed beams. *ACI Struct. J.* 92(6), 643–652 (1995)
- Tejchman, J., Wu, W.: Numerical study on shear band patterning in a Cosserat continuum. *Acta Mechanica* 99, 61–74 (1993)
- Tejchman, J.: FE modeling of shear localization in granular bodies with micro-polar hypoplasticity. In: Wu, W., Borja, R. (eds.) *Springer Series in Geomechanics and Geoengineering*. Springer, Heidelberg (2008)
- The Concrete Society. *Concrete industrial ground floors – a guide to design and construction*. 3rd ed. Technical Report 34 (2003)
- Topcu, I.B., Canbaz, M.: Effect of different fibers on the mechanical properties of concrete containing fly ash. *Construction and Building Materials* 21, 1486–1491 (2007)
- Tosun, K., Yazıcı, H., Yigiter, H., Aydın, S.: An investigation on sulphate resistance of mortars containing fly ash. TMMOB, Chamber of civil engineers. In: 5th National concrete congress proceedings, Istanbul, Turkey, pp. 17–26 (2003)
- Tye, N.V., Henze, S., Küchler, M., Schenck, G., Wille, K.: Ein optoanalytisches Verfahren zur Bestimmung der Faserverteilung und –orientierung in stahlfaserverstärktem UHFB. *Beton- und Stahlbetonbau* 10, 674–680 (2007), doi:10.1002/best.200700568
- Ulfkjaer, J., Krek, S., Brincker, R.: Analytical model for fictitious crack propagation in concrete beam. *ASCE J. Eng. Mech.* 121(1), 7–15 (1995)
- Unal, O., Uygunoglu, T.: An investigation on freezing-thawing durability of concretes with fly ash. In: Turkish ready mixed concrete association, concrete 2004 congress proceeding, Istanbul, Turkey, pp. 376–386 (2004)
- van Hauwaert, A., van Mier, J.G.M.: Computational modeling of the fibre-matrix bond in steel fibre reinforced concrete. In: Mihashi, H., Rokugo, K. (eds.) *Fracture Mechanics of Concrete Structures*, pp. 561–571. Aedificatio Publishers, Freiburg (1998)

- van Mier, J.G.M., Schlangen, E., Vervuurt, A.: Lattice type fracture models for concrete. In: Mühlhaus, H.-B. (ed.) *Continuum Models for Materials with Microstructure*, pp. 341–377. John Wiley & Sons, Chichester (1995)
- van Mier, J.G.M., van Vliet, M.R.A.: Influence of microstructure of concrete on size/scale effects in tensile fracture. *Engineering Fracture Mechanics* 70(16), 2281–2306 (2003)
- van Vliet, M.R.A., van Mier, J.G.M.: Experimental investigation of concrete fracture under uniaxial compression. *Mechanics of Cohesive-Frictional Materials* 1, 115–127 (1996)
- van Vliet, M.R.A.: Size effect in tensile fracture of concrete and rock. PhD thesis (2000)
- Vervuurt, A., van Mier, J.G.M., Schlangen, E.: Lattice model for analyzing steel-concrete interactions. In: Siriwardane, Zaman (eds.) *Computer Methods and Advances in Geomechanics*, Balkema, Rotterdam, pp. 713–718 (1994)
- Vidya Sagar, R.: Size effect in tensile fracture of concrete - a study based on lattice model applied to ct-specimen. In: *Proc. 21st Intern. Congress on Theoretical and Applied Mechanics, ICTAM 2004, Warsaw*, pp. 1–2 (2004) (cd-rom)
- Vorechovsky, M., Elias, J.: Relations between structure size, mesh density and element strength of lattice models. In: Bicanic, N., de Borst, R., Mang, H., Meschke, G. (eds.) *Computational Modelling of Concrete Structures*, pp. 419–431. Taylor and Francis, Abington (2010)
- Wafa, F.F., Ashour, S.A.: Mechanical properties of high-strength fiber reinforced concrete. *ACI Materials Journal* 89(5), 449–455 (1992)
- Walraven, J.C., Grünewald, S.: Regelung und Anwendung des Stahlfaserbetons in den Niederlanden. *Stahlfaserbeton – ein unberechenbares Material. Bauseminar 2002, Braunschweig* 164, 47–63 (2002)
- Walton, P.L., Majumdar, A.: Cement based composites with mixtures of different types of fibres. *J. Composite* 6, 209–216 (1975)
- Wang, N., Mindess, S., Ko, K.: Fibre reinforced concrete beams under impact loading. *Cement and Concrete Research* 26(3), 363–376 (1996)
- Ward, R.J., Li, V.C.: Dependence of flexural behavior of fiber reinforced mortar on material fracture resistance and beam size. *ACI Materials Journal* 87, 6 (1990)
- Wecharatana, M., Shah, S.P.: A model for predicting fracture resistance of fiber reinforced concrete. *Cement Concrete Research* 13, 819–829 (1983)
- Wells, G., Sluys, L.: A new method for modeling of cohesive cracks using finite elements. *Int. Journ. for Numerical Methods in Engineering* 50(12), 2667–2682 (2001)
- Wichmann, H.-J., Niemann, P., Droese, S.: Messung des Stahlfasergehaltes auf elektromagnetischer Basis. *Forschungsarbeiten aus dem Institut für Baustoffe. Massivbau und Brandschutz der Universität Braunschweig, Heft 144, Braunschweig* (1999)
- Yao, W., Lib, J., Wu, K.: Mechanical properties of hybrid fiber-reinforced concrete at low fiber volume fraction. *Cement Concrete Research* 33, 27–30 (2003)
- Yazıcı, S., Inan, G., Tabak, V.: Effect of aspect ratio and volume fraction of steel fiber on the mechanical properties of SFRC. *Construction and Building Materials* 21, 1250–1253 (2007)
- Yin, W., Hsu, T.C.C.: Fatigue behavior of steel fiber reinforced concrete in uniaxial and biaxial compression. *ACI Mater. J.* 92(1), 71–81 (1995)
- Yip, M., Li, Z., Liao, B.S., Bolander, J.E.: Irregular lattice models of fracture of multiphase particulate. *Int. J. Fract.* 140, 113–124 (2006)
- Zbib, H.M., Aifantis, C.E.: A gradient-dependent flow theory of plasticity: application to metal and soil instabilities. *Appl. Mech. Reviews* 42(11), 295–304 (1989)

- Zhang, B., Phillips, D.V., Wu, K.: Effects of loading frequency and stress reversal on fatigue life of plain concrete. *Mag. Concr. Res.* 48(177), 361–375 (1996)
- Zhang, J., Stang, H.: Fatigue performance in flexure of fiber reinforced concrete. *ACI Mater. J.* 95(1), 58–67 (1998)
- Zhang, J., Stang, H., Li, V.C.: Experimental study on crack bridging in FRC under uniaxial fatigue tension. *J. Mater. Civil Eng.* 12, 66–73 (2000)
- Zhang, J.: Modeling of the influence of fibers on creep of fiber reinforced cementitious composite. *Composites Science and Technology* 63, 1877–1884 (2003)
- Zollo, R.F.: Fiber-reinforced concrete: an overview after 30 years of development. *Cement Concrete Compos* 19(2), 107–122 (1997)

## List of Symbols

$A_f$	fibre area
$E$	modulus of elasticity
$G$	shear modulus
$d_f$	fibre diameter
$f_c$	compressive strength
$f_t$	tensile strength
$f_y$	yield stress
$k$	stiffness parameter
$l_c$	characteristic length of micro-structure
$l_f$	fibre length
$l_H$	anchorage length
$l_r$	rod length
$p$	stiffness ratio
$V_f$	fibre volume
$\varepsilon$	normal strain
$\varepsilon_{min}$	threshold local normal strain
$\varepsilon_{crit}^{gl}$	critical global strain increment
$\varepsilon_{22}$	vertical normal strain
$\sigma$	normal stress
$\sigma_{22}$	vertical normal stress
$\tau_m$	mean bond shear stress
$\omega$	weighting function
SFRC	steel fibre reinforced concrete
FRC	fibre reinforced concrete
FA	fly ash
ITZ	interfacial transition zone

# Springer Series in Geomechanics and Geoengineering

---

**Edited by W. Wu, R.I. Borja**

Tejchman, J.  
Shear Localization in  
Granular Bodies with Micro-Polar  
Hypoplasticity  
316 p. 2008 [978-3-540-70554-3]

Iskander, M.  
Modelling with Transparent Soils  
331 p. 2010 [978-3-642-02500-6]

Tejchman, J. and Kozicki, J.  
Experimental and Theoretical  
Investigations of  
Steel-Fibrous Concrete  
289 p. 2010 [978-3-642-14602-2]

## Summary

Concrete is still the most widely used construction material since it has the lowest ratio between cost and strength as compared to other available materials. However, it has two undesirable properties, namely: low tensile strength and large brittleness (low energy absorption capacity) that cause the collapse to occur shortly after the formation of the first crack. To improve these two negative properties and to achieve a partial substitute of conventional reinforcement, the addition of short discontinuous randomly oriented fibres (steel, glass, synthetic and natural) can be practiced among others. Steel fibres are the most used in concrete applications due to economy, manufacture facilities, reinforcing effects and resistance to the environment aggressiveness.

The inclusion of steel fibres improves the following properties of concrete during quasi-static and dynamic loading: flexural tensile strength, splitting tensile strength, ductility, first cracking strength, toughness (energy absorption capacity), stiffness, durability, impact resistance, fatigue, wear strength, shock vibration resistance, freeze-thaw resistance, shrinkage and creep since fibres limit the formation and growth of cracks by providing pinching forces at crack tips (they help in bridging the propagating cracks). The most important positive property is an increase of ductility. However, concrete workability decreases, and both concrete sorptivity and volumetric weight increase at the same time with an increase of fibres. The degree of concrete improvement depends upon: size, shape, anchorage, aspect ratio, volume fraction, orientation and surface roughness of fibres, ratio between fibre length and maximum aggregate size, volume ratio between long and short fibres and concrete class. In particular, the effect of the fibre orientation is of a major importance dependent upon flow direction of concrete against the casting direction.

The book consists of 2 main parts. The first one summarizes the most important mechanical and physical properties of steel-fibre-added concrete and reinforced concrete on the basis of experiments described in the scientific literature. The second one describes a fracture process at meso-scale in plain concrete and in fibrous concrete using a novel discrete lattice model. 2D and 3D calculations of plain concrete were performed for a uniaxial compression, uniaxial tension and shear-extension test. In addition, a size effect was studied. In 2D and 3D analyzes of fibrous concrete specimens under uniaxial tension and three-point bending, the effect of the fibre volume, fibre distribution, fibre orientation, fibre length, fibrous bond strength and specimen size on the load-displacement curve and fracture process was carefully analyzed. The calculated results were qualitatively in good agreement with the experimental results.